NUCLEAR MAGNETIC RESONANCE STUDIES OF $YBa_2Cu_3O_7$ IN THE SUPERCONDUCTING STATE

BY

SEAN ERIC BARRETT

A.B., Princeton University, 1987
M.S., University of Illinois, 1988

THESIS

Submitted in partial fulfillment of the requirements
for the degree of Doctor of Philosophy in Physics
in the Graduate College of the
University of Illinois at Urbana-Champaign, 1992

Urbana, Illinois

NUCLEAR MAGNETIC RESONANCE STUDIES OF $YBa_2Cu_3O_7$
IN THE SUPERCONDUCTING STATE

Sean Eric Barrett, Ph.D.
Department of Physics
University of Illinois at Urbana-Champaign, 1992
Charles P. Slichter, Advisor

In this thesis we report measurements of the ^{63}Cu Knight shift in the superconducting state for the plane (Cu(2)) and chain (Cu(1)) sites in $YBa_2Cu_3O_7$. We also have measured the temperature and field dependent $^{63}Cu(2)$ nuclear spin relaxation rates ($^{63}W1\alpha$) in the superconducting state.

The accurate determination of the ^{63}Cu Knight shift below Tc required a precise knowledge of the magnetic field strength inside the bulk of the sample. We have used ^{89}Y as an internal field marker to determine the amount of diamagnetic shielding present in our sample below T_c. Observation of the ^{89}Y resonance in the superconducting state required several unusual NMR techniques, such as using the Carr-Purcell-Meiboom-Gill pulse sequence to enhance the signal-to-noise ratio.

We have interpreted our Knight shift data within a generalized Bardeen-Cooper-Schrieffer (BCS) pairing theory, and find that a spin-singlet pairing state is strongly favored by these data. The temperature dependence of the Cu(1) Knight shift is slightly different from the temperature dependence of the Cu(2) Knight shift. It is possible to fit the data assuming either an orbital s-wave or an orbital d-wave pairing state, but in every case the energy gap seen by the Cu(2) apparently possesses a strong coupling temperature dependence, while the energy gap seen by the Cu(1) is much closer to the weak coupling gap assumed in the original BCS theory.

During our measurements of the temperature dependence of the Cu(2)

spin-lattice relaxation rates in the superconducting state ($^{63}W1\alpha$, where $\vec{Ho} \| \hat{\alpha}$), we discovered that the anisotropy ratio $^{63}W1a/^{63}W1c$, which was essentially independent of temperature in the normal state, drops sharply just below T_c (77 K < T< Tc). The data which we have measured in the smallest fields possible (Ho < 4.5 kGauss) show that as the temperature is lowered below T ~ 77 K the anisotropy ratio $^{63}W1a/^{63}W1c$ starts to increase, eventually exceeding the normal state anisotropy ratio. These low field data have been interpreted by several groups in terms of a generalized BCS pairing state. These groups successfully fit our data assuming a spin-singlet, orbital d-wave pairing state, but are unable to fit our data assuming a spin-singlet, orbital s-wave pairing state.

We also observe a sizeable field dependence of the spin-lattice relaxation rate in the superconducting state, which is much more pronounced when the magnetic field penetrates the CuO_2 planes ($^{63}W1c$) than when the field lies along the CuO_2 planes ($^{63}W1a$). These rates appear to be linearly dependent upon the field, indicating that flux lines may be contributing to the observed relaxation rates.

To Mom and Dad

Acknowledgements

I want to thank Professor C. P. Slichter for allowing me to join his research family. These past few years have been intensely stimulating and enjoyable. Charlie's good-humor and youthful energy permeate the lab. This always made a tremendous difference in the morale of our group, especially when our experiments broke down. After watching Charlie in action, I realize I have a lot of science to learn, but at least I have a better understanding of how to learn it.

I have been privileged to work in the Slichter lab with many gifted experimental physicists. Dr. Dale Durand, Professor Charles Pennington, and Dr. Chris Klug have always been willing to work on the problems which I encountered, despite the fact that my requests were sometimes made by desperate telephone calls to their homes after midnight. Dale and Charles were primarily responsible for teaching me how to study the High-Tc superconductors using NMR, and their skillful advice got me off to a running start in my research. They selflessly devoted much time and energy to the Knight Shift experiment, and their contributions made the experiment possible. Dr. James Norcross and Dr. Lino Becerra expanded my knowledge of NMR techniques and applications. Joe Martindale has worked closely with me on many projects and papers. His hard work, attention to details, and physical insights have been invaluable in all of the W1 anisotropy experiments. I have also learned many things during my discussions with Stewart DeSoto, Keith O'Hara, Dr. Takashi Imai, and Ken Sakie. The environment in the lab was relaxed and enjoyable because of the contributions of every member of the Slichter group.

This thesis would not have been possible without the work of

Professor Don Ginsberg and his students Dr. Tom Friedmann and Joe Rice. All of the samples studied in this thesis were produced in their labs. In addition, we had many interesting and helpful discussions with them on the present state and future directions of our research programs. The collaboration with these scientists was immensely rewarding.

We also enjoyed the theoretical guidance we received from our discussions with the group of Professor David Pines. In particular, Dr. Hartmut Monien, Dr. J. P. Liu, Phillipe Monthoux, and Dean Thelen have always been interested in discussing and analyzing the latest NMR data. We also benefitted from interactions with their collaborator, Dr. Andy Millis.

I would like to thank Aprel Orwick and Ann Wells for all of their help. The generous contribution of their time and energy enhanced our group's interaction with Charlie.

I want to thank Lisa Lipinski for assisting in the creation of Figure 3 and Figure 4 in this thesis.

Dr. Donald C. Schmalberger was my high school physics teacher. I want to thank him for his inspired teaching and challenging problems. I am in physics today because he showed his classes how much fun it could be.

Christopher Mudry is my good friend and colleague. We visited Illinois at the same time as undergrads and ended up entering in the same class. I have learned a lot about Europe, physics, and life in our many discussions, and we've seen some great movies along the way. I particularly want to thank him for putting up with the vagrant who camped on his living room floor during the final months of my thesis.

I would like to thank Nancy E. Vergara for all of the work she has put into this thesis. Nancy was always willing to listen patiently to my detailed

accounts of experimental breakthroughs, lab catastrophes, and everyday occurrences. This thesis was composed on her computer which she had graciously lent to me, and Nancy was instrumental in the last push to turn the thesis in. Nancy's love, support, and creativity made graduate school a pleasant experience.

I also want to thank my family for all of their help. My sister Erin, and my brothers Brendan and Brian, frequently called me with the latest news from home, which was a big morale booster. The Barrett, Flaherty, Gottbrath, McGuire, and Regan families always welcomed me into their homes, providing me with a much needed dose of family life. Most of all, I want to thank my parents, Mary and John. Their constant support made the pursuit of this degree possible, and I dedicate this thesis to them.

I gratefully acknowledge receiving a University of Illinois Fellowship and an IBM Predoctoral Fellowship. This work was supported by the Department of Energy, Division of Materials Science, under Contract DEFG02-91ER45439.

Table of Contents

List of Tables

List of Figures

Chapter 1. Introduction

Since the discovery of $La_{2-x}Ba_xCuO_4$ in 1986,[1] thousands of scientists around the world have actively participated in the field of High-T_c superconductivity. This intensive scrutiny has revealed many interesting and novel characteristics of these materials, but fundamental questions have yet to be answered. For instance, what is the proper description of the normal state charge carriers in these systems? The models which have been proposed range from the conventional Fermi liquid picture,[2] to variants of the conventional picture such as a marginal Fermi liquid[3] or an antiferromagnetic Fermi liquid,[4] to exotic pictures in which the spin-degree of freedom is decoupled from the charge degree of freedom.[5,6] Another important question is what theoretical framework describes the superconducting state (e.g. a generalized BCS theory, or some new theory which follows from an exotic normal state picture)? What microscopic mechanism is providing the attractive pairing interaction for the superconductivity (e.g. phonons, electron spin fluctuations, coherent charge carrier tunnelling between independent CuO_2 layers, etc.)? Why are the superconducting transition temperatures so high (T_c=40 K - 125 K)? These basic questions are being actively investigated using a wide spectrum of experimental and theoretical techniques.

Historically, NMR experiments have been a powerful tool in the investigation of "low temperature" BCS superconductors ($T_c \leq 28$ K). The observation of the Hebel-Slichter coherence peak in the nuclear spin-lattice relaxation rate,[7,8] when contrasted with the behavior of the ultrasonic attenuation measurements of several groups,[9,10] was the first experimental

test of the detailed structure of the Bardeen-Cooper-Schrieffer theory of superconductivity.[11,12] NMR is a sensitive probe of the predictions of the BCS theory because the nuclei in a metal are strongly affected by the electrons at the Fermi level, and these same electrons are the ones which are responsible for the superconductivity in the BCS theory. The two classic NMR measurements in the superconducting state are the nuclear spin-lattice relaxation rate and the Knight shift.

In this thesis, we report measurements of the both the ^{63}Cu Knight shift[13] and the planar ^{63}Cu nuclear spin-lattice relaxation rates in the superconducting state of $YBa_2Cu_3O_7$ (T_c=93 K).[14,15,16] To ensure the accuracy and reliability of these measurements, we utilized special sample preparation procedures and unusual NMR techniques.

The determination of the ^{63}Cu Knight shift involved measuring the temperature dependent frequencies of the ^{63}Cu NMR lines below T_c. The difficulty in this measurement is that the position of the NMR lines will shift in frequency for reasons of both macroscopic (diamagnetic shielding supercurrents) and microscopic (Knight shift, electric field gradient) origin. We only want to know the latter contribution to the shift. Our solution was to use the yttrium nucleus as a microscopic probe of the internal magnetic field, so we could isolate the microscopic shift of the ^{63}Cu lines.

The main result of our experiment was that the ^{63}Cu Knight shift data could be understood within a generalized BCS theory. Within this general framework, our data suggest that a spin-singlet pairing state is the appropriate description of the superconducting state in $YBa_2Cu_3O_7$. If this conclusion is correct, the data for the chemical shift of the copper in the planes and the chains are consistent with the picture that the copper sites are very close to

Cu^{++}, with a hole in the x^2-y^2 (y^2-z^2) state for the planes (chains).

Our measurement of the planar ^{63}Cu nuclear spin-lattice relaxation rates in the superconducting state of $YBa_2Cu_3O_7$ was made possible by a special manually aligned multiple single crystal sample. This sample allowed us to obtain the planar copper site NMR relaxation rate, $^{63}W1a$ ($^{63}W1c$), when the magnetic field was applied parallel (perpendicular) to the CuO_2 planes. In the normal state, the ratio $^{63}W1a/^{63}W1c$ is about 3.7 and is essentially independent of temperature. This measurement was also carried out in magnetically aligned powder samples, using a baseline subtraction technique, which we explain in Chapter 7, Section 7c. In these aligned powder samples, we also have some relaxation rate data for the planar oxygen and yttrium nuclei.

The main result of these relaxation rate measurements was that the anisotropy ratio $^{63}W1a/^{63}W1c$ sharply decreases just below T_c. We will show that this result was completely unexpected from the simplest extension below T_c of the normal state phenomenological theory. There are recent calculations within a generalized BCS framework which conclude that our result requires nodes in the energy gap (as in spin-singlet, orbital d-wave pairing).[17,18,19]

We have also observed a strong field dependence of $^{63}W1c$ at low temperatures. This result may be related to the presence of fluxoids in a mixed state measurement, but the mechanism for this effect remains unexplained.

In Chapter 2, we will present some characteristics of the $YBa_2Cu_3O_7$ compound. In Chapter 3, we will discuss some of the quantities measured in NMR experiments, as well as the results obtained in BCS superconductors.

The experimental techniques required for our measurements will be detailed in Chapter 4. Chapter 5 will be an overview of previous NMR results in $YBa_2Cu_3O_7$ and related High-T_c compounds, including a discussion of the conventionally accepted picture of the normal state electronic spin system. Chapter 6 will describe our ^{63}Cu Knight Shift experiment, including a detailed analysis of the data. Our $^{63}W1$ anisotropy measurements will be the subject of Chapter 7. We will discuss attempts to understand our earliest data and also recent calculations which explain some of our latest results. Chapter 8 will contain a summary of our conclusions.

Chapter 2. $YBa_2Cu_3O_7$

Section 2a. Introduction

After the initial discovery of $La_{2-x}Ba_xCuO_4$ (T_c~35 K) in 1986,[1] the T_c in this material was found to increase when pressure was applied to the material. Some investigators tried to simulate the effects of increased external pressure by substituting smaller rare earth ions for the La, in order to reduce the unit cell size. The material $YBa_2Cu_3O_7$ (T_c~90 K) was the second High-T_c superconductor to be discovered in 1987.[20] This material was especially noteworthy because it was the first superconductor to have a transition temperature higher than the boiling point of liquid nitrogen (T_{bp}=77.35 K). All of the measurements reported in this thesis have been made on this material.

The crystal structure of this material is shown in Figure 1.[21] The unit cell has orthorhombic symmetry, with dimensions: a=3.8231 Angstroms, b=3.8864 Angstroms, and c=11.6807 Angstroms.[22] Two-dimensional copper oxide planes containing the Cu(2), O(2), and O(3) sites appear in the unit cells of all of the High-T_c superconductors. $YBa_2Cu_3O_7$ has two of these CuO_2 planes separated by the Yttrium atom. Below the CuO_2 planes is a layer containing the Ba and O(4) sites. Finally, below the BaO layer is a layer of one-dimensional CuO chains which run along the $\hat{b}$-axis. The Cu(1) and O(1) sites make up these CuO chains.

Because of the small difference between the $\hat{a}$- and $\hat{b}$-axis unit cell dimensions, this material exhibits the phenomenon of twinning. When a bulk sample is grown, the one-dimensional chains rarely proceed in a straight

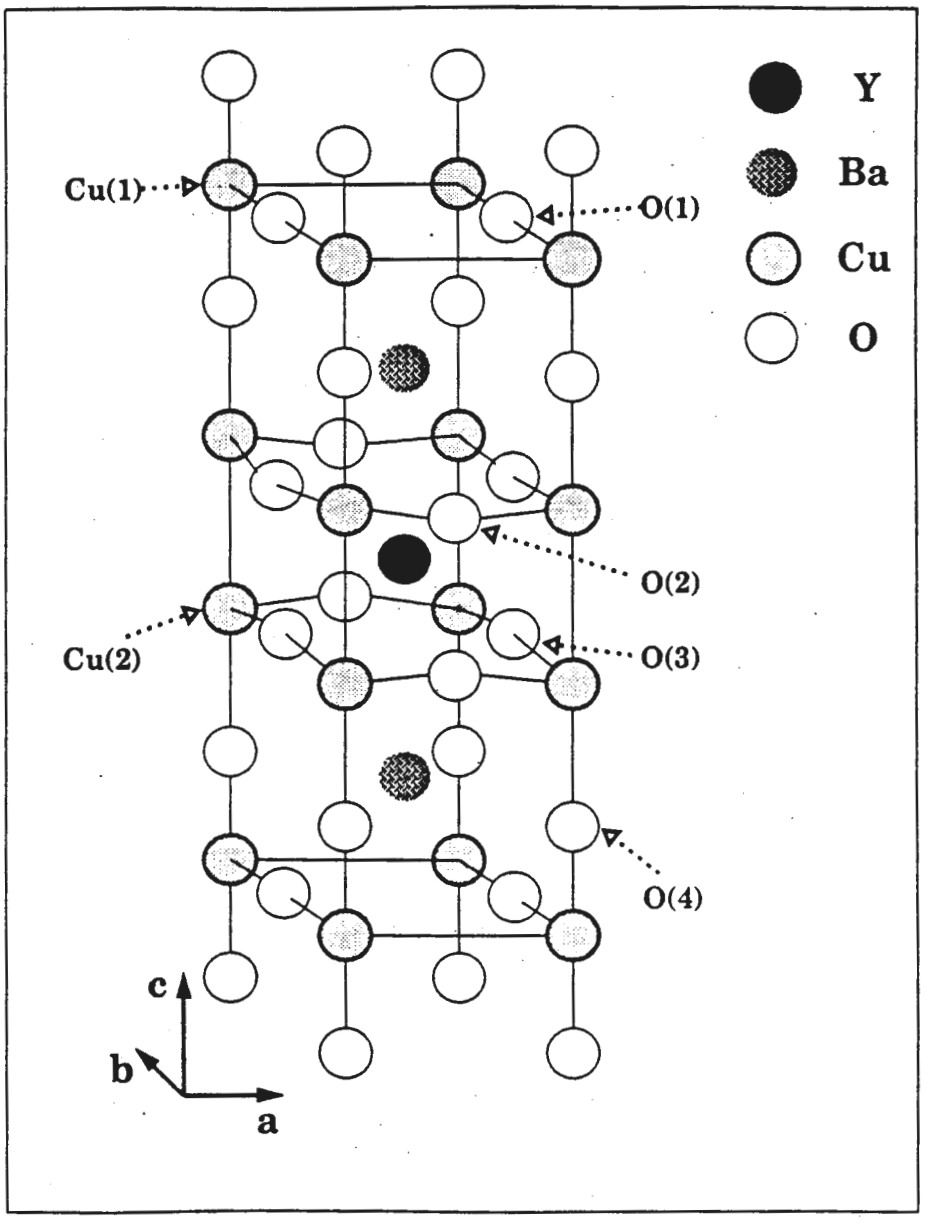

Figure 1. Crystal structure of $YBa_2Cu_3O_7$.[21]

line all the way across a sample. Instead, the chains will occasionally make right angle turns and travel in the new direction. The location of this turn is a twinning boundary, and the net effect is that a given direction in the crystal is no longer just the $\hat{a}$- or $\hat{b}$- axis, but is instead the $\hat{a}$-axis for a macroscopic distance, and then the $\hat{b}$-axis for another region, and then the $\hat{a}$-axis again, and so on. This disorder is frozen into the sample during the finite time spent growing them, unless extraordinary techniques are used to remove the twinning. We shall see later that this macroscopic twinning phenomena is not a big problem for our microscopic NMR measurements.

This perovskite loses oxygen from the O(1) site relatively easily, unless precautions are taken. When all of the O(1) sites are vacated, the resulting material, $YBa_2Cu_3O_6$, is an antiferromagnet with a Néel temperature of 400 K. The phase diagram for this material $YBa_2Cu_3O_{6+x}$ is shown in Figure 2.[23]

Section 2b. Comparison of $YBa_2Cu_3O_7$ with Other High-T_c Superconductors

There are many similarities between $YBa_2Cu_3O_7$ and the other High T_c superconductors shown in Table I. First of all, they all possess the two-dimensional CuO_2 planes as building blocks. All of the superconductors have a strong anisotropy of the normal state conductivity ($\rho_c/\rho_{ab} \sim 10^2 - 10^5$), indicating the preferential transport along the planes rather than perpendicular to them.[24] These superconductors can be made by adding carriers (mostly holes, sometimes electrons) to the antiferromagnetic parent compounds by doping. The resistivity along the planes is linear in temperature, which has been interpreted as evidence for a carrier scattering rate which goes as $h/\tau \sim k_B T$.[24] These materials also possess a large continuum

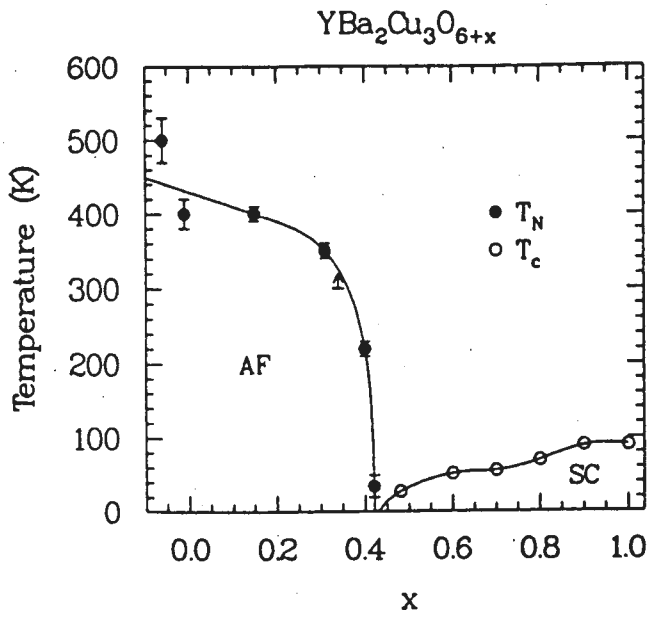

Figure 2. The phase diagram for the material $YBa_2Cu_3O_{6+x}$ as a function of oxygen content (x).[23] The Néel temperatures were determined by neutron diffraction; AF denotes antiferromagnetic, SC denotes superconducting. Solid lines are guides to the eye.

Superconductor	Tc
$La_{1.85}Sr_{0.15}CuO_4$	38 K
$YBa_2Cu_3O_{6.6}$	60 K
$YBa_2Cu_4O_8$	80 K
$Bi_2Sr_2Ca_1Cu_2O_8$	85 K
$YBa_2Cu_3O_7$	93 K
$Bi_2Sr_2Ca_2Cu_3O_{10}$	110 K
$Tl_2Sr_2Ca_2Cu_3O_{10}$	125 K

Table I. A selection of High-Tc compounds with typical superconducting transition temperatures.[26]

in the Raman scattering intensity which rises quickly at low energies and then is independent of energy as far up as anyone has looked.[25]

These materials also share many generic superconducting state properties. Measurements of the flux quantum and of Andreev reflection have indicated that the superconductivity involves hole (or electron) pairing.[24, 27, 28] All of the High-T_c materials are extreme Type II superconductors, with large anisotropies in the coherence length and the penetration depth.[27, 28]

There are several differences between $YBa_2Cu_3O_7$ and the other High-T_c superconductors listed in the table. The single layer of CuO chains is unique to $YBa_2Cu_3O_7$, although $YBa_2Cu_4O_8$ has a double layer of CuO chains.[29] The chains in $YBa_2Cu_3O_7$ appear to be the source of the charge carriers which move in the CuO_2 planes, although this may be too simplistic a picture.[27] There is no large isotope effect in $YBa_2Cu_3O_7$, although $La_{2-x}Ba_xCuO_4$ has shown a sizable effect.[30] Bulk magnetic susceptibility measurements of $YBa_2Cu_3O_7$ are almost independent of temperature in the normal state, but many of the other High-T_c materials show a substantial temperature dependence in $\chi_{magnetic}(T)$.[24] Optical conductivity measurements in untwinned $YBa_2Cu_3O_7$ show a substantial difference depending on whether the light is polarized parallel or perpendicular to the chains.[31] Untwinned $YBa_2Cu_3O_7$ resistivity measurements show that ρ_a/ρ_b ~2, indicating some effect of the chains on the material's conductivity along the CuO_2 planes.[32]

Section 2c. Comparison of $YBa_2Cu_3O_7$ to Normal Metals

There are some similarities between $YBa_2Cu_3O_7$ and metals which are typical BCS superconductors. Angle-Resolved Photoemission Spectroscopy (ARPES) data indicate that a Fermi surface is present, although the quasiparticle lifetime has an unusual energy dependence.[33] The normal state NMR properties of the oxygen, yttrium and chain copper sites are similar to typical metallic results as we will discuss in Chapter 5.

There are many more differences between $YBa_2Cu_3O_7$ and normal metals. The isotropic resistivity of copper metal at room temperature is $\rho_{copper}=1.8\mu\Omega$-cm,[34] while the smallest component of the anisotropic resistivity tensor for the ceramic $YBa_2Cu_3O_7$ is $\rho_b=70\mu\Omega$-cm.[32] $YBa_2Cu_3O_7$ also has an unusual temperature dependence for both the resistivity ($\rho_{ab}\propto T$, $\rho_c\propto 1/T$)[24] and Hall effect constant ($R_H\propto 1/T$).[35] As we mentioned in Section 2b, the ARPES determined quasiparticle lifetime seems to have a different energy dependence than the Fermi liquid prediction.[33] Optical conductivity measurements at low frequencies indicate a non-Drude energy dependence, which has been interpreted either as a frequency dependent scattering rate ($h/\tau^* \sim k_B T + h\nu$) of a single electronic component, or as absorption due to two electronic components (with intra- and inter-band transitions).[36] There is also neutron scattering evidence that the material $YBa_2Cu_3O_{6+x}$ with x close to 1 has antiferromagnetic tendencies, so somehow the antiferromagnetism of the parent compound persists into the metallic state.[23,27] Finally, there is the unusually high T_c, and the absence of an isotope effect.

Chapter 3. General NMR in Metals and Superconductors

Section 3a. Static Spin Hamiltonian

The energy levels of the nuclei are given by the following general nuclear spin Hamiltonian,[38] ignoring nuclear spin-spin couplings:

$$\hat{H} = -\frac{\gamma_n}{2\pi} h\hat{I}_\alpha (1 + K_{\alpha\alpha}) Ho_\alpha + \frac{h}{2I(2I-1)}\left[\nu_{zz}\left(3\hat{I}_z^2 - \hat{I}^2\right) + \left(\nu_{xx} - \nu_{yy}\right)\left(\hat{I}_x^2 - \hat{I}_y^2\right)\right] \quad (3\text{-}1)$$

The first term is the Zeeman energy of the nuclear magnetic moment, ($\hat{I}$ is a dimensionless operator), in the presence of the applied field $\overrightarrow{Ho} \| \vec{\alpha}$ ($\vec{\alpha}=\hat{x},\hat{y}$, or $\hat{z}$). $K_{\alpha\alpha}$ is the magnetic shift tensor, and it represents the extra fields produced at the nucleus by the electrons. $|K_{\alpha\alpha}|$ is usually small (typically < 2%). The magnetic shift tensor contains several parts:

$$K_{\alpha\alpha} = K^S_{\alpha\alpha} + K^L_{\alpha\alpha} + \sigma_{\alpha\alpha}. \quad (3\text{-}2)$$

The tensor $\sigma_{\alpha\alpha}$ is the shift due to all the closed shell electrons of an atom. Since one usually measures $K_{\alpha\alpha}$ relative to a closed shell reference, we can take $\sigma_{\alpha\alpha}$ to be zero. The tensor $K^L_{\alpha\alpha}$ is called the chemical shift, and it is due to the extra field at the nucleus contributed by the electronic orbital susceptibility of both the valence electrons of an atom and the closed shell electrons of its neighbors. Thus, the chemical shift is directly proportional to the Van Vleck susceptibility, χ^L. The tensor $K^S_{\alpha\alpha}$ is the Knight shift, and it represents the extra field at the nucleus due to the electronic spin susceptibility, χ^S (the Pauli susceptibility in metals). Thus if one knows or

can calculate the constants of proportionality (hyperfine coupling constants), a measurement of $K_{\alpha\alpha}$ yields the values of χ^L and χ^S.[39]

The second term in the above static spin Hamiltonian is the quadrupole interaction. The electric quadrupole moment of the nucleus couples to the electric field gradient present at the nucleus. Only nuclei with spins I>1/2 (e.g. ^{63}Cu, ^{65}Cu, and ^{17}O) can have this term. The $\nu_{\alpha\alpha}$ tensor gives the electric field gradient (in MHz) at the nucleus due to the electrons in the same atom and the surrounding ions.

We have ignored the nuclear dipole-dipole coupling in this Hamiltonian because this term is mainly a source of line breadth for the fields and nuclei in question, and relatively unimportant for determining the line position or the magnitude of the spin-lattice relaxation.

In thermal equilibrium, the number of nuclear spins which find themselves in an eigenstate $|a\rangle$ of the above Hamiltonian is proportional to $N \exp(-E_a/k_BT)$, where N is the total number of spins in the system, and Ea is the energy of an eigenstate $|a\rangle$. To observe NMR, one could apply an alternating magnetic field which has a non-zero matrix element between two states. When the frequency of this field matches the frequency separation of the levels ($\nu=\{E_a-E_b\}/h$), transitions between the two levels are allowed, and resonant absorption of energy occurs. Knowledge of this frequency, the nuclear spin eigenstates, and the applied field H allows one to determine the tensors $K_{\alpha\alpha}$ and $\nu_{\alpha\alpha}$. This experiment is typically performed using spin echoes, which are the subject of the next section. Notice that for nuclear spins which have a large quadrupole term in their Hamiltonian, one could in principle observe the same resonance phenomena in the absence of an applied field (the Zeeman term is then zero). This is a Nuclear Quadrupole

Resonance (NQR) experiment.

Section 3b. Spin Echoes

Most of the NMR carried out today uses strong radio frequency (RF) pulses to observe the nuclear magnetization.[40] The detection circuit must be extremely sensitive in order to detect the weak nuclear signal (typically ≤1 μV) present at the input of the first RF preamplifier stage. Unfortunately, the leakage of the applied RF pulses to this stage is much larger (~0.5 V), so it is often necessary to temporally separate these two signals. The spin echo sequence, discovered by Prof. Erwin Hahn, accomplishes this goal.[41]

We can treat the nuclear magnetization as a classical variable to understand the spin echo concept. Assume there is a nuclear magnetic moment possessing a non-zero angular momentum in a static magnetic field applied along the z-direction. The magnetic moment variable, $\vec{\mu}$, is related to its angular momentum, $\vec{J}$, by:

$$\vec{\mu} = \gamma \vec{J} \tag{3-3}$$

In this picture, the torque acting on a moment gives the time dependent change in its angular momentum:

$$\frac{d\vec{J}}{dt} = \vec{\mu} \times \vec{H}_{loc} \quad \Rightarrow \quad \frac{d\vec{\mu}}{dt} = \vec{\mu} \times \gamma \vec{H}_{loc} \tag{3-4}$$

Consider the simple case shown in Figure 3. The total NMR line consists of nuclear magnetic moments in three different regions each with their own local field along the z-axis, Ho-δH, Ho, and Ho+δH. We define the three frequencies (ω_s, ω_o, ω_f)= γ(Ho-δH, Ho, Ho+δH). In a reference frame rotating about the z-axis at frequency ω_o, the moments obey the equation:

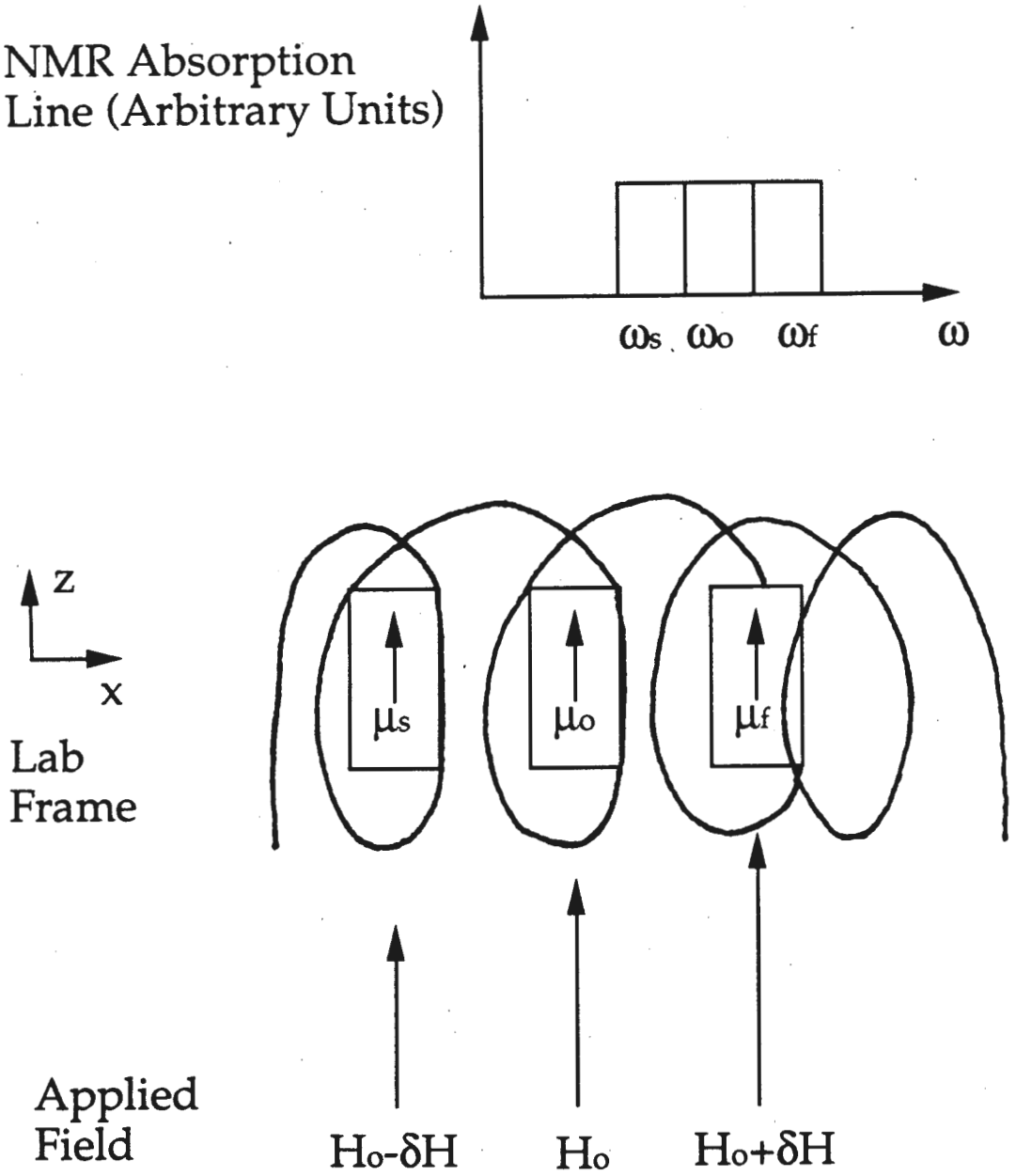

Figure 3. Gedanken experiment which is useful in understanding the nuclear Spin Echo concept. The three identical nuclear magnetic moments are completely enclosed by the solenoid which is fixed along the x-axis in the lab frame. Each moment experiences a slightly different value of the static local magnetic field, resulting in the breadth of the NMR line shown at the top of the figure. This is a simple example of an inhomogeneously broadened line.

$$\frac{\delta \vec{\mu}}{\delta t} = \vec{\mu} \times \gamma \left(\vec{H}_{loc} - \vec{Ho} \right) \qquad (3\text{-}5)$$

In equilibrium, all three nuclear magnetic moments are aligned along the z-axis, as shown in the figure. Suppose that this sample is enclosed by a solenoid which points along the lab frame's x-axis. In order to measure the nuclear magnetization, we apply to this solenoid a short pulse of RF power, which is sinusoidally varying at the rotating frame frequency ω_o. In the rotating frame, this RF pulse produces for a time T_θ a constant magnetic field of amplitude H1 which lies along some direction in the rotating frame's x-y plane. For a narrow NMR line, H1 » (H_{loc}-Ho), and we may write the rotating frame equation of motion as:

$$\frac{\delta \vec{\mu}}{\delta t} \cong \vec{\mu} \times \gamma \left(\vec{H1} \right) \qquad (3\text{-}6)$$

It is not always true that the line is narrow compared to the H1, but if we are on resonance (where H_{loc}=Ho), there is always some small region of the line which obeys this equation. During an applied pulse the magnetization will rotate through an angle of $\theta=(T_\theta\ (\gamma H1))$ about the H1 direction. We can write such a pulse as θ_α, where α is the direction of H1 in the rotating frame, and θ gives the total rotation angle of an on-resonance magnetic moment.

The description of the spin echo is now straightforward. Starting with the thermal equilibrium magnetization along the z-axis, as in Figure 4, we apply the following pulse sequence:

$$\pi/2_x - \tau - \pi_y - \tau - \text{echo.} \qquad (3\text{-}7)$$

The first pulse brings the three moments in our model along the rotating frame's y-axis. During the first time τ the moments fan out in the x-y plane (e.g. the ω_f spins move by an angle $(\omega_f - \omega_o)\tau$ away from the y-axis) because $\omega_s, \omega_f \neq \omega_o$, as we see in the figure. The π_y pulse flips the pancake over

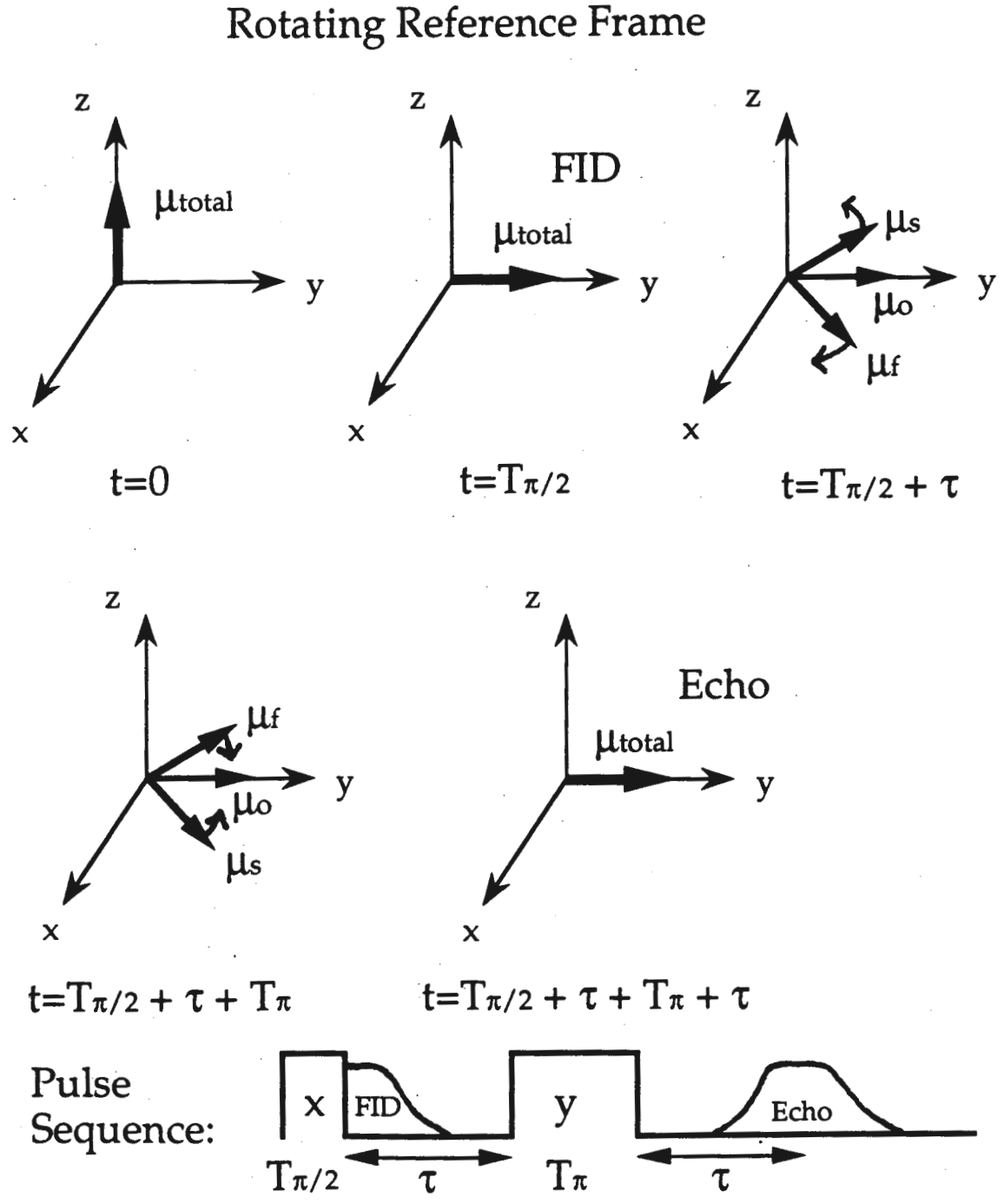

Figure 4. (Top) The effect of the pulse sequence given in Equation (3-7) on the nuclear magnetic moments in our solenoid, when viewed in a reference frame rotating at frequency ω_0. (Bottom) Occurrence of FID and Echo during pulse sequence.

about the y-axis, and the pancake is refocussed along the y-axis a time τ after the last pulse. The total magnetization along the y-axis at this time is directly proportional to the magnetization originally along the z-axis just before the $\pi/2$ pulse. We have ignored pulse imperfections and relaxation processes in this simple model, but including them does not alter this last result. This magnetization along the rotating frame's y-axis is precessing very rapidly in the x-y plane of the lab frame, inducing an alternating voltage (with frequency ω_o) in the solenoid, which is then measured by the detection system. This voltage dies away with a characteristic time (T2*) because the different nuclear magnetic moments dephase again.

The spin echo may also be described using the viewpoint taken in Section 3a. If we treat the nuclear magnetization as a quantum mechanical operator, the insight provided by the above classical picture is helpful. Ignoring quadrupole interactions, the equation of motion of the nuclear magnetic moment expectation value in the laboratory frame is given by:[38]

$$\frac{d\langle\vec{\mu}\rangle}{dt} = \langle\vec{\mu}\rangle \times \gamma\left(\vec{H}_{loc} + \vec{H1}(t)\right) \qquad (3\text{-}8)$$

The magnetic moment operator is defined to be $\vec{\mu} = \gamma\hbar\hat{I}/(2\pi)$, and the ket in the expectation value $\langle\Psi|\vec{\mu}|\Psi\rangle$ is the state vector of the nuclear spin, $|\Psi\rangle \equiv \Sigma_a c(a)|a\rangle$. The similarity of this equation with the earlier classical equation allows our earlier discussion of spin echoes to describe the quantum mechanical situation as well. Including quadrupole interactions can add effective magnetic fields and restrict the eigenstates $|a\rangle$ of the nuclear spin Hamiltonian which are included in the state vector, but these modifications are not important for our present purposes.[42]

Section 3c. Spin-Lattice Relaxation Rates (1/T1)

Another informative NMR experiment is a spin-lattice relaxtion time (T1) measurement. When one disturbs the thermal equilibrium population of the levels, T1 is the characteristic time that describes a system's return to equilibrium. In a magnetic relaxation process, which is the relevant mechanism for the nuclei we have studied in this material, rapidly fluctuating magnetic fields at the nucleus induce transitions between the eigenstates of the system, eventually restoring the equilibrium population to each level. If the spins are quantized along the $\hat{c}$-axis by a strong magnetic field, one can measure the relaxation rate $(1/T1)_c$. If we assume that each component of the fluctuating field is independent and exhibits an exponential autocorrelation function with an isotropic correlation time τ_o, we can write down the expression for the magnetic relaxation rate:[38]

$$\left(\frac{1}{T1}\right)_c = \left(\frac{3}{2}\right)\gamma_n^2 \left[h_a^2 + h_b^2\right] \tau_o \qquad (3\text{-}9)$$

This is the correct expression provided that each field component is fluctuating very rapidly compared to the Larmor frequency, i.e. $\omega_{nuclear} < 1/\tau_o$ (Pennington has shown that τ_o is 10^{-15} sec, while $\omega_{nuclear}$ is 10^9 sec^{-1}, so this limit is clearly satisfied.)[43] Measuring all three components of this relaxation rate tensor $(1/T1)_\alpha$ (where α is the quantization axis) reveals the anisotropy of these fluctuating fields. If the spins were quantized along a principal axis other than the $\hat{c}$-axis, the correct expression could be obtained from the above expression by cyclic permutation of the subscripts (a,b,c). This expression is the most general describing a magnetic relaxation process.

We can gain more insight from our measurements if we know the source of the fluctuating fields. If the fields at the nucleus are due to rapidly

fluctuating electronic spins, the T1 measurement tells us about the electronic spin system. If the electronic spins have the periodicity of a Bravais lattice (e.g. metallic spins, spins in an antiferromagnet, spins in an paramagnetic insulator), the above expression for magnetic relaxation for nucleus i can be quite generally written as:[44]

$$(3\text{-}10) \qquad {}^{i}\left(\frac{1}{T1}\right)_{\alpha} = \left(\frac{{}^{i}\gamma_n^2 \, k_B T}{2\,\mu_\beta^2}\right) \mathrm{Lim}_{\omega\to 0} \sum_{\vec{q},\alpha'\neq\alpha} \left|{}^{i}A_{\alpha'\alpha'}(\vec{q})\right|^2 \frac{\{\chi''_{\alpha'\alpha'}(\vec{q},\omega)\}}{\omega}$$

The $\chi''_{\alpha\alpha}(\vec{q},\omega)$ is the imaginary part of the $\vec{q}$- and ω-dependent electronic spin susceptibility tensor (taken to be isotropic in our case), and α are the principle crystalline axes, $(\hat{a},\hat{b},\hat{c})$. The limit $\omega\to 0$ is taken because this expression is evaluated at the Larmor frequency of the nucleus, typically around 10 mK, a very small energy on the scale of the electronic spin fluctuations. The advantage of this expression is that the anisotropy in the fluctuating fields in our earlier expression is now clearly contained within the hyperfine structure factors ${}^{i}A_{\alpha\alpha}(\vec{q})$. These structure factors are completely determined by the real space hyperfine coupling Hamiltonian. When both an anisotropic on-site and isotropic transferred hyperfine coupling are present for a nucleus (as for the Cu(2)) these ${}^{i}A_{\alpha\alpha}(\vec{q})$ terms will act as $\vec{q}$-filters which weight $\chi''_{\alpha\alpha}(\vec{q},\omega)$ differently for the different magnetic field orientations. We will use this equation quite often in the discussion of the T1 measurements. Within this framework, the Knight Shift is usually written in terms of the real part of the static electronic spin susceptibility tensor, $\chi'_{\alpha\alpha}(\vec{q},\omega=0)$:

$$(3\text{-}11) \qquad {}^{i}K^{S}_{\alpha\alpha} = \mathrm{Lim}_{\vec{q}\to 0}\left({}^{i}A_{\alpha\alpha}(\vec{q})\,\chi'_{\alpha\alpha}(\vec{q},\omega=0)\right)$$

If we can be even more specific and say that the magnetic relaxation process is due to the nuclear spin's scattering of conduction electron spins in a metal, then there is another conventionally used expression for the spin-

lattice relaxation rate:

$$\frac{1}{T1} \propto \int_0^{\infty} |\langle V_{e\text{-}n} \rangle|^2 \, \rho^2(E) \, f(E) \, (1\text{-}f(E)) \, dE \propto T \, \rho^2(E_F) \qquad (3\text{-}12)$$

This is the expression which is most often used to explain the NMR results in metals and BCS superconductors.[45] $\langle V_{e\text{-}n} \rangle$ is the matrix element for the electron nuclear interaction, $\rho(E)$ is the one electron density of states, and f(E) is the Fermi function. The Knight Shift in this notation can be written as:

$$K^S \propto \int_0^{\infty} \left(\rho(E) \frac{d\, f(E)}{d\, E} \right) dE \propto \rho(E_F) \qquad (3\text{-}13)$$

Thus one can relate the Knight shift and spin-lattice relaxation time in a normal metal:

$$(1/(T1*T))=\text{constant}*(K^S)^2. \qquad (3\text{-}14)$$

This is the Korringa law. The constant is determined by the relevant electron nuclear couplings, with a small correction of order unity when electron-electron interactions are included.

Section 3d. NMR Results for a Type I BCS Superconductor: ^{27}Al

NMR measurements have been made in several Type I superconductors in both the normal and superconducting states.[46] Care must be taken when selecting a sample because the applied static magnetic field is excluded from the interior of a Type I superconductor by the Meissner effect.[47] As a result, only the nuclei within a penetration depth, λ, of the surface can contribute to the NMR signal. This problem was typically solved by using samples whose size was comparable to λ, such as colloidal mercury specimens (diameter ~ 100 - 1000 Å)[48,49] or sandwiches of alternating

thin film aluminum (thickness ~ 60 - 200 Å) and SiO layers on a glass substrate.[50] Some of the classic superconducting state relaxation rate measurements required even more extreme solutions (e.g. field-cycling techniques).[7,8] We will discuss the results for ^{27}Al because this metal comes closest to the ideal case in both the normal and superconducting states.

Measurements of the normal state ^{27}Al spin-lattice relaxation time (T1) have been carried out by Spokas and Slichter up to 930K.[51,52] Their data, along with the liquid helium temperature data of Hebel and Slichter[7,8] as well as the data of Redfield and Anderson[53] are shown in Figure 5. The straight line fit to their data shows that the Korringa law (Equation 3-14) holds over a tremendous temperature range (1 K - 930 K) in ^{27}Al.

When the temperature is lowered below T_c, both K^S and T1 can be dramatically affected. The Knight shift data in ^{27}Al are shown in Figure 6.[50] There is a rapid decrease in K^S just below T_c, which reflects the modification of the normal state one-particle density of states at the Fermi surface. In the BCS theory, for a spin singlet, orbital s-wave pairing state, the density of excited quasiparticle states is given by:[46]

$$\rho_{BCS}(E - E_F) = \rho(E_F)\left[\frac{|E - E_F|}{\sqrt{((E - E_F)^2 - \Delta^2)}}\right], \qquad (3\text{-}15)$$

where Δ is an isotropic energy gap which opens up at T_c and is essentially independent of temperature below $T/T_c \sim 0.2$. Since the Knight shift in the normal state is proportional to $\rho(E_F)$, one indeed expects that $K^S \propto \chi^S \rightarrow 0$ as $T \rightarrow 0$. The temperature dependence of the Knight shift for this pairing state was first calculated by Yosida, by inserting the BCS single particle density of states expression (Eq. 3-15) into the definition of the Knight shift (Eq. 3-13), and then evaluating the integral.[54] The resulting temperature dependent

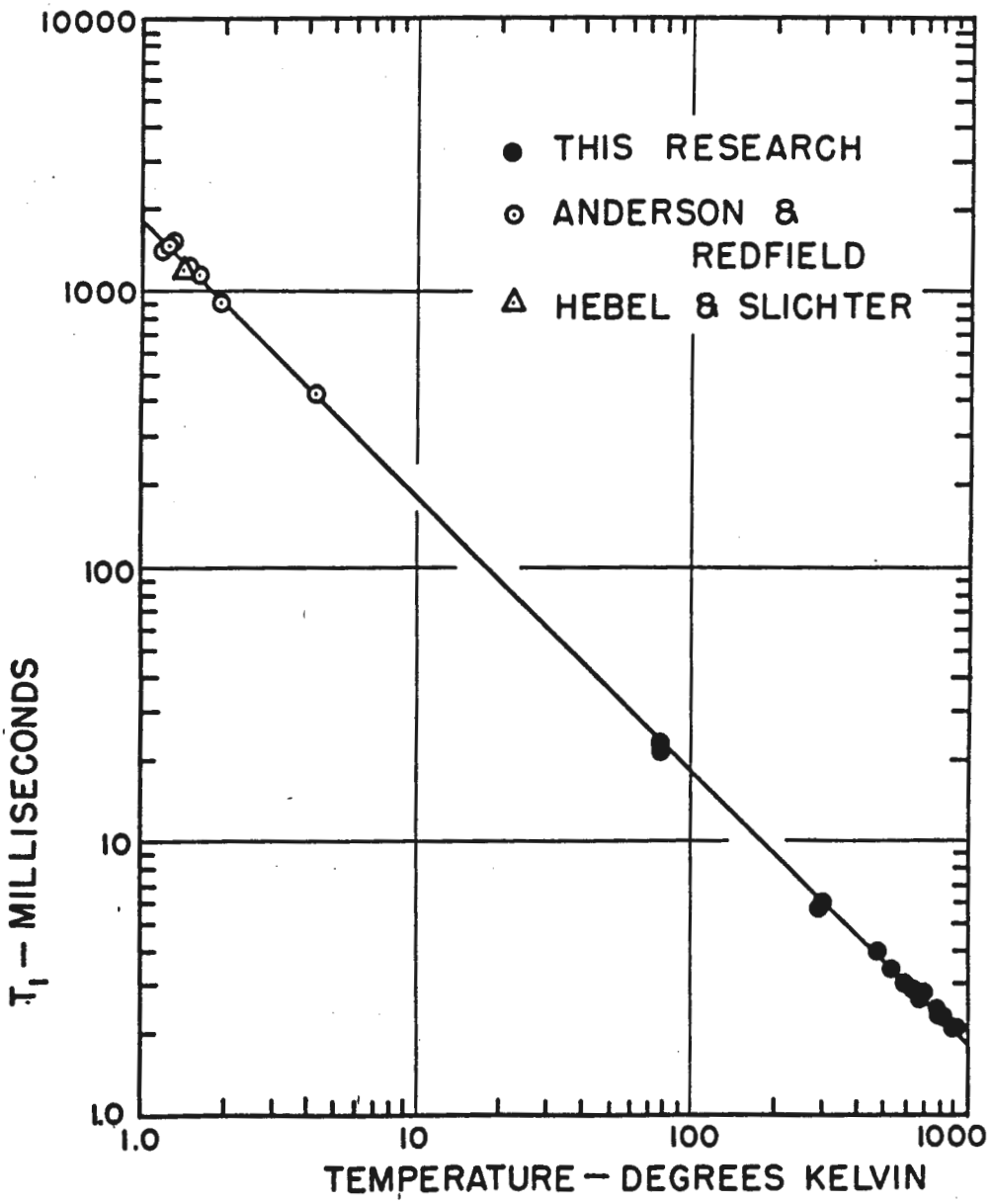

Figure 5. The nuclear spin-lattice relaxation time (T1) in ^{27}Al exhibits the behavior predicted by the Korringa law (figure from Reference 51). The straight line drawn through the data shows that (T1*T=constant) from 1 K to 930 K.

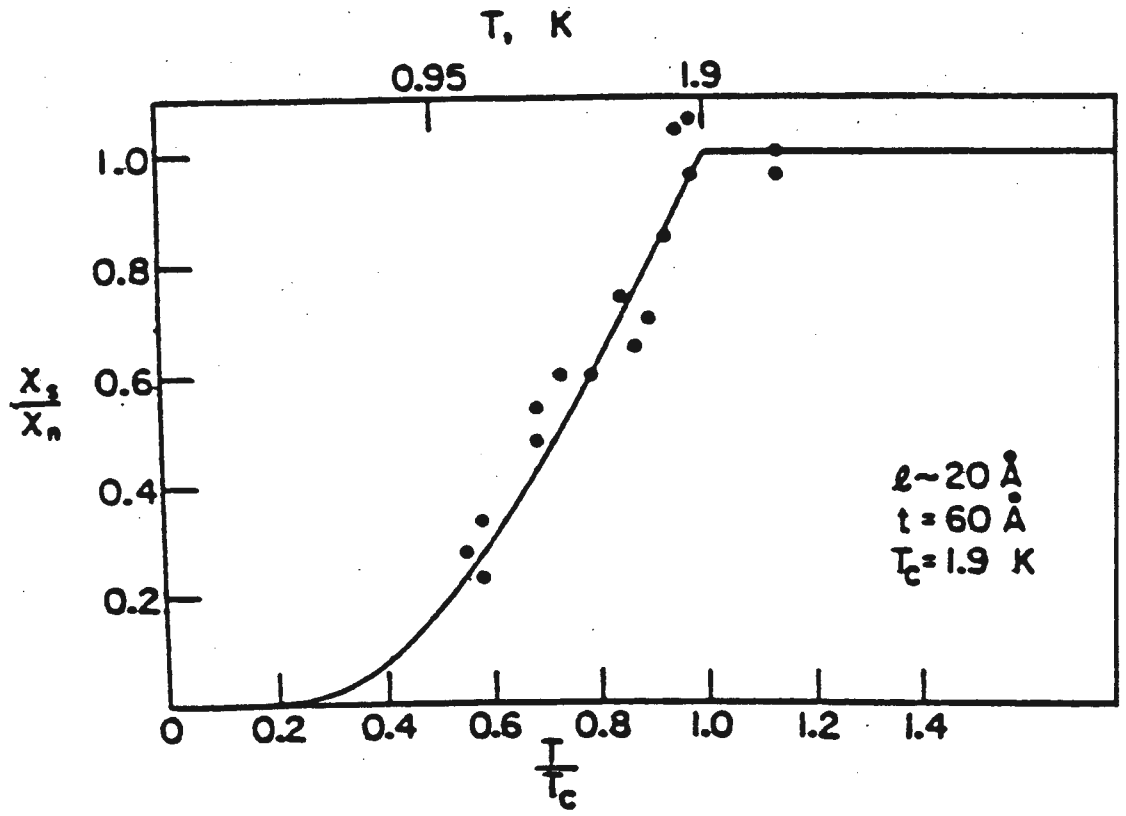

Figure 6. The normalized Knight shift data measured in ^{27}Al.[50] The dark line drawn through the data is the weak coupling, orbital s-wave, spin-singlet BCS pairing Yosida function.[54]

normalized Knight shift:

$$\frac{K^S(T<Tc)}{K^S(T=Tc)} = \int_{-\infty}^{\infty} \left(\left[\frac{|E - E_F|}{\sqrt{((E - E_F)^2 - \Delta^2)}} \right] \left(- \frac{d\, f(E)}{d\, E} \right) \right) dE = Y_0 (T/Tc) \qquad (3\text{-}16)$$

is conventionally referred to as the Yosida function ($Y_0(T/Tc)$). This function is plotted as the dark line in Fig. 6.

The T1 data also show a dramatic deviation from the Korringa law for $T<T_c$, as is seen in Figure 7a.[8] The two-fluid model of superconductivity would have predicted an increase in T1 just below Tc because of the decreasing number of normal state electrons. However, the relaxation time just below T_c is actually smaller than the T1 at $T=T_c$. The BCS theory of superconductivity explains this result quite naturally.[12] This decrease in T1 just below Tc (frequently referred to as the Hebel-Slichter coherence peak in the literature) is due to both the logarithmic singularity in $\rho_{BCS}(E-E_F)$ at the edge of the gap and to the BCS coherence factor which modifies $|\langle V_{e\text{-}n} \rangle|^2$, reflecting the correlated nature of the superconducting ground state. The BCS theory also predicts that the BCS coherence factor which is involved in measurements of the attenuation of longitudinal acoustic waves below Tc should be quite different from the NMR coherence factor, because of the different symmetry of the relevant electron scattering matrix element under time reversal. This BCS prediction describes the experimental situation precisely, while a two-fluid model of superconductivity is incompatible with the data.

The low temperature behavior of the spin-lattice relaxation rate is also an informative probe of the superconducting state. At low temperatures, when the gap is large and almost independent of temperature, the unpaired

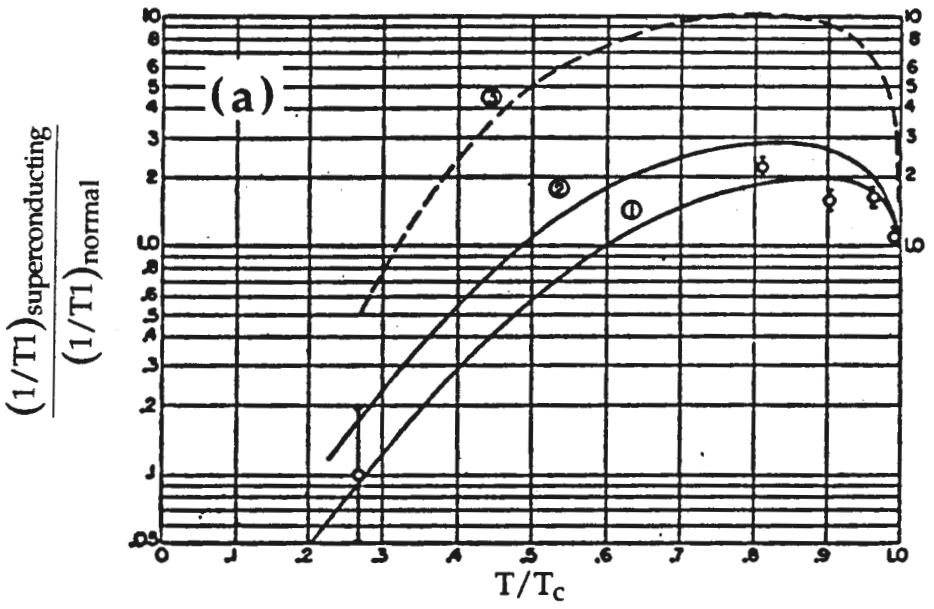

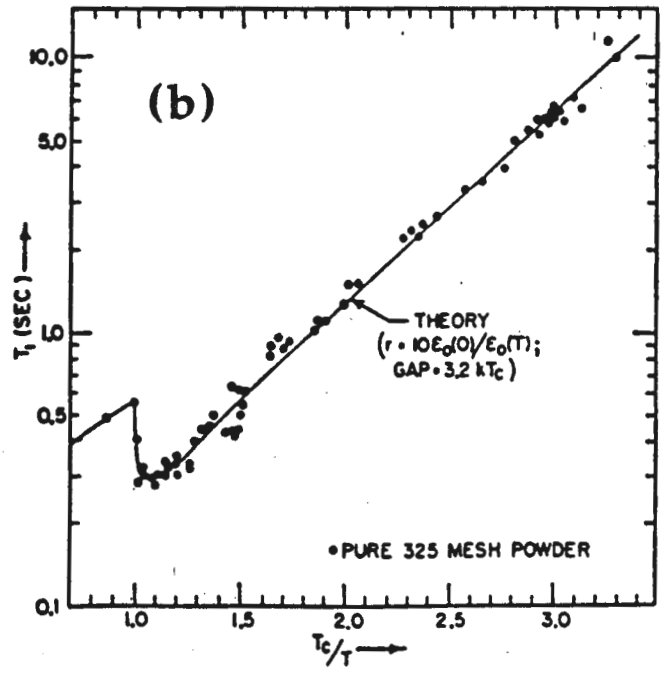

Figure 7. (a) Peak in the relaxation rate just below Tc.[8] (b) Peak in (1/T1) near Tc and the exponential temperature dependence at low T/Tc.[55]

electrons that relax the nuclei need to be excited across the energy gap, so:

(3-17) $$(1/T1) \propto \exp(-\Delta/k_BT).$$

This behavior is seen in the data of Masuda and Redfield in Figure 7b.[55]

Section 3e. NMR in Type II BCS Superconductors

If the material being investigated by NMR is a Type II superconductor, the superconducting state NMR signal can be greatly enhanced by working in the mixed state ($T<T_c$, $Hc_1<Ho<Hc_2$).[46,47] When the applied static field is of this magnitude, the field penetrates the interior of the sample through a lattice of fluxoids. This lattice could in principle affect both line shapes and relaxation rates. The field B in the center of each fluxoid will be slightly larger than the applied field Ho. In the limit of isolated fluxoids ($Ho \sim Hc_1$), the magnitude of B in the sample will decrease exponentially over the length scale of the penetration depth, λ., as one leaves the center of a fluxoid. The variation of internal magnetic field with distance from fluxoid cores will result in an additional source of inhomogeneous NMR line breadth. Experimentally, the field distribution of the vortex lattice has been observed by the NMR line shape (e.g. in V_3Si, V_3Ga,[56] and Nb[57]).

In V_3Sn[58] and V_3Si,[59] the spin-lattice relaxation rates have also showed some unusual characteristics in the mixed state. The application of fields which were significant fractions of $Hc_2(0\ K)$ has wiped out the coherence peak. In addition, at low T/T_c, a linear field dependence of T1 has been observed. This last effect has not been satisfactorily explained, but it suggests that fluxoids may affect the relaxation rates in the mixed state at low temperatures.

Chapter 4. Experimental Techniques

Section 4a. Samples: As Grown

The experiments described in this thesis were only possible because of the availability of extremely high quality samples of $YBa_2Cu_3O_7$. The Slichter group has enjoyed a long and fruitful collaboration with the group of Prof. Don Ginsberg while investigating these High-T_c materials. Two of Prof. Ginsberg's students, Dr. Tom Friedmann and Joe Rice, have made and characterized all of the samples measured for this thesis.

Dr. Tom Friedmann synthesized all of the powder (or polycrystalline) samples of $YBa_2Cu_3O_7$ which we have measured.[13] The resulting powders were investigated by X-ray diffraction and SQUID measurements to confirm that they were predominantly a single phase and that they are good superconductors with sharp transitions. Samples grown by this technique contained about four grams per batch. The individual polycrystalline particles looked black and roughly spherical when viewed under a microscope. All of the powder samples reported on in this thesis have passed through at least a 37 μm sieve (and sometimes an 18 μm sieve).

Joe Rice made all of the single crystal samples investigated in this thesis using flux growth.[60] These single crystal samples were also confirmed to be single phase superconductors with sharp transitions by X-ray diffraction and by SQUID measurements. The largest high quality single crystal obtained by this technique weighed about one milligram. This large crystal was the primary sample studied in Dr. C. H. Pennington's thesis.[43]

The single crystals tended to grow into a platelet shape, with the

smallest dimension along the $\hat{c}$-axis (<100 μm). When viewed from directly above, the large (0.5mm X 0.5mm) flat face ($\hat{a}$-$\hat{b}$ plane) was black unless it was illuminated by the microscope light when it would become blindingly shiny. These single crystals were usually heavily twinned. This last phenomena reflected the slight difference in unit cell size parallel (b=3.8864 Angstroms at room temp) and perpendicular (a=3.8231 Angstroms at room temp) to the Cu-O chains.[22] Thus, as one travels along the $\hat{a}$-axis of a single crystal, it switches to the $\hat{b}$-axis of the crystal upon crossing a twinning boundary. This energetically favorable crystal structure has been cleverly defeated by the Ginsberg group to reveal many anisotropies of the $\hat{a}$- and $\hat{b}$- axes. For our purposes, the twinning boundaries make possible the alignment of the applied field $\vec{Ho}$ with the $\hat{a}$- and $\hat{b}$-axis simultaneously.

Section 4b. Samples: Manipulation for NMR Purposes

As we shall see in this thesis, most of the quantities which can be measured in the High-T_c materials are extremely anisotropic. To probe the NMR tensors of $YBa_2Cu_3O_7$ we needed to simplify the complicated data by knowing which crystalline axis was along our applied field. Two low temperature probes designed and built by Dr. Dale Durand were used for these experiments.[43] A probe is essentially a four foot long metal pole which places the sample in the center of the magnetic field. The signal cable and temperature control wires also run along the pole. These probes had faces milled to be accurately perpendicular to the applied field. A plexiglass stand with accurately milled surfaces (either parallel or perpendicular to $\vec{Ho}$) was installed in the probe can. An aligned sample holder specific to the sample

type was then attached to this stand, as we see in Figure 8.

For the single crystal samples, it was possible to align many crystals manually so that they shared a common $\hat{c}$-axis and $\hat{a}$-/$\hat{b}$-axis direction. To orient the $\hat{c}$-axis of these samples, we selected only single crystals which had clean, flux-free surfaces, and which reflected light evenly from their largest faces. These two qualities indicated that the crystalline $\hat{c}$-axis was accurately perpendicular to the biggest face. The large faces of these crystals were then placed flat on a narrow plexiglass strip. Orientation of the $\hat{a}$/$\hat{b}$-axis was obtained by viewing the crystals through a polarizing microscope in the crossed-polarizer configuration. When the crystalline $\hat{a}$/$\hat{b}$-axis was placed parallel to the incident light polarization direction, the reflected light would have the same (unrotated) polarization. This reflected light would be blocked by the crossed-polarizer, and the sample face would appear black. A small rotation (< 3 degrees) of the crystal from this configuration would cause the sample face to become visible. Each individual single crystal was adjusted on the sample holder until the faces of all the crystals appeared black simultaneously, and then they were glued in place using several coats of Crystal Clear, a commercial electronics sealant. In this way it was possible to establish a common direction for the $\hat{a}$/$\hat{b}$-axis of many single crystals being used for a single NMR sample. Thus NMR measurements could be made with the magnetic field applied along the $\hat{c}$- or $\hat{a}$-/$\hat{b}$- axis direction. Dale Durand used this property of the as-grown single crystals to construct an NMR sample of total mass 2-3 milligrams using ~50 single crystals, with common directions for both the $\hat{c}$-axis and the $\hat{a}$-/$\hat{b}$-axis. When this sample was not being used, it was kept in a desiccator to prevent degradation of the material.

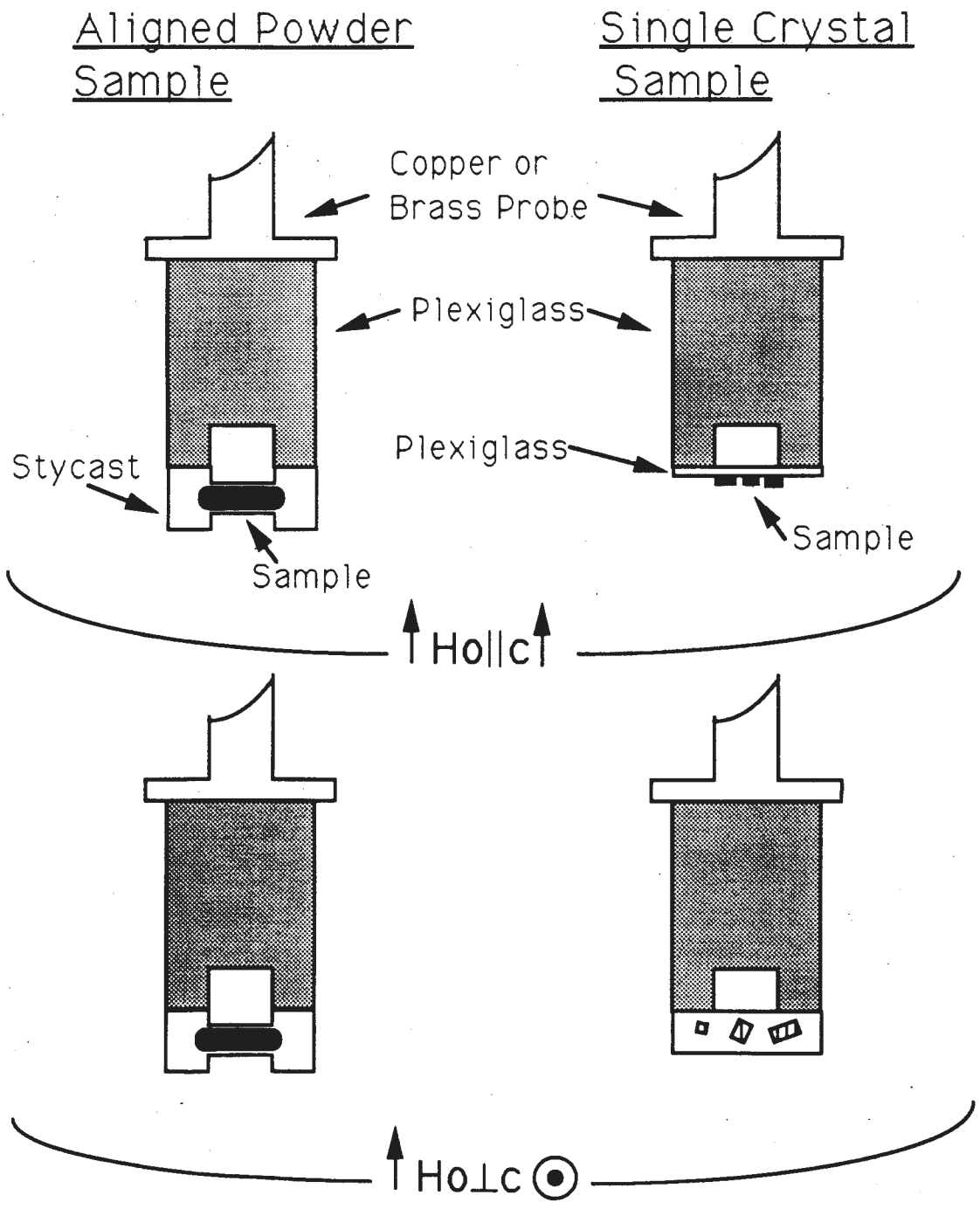

Figure 8. Aligned sample holders used for all of the NMR measurements presented in this thesis.

For the polycrystalline samples, the manual alignment techniques described above weren't an option. The method of Farrell et al. was used to create uniaxially ($\hat{c}$-axis only) aligned samples.[61] A cylindrical cast of Stycast 1266 epoxy was cured. This large cylinder was then machined to become a smaller cylinder with square blocks on either end. The superconductor was then fixed in this sample holder so that the $\hat{c}$-axis was perpendicular to two of the square block's faces. This was done by mixing together a fresh batch of Stycast 1266 and some $YBa_2Cu_3O_7$ powder (typically taking up 2%-30% by volume), inserting this mixture into the sample holder, sealing the open end with wax, and placing the whole assembly in an 8 Tesla magnet. The large anisotropy of the bulk magnetic susceptibility in these materials causes the $\hat{c}$-axes of the individual powder particles to align themselves along the magnetic field. The sample holder remains in the magnet until the epoxy has cured, freezing the crystallites in place.

Prior to making the aligned polycrystalline samples in the epoxy matrix, we had checked for an effect of the glue on the $YBa_2Cu_3O_7$. Starting with a large batch of powder, we placed a small quantity in a five-minute epoxy, Duro TM-51, and another small quantity in Stycast 1266. The NQR lineshapes and T1 of these glued samples were compared to those of the loose powder sample. No dramatic difference was observed.

We have conducted a systematic study of the alignment process using some $YBa_2Cu_3O_7$ powder and glycerol, a fairly viscous liquid. Using the width of the $^{63}Cu(2)$ central transition as our guide, we have established the following points on these magnetically aligned $YBa_2Cu_3O_7$ powder samples. First, when the matrix has the viscosity of glycerol at 300K, the alignment in an 81 kGauss field is complete in less than 2 minutes. This was determined

by placing a freshly stirred sample into the magnet and then periodically measuring the 63Cu(2) 1/2,-1/2 linewidth using fast Fourier transforms. Second, the volume fraction of $YBa_2Cu_3O_7$ powder can be at least 35% without affecting the alignment. In Figure 9, we show that the scaled NMR lineshapes for the $\vec{Ho} \,||\, \hat{c}$, $^{63}Cu(2)$ central transition taken during the 12.5% and the 35% packing fraction tests are virtually indistinguishable. Third, even in a matrix as viscous as glycerol, significant settling of the powder occurs over a several hour period. Thus, in order to prevent the sample from becoming grossly inhomogeneous, the $YBa_2Cu_3O_7$ powder should be mixed with the Stycast 1266 only after the curing process has begun, and the viscosity of this Stycast 1266 is approximately that of the glycerol. This is easier said than done because the viscosity of the Stycast 1266 always increased exponentially with time, but the time constant seemed to depend sensitively on the age of the starting materials, the batch size, and the shape of the container.

To ensure that the YBa2Cu3O7 powder was added to the curing glue when the Stycast's viscosity was approximately that of the glycerol, we tested each batch individually. In this procedure, a freshly mixed batch of Stycast 1266 was divided and placed into two test tubes. The viscosity of the Stycast in the first test tube was determined by periodically dropping stainless steel ball bearings into the curing epoxy. The time taken by the ball bearings to traverse a one inch drop through the epoxy (t_{Sty}) was compared to the time for an identical test in glycerol (t_{gly}). About 1.5-3 hours after the batch was mixed, these times were identical ($t_{Sty} \approx t_{gly}$). The Stycast from the second test tube was then used to make the aligned powder sample.

In one aligned powder sample discussed in this thesis, we have

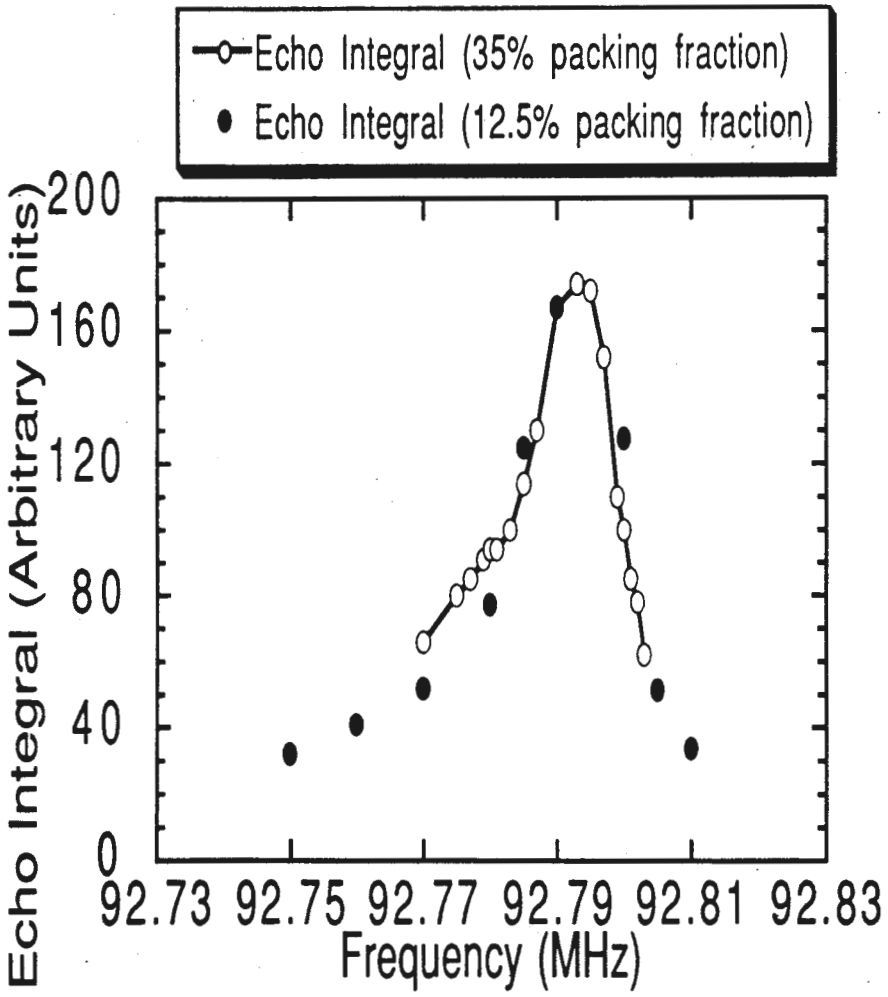

Figure 9. The $\vec{Ho} \| \hat{c}$, $^{63}Cu(2)$ central transition lineshape measured in a sample containing glycerol and $YBa_2Cu_3O_7$. The filled(empty) circles were obtained when the $YBa_2Cu_3O_7$ filled 12.5%(35%) of the total sample volume, the rest being glycerol.

measured the properties of the oxygen site using ^{17}O NMR. Since the natural abundance of ^{17}O is so small (3.7×10^{-2} %), this required an isotopic enrichment of one of Tom Friedmann's superconducting samples. Because the cost of ^{17}O enriched O_2 is prohibitive and its availability was limited after the discovery of High-T_c, it was necessary to enrich a sample in the most efficient way we could. To do this, we constructed our own exchange chamber and developed a recipe for enrichment based on the literature and the consultations of the Ginsberg group (see Appendix A). The sample which resulted from our group effort was a 93K superconductor, with a slightly lower Meissner and shielding fraction and a slightly broader transition than the starting material, as we see in Figure 10. The copper NQR linewidth (see figure) and yttrium lineshape were broader than the spectra in Tom's best samples, consistent with a slightly lower oxygen content and perhaps less homogeneity in the enriched sample. Nevertheless, the copper and oxygen relaxation rates and line positions were in agreement with the other published data.

In Table II we list all of the samples measured in this thesis, and we list some of their relevant properties.

Section 4c. NMR Techniques

Most of the experiments described in this thesis were carried out in an Oxford Instruments 89mm/360MHz magnet which was operated in the persistent current mode. The usual field was about 81 kGauss. In addition, an older Varian electromagnet was used for the weak field measurements (~4.5 kGauss). NQR experiments were carried out in regions of the lab where

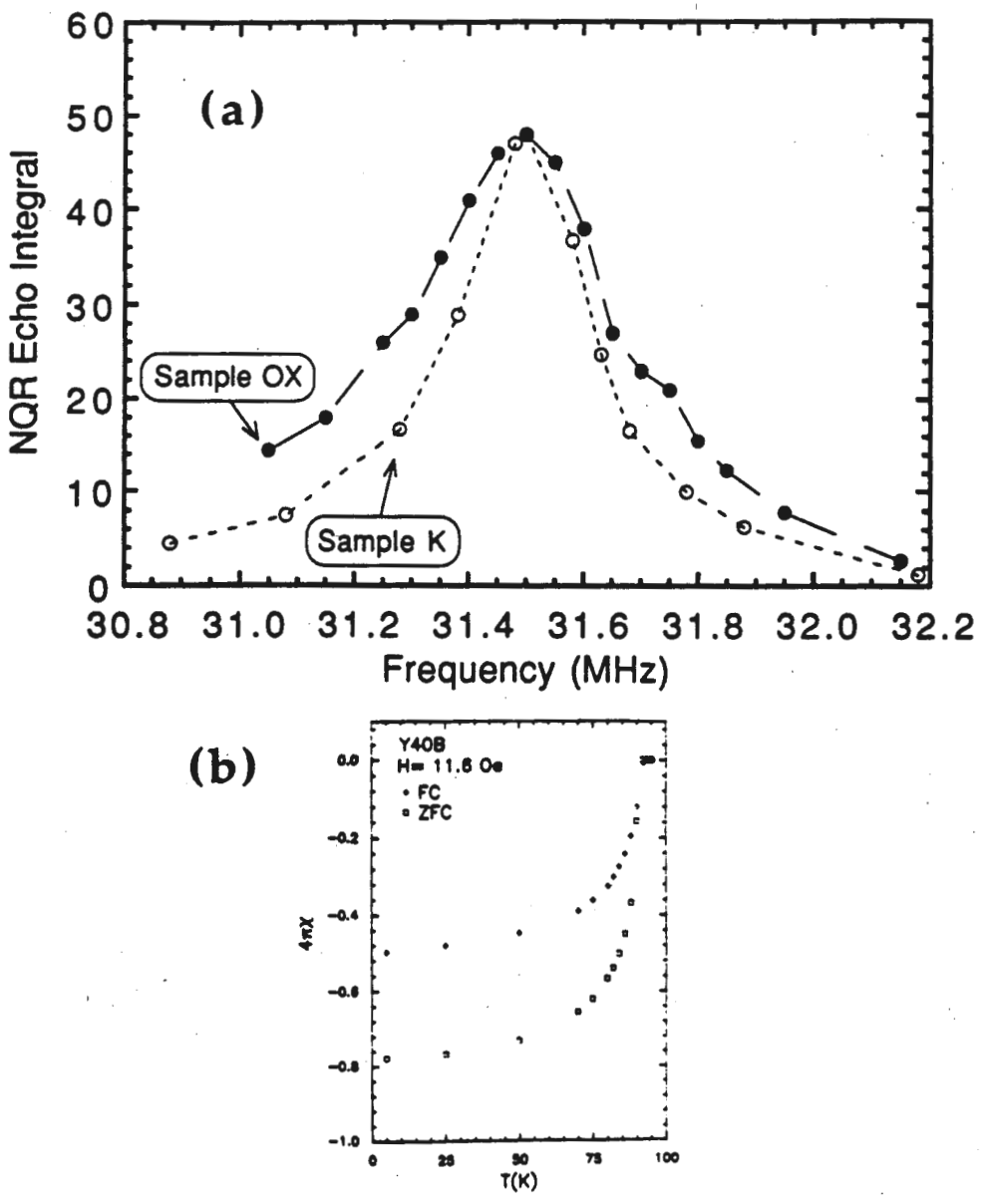

Figure 10. (a) NQR linewidth of Sample OX (^{17}O enriched) is broader than for our best $YBa_2Cu_3O_7$ samples (e.g. Sample K). (b) Field-cooled and zero-field-cooled SQUID susceptibility measurements of Sample OX (Ho~12 Gauss).

Sample Name	Mass	Sample Packing Fraction (in glue)	Particle Size	Sample Type	Label in Barrett, Durand, et al.[13]	Label in Barrett, Martindale, et al.[14]	Label in Martindale, Barrett, et al.[16]	Notes
K	1.98 g	10 %	< 38 µm	A. P.	A. P.	# 5	A. P.	Batch Y30
DURAND	2.5 mg	100 %	50 single crystals	S. C.	S. C.	# 1	----	J. P. Rice Batch
X	75 mg	2 %	< 18 µm	A. P.	----	# 4	----	Batch Y36
OX	375 mg	30 %	< 18 µm	A. P.	----	# 6	----	Batch Y40B. 17O enriched
Y	1.8 g	100 %	< 38 µm	R. P.	NQR Powder	----	----	Batch Y30. Cu NQR
Y	1.8 g	50 %	< 38 µm	R. P.	----	----	----	Batch Y30. Yttrium T1.
Y41	3.6 g	100 %	< 38 µm	R. P.	----	# 2	----	Batch Y41
Z	2 g	25 %	< 18 µm	A. P.	----	----	----	Batch Y41

Table II. Master list of all samples used in this thesis. The packing fraction is the volume fraction of the superconductor in an epoxy matrix. The sample types are:A.P.-aligned powder, S.C.-aligned single crystals, R.P.-unaligned random powder. The Batch labels refer to the labeling system of Dr. Tom Friedmann, who provided the samples.

the local field was less than 5 Gauss.

The experiments were performed using a homemade pulsed radiofrequency spectrometer.[43] A schematic diagram is shown in Figure 11. The same rig has been altered to make measurements from Fo=5 MHz to Fo=127 MHz. The NMR experiments are controlled by a master program written by Dale Durand for the IBM XT.[62] This program is the user friendly way to control the pulse generation equipment. One key part of this equipment is the pulse sequence generator (PSG) built by Charles Pennington.[43] The PSG could be programmed by the computer to repeatedly step through up to 8192 output states, spending a flexible time of between 0.2 μs and ~1 day in each state. Each output state consists of a defined value for 24 independent TTL outputs (which could create pulses, open gates, trigger scopes, trigger amplifiers, etc). Once a pulse sequence has been loaded into the PSG and it has begun to step through the sequence, it requires no further assistance from the computer. The pulse generation part of the rig was typically set up to generate RF pulses (minimum length 0.2 μs, step size 0.1 μs) which could be phase shifted some multiple of 90 degrees relative to a reference. These pulses would then be amplified by a commercial amplifier (≤ 400Watts) and sent to the probe circuit.

The probe circuit, shown in Figure 12, contained the sample and was the standard series-parallel resonant circuit. The probe was tuned at resonance to have an impedance of 50 Ω. Typical values of Q for the probe circuit are 50-200. Ideally, the pulses would be amplified to the upper limit of the high power amplifier, so that the signal amplitude and spectral coverage would be largest. In general, however, arcing restricted the applied pulses to lower voltage levels. When power pulses above the arcing limit were applied,

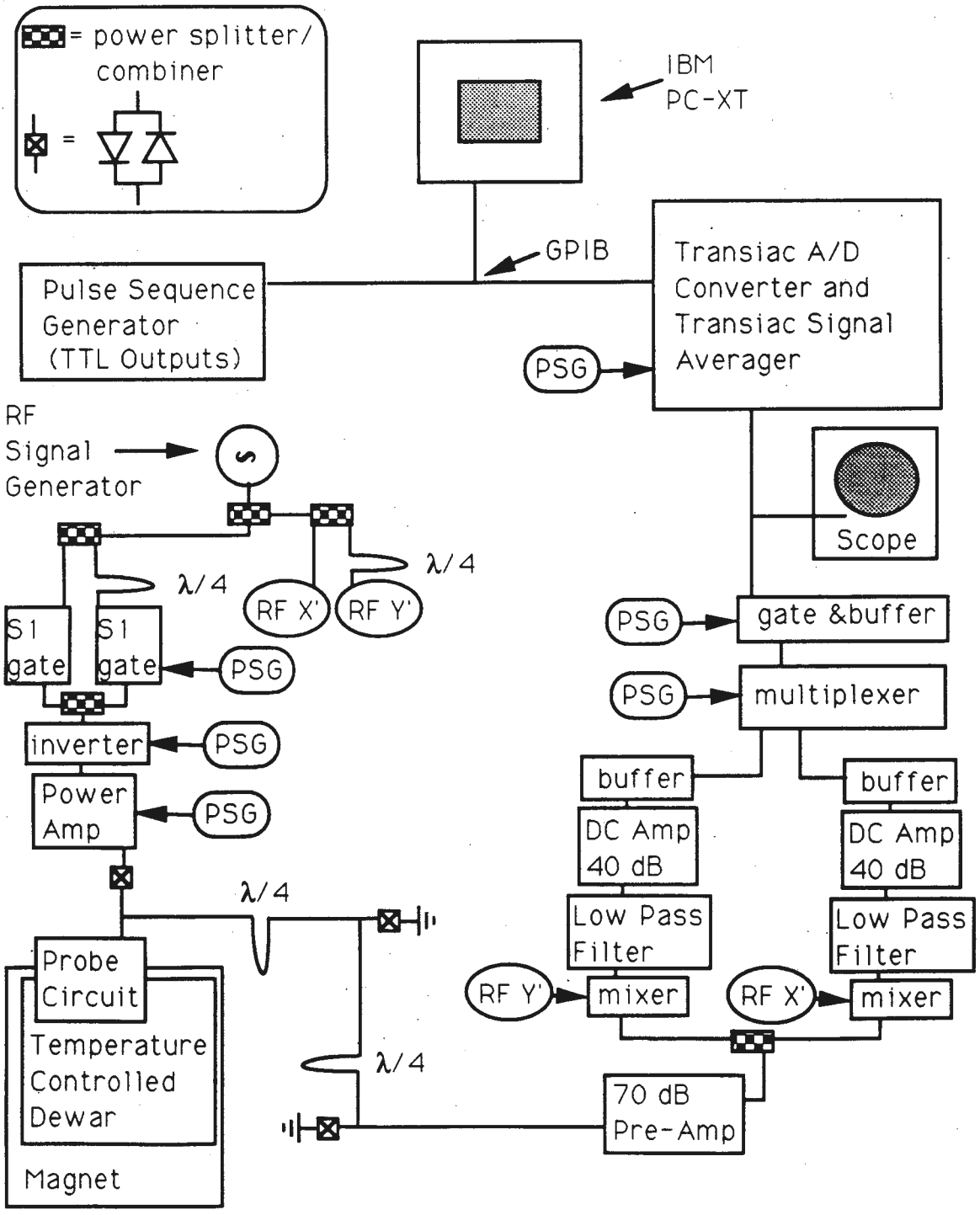

Figure 11. Schematic diagram of the radio frequency spectrometer used for all NMR/NQR experiments reported in this thesis. All signals are measured using quadruture detection.

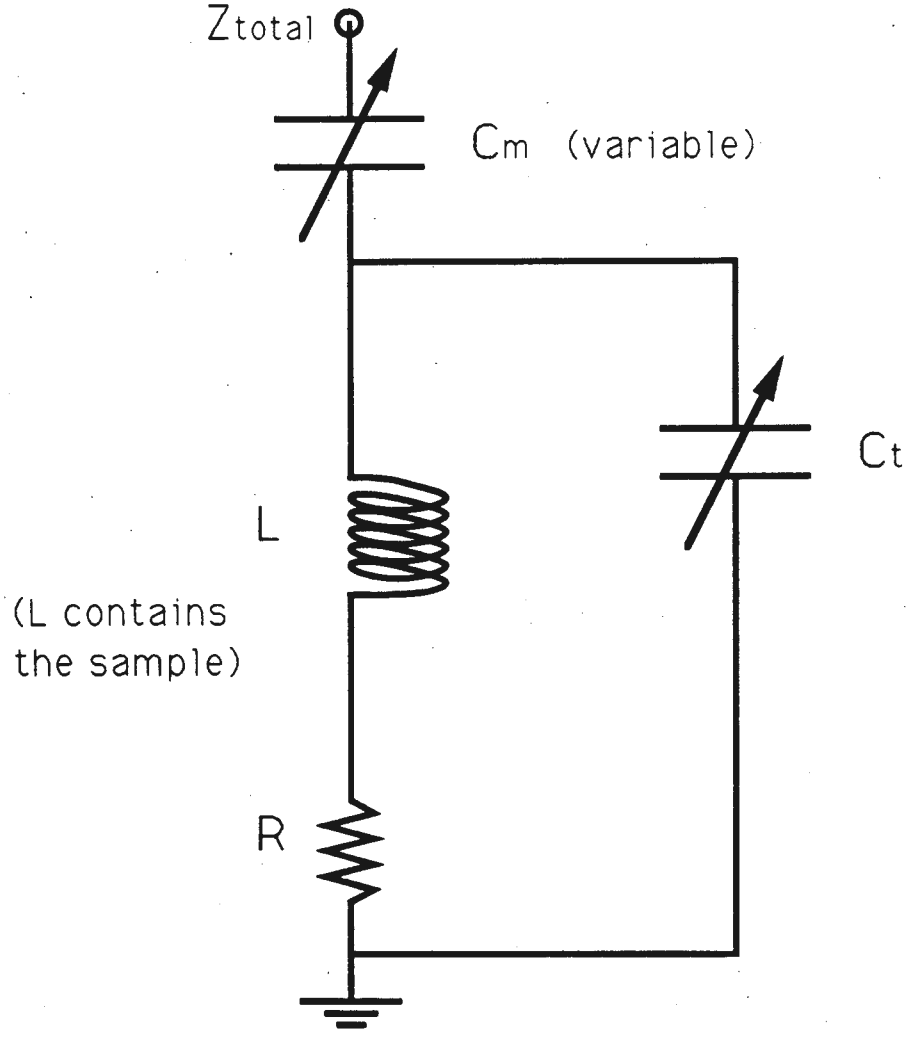

Resonant Conditions:

Complex Impedance: $\mathrm{Re}(Z_{total}) = 50\ \Omega$

$\mathrm{Im}(Z_{total}) = 0$

$$C_t + C_m = \frac{1}{\omega^2 L} \qquad C_m = \sqrt{\frac{R}{50\ \Omega}}\,\frac{1}{\omega^2 L}$$

Figure 12. Series-parallel resonant circuit used in our probes. The inductor (L) is wrapped around the sample. The quality factor is given by $Q=\omega L/R$.

the high voltages generated in the resonant circuit could not be sustained and a high voltage point would arc to a lower voltage point through some dielectric (e.g. from one side of the matching capacitor through the exchange gas to the probe can). This problem became much worse in a Helium gas atmosphere or at low pressures. To combat this problem, it was necessary to avoid sharp points in the circuit, to separate spatially high and low voltage points, to use series capacitors, and to wrap capacitors with layers of mylar. Even with these precautions, the excitation pulses were rarely large enough to cover the NMR line of interest. The range of applied alternating field excitation pulses was H1~5-50 Gauss.

The solenoids used in our probe circuit were different for each sample and each nucleus. The coils for the Y NMR were made from brass. These coils typically had ~35 turns which were separated from each other by fishline or heat shrink tubing. The Cu (~6 turns) and O (~10 turns) NMR coils were silver. A background Cu metal signal was observed when the regular brass or copper probe cans were used, but it was much smaller when a silver plated probe can was substituted. This background signal was eliminated just as effectively using an Al foil lining of the regular can which was kept in place by Mylar sheets. The low field copper measurements at 10 MHz used a ~50 turn solenoid; the turns of this solenoid were kept insulated from one another by several coats of Crystal Clear. The copper NQR measurements used copper metal coils (~25 turns). A Q-limiting resistor (~50 kΩ,metal film, ± 1%) was sometimes used in parallel with the solenoid to prevent an excessive temperature dependence of the tuning range of our probe circuits.

The tuning of our resonant probe circuit was dramatically affected upon entering the superconducting state. The diamagnetic supercurrents

changed the effective inductance of the coil, which upset the resonance condition. This change in L_{eff} may be compensated for by adjusting the capacitance of the circuit, but it usually took about 20 minutes before this tuning drift died out. This effect is seen in glued samples in a strong field and in both glued and loose powder samples in zero field. In one experiment, we attempted to look at the NMR signal of an unaligned packed powder in the 81 kGauss field at 4.2 K. The tuning oscillated horribly for over 12 hours and showed no signs of stopping. This same sample (Sample Y) was then imbedded in five minute epoxy (Duro TM-51) using a 50% packing fraction. The resulting glued sample showed the usual tuning drift in the 81 kGauss field at 4.2 K which died away after a short time (~20 minutes). There are several possible causes of this effect, including shielding currents jumping from crystallite to crystallite, frustrated attempts by the individual crystallites to align their $\hat{a}$-axis along the applied field, and particles levitating above one another. This effect shows the importance of the sample holder for the NMR measurements in the superconducting state.

Quadruture detection was employed, simplifying the data collection and enhancing the signal to noise ratios. This technique effectively allows one to measure the nuclear magnetization along the x- and y-axis in the rotating frame. The information in both channels was stored simultaneously by multiplexing into a single channel Transiac 2008 analog/digital converter which feeds into a Transiac 2101 signal averager. Since the signal to noise ratio for many of these experiments was less than one after a single measurement, the measurements were repeated many times (sometimes 10^6 repetitions) until the signal to noise ratio was satisfactory. The information stored in the signal averager was occasionally dumped to the computer at the

request of the master control program, where it was displayed in graphical form and could be easily manipulated (e.g. echo integration and fast Fourier transforms of the second half of the echo).

Three pulse sequences were used repeatedly for this thesis. We use the notation for pulses that we introduced in Section 3b. NMR absorption lines were measured using the spin echo sequence (ECHO4PH.PUL):

(4-1) $\pi/2 - \tau - \pi - \tau$ - echo.

The phases of the pulses for this and the other pulse sequences are described and explained at the end of this section. When the width of the absorption line was much smaller than the frequency width of the excitation pulse (the large H1 limit), the spectrum could be obtained by Fourier transform of the second half of the echo. For many of the experiments described in this thesis, the NMR absorption lines were too broad to be accurately revealed by a Fourier transform. In this case the line shape was taken "point by point". This technique involved stepping through the frequency range of the spectra, and integrating the echo that is formed at each frequency (this is equivalent to performing a Fourier transform at each frequency, but recording only the size of the transform at the oscillator frequency). The lineshape that results is identical to the Fourier transform lineshape that would be obtained if the excitation pulse was large enough to cover the whole line.

Spin-lattice relaxation times were measured using the inversion recovery technique (T17.PUL):

(4-2) $\pi - t_{inv} - \pi/2 - \tau - \pi - \tau$ - echo.

To minimize the effects of electronics drift, this sequence was loaded into the PSG so that eight different t_{inv} times (including $t_{inv} = 7(T1) \sim t_{inv} = \infty$) are cycled through in turn. The sequence was then repeated many times to

improve the signal-to-noise ratio.

Low temperature yttrium lineshapes were measured using the Carr-Purcell-Meiboom-Gill sequence[63,64] (LONGCP.PUL):

(4-3) $\pi/2 - \tau_1 - \pi - \tau_2 -$ echo $- \tau_1 - \pi - \tau_1 -$ echo $- \tau_1 - \pi - \tau_1 -$ echo $- \ldots$

This sequence was used to create a train of 16 echoes in our experiments. The effect of a finite H1 is compensated for by making $\tau_2 = \tau_1 + \frac{2}{\pi} T_{\frac{\pi}{2}}$ This pulse train was completed in less than 20 msec, while the shortest T1 during this experiment was about 60,000 msec. Each succeeding echo in the train was added together in weighted sum to optimize signal to noise. The weighting factor for each echo was the ratio of its amplitude to the amplitude of the first echo. The signal to noise ratio of the weighted sum of n-echoes is:

(4-4) $$\left(\frac{S}{N}\right)_n = \left(\frac{S}{N}\right)_0 \frac{1}{\sqrt{n}} \left(\frac{1 - r^n}{1 - r}\right),$$

where r is the ratio of successive echo amplitudes in the train, and $(S/N)_0$ is the signal-to-noise ratio of the first echo in the train. In our experiment we were able to use 16 echoes in the train. This resulted in a signal-to-noise enhancement of 2.5 over the usual spin echo for the same total measurement time (or a reduction of measurement time by $(1/(2.5))^2$ for the same signal-to-noise ratio).

There were also two other pulse sequences which were used to measure some of the yttrium relaxation rate data. The first was a hybrid of the inversion recovery and CPMG sequences (T17CPMG.PUL):

(4-5) $\pi - t_{inv} - \pi/2 - \tau_1 - \pi - \tau_2 -$ echo $- \tau_1 - \pi - \tau_1 -$ echo $- \ldots$

A four echo train was added in a weighted sum for each t_{inv}. This pulse sequence gave the same result for the yttrium T1 as was obtained in a simple inversion recovery measurement in a shorter (~1/2) measurement time.

Another useful sequence was a hybrid of the CPMG and a saturation recovery sequence (NEV.PUL):

(4–6) $(\pi/2 - T2^*-)_n - t_{sat} - \pi/2 - \tau_1 - \pi - \tau_2 -$ echo $- \tau_1 - \pi - \tau_1 -$ echo $- \ldots$

The $(\pi/2 - T2^*-)$ unit is repeated n=5 times, to saturate the magnetization. At the end of this comb pulse the magnetization is identically zero along every axis in the rotating frame, and it recovers along the z-axis during the time t_{sat}. This magnetization along z is then measured by a four echo CPMG train. This sequence was used for the 4.2 K measurement of the yttrium T1, and it also yielded values for the yttrium T1 at high temperatures which were consistent with the inversion recovery measurements. One important difference between the saturation recovery and inversion recovery technique is the total time required for a T1 measurement. The wait time after each echo train in a measurement sequence should be at least (could be shorter than) several T1's because measurements using inversion recovery (saturation recovery) assume the experimental condition, $\vec{M} = -\vec{M}_\infty$ ($\vec{M}=0$), exists just before the evolution time, t_{inv} (t_{sat}). Thus the total time required by a saturation recovery experiment is less than that required by the analogous inversion recovery experiment. Since the experimental conditions necessary for accurate inversion recovery T1 measurements are easier to obtain in practice, inversion recovery results are considered to be more reliable, and the extra time required by these experiments is tolerated. However, saturation recovery must be turned to when T1 becomes exceedingly long (as is the case for the yttrium nucleus at 4.2 K, when T1~480 seconds).

The size of the echo produced in these experiments was rarely much larger than the "ringing down" of the resonant circuit due to the large

excitation pulses. In order to isolate the echo signal, phase cycling techniques were required.[43] The spin echo was always performed in a four phase sequence:

(4-7a)	ADD	$\pi/2_x$ - τ - π_x - τ - echo (along -y)
(4-7b)	SUB	$\pi/2_{-x}$ - τ - π_x - τ - echo (along +y)
(4-7c)	ADD	$\pi/2_{-x}$ - τ - π_y - τ - echo (along -y)
(4-7d)	SUB	$\pi/2_x$ - τ - π_y - τ - echo (along +y).

By adding and subtracting the sequence shown above the echoes add constructively, and the ringdown from the pulses cancels. The T1 measurement was made using the alternating phase inversion recovery. The above sequence was used for the echo formation, and the initial inversion pulse was alternated between π_x and π_{-x}, and the results were added. This last technique was important for cancelling out stimulated echoes. For the Carr-Purcell-Meiboom-Gill sequence, the pulse train involved either $\pi/2_x$ or $\pi/2_{-x}$ followed by sixteen π_y pulses. This choice of phases is less sensitive to pulse imperfections than the Carr-Purcell sequence.

Section 4d. Temperature Control

Experiments in this thesis were performed in the temperature range 4.2 K to 300 K. Two separate dewars were used to achieve these sample temperatures within the room temperature bore of the magnets. A homemade stainless steel dewar was used in the range 70 K to 300 K.[65] A liquid nitrogen bath in the outer reservoir cooled a large copper radiation shield which was separated from the probe space by an evacuated region. The probe space was filled with the probe and 1 ATM of Nitrogen gas. This

configuration cooled the sample down to temperatures of ~83 K. It was possible to achieve lower probe temperatures (~80 K) by pumping on the nitrogen bath in the outer reservoir. Filling the probe space with liquid nitrogen made the sample temperature 77.4 K. We were able to cool down to 70 K by pumping on this liquid nitrogen filled probe space through a manostat borrowed from Dr. Tom Friedmann. Filling the probe space with liquid helium allowed us to take points at 4.2 K. Temperatures were measured using a copper-constantan thermocouple on the brass probe can. This thermocouple was calibrated against other new temperature sensors (e.g. a Ge diode thermometer, and a carbon glass resistor) in the temperature range near T_c. An Artronix temperature controller monitored this temperature and applied a controlled current to a 30Ω heater wire on the probe can to stabilize the sample temperature.

For temperatures less than 77 K, a Janis Varitemp continuous flow helium cryostat was used. This dewar cooled the probe by allowing a small flow of liquid helium from a storage dewar, through a transfer line, and into the bottom of the probe space where it evaporated and rose towards the probe can. Temperatures were measured with a Lake Shore carbon glass resistor on the copper can. The Artronix controlled this temperature by heating the gas (Knight Shift experiment) or the can (W1 anisotropy experiment). The disadvantage of this dewar was the helium gas atmosphere, which made arcing occur at a much lower RF pulse voltage.

Since quantities like the W1 vary as fast as the fifth power of the temperature near T_c, it is very important to have a stable temperature control system and to know what the actual sample temperature is as well. We have found that it is very hard to know the actual sample temperature in the

region just below T_c, because the sample is apparently heated by the RF pulses. We have found methods to minimize this problem, but this is the reason our data points do not go continuously through the transition.

As we discussed in the last section, the change in the sample's macroscopic magnetic susceptibility χ_{mag} below T_c affects the tuning condition of our resonant circuit:

(4-8) $C_{total}=1/(\omega_o^2 L_{eff})$, where $L_{eff} = L_o (1 + 4\pi\chi_{mag})$.

In this expression, L_o is the coil inductance, and C_{total} is the total capacitance in the probe circuit.[66] Since we are usually interested in looking at an NMR line at a particular frequency ω_o, this change in χ_{mag} is compensated for by changing C_{total}. However, we could also keep C_{total} fixed, changing ω to keep the circuit tuned below T_c. If there is no applied field, this change in frequency $\Delta\omega$ (e. g. 4 MHz out of 32 MHz) maps out the function $\chi_{mag}(T)$ in the superconducting state, as we see in Figure 13. We have used this property of the samples to determine the zero-field superconducting transition temperature of our samples (T_c=93 K). Once we have made such a curve, we know the tuning frequency, $\omega_o + \Delta\omega$, of the circuit as a function of temperature. In one series of experiments, we adjusted the frequency and temperature so that the circuit was tuned at 88 K. When we applied RF pulses with an amplitude ($V_{\text{to the probe}}$~200 Volts peak-to-peak, so that T_{90}= 5 μsec) and repetition rate (Trep ~ 4 msec) used just above T_c, the circuit detuned in a very short time (≤ 1 minute). Immediately after stopping the pulses, the circuit tuned at a new frequency consistent with a sample temperature increase of about 2 K. The tuning frequency of the circuit would eventually drift back to its original value at 88 K over a period of approximately ten minutes. This cycle could be repeated as many times as we

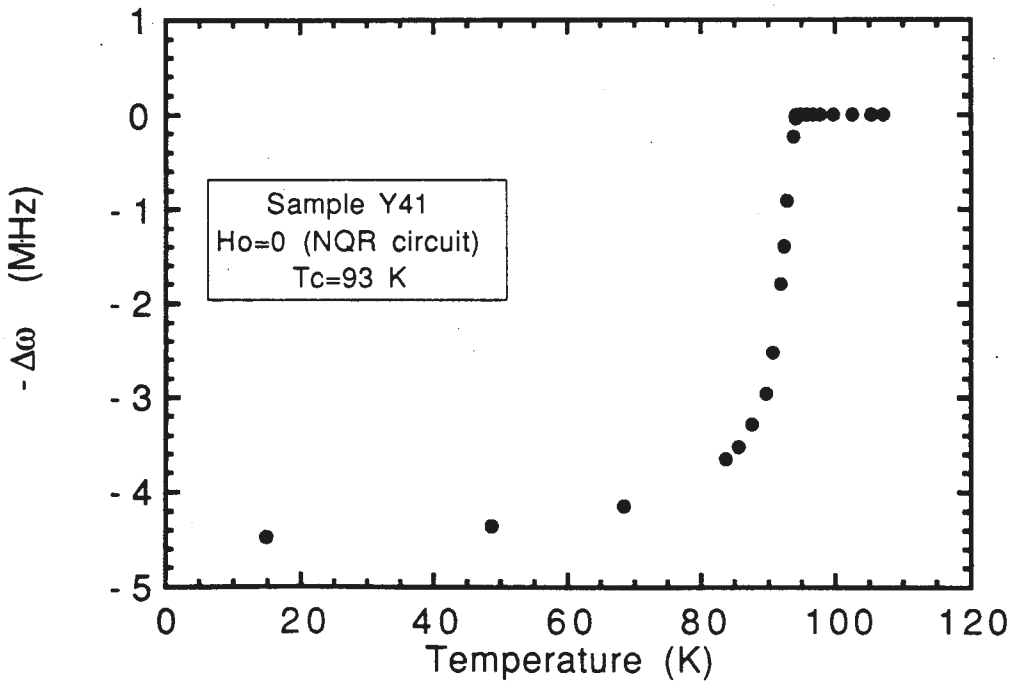

Figure 13. Temperature dependent change in the optimal tuning frequency of an NQR circuit containing sample Y41 for fixed capacitor values. This curve indicates that the zero-field superconducting transition temperature for this sample is Tc(Ho=0) = 93 K.

wished. Thus, we have clear evidence for sample heating by the application of RF pulses just below T_c.

We checked whether this sample heating was due to the direct interaction with the RF fields or the joule heating of the coil. Placing a thick layer of cotton between the sample and coil did not reduce the heating effect at all. The detuning was also observed as it happened using a second pick-up coil in the can; the heating occurred on the time scale of seconds. These two results are consistent with sample heating due to the direct interaction with the RF fields. To reduce this heating effect, we applied a much smaller average power to the sample, and the circuit remained tuned. We have tried both much smaller RF pulses ($V_{\text{to the probe}}$~30 Volts peak-to-peak, so that T_{90}= 30 μsec) and much slower repetition rates (Trep ~225 msec). For very small signals, the latter technique works better because the resulting spin echo is narrower, and errors due to baseline roll are negligible. These techniques were necessary for measurements made on powder samples between 80 K and T_c.

Chapter 5. Previous NMR Results in $YBa_2Cu_3O_7$

Section 5a. Early Normal State Data and Interpretations.

All of the nuclei in $YBa_2Cu_3O_7$ are potential candidates for NMR study.[67,68,69] Table III shows the NMR properties of the various isotopes in this material. Much of the earliest work in unaligned powder samples focused on the copper sites, and showed that one could distinguish the resonances of the planes and the chains (Cu(2) and Cu(1)).[70,71,72,73] The Cu(1) relaxation rate was Korringa-like (that is T1T= a constant) between T_c and 200 K, however the Cu(2) relaxation rate depended only weakly on temperature. Some NQR T1 measurements by Dr. C. P. Pennington are shown in Figure 14.[13] The comparison of the measured relaxation rates for the two isotopes (e. g. ^{63}Cu(2) at 92 MHz and 65Cu(2) at 100 MHz for $\vec{Ho} \,||\, \hat{c}$ = 81 kGauss) revealed that the relaxation was magnetic in origin. The measured relaxation rates were surprisingly fast, surpassing not only the expected magnitude of an orbital relaxation rate, but also exceeding (by a factor of 10) the measured relaxation rate for Cu metal at room temperature.[72]

The single crystal studies of Pennington et al. revealed the information on the material's anisotropy which was hidden in random powder sample measurements.[74,75] By using a completely aligned sample, they were able to apply the static field $\vec{Ho}$ along each principle axis $\vec{\alpha}=\hat{a},\hat{b},\hat{c}$ of the crystal. The families of resonance lines measured in each case allowed one to determine for both Cu(1) and Cu(2) the elements of the magnetic shift ($K_{\alpha\alpha}$), electric field gradient ($\nu_{\alpha\alpha}$), and spin-lattice relaxation rate ($W1_\alpha$) tensors.[76] W1 is directly proportional to (1/T1) described earlier. All three tensors exhibited

Isotope	Spin	Natural Abundance	$(\gamma_n/(2\pi)) \times$ 100 kGauss	Quadrupole Moment ?
^{63}Cu	3/2	69 %	113 MHz	Yes
^{65}Cu	3/2	31 %	121 MHz	Yes
^{89}Y	1/2	100 %	21 MHz	No
^{17}O	5/2	3.7×10^{-2} %	58 MHz	Yes
^{135}Ba	3/2	7 %	42 MHz	Yes
^{137}Ba	3/2	11 %	47 MHz	Yes

Table III. NMR properties of the various isotopes in $YBa_2Cu_3O_7$.

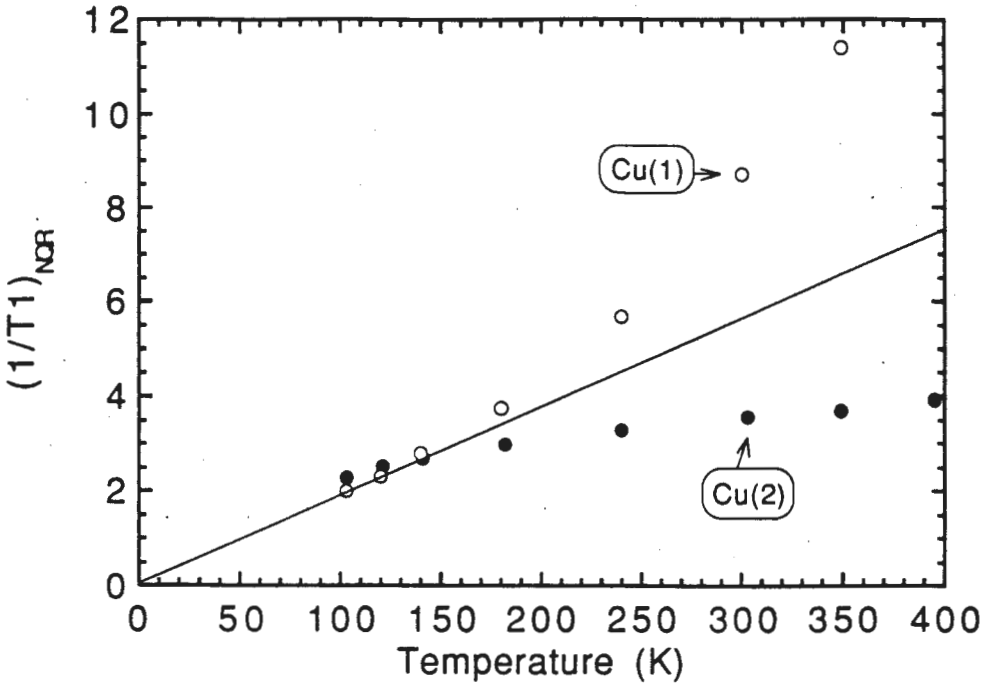

Figure 14. The filled(empty) circles are the $YBa_2Cu_3O_7$ NQR spin-lattice relaxation rate data for the ^{63}Cu plane(chain) sites in Sample Y.[13] The dark line in the figure shows the Korringa-like behavior expected in a normal metal.

strong anisotropy.[77,78]

To explain their data, Pennington et al. proposed a model which was essentially the permanent moment limit.[76] The copper atom was Cu^{++} ($3d^9$) and the spin 1/2 associated with the atom was due to a hole in the x^2-y^2 (y^2-z^2) ground state for the plane (chain) site. The chemical shift K^L was then due to the orbital susceptibility of the hole. The Knight shift arose from the hyperfine coupling between the nuclear spin and the on-site spin of the hole. They used expressions for the hyperfine coupling constants of a Cu^{++} permanent ion. Within this model, they showed that there must be both a chemical shift and a Knight shift to explain the observed magnetic shift anisotropy.

Further measurements of the T1 in NQR experiments confirmed the distinct difference between the chain and plane sites. The NQR T1 measurements of Imai et al. were crucial in establishing the trends of the Cu(2) relaxation rates for the various High-T_c compounds.[79,80,81,82] They argued that their Cu(2) T1 data, shown in Figure 15, followed a universal form at high temperatures ($T > T^* \sim 150$ K):

$$(5\text{-}1) \qquad (1/T1)_{NQR} \cong A+BT.$$

The unusual (non-Korringa) character of the planar copper's temperature dependence is due to the presence of the term A, which becomes progressively more important than the B term as the temperature is lowered. For temperatures close to T^*, the relaxation rate of the planar copper is greatly enhanced compared to its Korringa value. They proposed that this enhancement of the relaxation rate (the A term) was due to antiferromagnetic correlations of the Cu(2) electronic spins, which were building up as the temperature was lowered towards T_c.

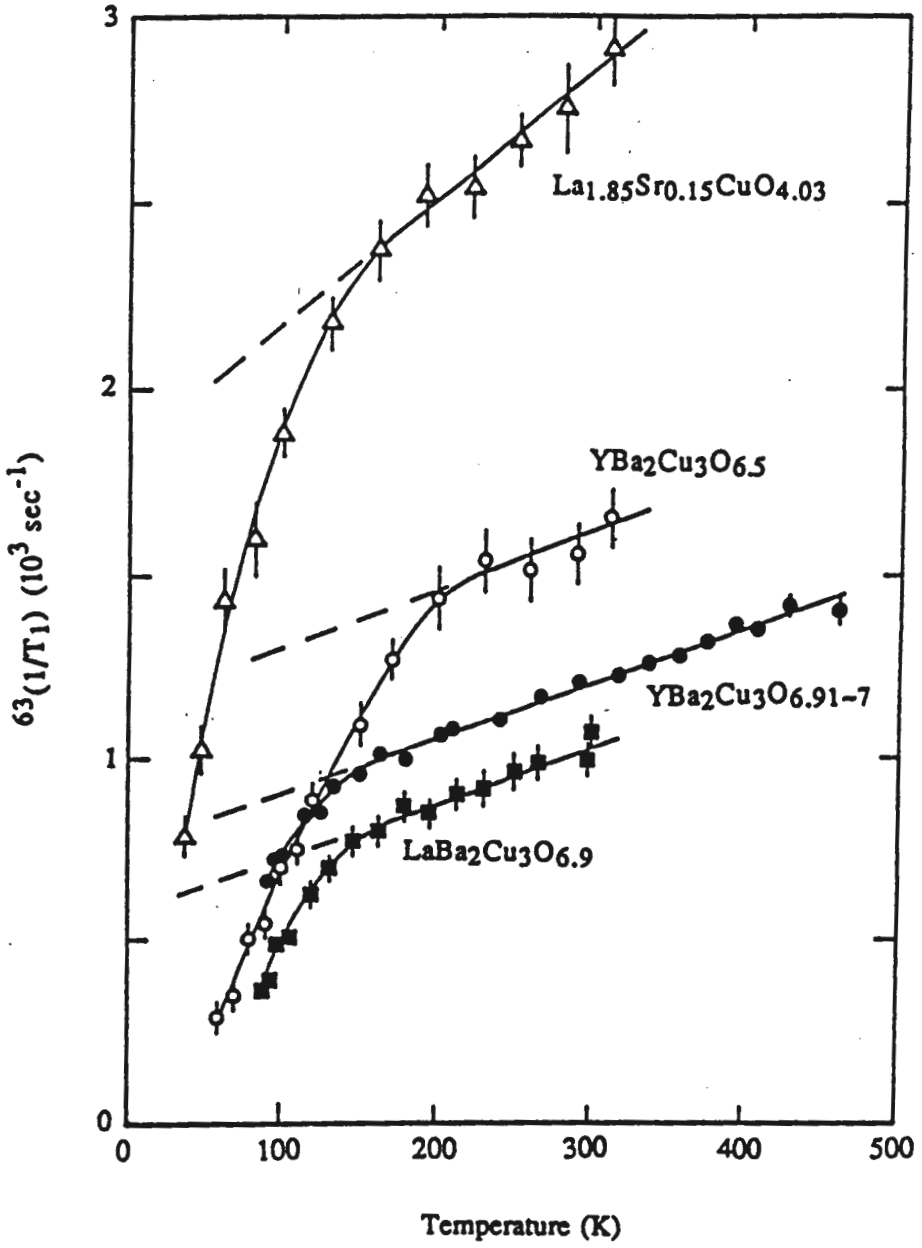

Figure 15. Temperature dependence of the ^{63}Cu(2) NQR spin-lattice relaxation rate for several High-T_c materials.[82] The dashed lines through the data suggest that $(1/T1)_{NQR} \cong A+BT$ at high temperatures.

Measurements of yttrium NMR (100% natural abundance) in unaligned powders showed that the total magnetic shift K_Y was small compared to that of the copper sites ($K_Y < 0.1\ K_{Cu}$).[71,83,84,85,86] In the 90K material, the shift K_Y was essentially independent of temperature above T_c. In Figure 16, we see that the Y relaxation rate 1/T1 was Korringa-like.

An important breakthrough occurred when Farrell et al. showed that one could make a $\hat{c}$-axis aligned powder.[61] The $\vec{Ho} \| \hat{c}$ and $\vec{Ho} \| \hat{a}/\hat{b}$ resonances may now be distinguished in such a sample.

Measurements of ^{17}O NMR in isotopically enriched aligned powder samples revealed that there were three distinct oxygen resonances.[87,88,89] One resonance was due to the two nearly equivalent oxygen sites in the plane (O(2) and O(3)). Another resonance was due to the oxygen site in the chain (O(1)). The last resonance was that of the bridging (or apical) oxygen site (O(4)) which lies on the $\hat{c}$-axis between the Cu(2) and the Cu(1). None of the measured oxygen magnetic shifts were temperature dependent, and they were all smaller than the copper magnetic shifts. All of the relaxation rates were Korringa-like, as is shown in Figure 17.[90,91] The O(4) relaxation rate was approximately 100 times slower than the plane or the chain rates.

Because the CuO_2 planes are the one structural unit of $YBa_2Cu_3O_7$ which appear in every other High-T_c superconductor (containing Cu), theorists concentrated their efforts on explaining the behavior of the Cu(2), O(2,3), and Y site in this material. One obvious way to explain why the Cu(2) relaxation rate did not have the same temperature dependence as the Y and O(2,3) was to say that those different nuclei coupled to different systems, e.g. one a set of Cu(2) spins, the other an O hole band.[92] This is a two-component theory of the electron spin system of the CuO_2 planes. However, some

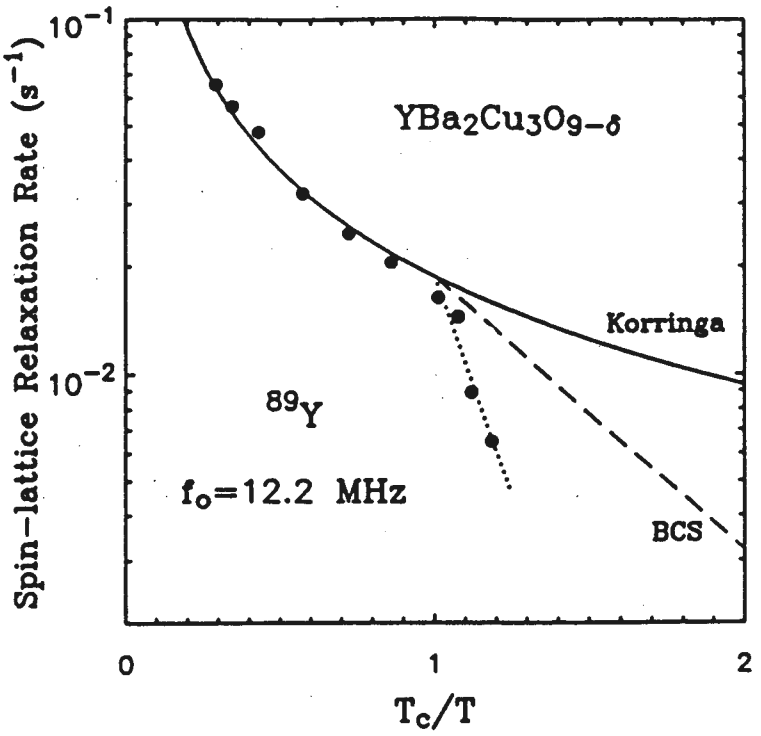

Figure 16. Spin-lattice relaxation rate for ^{89}Y in the 90 K superconductor ($YBa_2Cu_3O_{9-\delta}$, $\delta \cong 2.1$), demonstrating the Korringa behavior in the normal state.[83]

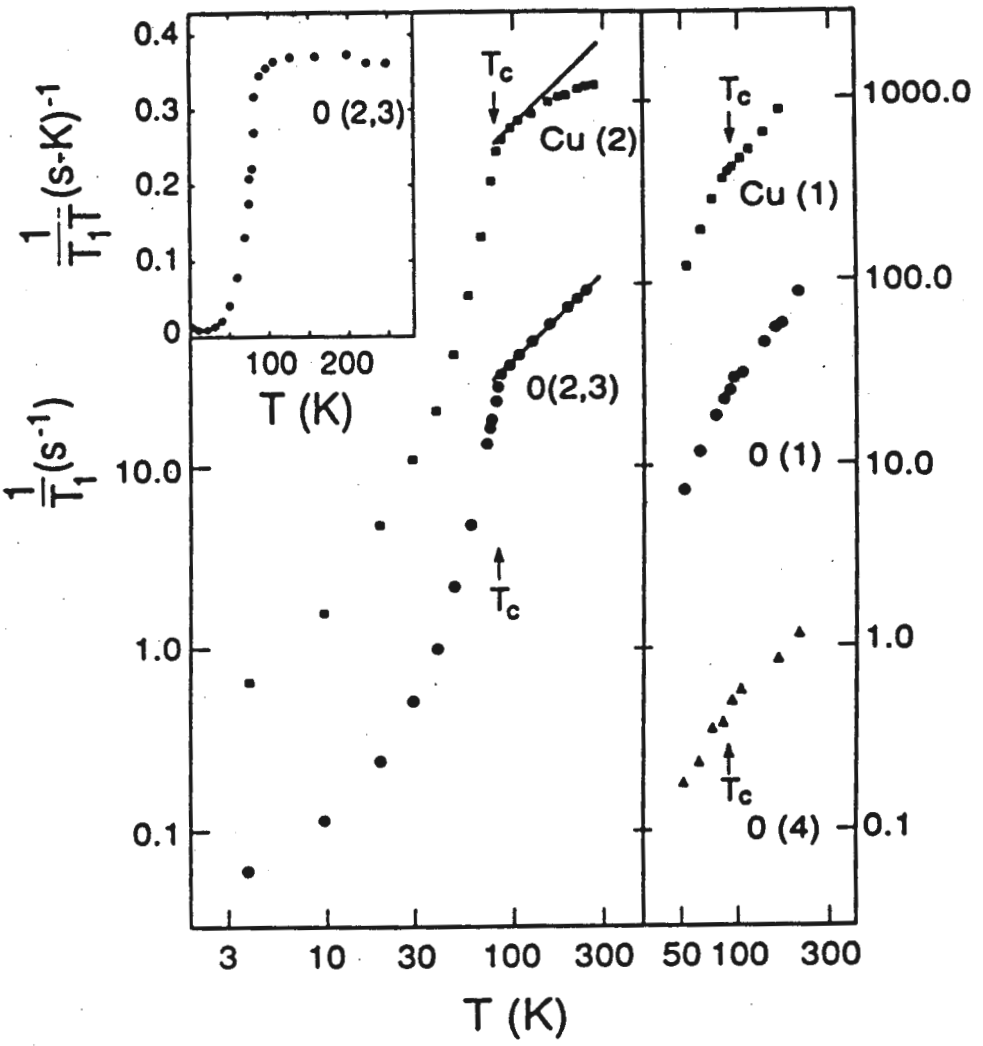

Figure 17. The NMR, $\vec{H}o \,||\, \vec{c}$, relaxation rates versus temperature for all four oxygen sites in $YBa_2Cu_3O_7$.[90] The inset shows the Korringa-like behavior of the planar oxygen (O(2,3)) relaxation rate in the normal state.

theorists believe that the two systems are so strongly coupled that they would act as a single system, at least for the low energy scale probed by NMR.[93] We now turn to experimental evidence for this viewpoint.

Section 5b. Experimental Evidence for a One-Component Theory

NMR experiments in reduced oxygen samples of $YBa_2Cu_3O_{6+x}$, where $x<1$, show dramatically different behavior from the NMR results of the last section. Yttrium measurements by Alloul et al. in a series of reduced oxygen samples yielded the surprising result that the magnetic shift of the Y was strongly temperature dependent in the normal state for $x\sim0.4$ - 0.8.[86] Their data are shown in Figure 18. Comparison of the Y Knight shift measurements and the macroscopic magnetic susceptibility were interpreted as showing that the spin shift for each nucleus was directly proportional to a single spin susceptibility that could be associated with the spin on the Cu(2) atom. Later, Cu(2) and O(2,3) experiments were performed on a sample of $YBa_2Cu_3O_{6.63}$, where T_c = 62 K.[94] These experiments showed that the isotropic magnetic shift for the Cu(2) and the O(2,3) was temperature dependent and directly proportional in the normal state, as is shown in Figure 19. This was interpreted as evidence that the O(2,3) nuclei couple to the same spin susceptibility as the Cu(2) nuclei. Measurements of the Cu(2) and Y in another reduced oxygen sample by the Bell Labs collaboration was consistent with the results of the other groups.[95,96] Thus all three nuclei apparently couple to the real part of the same electronic spin susceptibility $\chi^S(\vec{q}=0, \omega=0)$. This is a single-component model for the electron spin system (of the CuO_2 planes).

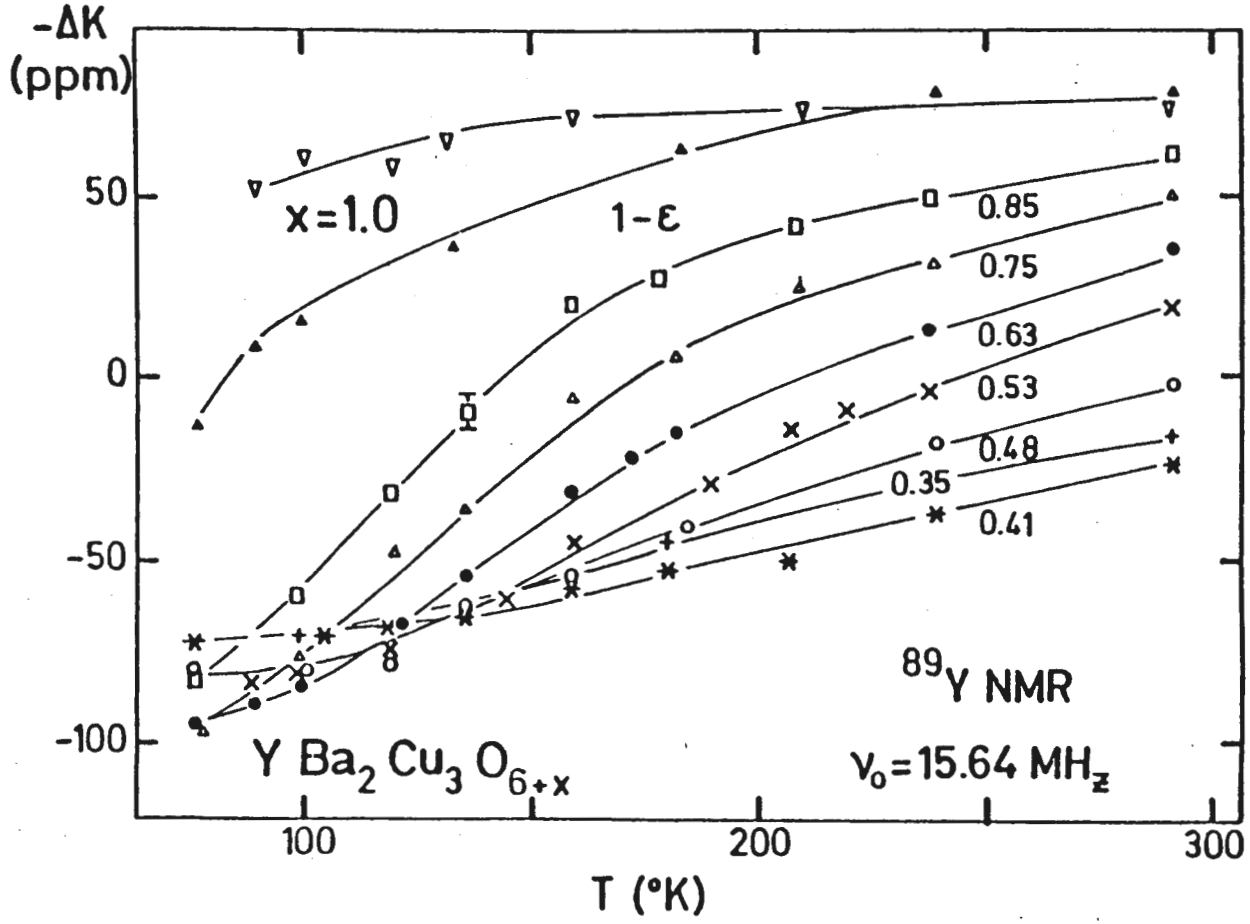

Figure 18. The temperature dependence of the quantity -ΔK (=(-1)*(magnetic shift, referenced to YCl_3)) for the ^{89}Y in $YBa_2Cu_3O_{6+x}$ ($0.35 \leq x \leq 1$).[86] Only the x=1 material (Tc=90 K) behaves like a normal metal.

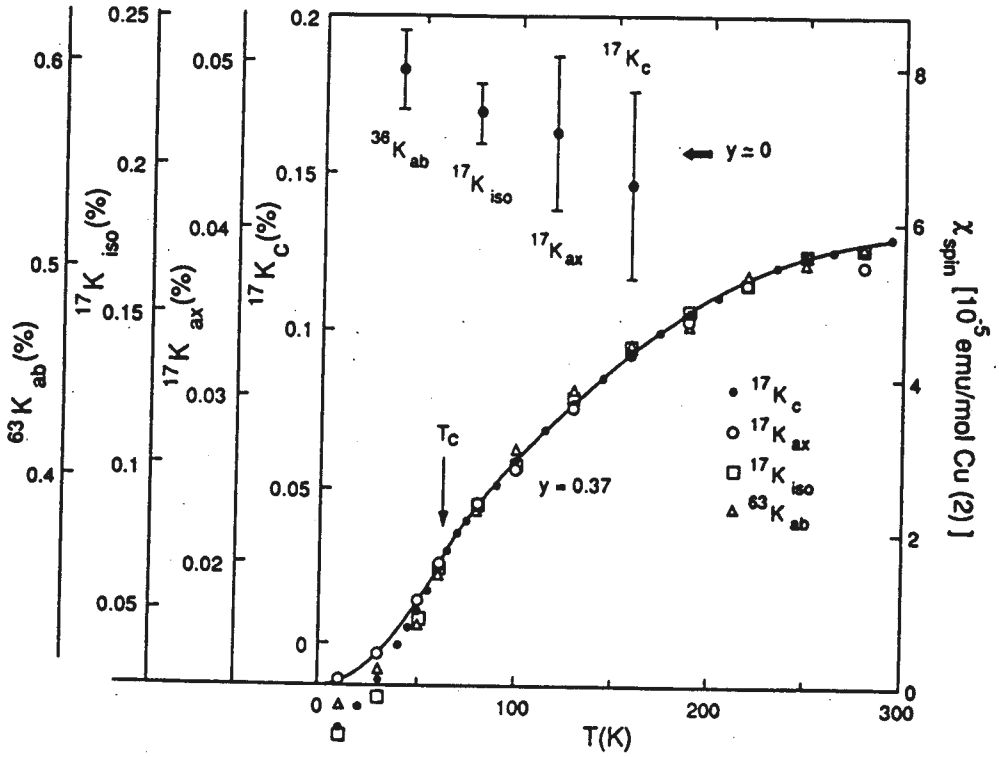

Figure 19. The temperature dependent components of the planar copper and planar oxygen magnetic shift tensors for $YBa_2Cu_3O_{7-y}$ (y = 0.37, Tc=62 K) plotted against temperature with different vertical scales and origins.[94] The temperature independent Knight shift values for the y=0 material are shown for comparison.

It is worth noting that the above evidence is very convincing, but not ironclad. There is some uncertainty in the zero temperature values for the magnetic shifts of the O(2,3) and Y. This uncertainty calls into question whether $^{17}K^S$ and $^{89}K^S$ are each directly proportional to or just linearly related to $^{63}K^S$. A single-component model would require direct proportionality of all three Knight shifts.

Section 5c. One-Component Model for the CuO_2 Planes

The conventionally accepted model for the relaxation rates of the Cu(2), O(2,3) and Y starts with the Mila-Rice Hamiltonian for the Cu(2).[97] This Hamiltonian for the hyperfine couplings of the ith Cu(2) nucleus is:

$$\hat{H} = \sum_{\alpha=a,b,c} \left[A_{\alpha\alpha} \hat{I}^i_\alpha \hat{S}^i_\alpha + \sum_j B \hat{I}^i_\alpha \hat{S}^j_\alpha \right]. \tag{5-2}$$

The first term is the anisotropic on-site coupling proposed by Pennington et al. to explain the anisotropic $W1_\alpha$ and $K_{\alpha\alpha}$ tensors.[76] This term represents the extra fields at the nucleus due to the hole spin in the x^2-y^2 $3d^9$ orbital. The next term is an isotropic transferred hyperfine coupling of the four nearest neighbor Cu(2) spins to the nucleus. This coupling is isotropic and quite large because it is due to the overlap of the nearest neighbor copper spin (x^2-y^2) orbital with the unfilled 4s orbital of the on-site Cu(2) atom, mediated by the intervening O(2,3) 2pσ orbitals. Mila and Rice proposed that this second term was present to explain the observation by Takigawa et al. that the isotropic average of the Knight shift was positive for the Cu(2).[98] We will discuss Takigawa et al.'s measurement in Section 5f.

The experimental work of various groups[90,99] demonstrating the

striking difference in the temperature dependence of the O(2,3) and Cu(2) relaxation rates and the theoretical work of Shastry[100] to explain these data led to the conventionally accepted picture.[101] The O(2,3) has a transferred hyperfine coupling to the two nearest neighbor Cu(2) spins. The earlier experimental work by Alloul et al.[87] on the Y also showed that the yttrium susceptibility tracked that of the copper, so the yttrium has a hyperfine coupling to its eight nearest neighbor copper spins: four in the plane above and four in the plane below. Thus the oxygen,yttrium and copper are coupled to the same spin system. The difference in the temperature dependence of their relaxation rates is rooted in their real space hyperfine couplings. The complete one-component hyperfine coupling Hamiltonian is now:[101]

$$\hat{H} = \sum_{\alpha=a,b,c} \left[A_{\alpha\alpha}\, {}^{63}\hat{I}^{i}_{\alpha}\, \hat{S}^{i}_{\alpha} + \sum_{j} B\, {}^{63}\hat{I}^{i}_{\alpha}\, \hat{S}^{j}_{\alpha} + \sum_{l} C\, {}^{17}\hat{I}^{k}_{\alpha}\, \hat{S}^{l}_{\alpha} + \sum_{n} D\, {}^{89}\hat{I}^{m}_{\alpha}\, \hat{S}^{n}_{\alpha} \right] \tag{5-3}$$

C and D are assumed isotropic in the conventional model. These couplings emphasize different regions of the $\chi''_{\alpha\alpha}(\vec{q},\omega)$. Within this model the T1 is written as:[44]

$$ {}^{i}\left(\frac{1}{T1}\right)_{\alpha} = \left(\frac{{}^{i}\gamma_n^2\, k_B T}{2\,\mu_\beta^2}\right) \mathrm{Lim}_{\omega\to 0} \sum_{\vec{q},\alpha'\neq\alpha} \left|{}^{i}A_{\alpha'\alpha'}(\vec{q})\right|^2 \frac{\left\{\chi''_{\alpha'\alpha'}(\vec{q},\omega)\right\}}{\omega} \tag{5-4}$$

This expression is valid for i=63,17,89 (Cu(2), O(2,3), and Y), the only difference being the quantity $|{}^{i}A_{\alpha\alpha}(\vec{q})|$, which is the $\vec{q}$-space expansion of the real space hyperfine coupling constants.

We can see the difference between the various $|{}^{i}A_{\alpha\alpha}(\vec{q})|^2$ in Figure 20.[107] Because the fluctuating fields perpendicular to the quantizing field are responsible for the relaxation, we can see from the figure how sensitive the various rates are to the different regions of $\vec{q}$-space. For our purposes the

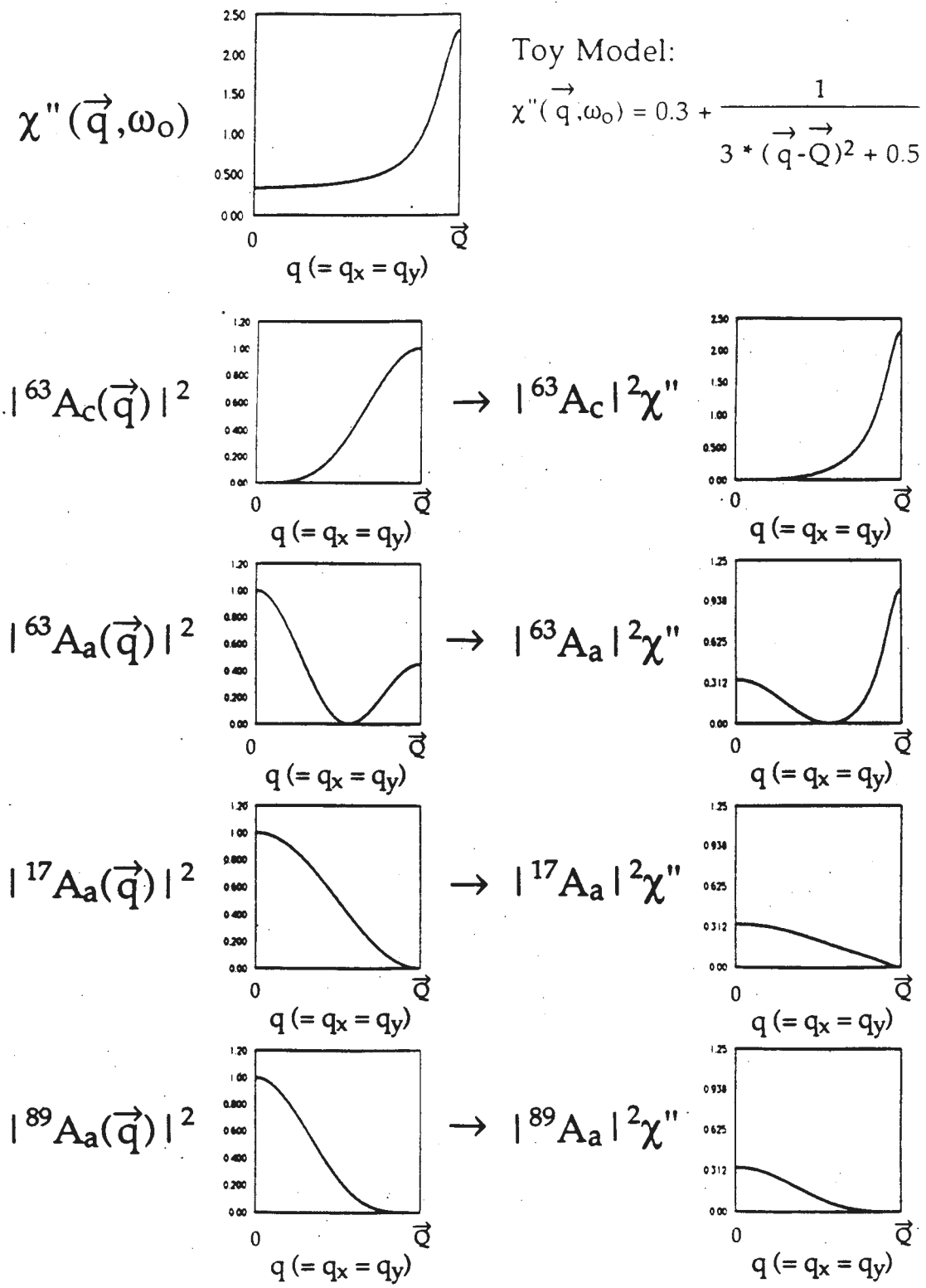

Figure 20. Each hyperfine form factor (left side) multiplied by χ" (top) yields a uniquely q-dependent product (right side) found in Equation (5-4).[107]

most important regions of the two-dimensional Brillouin zone are large $\vec{q}$ ($\vec{q}\sim\vec{Q}=(\pi/a,\pi/a)$) and small $\vec{q}$ ($\vec{q}\sim 0$). With this in mind, we can rank the relaxation rates in order of decreasing sensitivity to the large $\vec{q}$ region of $\chi''(\vec{q},\omega)$: ^{63}W1a,^{63}W1c,^{17}W1c,^{89}W1c. To illustrate this, we show the products $|{}^{i}A_{\alpha'\alpha'}(\vec{q})|^2\,\chi''_{\alpha'\alpha'}(\vec{q},\omega)$ in Figure 20 for $\vec{q}$ along the zone diagonal, using a toy model of $\chi''(\vec{q},\omega)$ which has a big peak at $\vec{q}=\vec{Q}$ (due to antiferromagnetic correlations of the Cu(2) electronic spins). If this big peak had a different temperature dependence from the $\vec{q}=0$ region, the Cu(2) relaxation rates would have a different temperature dependence from the O(2,3) and Y relaxation rates, as is experimentally observed.

The hyperfine couplings we have discussed so far and their implications within a one-component model are widely accepted concepts. However, the actual form chosen for $\chi''(\vec{q},\omega)$ and the microscopic justification for that form is a much more controversial issue. Many of the theoretical models for the normal state, including a Fermi liquid,[2] an antiferromagnetic Fermi liquid,[4] and a marginal Fermi liquid,[3] have proposed their own form for $\chi''(\vec{q},\omega)$, all strongly influenced by the Cu(2) NQR data and analysis of Imai et al..[81]

One particular model, proposed by Millis, Monien, and Pines (MMP), achieved great success in quantitatively fitting the normal state data (K^S and T1).[4] One potential difficulty with this model is reconciling its form for $\chi''(\vec{q},\omega)$ with the neutron scattering data. In particular, the MMP chosen temperature dependence of the peak at large $\vec{Q}$ disagrees with the interpretation of some of the neutron scattering data.[37,103] It is important to note that the neutron scattering measurements probe $\chi''(\vec{q},\omega)$ at finite ω, while the NMR experiments are only sensitive to $\chi''(\vec{q},\omega\sim 0)$.

Section 5d. Anomalies in Other High-T_c Compounds: Is $YBa_2Cu_3O_7$ an Exception?

Many measurements have been made on the Cu(2) sites (and sometimes the O(2,3) sites) in other materials, such as $YBa_2Cu_3O_{6+x}(x<1)$,[94,95,96] $YBa_2Cu_4O_8$,[104,105] $La_{2-x}Sr_xCuO_4$,[81] $Bi_{2-x}Pb_xSr_2CaCu_2O_8$,[106] and $Bi_{2-x}Pb_xSr_2Ca_2Cu_3O_{10}$.[107] These data have been interpreted as implying: (1)- $A_{\alpha\alpha}$ and B are about the same size in all of these materials,(2)- ^{63}Kab, and ^{17}Kc are temperature dependent in the normal state (T<300 K),(3)- the spin susceptibility as determined from bulk susceptibility measurements is temperature dependent in the normal state,[108] and (4)- (1/T1) has a unique temperature dependence in the normal state consistent with a temperature dependent spin susceptibility. The NMR properties of these materials are quite different from the NMR properties of $YBa_2Cu_3O_7$.

This unusual change in the behavior of the spin susceptibility of these other materials for T<300 K is apparently not affecting the charge sensitive properties (e.g. resistivity measurements). It has been suggested that a spin gap opening up in the normal state could explain the above data.[69] At present there is no widely accepted mechanism for such a spin gap. Nevertheless, some of the neutron scattering data have been interpreted as evidence for this spin-charge separation.[103,109] Of course, the controversial idea of a spin gap opening up in the normal state is not a unique explanation of the temperature dependent spin susceptibility in the normal state of these materials. However, at present, no other quantitative theoretical explanation exists.

If the unusual normal state NMR properties of these other materials

share a common origin, one is led to ask why this anomalous behavior is absent in $YBa_2Cu_3O_7$? Recently, careful measurements of the normal state Knight shift and susceptibility have indicated that the spin susceptibility in even this material is slightly temperature dependent.[110,111] These data have been interpreted as evidence for superconducting fluctuation diamagnetism above Tc. However, if all the known High-Tc superconductors have some temperature dependence in their spin susceptibility, the most general statement we can make is that the normal state magnetic behavior of the High-T_c compounds is decidedly non-metallic. This problem deserves more data and theoretical analysis.

Section 5e. Early Superconducting T1 Measurements

No Hebel-Slichter coherence peak is seen at any site for any nucleus.[71,73,83,90] In addition, (1/T1) does not follow the exponential behavior at low temperatures expected for a BCS spin-singlet, orbital s-wave pairing state. Imai et al fit their $(1/T1)_{NQR}$ data to a T^3 form, but this only fit the data over 2 decades (see Figure 21).[80] Several groups suggested that these results implied either a strong pair breaking mechanism or an unconventional superconducting state.

Subsequently, Hammel et al. reported the surprising result that the Cu(2) ^{63}W1c and the O(2,3) ^{17}W1c measurements tracked each other for 20K<T<120K, as is shown in Figure 22.[90,91] Within a single-component model, as we saw earlier, ^{63}W1c is more sensitive to the large $\vec{q}$ values of $\chi''(\vec{q},\omega)$, while ^{17}W1c is only sensitive to the small $\vec{q}$ region. Because ^{17}W1c was Korringa-like and ^{63}W1c wasn't, it was believed that the large $\vec{q}$ region

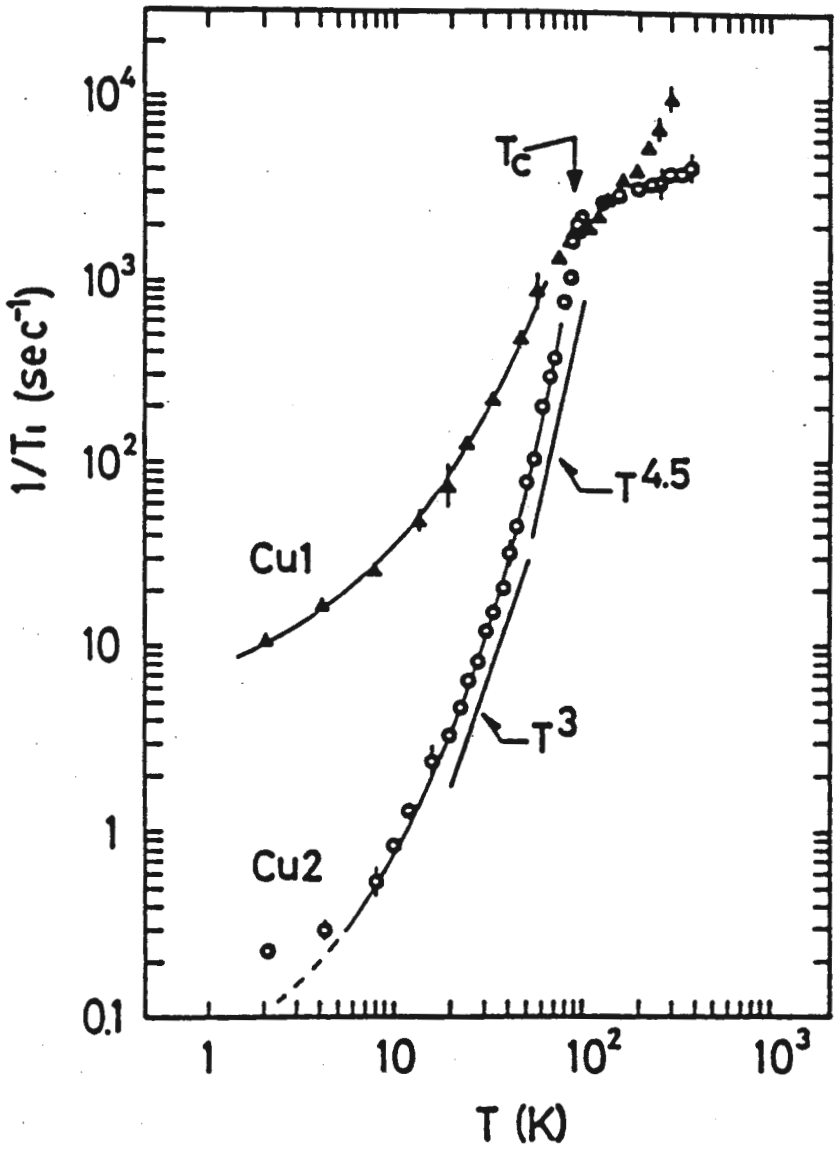

Figure 21. NQR spin-lattice relaxation rate data for the ^{63}Cu plane (Cu(2)) and chain (Cu(1)) sites.[80] For a BCS d-wave pairing state, one expects that $(1/T1) \propto T^3$ as $T \rightarrow 0$.

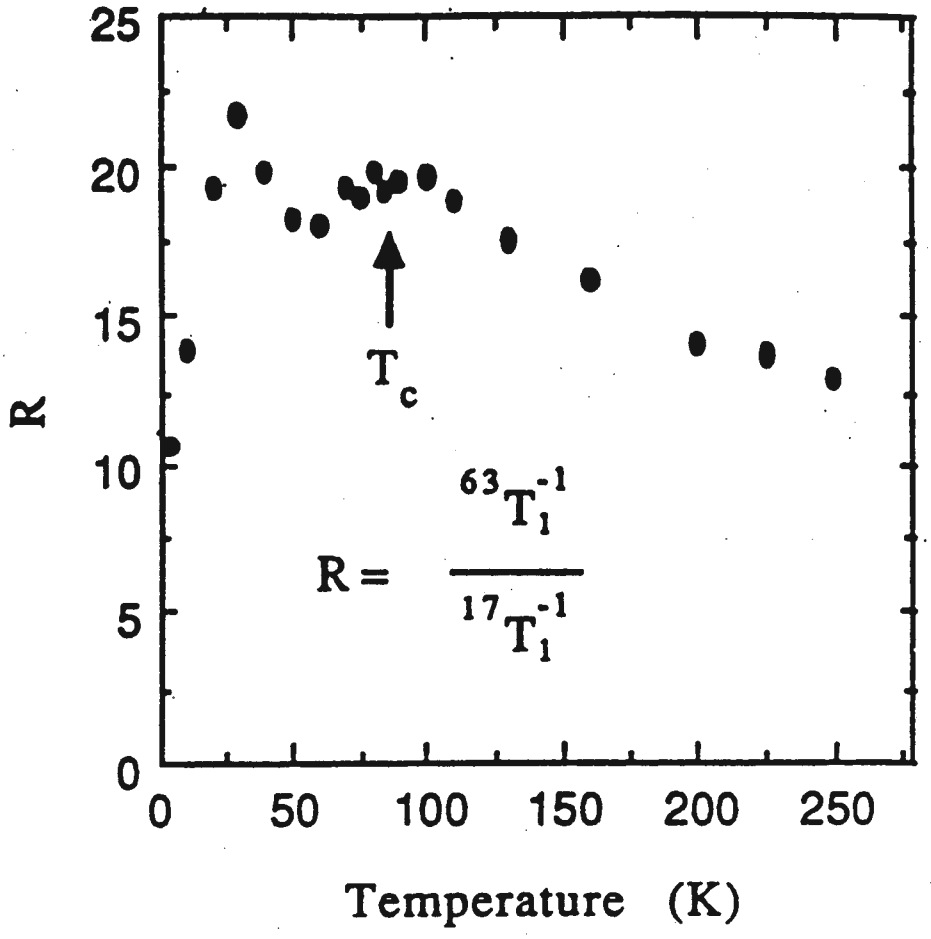

Figure 22. Plot of the quantity $R \equiv (^{63}W_{1c}/^{17}W_{1c})$ for the Cu(2) and O(2,3) sites as a function of temperature for a 70 kGauss field applied along the $\vec{c}$-axis.[91]

and the small $\vec{q}$ region of $\chi''(\vec{q},\omega)$ had different temperature dependences. Hammel's strong field (70 kGauss) measurement implied that below T~120K, all $\vec{q}$ regions of $\chi''(\vec{q},\omega)$ locked together and followed a common temperature dependence, right through the superconducting transition at T_c~90 K. This experiment was a strong constraint on attempts to understand our superconducting state NMR data.

Recently we have learned of an experiment by Yoshinari,Yasuoka et al. which shows quite a different behavior for the ^{63}W1c/^{17}W1c ratio for temperatures 50 K <T< 120 K, as we see in Figure 23.[112] One potential explanation for the discrepancy between these two experiments is a sample difference. Another possible explanation for the disagreement is the experimental difficulty of measuring such fast relaxation rates because of stimulated echoes. This last problem refers to the possible creation of more than one echo for a three pulse sequence used to measure relaxation rates. This complication can be avoided if phase-cycling techniques are used. J. Martindale has measured 63W1c/17W1c in a 40 kGauss field down to T = 20 K using these phase-cycling techniques. He also finds 63W1c/17W1c to be temperature dependent below 120 K, with a ratio which would lie in between the data of the other two groups.[113] It remains to be seen which experiment reflects the intrinsic behavior of the material.

Section 5f. Early Superconducting Cu Knight Shift Measurements

The early superconducting state T1 measurements in this material were hard to reconcile with the expectations of the conventional spin-singlet, orbital s-wave BCS pairing state.[12] It was clearly very important to measure

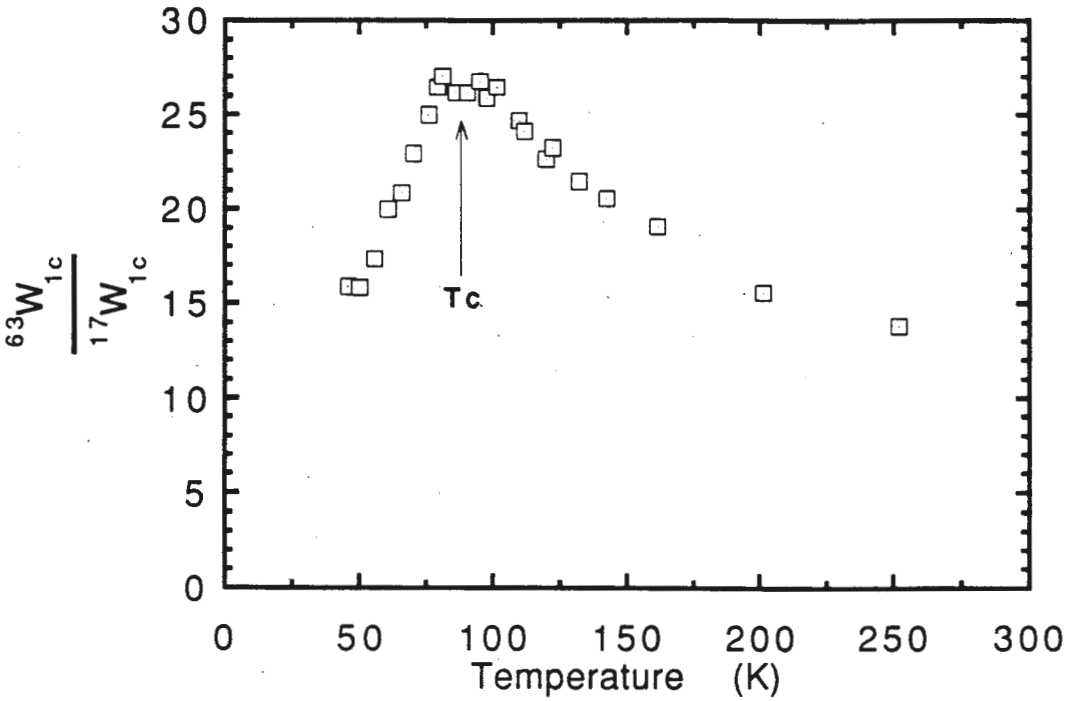

Figure 23. Measurement of the quantity ($^{63}W_{1c}/^{17}W_{1c}$) for the Cu(2) and O(2,3) sites as a function of temperature.[112] This result is quite different from that shown in Figure 22.

the temperature dependence of the Knight shift below T_c, another classic probe of the BCS pairing state.

The first Knight shift experiment was performed on the ^{63}Cu nuclei by Takigawa et al..[98] There was a significant amount of uncertainty in their results due to the difficulty in determining the value of the internal field (B_{int}), that each nucleus sees. In the mixed state ($Hc_1<Ho<Hc_2$), $B_{int} \neq Ho$ because of superconducting diamagnetic screening currents. Indeed, in this mixed state there will be a spread in the values of B_{int} which will result in an additional broadening of the NMR line. To understand the problem this causes, we recall that the positions of the NMR resonance lines are given by:[74,75]

(5-5) $\nu(T)=const*(1+ K^L + K^S(T))*B_{int}(T) + \nu_Q(T)$.

The goal of the experiment is to obtain the temperature dependence of the quantity $K^S(T)$ by measuring the temperature dependent line positions $\nu(T)$. To do this accurately, it is necessary to know the internal field $B_{int}(T)$ and quadrupole contribution to the resonance frequency $\nu_Q(T)$. Takigawa et al. attempted to determine $B_{int}(T)$ by a macroscopic magnetization technique. They measured the macroscopic magnetization ($\vec{M}$) of the sample as a function of temperature in fields up to the maximum field of their magnetometer (50 kGauss). They then measured the NMR line positions at 7 K for several applied fields (50 kGauss - 80 kGauss). By comparing the applied field ($\vec{Ho}$) dependence of the line position at 7 K with the magnetization (extrapolated to these large applied fields from their low field data), they determined the average $\vec{B}_{int}$ as a function of $\vec{Ho}$ and $\vec{M}$. Using this information, they then measured the NMR line positions,$\nu(T)$, at other temperatures in a 74 kGauss field, and they calculated $\vec{B}_{int}(T)$ using the

temperature dependence of the macroscopic magnetization. The values of K(T) which result are shown in Figure 24.

The correction to K(T) implied by their macroscopic magnetization measurement of B_{int} has a substantial effect on the results. They state in their paper that the low temperature behavior of their corrected data is probably spurious. Indeed, the chemical shift anisotropy values that are implied by their data and the assumption of spin-singlet pairing are hard to understand in terms of the Pennington et al. picture for the Cu(2) and Cu(1) electronic states. Nevertheless, their results showed that the isotropic part of K^S was positive. This was a tremendously important and surprising result, as we explain below.

In the Cu(2) nuclear spin Hamiltonian proposed by Pennington et al., the electron spin responsible for K^S is a d-shell hole. The isotropic part of the on-site hyperfine coupling constant, $A_{\alpha\alpha}$, for such a hole is primarily due to the core polarization effect. This core-polarization refers to the exchange interaction between the d-shell hole and interior, closed shell s-electrons. This exchange energy results in a slight radial distortion of the interior s-electron orbitals which is different for the two spin orientations. The result is a large isotropic negative contribution to $A_{\alpha\alpha}$, so K^S_{iso} should be negative. To explain the positive experimental value for K^S_{iso}, Mila and Rice proposed extending the Pennington et al. model by including in the nuclear spin Hamiltonian an isotropic transferred hyperfine coupling B due to the four nearest neighbor Cu(2) spins.[97] Transferred hyperfine interactions were first shown to be important in the study of concentrated magnetic impurities in salts.[114] Mila and Rice reasoned that the coupling B would be isotropic since it reflects the mixing of a Cu 4s orbital with the $3d^9$ (x^2-y^2) orbital of its

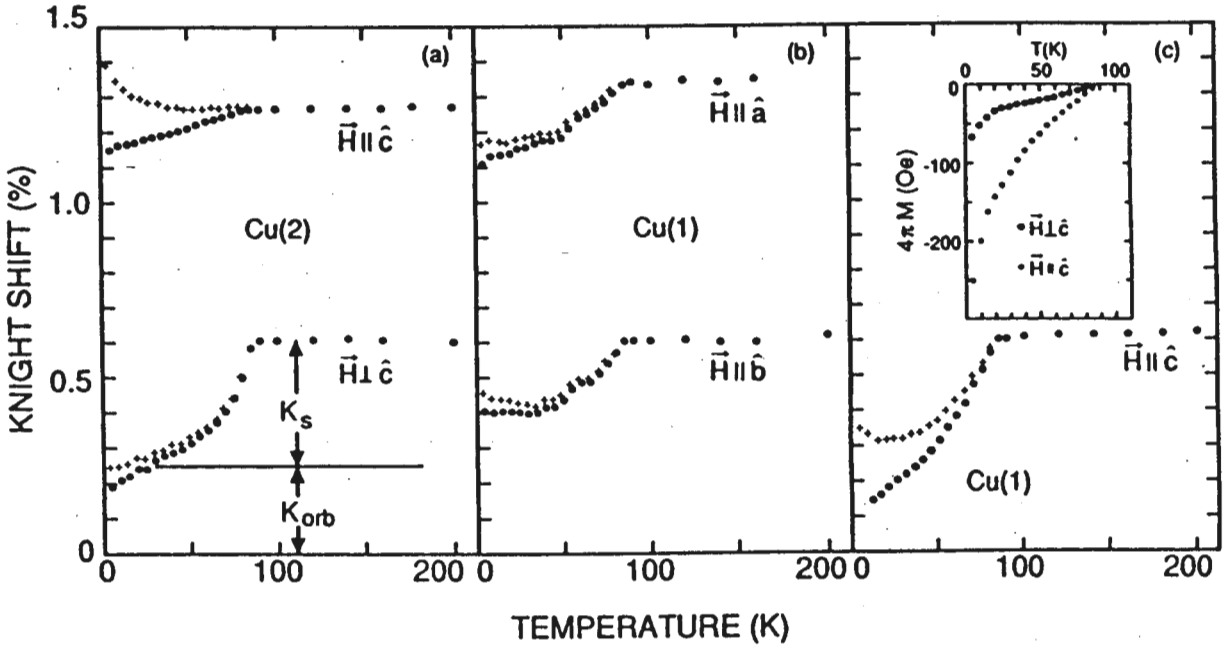

Figure 24. The temperature dependence of the ^{63}Cu Knight shift obtained by Takigawa et al..[98] The crosses and filled circles are the results with and without the diamagnetic field correction respectively. The inset shows the temperature dependences of the magnetization extrapolated to the field used for the NMR measurements (74 kGauss).

neighbor in a superexchange process mediated by the planar oxygen orbitals. The resulting hyperfine coupling Hamiltonian for the Cu(2) nuclei is conventionally referred to as the Mila-Rice Hamiltonian.

The importance of the Knight shift as a probe of the superconductivity in $YBa_2Cu_3O_7$ made it desirable to improve upon the accuracy of this pioneering experiment.

Chapter 6. ^{63}Cu Knight Shift Measurement in $YBa_2Cu_3O_7$

Section 6a. Introduction

We want to measure the ^{63}Cu Knight shift $K^S(T)$ in the superconducting state. The central transition frequency of a particular copper site in this material is given by:

(6–1) $\nu_{Cu}(T)=const*(1+K^L+K^S(T))*B_{int}(T) + \nu_Q(T)$.

We need to determine $B_{int}(T)$, $\nu_{Cu}(T)$, and $\nu_Q(T)$. We will discuss each of these in turn, in Sections 6b through 6d. The magnetic shift and Knight shift tensors which result at each temperature will be discussed in Sections 6e and 6f. An analysis of the detailed Knight shift temperature dependence will be presented in Section 6g. Sections 6b through 6g follow very closely the original data analysis presented in the Durand et al.[115] and Barrett et al.[13] Knight shift papers.

Section 6h contains an alternative theoretical analysis of our original data.

In Section 6i, we present a different analysis of the temperature dependence of the $\vec{Ho} \,||\, \hat{a}/\hat{b}$, Cu(2) Knight shift, which is based upon a new interpretation of the yttrium data.

Section 6b. Measuring the Internal Field with ^{89}Y NMR

Because our measurement of the Knight shift was made in the mixed state ($Hc_1<Ho<Hc_2$), the internal magnetic field was reduced, so $B_{int} \neq Ho$. Since the magnetic shift of the yttrium was known to be small compared to

that of the copper ($K_Y < K_{Cu}/10$),[83,84,85,86] we used the yttrium resonance as an internal field marker. The Y, being a spin 1/2 nucleus, has the Zeeman term but no Quadrupole term in its nuclear spin Hamiltonian. Measuring the position of the Y line in the superconducting state gives one a good idea of $B_{int}(T)$, since:

(6-2) $$\nu_Y(T)=(\gamma_Y/2\pi)*(1+K_Y(T))*B_{int}(T)\sim(\gamma_Y/2\pi)*B_{int}(T).$$

Observation of the yttrium signal in this material is difficult because of its low gyromagnetic ratio γ_Y and because the yttrium relaxation time becomes extremely long at low temperatures (~10 minutes at 4.2 K). In Figure 25 we see the recovery of the yttrium magnetization in another unaligned sample following a saturation comb pulse sequence at 100 K and 4.2 K.

We used two special NMR techniques to observe the yttrium signal in the superconducting state. First, we employed a Carr-Purcell-Meiboom-Gill (CPMG) sequence to take our point-by-point Y lineshapes.[63,64] This technique had been successfully used in previous Slichter group experiments.[65,116] We used this CPMG sequence because the Y nuclei possessed a fairly long spin-spin (or transverse) relaxation time T2 in addition to the extremely long spin-lattice (or longitudinal) relaxation time T1. The T2 is a measure of how long the spins retain a phase memory of their initial condition in the plane perpendicular to the applied field. If the spins have phase memory, magnetization can be refocused into another echo and measured.[66] To understand the benefit of this, we recall that an ordinary spin echo sequence destroys the magnetization:

(6-3) $\pi/2$-τ-π-τ-ECHO-wait time.

This wait time is required to allow the magnetization to grow along the field direction again (typically >T1) so the spin echo may be repeated. On the other

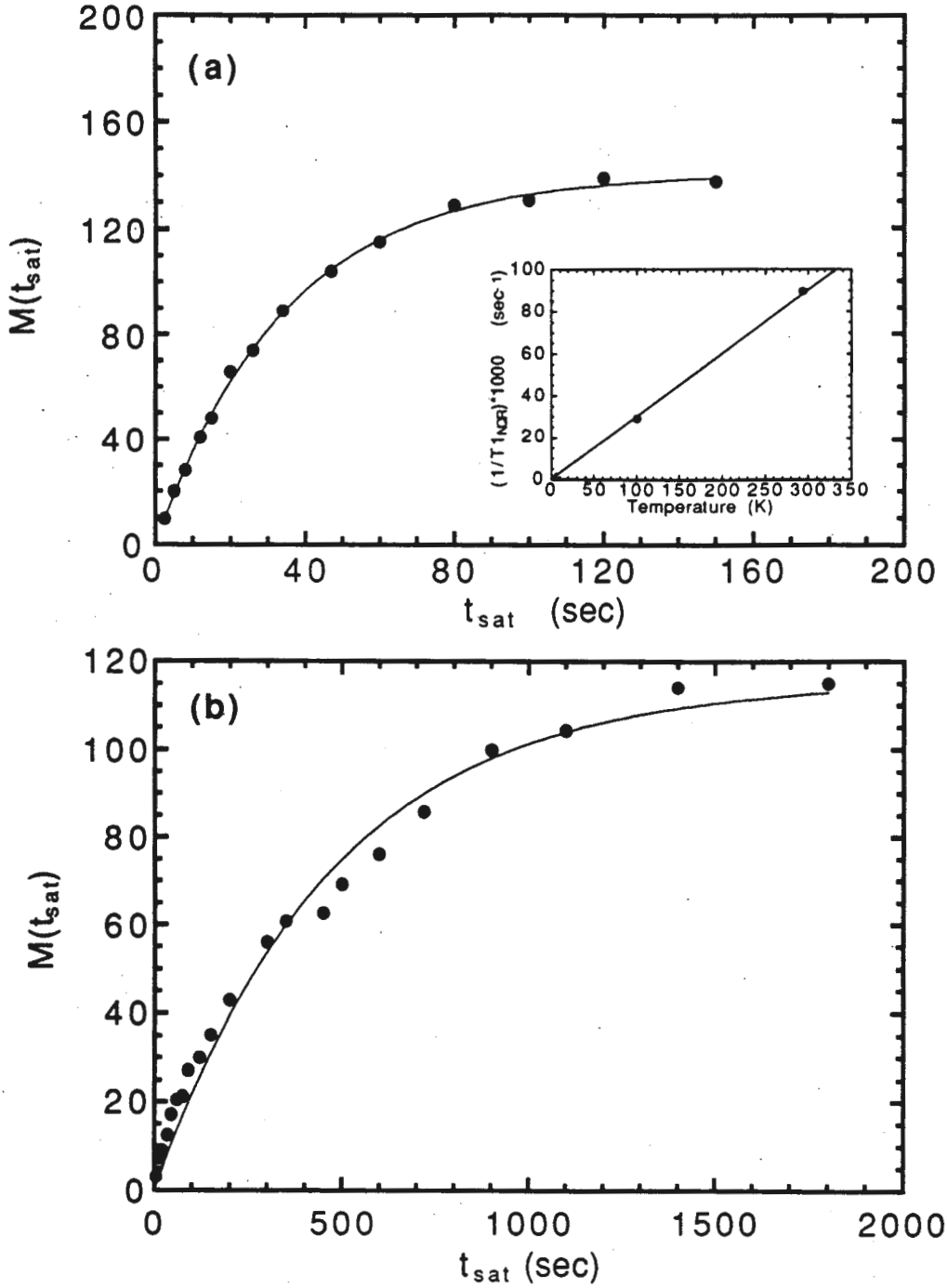

Figure 25. (a) Saturation recovery data for ^{89}Y in unaligned powder Sample Y. Solid line fit is $M(t_{sat}) = M_o*(1 - \exp(-t_{sat}/T1))$. T1(100 K) = 34.2 sec. **(a inset)** Demonstration of Korringa behavior ($1/T1 \propto T$) of ^{89}Y in this sample, including a room temperature point: T1(294 K) = 11.14 sec. (b) Fit to the 4.2 K data, with T1(4.2 K) = 480 sec.

hand the CPMG sequence repeatedly refocuses the magnetization after the first echo so that many echoes are recorded in a single wait time:

(6-4) $\pi/2\text{-}(\tau\text{-}\pi\text{-}\tau\text{-ECHO})_n$-wait time.

For this experiment, we were able to record n=16 echoes, adding them together with a weighting factor for best signal-to-noise, as we discussed in Section 4c. In this experiment, $(S/N)_{n=16} \sim 2.5(S/N)_0$ so the CPMG sequence was giving us the same signal-to-noise ratio as the ordinary spin-echo sequence in one-sixth the time.

The second technique used to observe the Y resonance was proposed by Dr. C. H. Pennington and was required because of the long Y T1. Because of the small size of our H1 (due to arcing), we were unable to cover the whole Y line at low temperatures. To take a point by point lineshape, we divided the Y line into three frequency regions, all larger than H1. For the experiment, we would take a point in region 1, region 2, region 3, and then return to a new point in region 1, a new point in region 2, etc.. This made efficient use of the recovery time for spins in each region.

The yttrium lineshapes that we obtained using the above technique are shown in Figures 26 and 27. The lines shift and broaden as a function of temperature for both $\vec{Ho} \,||\, \hat{c}$ and $\vec{Ho} \,||\, \hat{a}/\hat{b}$. The fact that the Y lineshape behaves differently for these two field orientations reflects the anisotropy of the superconducting parameters (coherence length, penetration depth) of this material. The quantity $\nu_Y(T)$ was obtained by fitting these lineshapes to a Gaussian. The best fits to the T=4.2 K data are shown in Figure 28. It is interesting to note that these lineshapes do not have the theoretically predicted form that should occur in the presence of a fluxoid lattice, even at the lowest temperatures.[46] Because the sample is an aligned powder with a

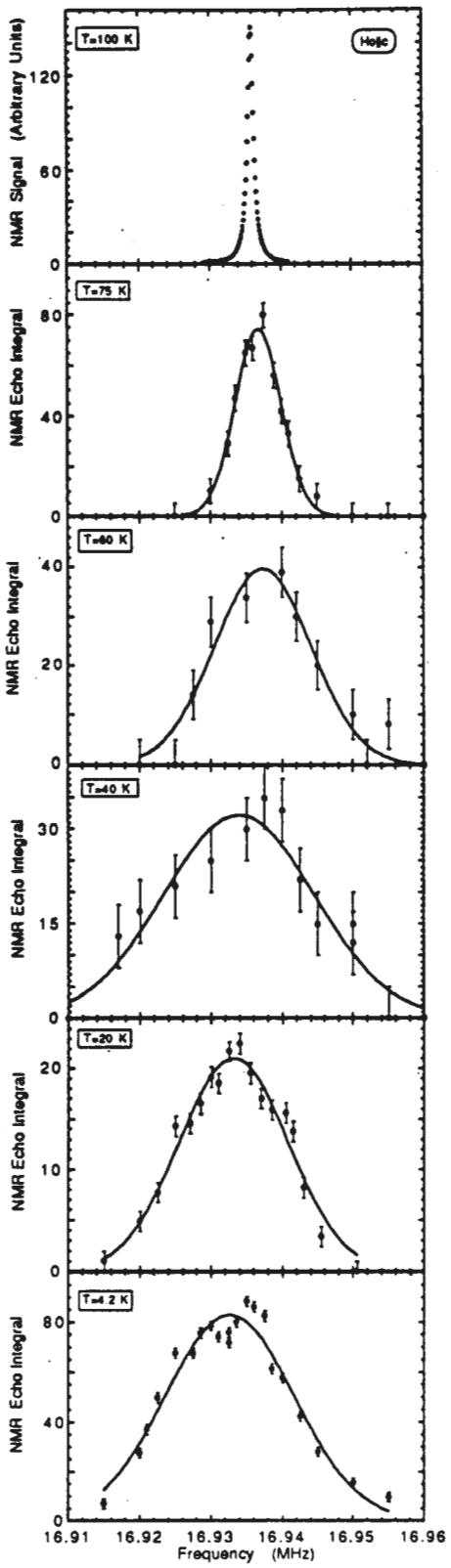

Signal = $(C * \sigma^2) / ((f-fo)^2 + \sigma^2)$

C = 150

fo=16.9358

σ = 0.00050

Integral = $C * \exp(-(f-fo)^2/\sigma^2)$

C = 74.5

fo=16.9368

σ = 0.00457

C = 39.8

fo=16.9373

σ = 0.00956

C = 32.3

fo=16.9339

σ = 0.01504

C = 21

fo=16.9331

σ = 0.01081

C = 82.9

fo=16.9326

σ = 0.01284

Figure 26. Ho | | c, Y lineshape obtained at each temperature. The Gaussian (Lorentzian) fits to the superconducting (normal) state data are given.

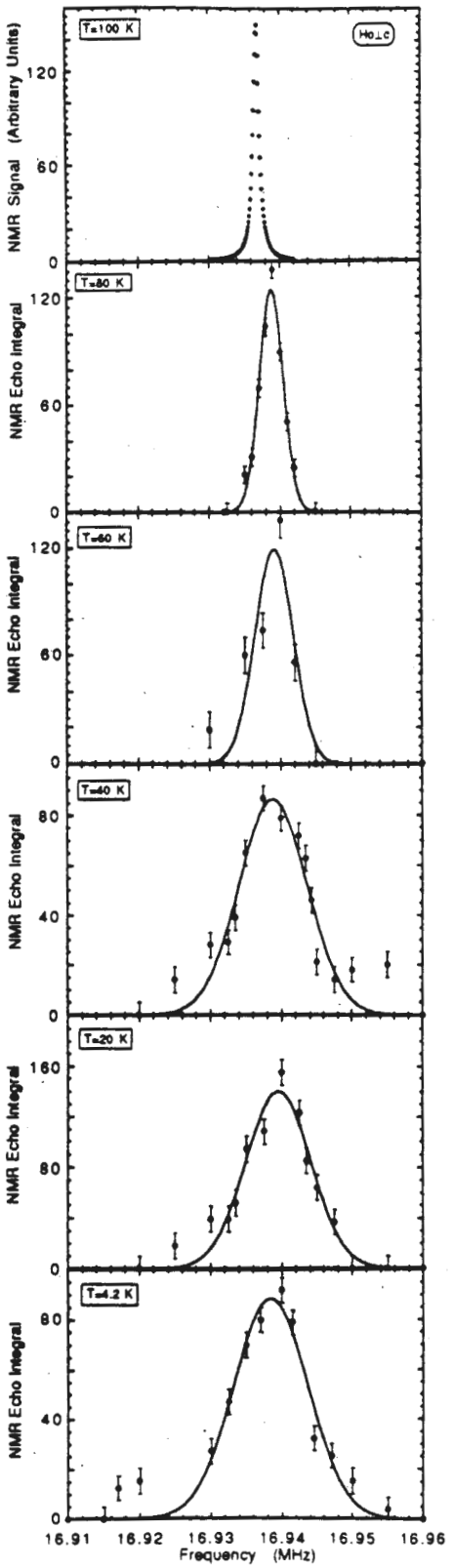

Signal = $(C * \sigma^2) / ((f-fo)^2 + \sigma^2)$

C = 150

fo=16.9368

σ = 0.00050

Integral = $C * \exp(-(f-fo)^2/\sigma^2)$

C = 124.6

fo=16.9388

σ = 0.00239

C = 119.5

fo=16.9391

σ = 0.00380

C = 86.6

fo=16.9389

σ = 0.00676

C = 140.0

fo=16.9395

σ = 0.00649

C = 88.8

fo=16.9384

σ = 0.00736

Figure 27. Ho $\perp$ c, Y lineshape obtained at each temperature. The Gaussian (Lorentzian) fits to the superconducting (normal) state data are given.

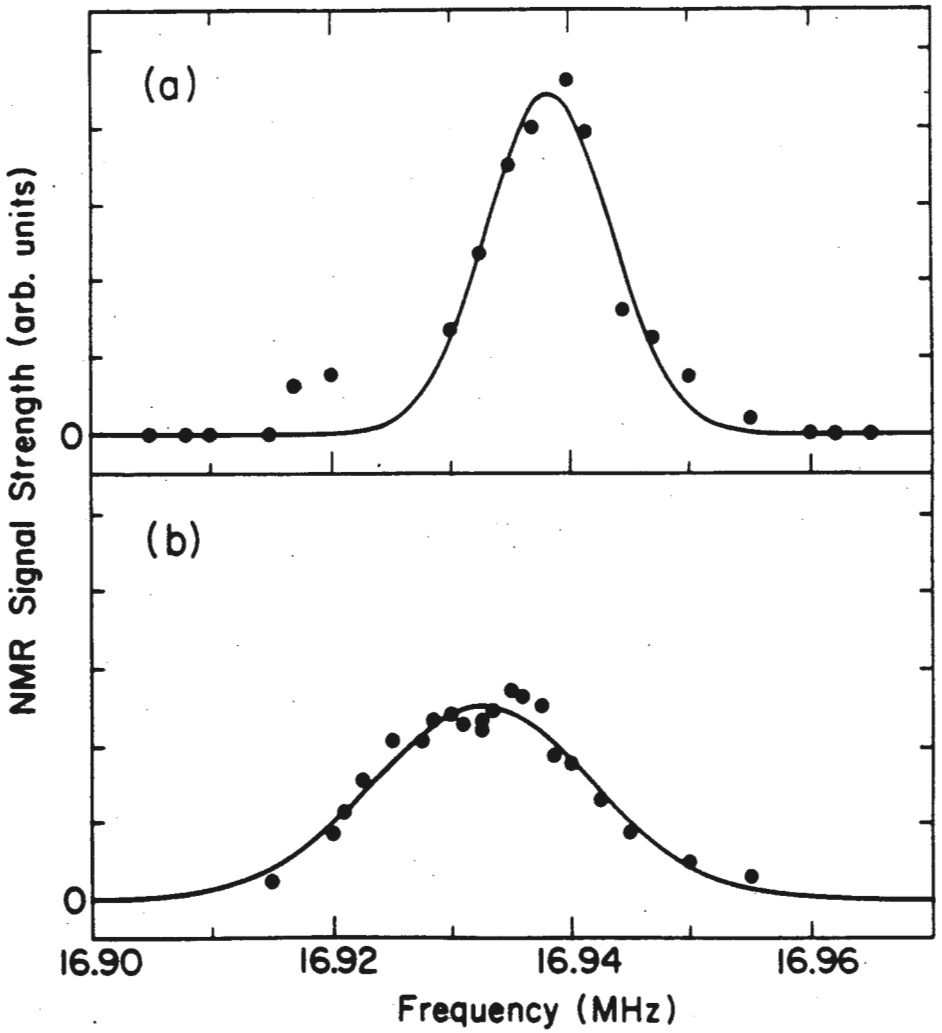

Figure 28. The ^{89}Y NMR lineshape of aligned powder Sample K at 4.2 K for (a) $\vec{H}o \perp \vec{c}$ and (b) $\vec{H}o \parallel \vec{c}$. The solid lines are the Gaussian fits determined by the method of least-squares where the center frequency, amplitude, and width are adjusted to optimize the fit to the data. The plots are scaled to have equal areas under the Gaussian fits.[13]

10% packing fraction, we expect at least two other random sources of broadening could contribute to the observed Y lineshape. The first is the spread in demagnetizing factors due to the different shape of the crystallites which make up this sample. The second potential source of line broadening would be additional randomly oriented magnetic fields at the position of a crystallite due to the magnetic moments of neighboring crystallites. The fact that the Y lineshapes are Gaussian implies either that these last two sources of broadening wipe out the lineshape characteristic of a fluxoid lattice, or that the fluxoids are not in a regular lattice in the first place.

Once we have obtained $\nu_Y(T)$, our next task is to determine $B_{int}(T)$. We recall that:

(6-5) $$\nu_Y(T)=(\gamma_Y/2\pi)*(1+K_Y(T))*B_{int}(T).$$

We know the value for K_Y at 100 K from direct measurement of $\nu_Y(100\ K)$ and $\vec{B}_{int}(100\ K)=\vec{Ho}$. An anisotropy in the magnetic shift is observed in this way, since $K_Y(T=100\ K)$= -150 ppm (-95 ppm) relative to YCl_3 when $\vec{Ho}\,||\,\hat{c}$ ($\vec{Ho}\,||\,\hat{a}/\hat{b}$). Several groups have worked on determining how large the chemical shift part (K_Y^L) of K_Y is.[83,84,85,86] The remainder of K_Y is then the Knight shift (K_Y^S) of the yttrium. We recall that the magnetic shift is given by:

(6-6) $$K_Y(T)=K_Y^L + K_Y^S(T).$$

There are three ways one could consider analyzing the yttrium data to determine $B_{int}(T)$. The first is to assume that $K_Y^S(100K)$ is zero, so that the temperature dependence of the yttrium resonance frequency is only due to $B_{int}(T)$. A second analysis would assign a value to $K_Y^S(100K)$ using Equation (6-6), and assume that its temperature dependence is given by the s-wave, weak coupling Yosida function.[54] The third way is to use the same value for

$K_Y^S(100K)$, but then to assume that $K_Y^S(T) \propto K_{Cu(2)}^S(T)$, as would be expected in a single component model of the CuO_2 planar electronic susceptibility. This would result in a temperature dependence of $K_Y^S(T)$ which is slightly steeper near Tc than for the weak coupling case. We will show in Section 6i that these three different analyses produce ^{63}Cu Knight shift results which are qualitatively quite similar, since $K_Y^S(T=100\ K) \ll K_{Cu}^S(T=100\ K)$.

In our original papers,[13,115] we decided to use the second analysis of the data, since the yttrium was thought to have a non-zero Knight shift and the temperature dependence of the yttrium relaxation rate data was quite different from that of the planar copper site, so a two-component model seemed more likely. Following the second method of analyzing the yttrium data, $\vec{B}_{int}(T)$ was determined using isotropic Knight shift ($K_Y^S(T=100\ K)$) values of -100 ppm and -300 ppm. The qualitative behavior of the data is quite similar, so we show only the ^{63}Cu Knight shift result for the $K_Y^S(T=100\ K)$= -300 ppm case, which is the value agreed upon by various groups.[85,86,95,96] The temperature dependence of $K_Y^S(T)$ was assumed to be the standard s-wave, weak coupling Yosida function. This Yosida function is independent of temperature below ~30 K, so the behavior of the low temperature data should be insensitive to this choice. We have made the above reasonable assumptions to improve the quantitative accuracy of the results. These assumptions are used in every section except Section 6i.

Section 6c. Determination of the ^{63}Cu Resonance Positions

There are two inequivalent copper sites in this material, the plane (Cu(2)) and chain (Cu(1)) sites. Pennington et al. demonstrated that the

magnetic shift and electric field gradient tensors for these two sites were different and anisotropic.[76] In addition, the two isotopes, ^{63}Cu and ^{65}Cu, have different gyromagnetic ratios and electric quadrupole moments which make these two isotopes easily distinguishable at high fields. Most of the data presented in this thesis were obtained using the more abundant ^{63}Cu isotope. For the field along each of the principle axes ($\hat{a}$,$\hat{b}$,$\hat{c}$), Pennington found the expected family of three lines each for both the Cu(2) and Cu(1) sites (see Appendix B). Our sample is aligned along only the $\hat{c}$-axis, so we expect to obtain results similar to Pennington et al. for the field along the $\hat{c}$-axis. For the field perpendicular to the $\hat{c}$-axis, we expect to have a restricted powder pattern. That is, for some crystallites the field will be along the $\hat{a}$/$\hat{b}$-axes, and for other crystallites it will be in between these two axes. The spectra obtained from this sample at 100 K are shown in Figure 29, along with marks indicating the line positions determined from the single crystal study of Pennington et al..[76]

Clearly the single crystal positions appear as distinctive points in the powder spectrum, but there is significant signal intensity elsewhere as well. We have tried to minimize this extra intensity by attaining better alignment, but we seem to be limited by the nature of the crystallites. Our present understanding of this extra intensity is that some large crystallites may have a smaller crystallite grown onto them with a different $\hat{c}$-axis orientation. Such crystals have been seen in electron micrograph pictures that Keith O'Hara made of one of our powder samples. If the larger crystallite aligns its $\hat{c}$-axis along the applied field when we make the sample, the smaller crystallite will have its $\hat{c}$-axis frozen in some different direction.

The central transitions of the Cu(1) and Cu(2) sites for $\vec{Ho} \,||\, \hat{c}$ and

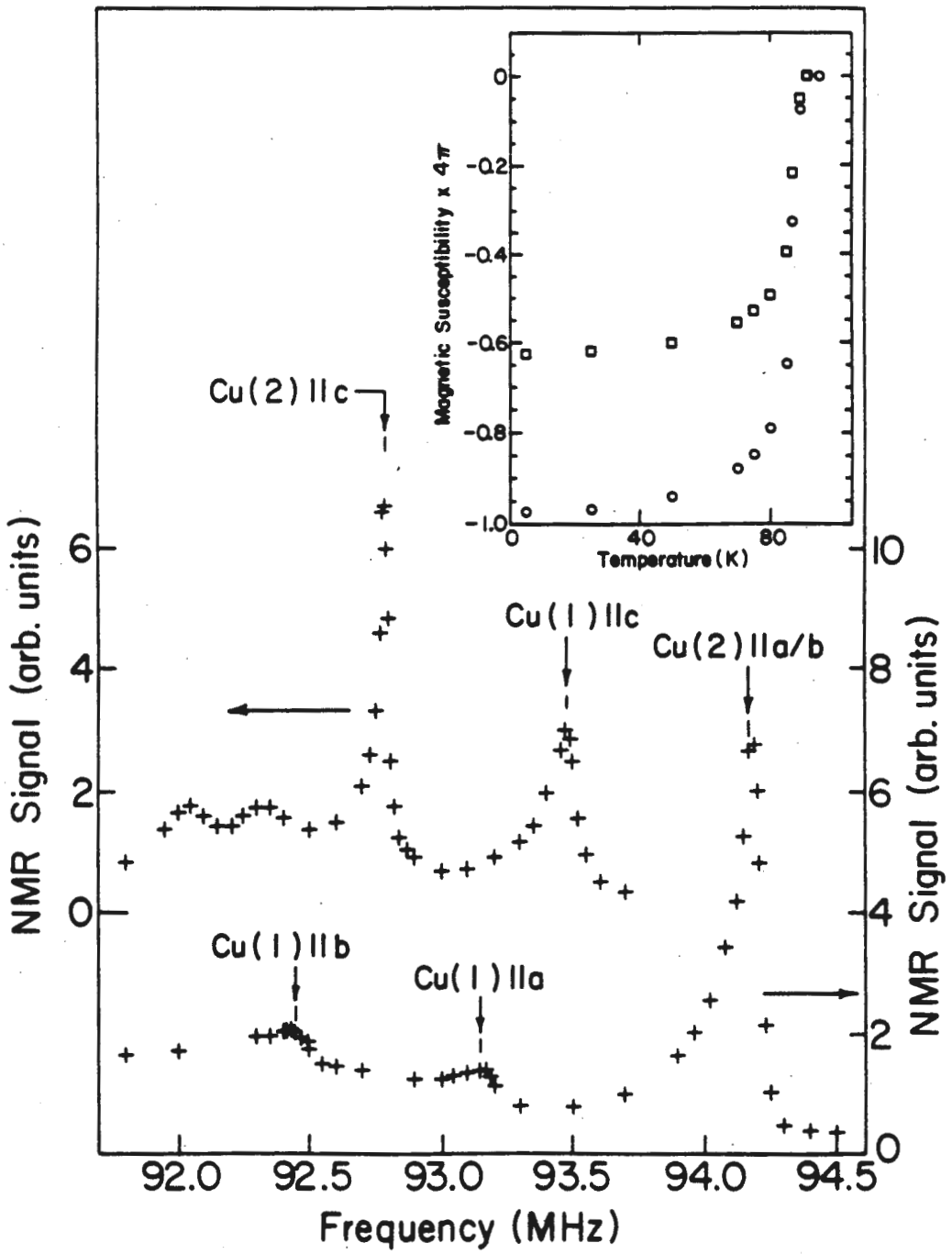

Figure 29. Inset: The squares (circles) show the field-cooled (zero-field-cooled) magnetization in 16 Oe of the powder used in Sample K vs. temperature. **Main Figure:** The upper (lower) curve is the ^{63}Cu NMR lineshape of Sample K at 100 K with $\vec{Ho} \parallel \hat{c}$ ($\vec{Ho} \perp \hat{c}$).[13] The arrows above both curves indicate the single crystal line positions.[76] The two unlabeled peaks at the low-frequency end of the upper curve are the ^{63}Cu(1) $\pm 3/2$, $\pm 1/2$ transitions.

$\vec{Ho} \| \hat{a}/\hat{b}$ are shown as a function of temperature in Figures 30 and 31. The singularities present in the 100 K spectra remain down to 4.2 K, but they shift and broaden appreciably. To measure accurately the low temperature line position of the various features in the powder spectra, we needed to take this broadening into account. The same spread in $B_{int}(T)$ which increased the width of the Y line contributes to the width of the Cu lines. This effect was included by convoluting the experimental Cu resonance at 100 K with a Gaussian of the Y frequency width scaled up by (γ_{Cu}/γ_Y). This broadened 100 K experimental line was then shifted in frequency until it fit the low temperature data, as is shown in Figure 32. This frequency shift was then subtracted from the single crystal resonant frequencies to obtain $\nu_{Cu}(T)$.

During this procedure, we discovered an extra broadening of the Cu(2) $\| \hat{a}/\hat{b}$ line. The experimental 4.2 K Cu(2) $\| \hat{a}/\hat{b}$ lineshape is too broad to be fit by the yttrium broadened 100 K Cu data, as is seen in Figure 33. We investigated several sources of this extra breadth. A comparison of the ^{63}Cu and ^{65}Cu central transitions at 4.2 K showed this broadening was of magnetic origin. Measurements of the width and position of the ^{63}Cu upper satellite line at 4.2 K ruled out the possibility that $(K_{aa}-K_{bb})$ or $(\nu_{aa}-\nu_{bb})$ had become large enough at low temperatures to account for the extra broadening. We also measured the Cu(2) $\vec{Ho} \| \hat{a}/\hat{b}$ lineshape again, using a recovery time between successive echoes (Trep) of 10 sec. This Trep was 33 times longer than the original Trep used, but the new line was the same shape and width as the original lineshape. This result, combined with the fact that we observed about the same size signal for $\vec{Ho} \| \hat{c}$ and $\vec{Ho} \| \hat{a}/\hat{b}$, rules out the possibility that we are missing a long T1 component of the line, which was another possible explanation for the extra breadth. Assuming that the extra

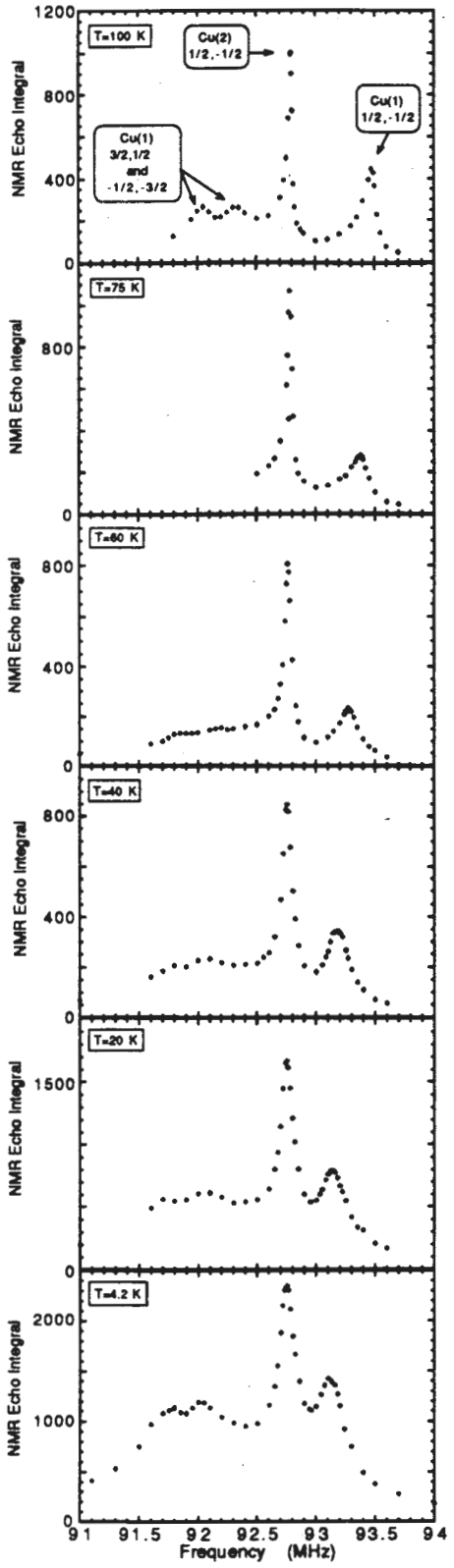

Figure 30. The $\vec{Ho} \| \hat{c}$, ^{63}Cu lineshape obtained at each temperature.

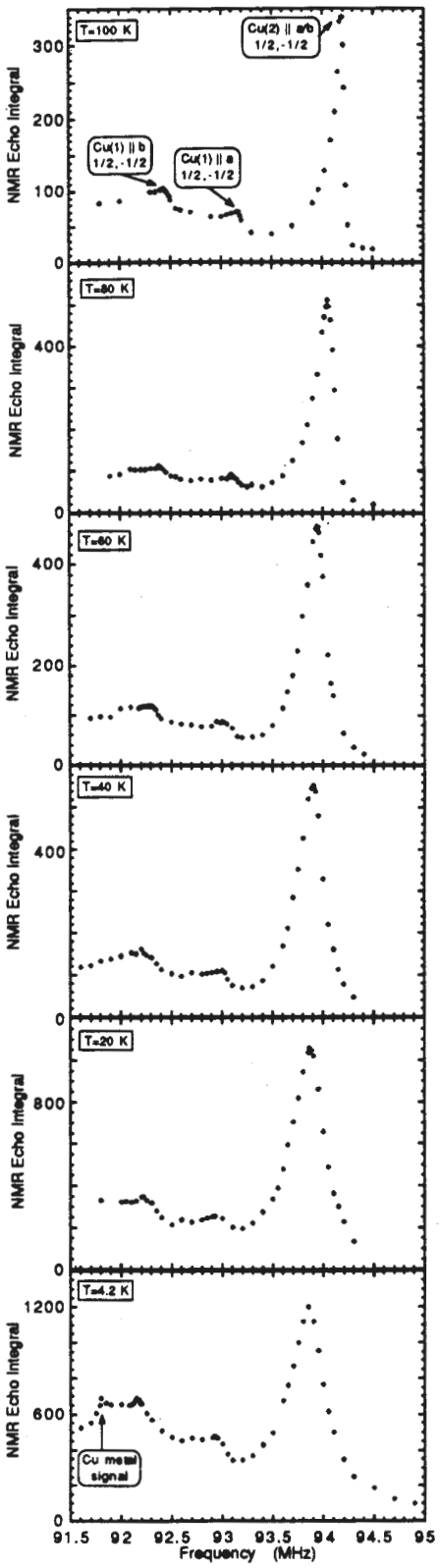

Figure 31. The $\vec{Ho} \perp \hat{c}$, ^{63}Cu lineshape obtained at each temperature.

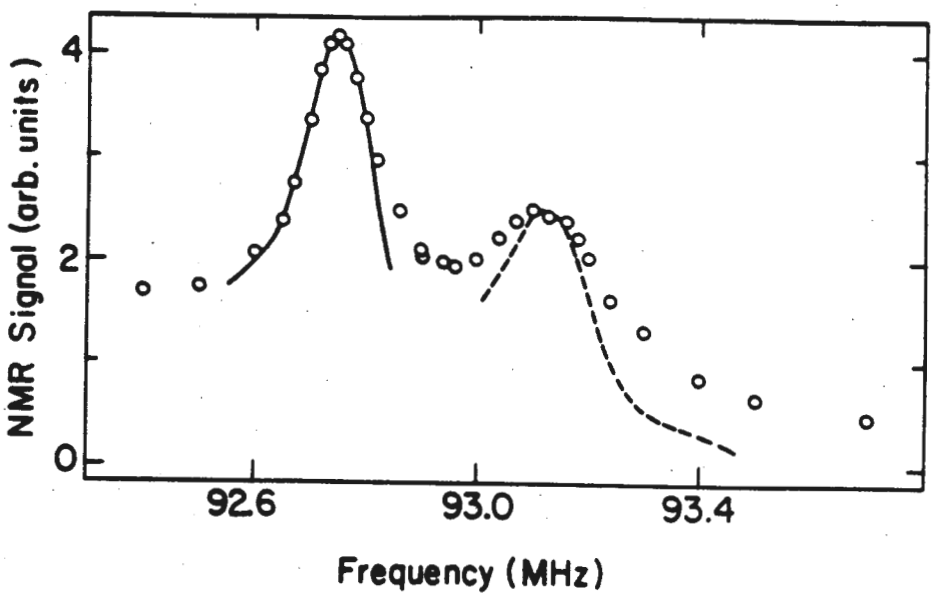

Figure 32. A demonstration of how the low-temperature lines are fit with the broadened T = 100 K data. The points are the measured lineshape at T=4.2 K with $\vec{Ho} \| \hat{c}$. The solid and dashed lines are the broadened and shifted T= 100 K line shapes of the Cu(2) and Cu(1) central transitions, respectively. The broadening used is Gaussian with a width implied by the measured ^{89}Y linewidth. Because this broadening accounts for most (or all) of the low-temperature linewidth, the low-temperature broadening represents a distribution of magnetic fields throughout the sample.[13]

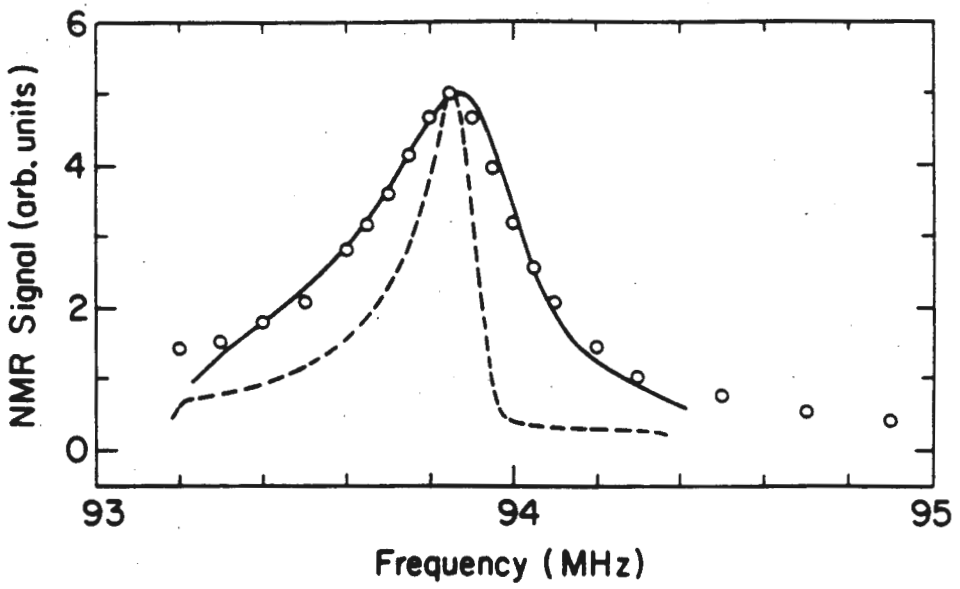

Figure 33. The points are the $^{63}Cu(2)$ lineshape at T = 4.2 K for $\vec{Ho} \perp \hat{c}$. The dashed curve is an unsuccessful attempt to fit the low-temperature line shape with the broadened and shifted T = 100 K line as we did in Figure 32. The solid curve is a fit to the T= 4.2 K data using the broadened and shifted T = 100 K line which was convoluted with an additional Lorentzian broadening.[13]

broadening does not lead to a net shift in the Cu(2) line, we proceed with our determination of $\nu_{Cu}(T)$ by convoluting the yttrium broadened 100 K data with an additional broadening. This additionally broadened line was then shifted until it was superposed on the low temperature data. The best fit to the data was obtained when this additional broadening was a Lorentzian of half-width B, as is shown in Figure 33. Following this procedure at each temperature in the superconducting state, we found that the quantity B follows a Néel temperature dependence as shown in Figure 34. The line in this figure is given by:

(6-7) $B(T) \cong (4\ K\ MHz)/(T + 34\ K)$.

To confirm the results of the $\vec{Ho} \| \hat{a}/\hat{b}$ measurements, which were particularly difficult for the Cu(1) sites since the restricted powder pattern for that site did not provide very sharp features, Dale Durand made a multiple single crystal sample with both the $\hat{c}$-axis and $\hat{a}/\hat{b}$-axis completely aligned. The chain resonances for that sample at 100 K and 4.2 K are shown in Figure 35, confirming our aligned powder result that both resonances shift by about the same amount. His measurements in this sample also confirmed the presence of the extra breadth of the Cu(2) $\vec{Ho} \| \hat{a}/\hat{b}$ line. This anomalous broadening has also been reported by Takigawa et al.[117]

Section 6d. The Electric Quadrupole Contribution to the Line Position

The remaining variable we needed to determine in order to find the copper magnetic shift was the electric quadrupole contribution to the line position. The electric field gradient tensor at 100 K was accurately determined by the single crystal measurements of Pennington et al..[76] We assumed that

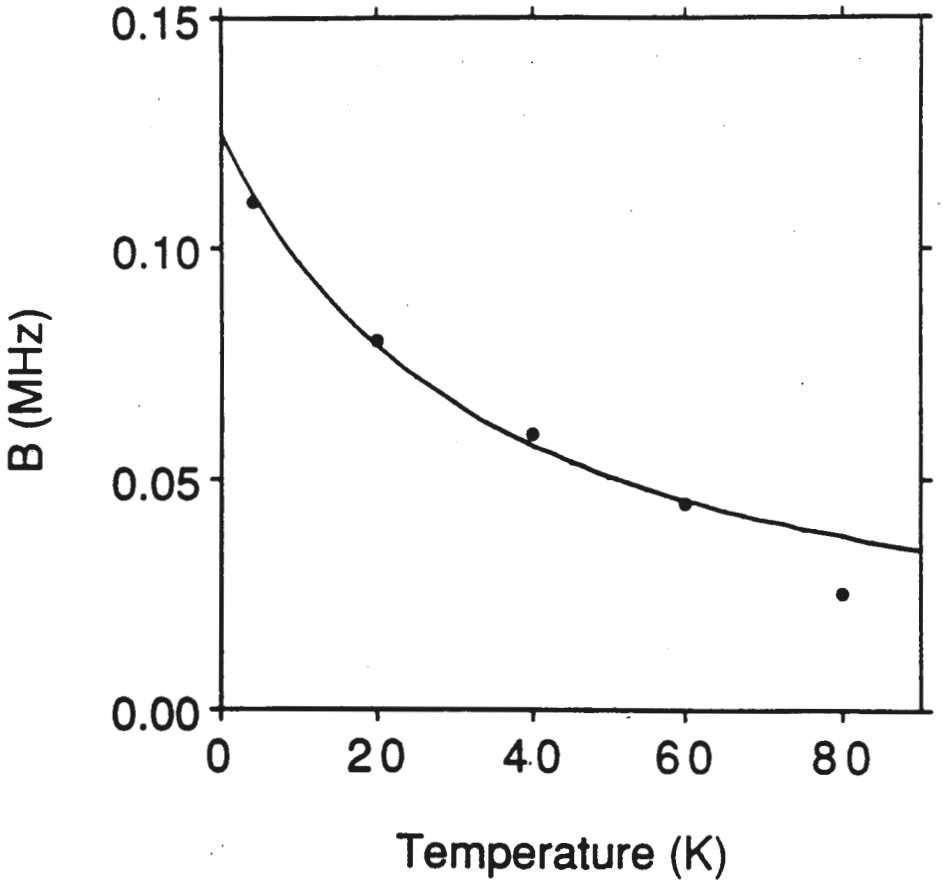

Figure 34. The solid points are the extra broadening, over and above that implied by the measured ^{89}Y linewidth, needed to fit the low-temperature Cu(2) central transition with $\vec{Ho} \perp \hat{c}$ (the solid line in Figure 33). B is the half-width of a Lorentzian, and the solid line shows the Néel temperature dependence described in Equation (6-7).[13]

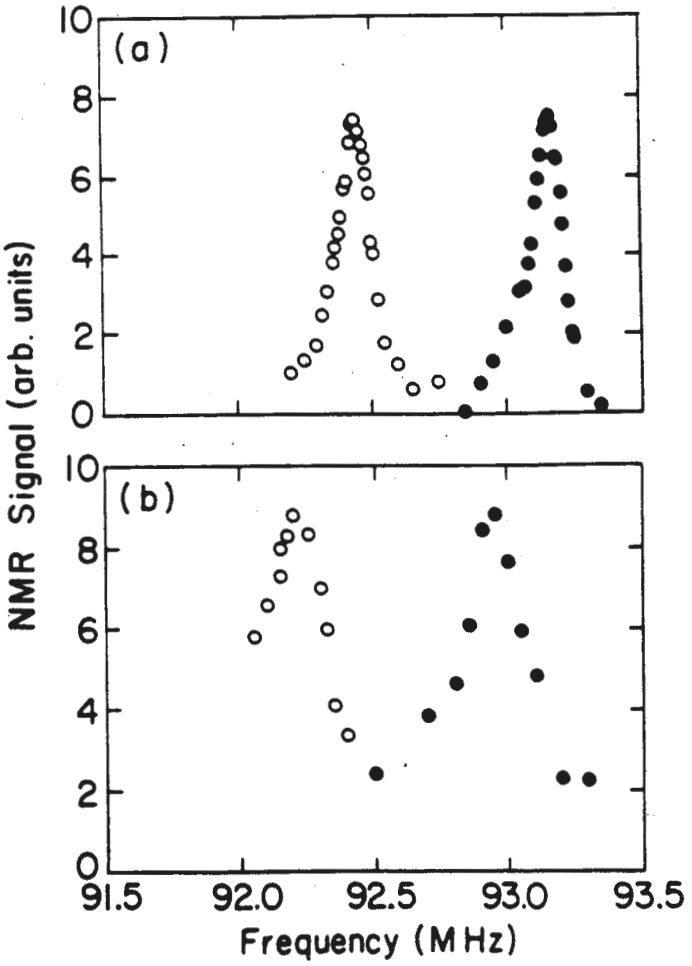

Figure 35. The ^{63}Cu(1) resonance lines with $\vec{Ho} \| \hat{a}$ (filled circles) and $\vec{Ho} \| \hat{b}$ (empty circles) in the Durand aligned single crystal sample at (a) T = 100 K and (b) T = 4.2 K. In this sample the field is along either the $\hat{a}$ or $\hat{b}$ axis of any given untwinned region in each of the crystals. The fact that the separation between these peaks is approximately the same at both these temperatures is consistent with our finding (from measurements made on aligned powder Sample K) that the Cu(1) Knight shift is roughly isotropic.[13]

this tensor had the same anisotropy in the superconducting state, and that each of its components had a small linear temperature dependence consistent with the experimentally measured nuclear quadrupole resonance frequency. This assumption is probably quite good for the Cu(2), since this site possesses nearly 4-fold symmetry about the $\hat{c}$-axis, but this assumption may not be as good for the Cu(1) site. The values we used are shown in Table IV.

Section 6e. Determination of the Magnetic Shift

Following the above procedures, we have determined $B_{int}(T)$ for both field orientations, as well as $\nu_{Cu}(T)$ and the electric field gradient tensor for both copper sites and both field orientations. Using this information, the magnetic shift was determined using an exact diagonalization of the copper nuclear spin Hamiltonian, shown in Appendix B. Explicitly, for each temperature, field orientation, and copper site, the central transition resonance frequency was calculated using the values for $B_{int}(T)$, the electric field gradient tensor, and an initial guess for the magnetic shift K(T). The calculated value was then compared to the experimental value $\nu_{Cu}(T)$, and the quantity K(T) was adjusted using a least squares procedure until the calculated and experimental frequencies agreed. The total magnetic shift determined by this procedure is shown in Figure 36.

Section 6f. Determination of the Knight Shift

We consider the implications of the experimentally determined Knight shifts within a generalized BCS theory. Unfortunately, no detailed

Temperature	Cu(1) EFG Tensor (MHz)			Cu(2) EFG Tensor (MHz)		
(K)	$\nu_{aa}(T)$	$\nu_{bb}(T)$	$\nu_{cc}(T)$	$\nu_{aa}(T)$	$\nu_{bb}(T)$	$\nu_{cc}(T)$
4.2	-18.97	19.14	-0.17	16.03	15.62	-31.65
20	-18.98	19.15	-0.17	16.02	15.61	-31.63
40	-18.99	19.16	-0.17	16.00	15.59	-31.59
60	-18.99	19.16	-0.17	15.98	15.57	-31.56
75	-19.00	19.17	-0.17	15.97	15.56	-31.53
80	-19.00	19.17	-0.17	15.97	15.56	-31.52
100	-19.01	19.18	-0.17	15.95	15.54	-31.49

Table IV. Temperature dependence of the Electric Field Gradient (EFG) tensor used in our determination of the copper magnetic shift $^{63}K(T)$.

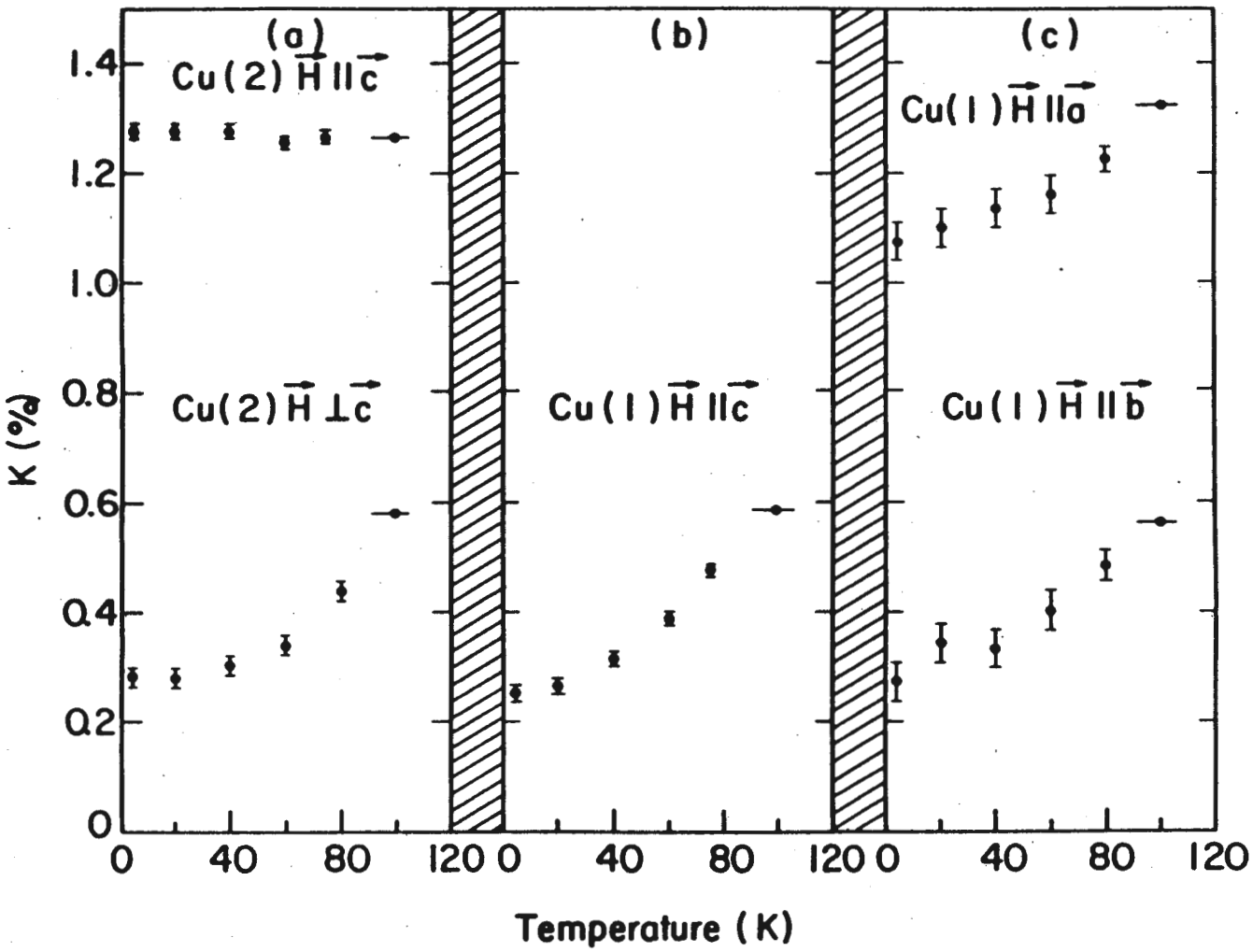

Figure 36. ^{63}Cu magnetic shift obtained as described in the text for the (a) Cu(2) and (b, c) Cu(1) sites.

predictions exist for the behavior of the magnetic shift for any of the novel exotic theories of High-T_c superconductivity (e.g. anyons).

In the original BCS theory, designed to explain the behavior of the elemental superconductors, the superconducting wave function involved pairing of electrons into states which are spin-singlets with orbital angular momentum zero (s-wave, spin-singlet pairing). By considering other sources of the attractive interaction between fermions, this original theory was subsequently extended to explain the behavior of other systems (e.g. ^{3}He, nuclear matter, neutron stars, heavy fermion superconductors). In addition, other pairing states were considered, including both spin-triplets and spin-singlets, as well as other orbital angular momentum states (spin-singlets require even-L orbital angular momentum, spin-triplets require odd-L orbital angular momentum). These matters are treated extensively in the review article of Leggett on Fermi liquids.[118] There it is shown that one expects to find that the components of the spin susceptibility tensor, χs, in the superconducting state are either unaffected by the transition

(6-8) $$\chi s = \chi n,$$

where χn is the susceptibility in the normal state, or

(6-9) $$\chi s = Y_L(T)\chi n,$$

where $Y_L(T)$ is some function which depends on the angular momentum L involved in the pairing. [Ordinarily the second equation holds for all three components of the susceptibility, or the first equation holds for two components and the second equation holds for the third. The so-called planar state is one example we know of where the first equation holds for one component and the second equation holds for the other two.] An example of $Y_L(T)$ is the L=0 function for spin-singlets named after Yosida.[54] The

temperature dependence of $Y_L(T)$ as T approaches zero depends on L and the pairing state. For a system with no nodes, $Y_0(T)$ has zero slope at T=0. For a d-wave pairing state (L=2), $Y_2(T)$ varies linearly with T as T approaches 0 K. We expect that the temperature dependence of the Knight shift tensor will reflect the superconducting pairing state.[119]

Having obtained the temperature dependence of the magnetic shift tensor, $K_{\alpha\alpha}(T)$, as shown in Figure 36, we next want to extract the temperature dependent Knight shift tensor. We recall that these two tensors are related by:

(6-10) $$K_{\alpha\alpha}(T)=K^L_{\alpha\alpha}+K^S_{\alpha\alpha}(T).$$

The temperature independent tensor $K^L_{\alpha\alpha}$ is the chemical shift, proportional to the Van Vleck susceptibility. This tensor involves electronic orbital energies (10^4 K), so the superconducting state transition (10^2 K) is expected to leave this tensor unchanged.

The model for the electronic state of the copper sites first proposed by Pennington et al.[76] and extended by Mila and Rice[97] makes specific predictions for this chemical shift tensor. In this model, the copper atomic ground state is assumed to be Cu^{++} with a single d-shell hole in the x^2-y^2 (y^2-z^2) state for the Cu(2) (Cu(1)). We have set the crystalline axes $(\hat{a},\hat{b},\hat{c})=(x,y,z)$. The application of a magnetic field mixes in some excited electronic orbital states, producing an additional magnetic field at the nucleus. This paramagnetic chemical shift is given by:

(6-11a) $$K^L_{\alpha\alpha} = 2\beta^2\left[\sum_n \frac{\langle 0|L_\alpha|n\rangle\langle n|L_\alpha/r^3|0\rangle}{E_n - E_0} + \text{c.c.}\right]$$

(6-11b) $$= 4\beta^2\left\langle\frac{1}{r^3}\right\rangle\sum_n \frac{|\langle 0|L_\alpha|n\rangle|^2}{E_n - E_0} \quad = 2\left\langle\frac{1}{r^3}\right\rangle\chi^L_{\alpha\alpha}$$

In this expression, α=a,b,c, and $\chi^L_{\alpha\alpha}$ is the Van Vleck susceptibility tensor. We can evaluate this expression within the Pennington et al. model for the Cu(2), if we assume the ground state for the hole is x^2-y^2 state, and the crystal field is axially symmetric about the z-axis. We find:

(6-12a) $K^L_{zz}=16\beta^2<1/r^3>(1/E_{xy})$,

(6-12b) $K^L_{xx}= 4\beta^2<1/r^3>(1/E_{yz}) = K^L_{yy}$ for axial symmetry about z.

For axial symmetry about z, one expects Eyz ≥ Exy. We can apply the above result directly to the Cu(2) site. The calculation for the Cu(1) site is straightforward, with the modification that the crystal field, to a first approximation, is now axially symmetric about the x- ($\hat{a}$-) axis. Thus the Pennington et al.[76] and Mila-Rice[97] model for the copper electronic state makes the following predictions for our experiment:

(6-13a) $K^L_{cc} \geq 4K^L_{aa} = 4K^L_{bb}$ for the Cu(2),

(6-13b) $K^L_{aa} \geq 4K^L_{bb} = 4K^L_{cc}$ for the Cu(1).

The equality would be satisfied for the case that the excited states xy, yz (yz, xz) are degenerate for the Cu(2) (Cu(1)). This model places important constraints on the values of the Knight shift.

We determine the temperature dependent Knight shift tensors by assuming both a spin-singlet and a spin-triplet pairing state in turn. The chemical shift tensors that result for these two assumptions are compared to the predictions of the above model.

First we assume that this material has a BCS spin-singlet pairing state. In this case, the pairing will cause the spin susceptibility to vanish at T=0, so $K^S_{\alpha\alpha}$(T=0 K)=0. As we pointed out in Chapter 3, this behavior was observed in ^{27}Al.[50,120] However, this result was not obtained for the heavier elements of mercury and tin, where strong spin-orbit coupling is present.[121,122] Since

copper is lighter, the spin-orbit effects are expected to be much smaller. We will assume that $K^S_{\alpha\alpha}(T=0\ K)=0$, and consider the consequences. For this case, we identify our lowest temperature values of the magnetic shift as the temperature independent chemical shift, $K_{\alpha\alpha}(T=4.2\ K) = K^L_{\alpha\alpha}$. We then end up with the chemical shift anisotropy in Table V. These values are consistent with the Pennington et al. and Mila-Rice pictures of the copper electronic states. For these assumptions, the Knight shift tensors at 100 K are given by $K^S_{\alpha\alpha}(T=100\ K)= K_{\alpha\alpha}(T=100\ K) - K_{\alpha\alpha}(T=4.2\ K)$. These values are listed in the table as well. We see that the components of the Cu(1) Knight shift tensor are almost isotropic. The result for the Cu(2) Knight shift tensor are drastically different. $K^S_{aa}(T=100\ K)$ and $K^S_{bb}(T=100\ K)$ are identical and about the same size as the Cu(1) Knight shift tensor components. However, $K^S_{cc}(T=100\ K)$ is essentially zero. To see how this last result could be consistent with spin-singlet pairing and a single-component theory of the CuO_2 planar spin susceptibility, we recall the Mila-Rice expression for the planar copper Knight shift tensor:[97]

(6-14a) $$K^S_{cc}(T)=(A_{||} + 4B)\ \chi'_{cc}(\vec{q}=0,\omega=0,T),$$

(6-14b) $$K^S_{aa}(T)=K^S_{bb}(T)=(A_{\perp} + 4B)\ \chi'_{aa}(\vec{q}=0,\omega=0,T).$$

Spin-singlet pairing implies $\chi'_{aa}(\vec{q}=0,\omega=0,T) = \chi'_{bb}(\vec{q}=0,\omega=0,T) = \chi'_{cc}(\vec{q}=0,\omega=0,T)$. Measurements of the temperature dependence of $^{17}K_{cc}(T)$ for the O(2,3) site imply $\chi'_{cc}(\vec{q}=0,\omega=0)$ is temperature dependent in a single-component theory.[123,124] The result $K^S_{cc}(T=100\ K) = 0$ then requires $A_{||}+4B=0$. This accidental cancellation of the two hyperfine coupling constants is the only element of this spin-singlet pairing picture which is hard to believe at first sight. Nevertheless, this result is consistent with the spin-lattice relaxation results as well.[4]

Site	Axis Along Field	^{63}K (T=100 K) {in %}	^{63}K(80 K)	^{63}K(75 K)	^{63}K(60 K)	^{63}K(40 K)	^{63}K(20 K)	^{63}K(4.2 K) {$\equiv {}^{63}K^{L}$ For Spin-singlet Pairing}	^{63}K(100 K) - ^{63}K(4.2 K) {$\equiv {}^{63}K^{S}$(100 K) For Spin-singlet Pairing}
Cu(1)	Ho||c	0.588	-----	0.48 ± 0.01	0.39 ± 0.01	0.32 ± 0.01	0.27 ± 0.01	0.25 ± 0.01	0.33 ± 0.01
Cu(1)	Ho||a	1.323	1.23 ± 0.02	-----	1.16 ± 0.02	1.14 ± 0.02	1.10 ± 0.02	1.08 ± 0.04	0.25 ± 0.04
Cu(1)	Ho||b	0.561	0.48 ± 0.03	-----	0.40 ± 0.04	0.33 ± 0.04	0.34 ± 0.04	0.27 ± 0.04	0.29 ± 0.04
Cu(2)	Ho||c	1.267	-----	1.26 ± 0.01	1.25 ± 0.01	1.28 ± 0.01	1.28 ± 0.01	1.28 ± 0.01	-0.01 ± 0.01
Cu(2)	Ho⊥ c	0.580	0.44 ± 0.02	-----	0.34 ± 0.02	0.30 ± 0.02	0.28 ± 0.02	0.28 ± 0.02	0.30 ± 0.02

Table V. The total copper magnetic shift tensor $^{63}K(T)$. The normal state values (^{63}K(100 K)) do not include limits of error because the procedure for determining the superconducting state values uses the ^{63}K(100 K) values as given. The values of ^{63}K(100 K) were determined from the single crystal data of Pennington et al.[76] using a least squares fit. The Yttrium Knight shift was taken to be -300 ppm and isotropic. The last two columns of data can be identified as the chemical shift $^{63}K^{L}$ and normal state Knight shift $^{63}K^{S}$(100 K), respectively, for the case of generalized BCS spin-singlet pairing with negligible spin-orbit coupling.

We have also investigated the possibility of a BCS spin-triplet pairing state. The temperature dependences of both the Cu(2) and Cu(1) Knight shift tensors are inconsistent with the behavior discussed in Leggett's review article for the simplest triplet states. An exotic triplet state (e.g. the planar state) could be constructed that would satisfy the requirement that only one component of the susceptibility tensor remains temperature independent below T_c, which would be consistent with Kcc(T=4.2 K) = Kcc(T=100 K) for the Cu(2). All of the exotic states that we were aware of at the time of our original paper[13] have the property that the zero temperature values of the remaining two temperature dependent spin susceptibility components are some fraction $\geq 1/2$ of their normal state values.[119] In this case, the Cu(2) magnetic shift for $\vec{Ho} \perp \hat{c}$ is given by:

(6-15a) $K_{aa}(T=100\ K)=K^L_{aa} + K^S_{aa}(T=100\ K)$, and

(6-15b) $K_{aa}(T=4.2\ K) \geq K^L_{aa} + (1/2)K^S_{aa}(T=100\ K)$.

We can see from our table of the magnetic shift tensor values (Table V), that the above equation and inequality would require a negative value of K^L_{aa}, which is inconsistent with this chemical shift being a paramagnetic contribution to the local field. We could not rule out with this argument any exotic spin-triplet pairing state whose temperature dependent susceptibility components obeyed the relation $\chi S\ (T=0\ K) < (1/2)\ \chi S\ (T=100\ K)$, but such a state would require a modification of the Pennington et al.[76] and Mila-Rice[97] Cu^{++} picture. Recently, Duan and Leggett have proposed an exotic pairing state that satisfies this last requirement.[125] The additional constraint on an exotic triplet pairing state such as this is the measurement of the magnetic shift of the planar oxygen site by various groups.[123,124] All three components of the planar oxygen Knight shift are temperature dependent, and

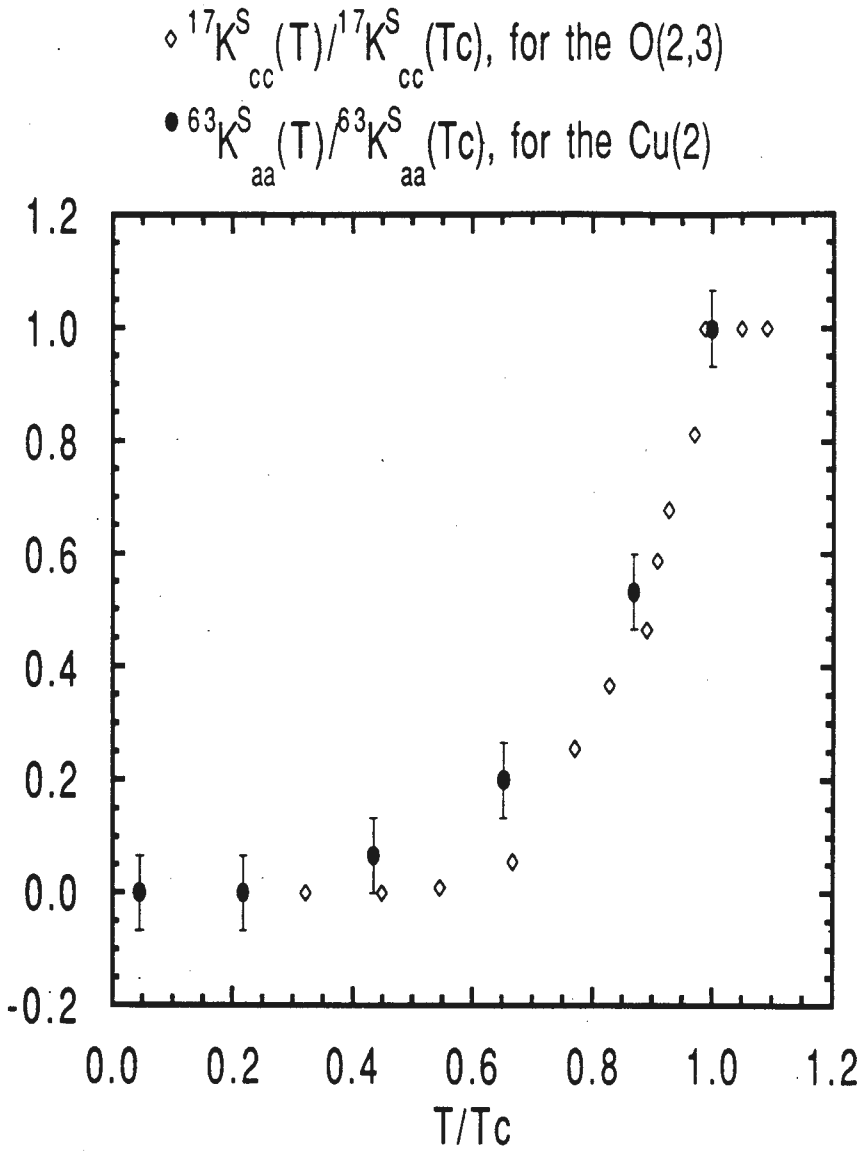

Figure 37. The closed circles are the normalized Knight shift versus temperature with $\vec{Ho} \perp \hat{c}$, $^{63}K^{S}_{aa}(T)/^{63}K^{S}_{aa}(T = 100\,K)$, for the Cu(2), determined as described in the text. The open diamonds are the normalized Knight shift versus temperature with $\vec{Ho} \parallel \hat{c}$, $^{17}K^{S}_{cc}(T)/^{17}K^{S}_{cc}(T_c)$, for the O(2,3).[123]

$^{17}Kcc(T) \propto {}^{63}Kaa(T)$, as is seen in Figure 37. This result is easily understood assuming a single component model and spin-singlet pairing, while it is apparently in contradiction with any triplet pairing which would make χ^S_{cc} independent of temperature.

We conclude from our analysis that the ^{63}Cu Knight shift data favor a BCS spin-singlet pairing state, and the picture of Pennington et al.[76] and Mila-Rice[97] for the copper electronic state is consistent with these data. Therefore, we define the Knight shift tensor for each copper site as:

(6-16) $$K^S_{\alpha\alpha}(T) \equiv K_{\alpha\alpha}(T) - K_{\alpha\alpha}(T=4.2\ K).$$

Section 6g. Analysis of the Knight Shift Data

We can now analyze the temperature dependence of the Knight shift tensors for both the Cu(1) and Cu(2) sites in turn.

The normal state Cu(1) Knight shift tensor is to a good first approximation isotropic, with $K^S_{1\alpha\alpha}(T=100\ K) \approx 0.29 \pm 0.04\%$. We recall that the Pennington et al. picture of the Cu(1) electronic state agrees well with the chemical shift tensor we obtain for this site.[76] The Pennington et al. picture expects that there is a permanent moment-like spin 1/2 associated with the hole in the y^2-z^2 d-shell orbital. As we discussed in Chapter 5, this d-shell spin should produce a dominant isotropic negative contribution to the spin-shift through the core polarization effect. The fact that the normal state value of the Cu(1) Knight shift is isotropic and positive could be interpreted in two ways. The first way is that there is a large isotropic transferred hyperfine coupling which overwhelms the on-site interaction. The second, more likely explanation is that there may be a significant amount of 4s orbital mixed into

the Cu^{++} wavefunction since the Cu(1)-O(4) distance is shorter than the Cu(1)-O(1) distance. Because an unpaired electronic spin in an s-orbital couples to the nucleus via the Fermi contact interaction, a small admixture of 4s into the wavefunction can have a big effect on the NMR properties. Both of these explanations of the Cu(1) Knight shift tensor are consistent with the nearly isotropic Cu(1) spin-lattice relaxation rate tensor determined by Pennington et al..[76] In addition, the superconducting state temperature dependence is about the same for all three components of this tensor, although $K^S_{1aa}(T)$ and $K^S_{1bb}(T)$ are the two toughest quantities to measure accurately because of the restricted powder pattern in our sample. To analyze the temperature dependence of the data, we plot in Figure 38 our most precise data $K^S_{1cc}(T/T_c)$ versus T/T_c. In our paper,[13] we used $T_c(\vec{Ho} \,||\, \hat{c}$=81 kGauss)=91 K, but we now believe the correct value for the field depressed T_c is $T_c(\vec{Ho} \,||\, \hat{c}$=81 kGauss)=88 K.[126,127] We use this new value in our new figure. Included in this figure are two theoretical fits to these data. The dashed line is the weak-coupling, spin-singlet, L=0 Yosida function that fits ^{27}Al.[54] A better fit to the data is provided by the solid line, which is a spin-singlet, orbital d-wave Yosida function.[141] For both the s-wave and d-wave fits to the Cu(1) data, the temperature dependence of the Knight shift near T_c is consistent with a weak-coupling BCS energy gap. We will see below that the behavior of the chain copper Knight shift is apparently different from that of the planar copper Knight shift.

We turn now to an analysis of the Cu(2) Knight shift. Our present analysis of the temperature dependences of the Cu(2) Knight shift data is considerably different from the analysis presented in our original paper.[13] In our earlier paper, we had analyzed the planar copper Knight shift data using a

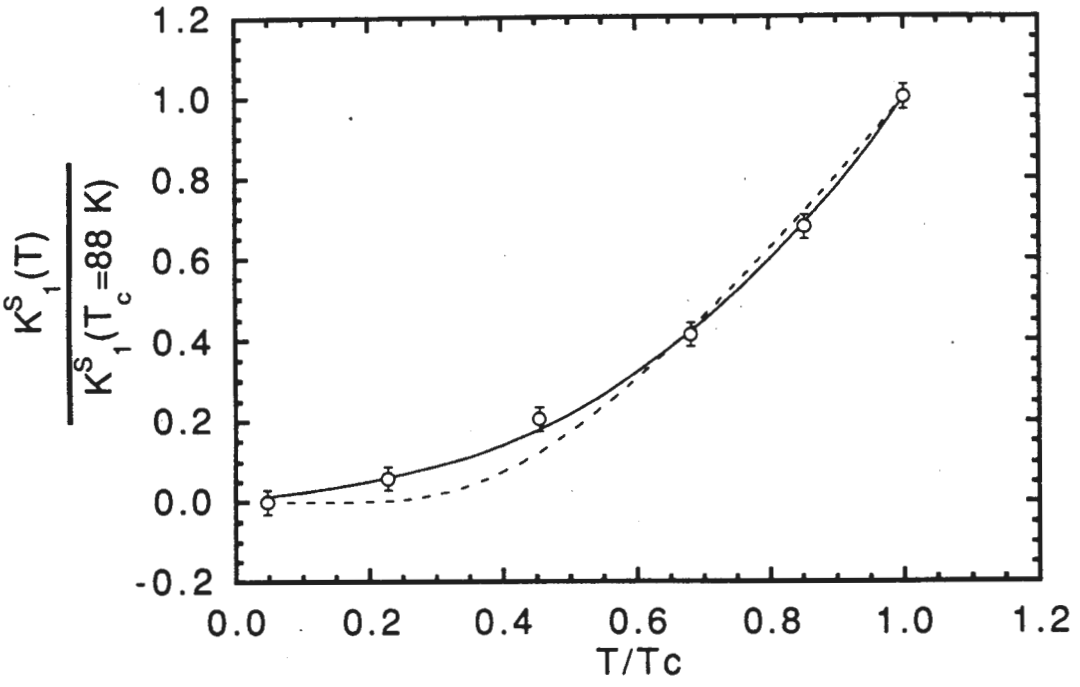

Figure 38. The points are the normalized Knight shift data for the Cu(1) nuclei with $\vec{Ho} \| \hat{c}$, $K^S_{cc}(T)/K^S_{cc}(T_c)$. The dashed line is the Yosida function as calculated for BCS, weak-coupling, spin-singlet, L=0 pairing.[54] The solid line assumes a spin-singlet, orbital d-wave, pairing state.[141] For the latter fit, $E(\vec{k})$ = $\cos(k_x) + \cos(k_y)$, $\Delta(T) = \Delta(T=0)\ \tanh\left(\alpha \sqrt{T_c/T - 1}\right)$, and $\Delta(\vec{k}) = \cos(k_x) - \cos(k_y)$ were used. The optimal parameters obtained in this fit are $\Delta_{max}(T=0)/k_B T_c = 2.3$, and $\alpha=1.74$.

two component model for the CuO_2 planar spin susceptibility. We plotted the quantity ($K^S_{2aa}(T/T_c) - K^S_{2cc}(T/T_c)$) versus T/Tc, in order to distinguish the temperature dependence of the the planar copper spin susceptibility from the temperature dependence of a distinct oxygen hole susceptibility. However, we now believe that there is only a single spin susceptibility in the CuO_2 planes, so that each component of the Knight shift tensor is directly proportional to this one component spin susceptibility. This is the picture contained in the Mila-Rice Hamiltonian (Eq. 6-14).[101] In this new light, the implications of our data are straightforward. First, for $\vec{Ho} \| \hat{c}$, the temperature independence of the Cu(2) Knight shift K^S_{2cc} in the superconducting state provides the important constraint for the Mila-Rice Hamiltonian that $A_{\|}+4B=0$, as we discussed earlier. Second, for $\vec{Ho} \perp \hat{c}$, the temperature dependence of $K^S_{2aa}(T/T_c)$ is directly proportional to the temperature dependence of the one component planar spin susceptibility, as is seen in the Mila-Rice Hamiltonian (Eq. 6-14b). This new picture of the CuO_2 planes yields a slightly different temperature dependence for the electronic spin susceptibility of the Cu(2) site. Another difference in our current understanding of the data is the value of $T_c(\vec{Ho})$. In our earlier paper, we used $T_c(\vec{Ho} \perp \hat{c}$=81 kGauss)=91 K, but we now believe the correct value for the field depressed T_c is $T_c(\vec{Ho} \perp \hat{c}$=81 kGauss)=92 K, which we use in our new plots.[126,127] We plot the temperature dependence of $\chi^S(T/Tc)/\chi^S(T=Tc)$ determined in our earlier paper[13] along with our new value of $K^S_{2aa}(T/T_c)/K^S_{2aa}(T=T_c)$ versus T/Tc in Figure 39. Our newly determined spin susceptibility has a slightly different temperature dependence (for $0.6<T/Tc<1$) from the temperature dependence of the originally published data, but all of our original conclusions still hold. The

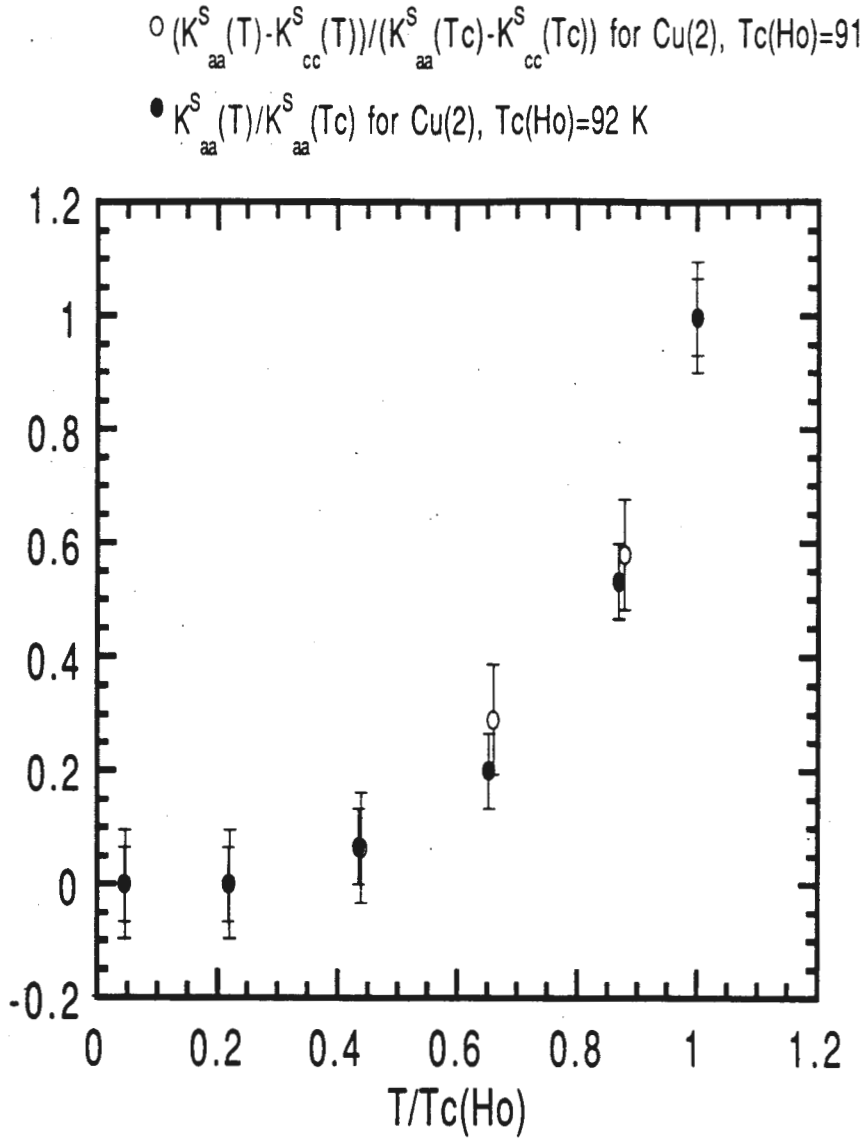

Figure 39. We have re-analyzed our data as described in the text in light of the development of the single component model for the spin susceptibility of the CuO_2 planes, as well as our improved knowledge of the magnetic field-depression of T_c.[126,127] The filled circles show our latest analysis of the Cu(2), $\vec{Ho} \perp \hat{c}$, normalized Knight shift, which is directly proportional to the static electronic spin susceptibility on the planar copper site. The empty circles are our previously published data for the temperature dependence of the static electronic spin susceptibility on the Cu(2) site.[13]

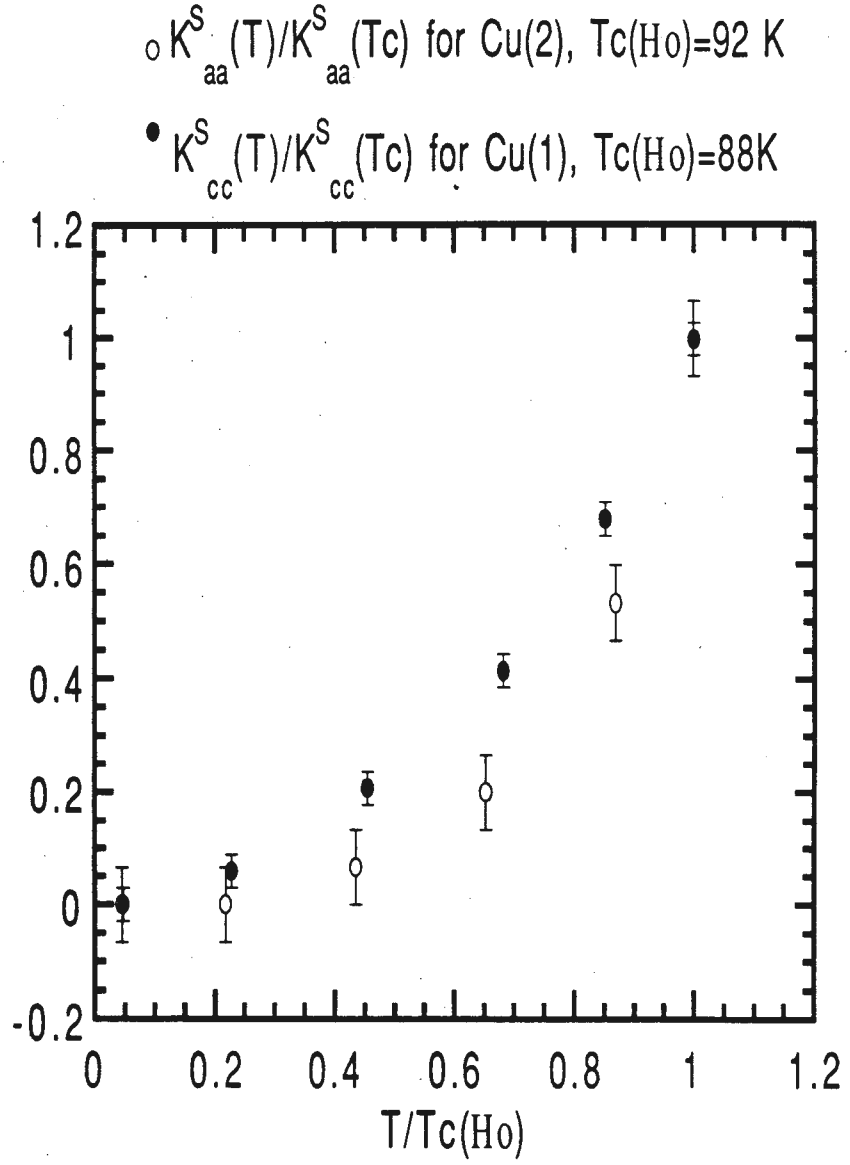

Figure 40. The filled circles are the normalized Knight shift data for the copper site in the chains, with $\vec{Ho} \parallel \hat{c}$, using Tc(Ho) = 88 K. These data have a different temperature dependence from the empty circles, which are the normalized Knight shift data for the copper site in the planes, with $\vec{Ho} \perp \hat{c}$, using Tc(Ho) = 92 K.

lowest temperature data is essentially independent of T/Tc, and the normalized spin susceptibility still drops off much faster than the weak-coupling, spin-singlet, L=0 Yosida function.[54] The behavior of these data is still distinct from the temperature dependence of the Cu(1) Knight shift data, as we see in Figure 40. If strong coupling is considered, so that both the magnitude of $\Delta(T=0\ K)$ and the value of $d\Delta(T)/dT$ near T_c are free parameters, the data may be fit with either orbital s-wave or d-wave (L=0 or 2) energy gaps as is shown in Figures 41 and 42.[119,128] Considering the flatness of the lowest Knight shift points, the s-wave fits seem to be better. Nevertheless, these data can also be fit by a spin-singlet state with nodes in the gap (e.g. orbital d-wave). In fact, if the gap opens up very quickly as one moves in k-space away from the nodes, and the energy gap's maximum value is quite large, the theoretical curve which would result would be very hard to distinguish from an s-wave case (nodeless) at low temperatures. Perhaps the relaxation rate anisotropy measurements which we will discuss in the next chapter will be a more sensitive probe of the symmetry of the gap function. The contrast of the Cu(1) and Cu(2) Knight shift data suggests that these two nuclei are seeing different energy gaps.

Section 6h. Additional Interpretations of the Knight Shift Data

Recently we have received a preprint by M. Tachiki and S. Takahashi which analyzes our Knight shift data using a different model from those described above.[129] They assume some pairing interaction generates BCS s-wave superconductivity in the CuO_2 plane layer. The presence of a weak electron transfer between the CuO_2 plane layer and the CuO chain layer then

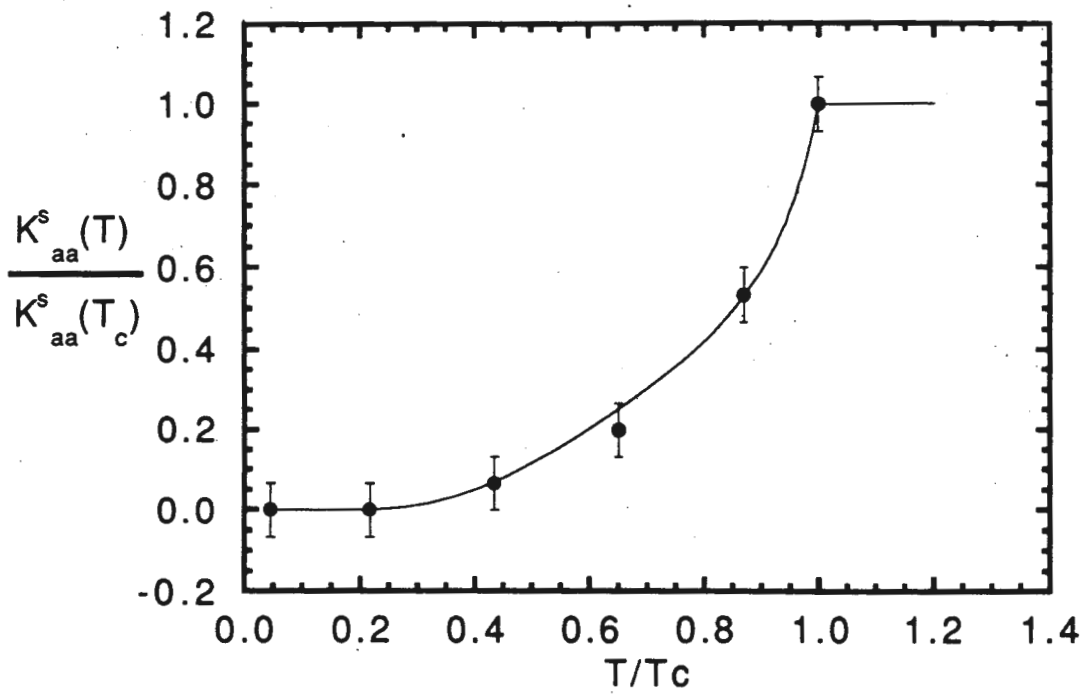

Figure 41. The points are the normalized Knight shift data for the copper site in the planes, with $\vec{Ho} \perp \hat{c}$, using Tc(Ho) = 92 K. The solid line is a strong-coupling Yosida function derived by Monien assuming a spin-singlet, orbital s-wave pairing state calculated on a cylindical Fermi surface.[119,128] The BCS weak-coupling parameters for this state are $\Delta(0)=1.76\ k_BT_c$ and $\Delta C/C=1.43$, while the optimal fit to our data shown above required $\Delta(0)=1.90\ k_BT_c$ and $\Delta C/C=2.77$.

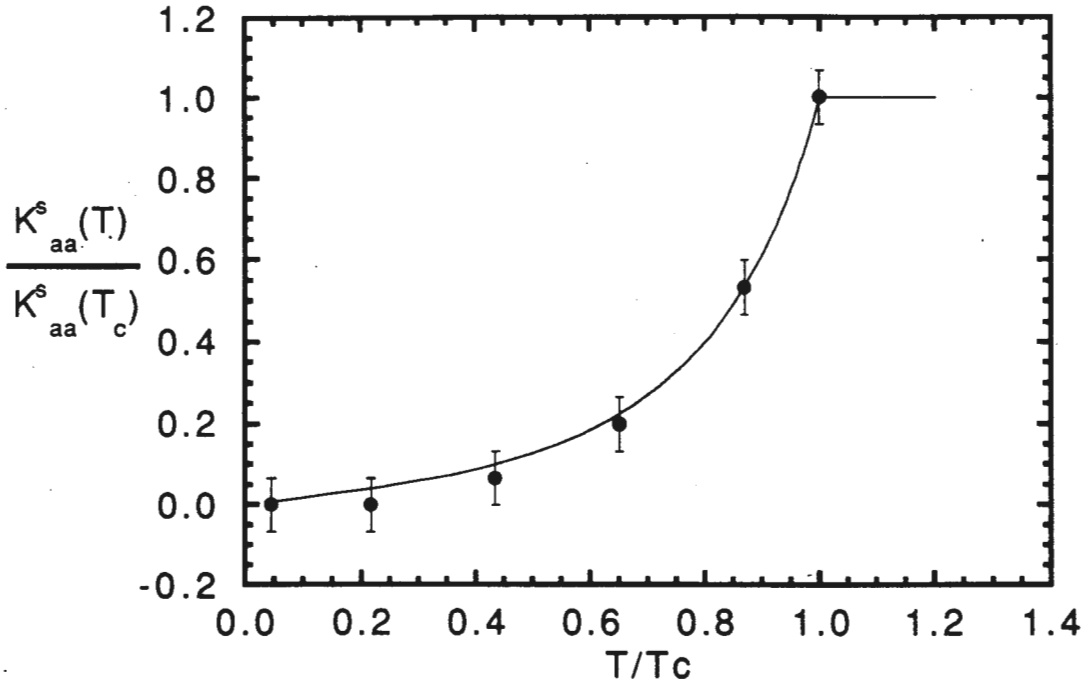

Figure 42. The points are the normalized Knight shift data for the copper site in the planes, with $\vec{Ho} \perp \hat{c}$, using Tc(Ho) = 92 K. The solid line is a strong-coupling Yosida function derived by Monien assuming a spin-singlet, orbital d-wave pairing state with an admixture of higher L calculated on a cylindical Fermi surface.[119,128] The BCS weak-coupling parameters for this state are $\Delta(0)_{max}=1.93\ k_BT_c$ and $\Delta C/C=1.17$, while the optimal fit to our data shown above required $\Delta(0)_{max}=3.13\ k_BT_c$ and $\Delta C/C=2.14$.

induces a weak superconductivity in the CuO chain layers. This is how they explain the apparent existence of different gaps for the plane and chain copper sites. The effective masses in the chain and plane bands and transfer integrals are fitting parameters. The fits to our data are shown in Figure 43.

Section 6i. A General Approach to Obtain $^{63}K^{S}(T)$ Using the Yttrium Data.

Some feeling for the robustness of the above results may be obtained in the following analysis. We recall that for a particular field orientation and temperature, the position of the yttrium and central copper resonance lines are given by:

(6-17a) $\nu_Y(T)=(\gamma_Y/2\pi)*(1+^{89}K_Y(T))*B_{int}(T)$,

(6-17b) $\nu_{Cu}(T)=const*(1+^{63}K^{L}+^{63}K^{S}(T))*B_{int}(T) + \nu_Q(T)$.

We can subtract off the small quadrupole part of the copper resonance line position using the perturbation theory expression of the frequency and the values of the electric field gradient tensor used in Section 6d. What remains is the magnetic contribution to the copper line position, $\nu_{Cu,mag}(T)$ ($=\nu_{Cu}(T)-\nu_Q(T)$). We can than take the ratio of the magnetic line position for the copper to the yttrium line position, and the internal field drops out:

(6-18) $\nu_{Cu,mag}(T)/\nu_Y(T)=const.*(1+^{89}K_Y(T))/(1+^{63}K^{L}+^{63}K^{S}(T)) \sim$ const. $*(1 + (^{89}K_Y{}^{L} - {}^{63}K^{L}) + (^{89}K^{S}(T) - {}^{63}K^{S}(T)))$.

The only approximation made to this point was that terms of order K*K are small compared to unity, which is definitely true. Thus this formula is quite general and may be used to compare the three possible ways of using the yttrium data which we first mentioned in Section 6b. First, the method which we used to obtain the Knight shift data discussed in all of the previous

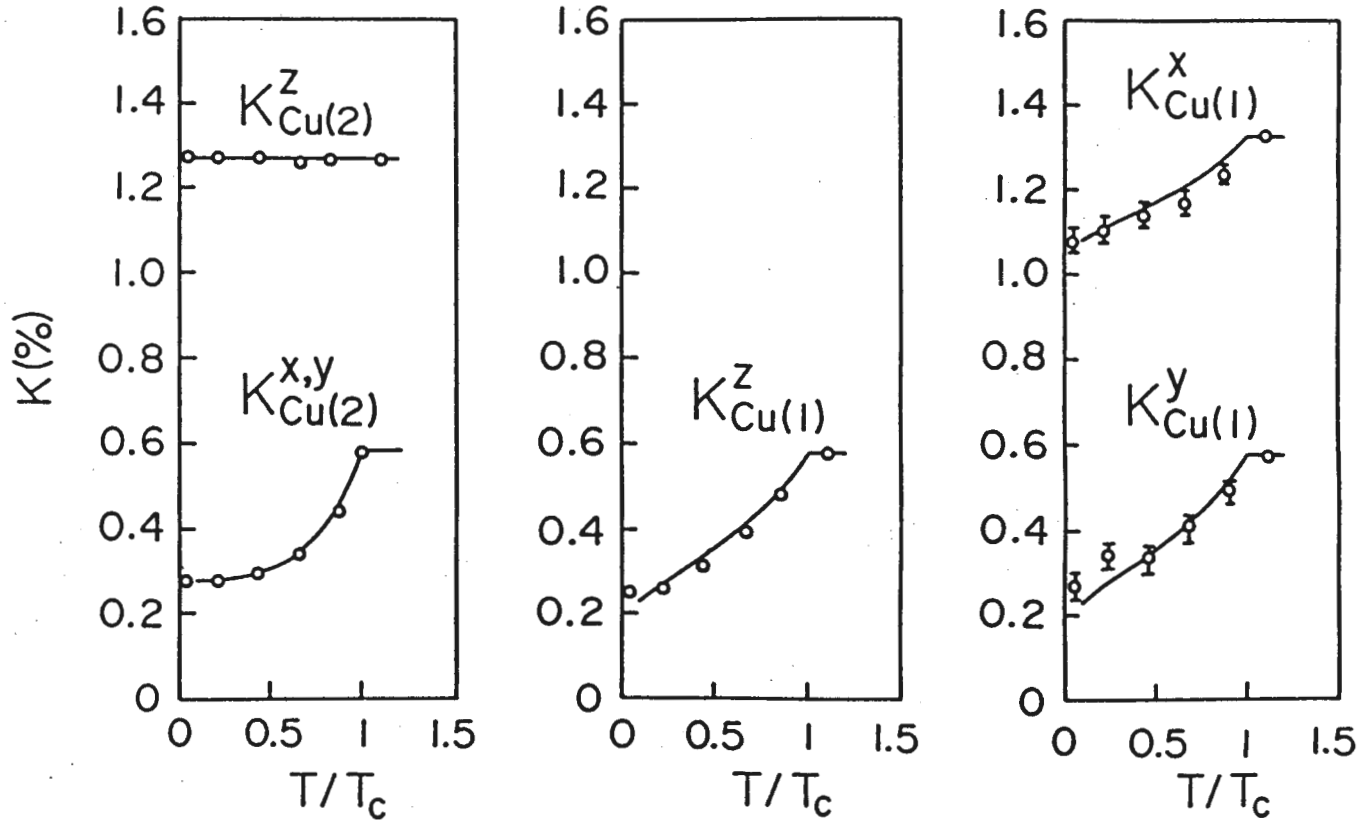

Figure 43. Fit to our data by M. Tachiki and S. Takahashi, which stresses the layered structure.[129] A BCS s-wave pairing interaction exists in the CuO_2 plane layer, and electrons hop between the planes and the chains.

sections involved picking a value for $^{89}K_Y{}^L$ and $^{89}K^S(T=100\ K)$, as well as assuming that $^{89}K^S(T)$ followed the s-wave weak coupling Yosida function. These assumptions resulted in the copper magnetic shift data shown in Table V.

We could also assume that the yttrium Knight shift was directly proportional to the copper Knight shift:

(6-19) $$^{89}K^S(T) = \Gamma\ ^{63}K^S(T).$$

Plugging this expression into Equation (6-18), we obtain:

(6-20) $$\nu_{Cu,mag}(T)/\nu_Y(T) - \nu_{Cu,mag}(0)/\nu_Y(0) = const^*\ ^{63}K^S(T).$$

Thus the temperature dependence of the ratio of the magnetic contribution to the raw data should be directly proportional to the copper Knight shift. This proportionality covers both of the other possible analyses of our data which we mentioned in Section 6b, because $\Gamma = 0$ is case one (i. e. no yttrium Knight shift) and $\Gamma \neq 0$ is case three (i. e. yttrium and planar copper couple to a single spin susceptibility). We can calculate the Cu(2), $\vec{Ho} \mid \mid \hat{a}/\hat{b}$, Knight shift quite easily using this method, and the results are listed in Table VI. These data are plotted in Figure 44 along with the data determined in Section 6b using the weak coupling temperature dependence for the yttrium Knight shift. As one might expect, the only noticeable difference between these data sets is in the region near Tc (T/Tc > 0.6), where it is interesting to note that these new points are even farther away from the weak coupling Yosida function temperature dependence. However, even this difference is quite small, and the the assumptions employed in analyzing the yttrium data seem to have only a limited effect on the copper Knight shift. Thus the temperature dependence for the planar copper spin susceptibility which we have determined should be quite reliable.

T/Tc=92 K	K^{S}_{aa}(T/Tc) for Cu(2), for Proportional Yttrium Knight Shift
0.045652	0.0000
0.21739	0.0000
0.43478	0.0625
0.65217	0.1875
0.86957	0.5000
1.00000	1.0000

Table VI. The values obtained for K^{S}_{aa}(T/Tc) for the Cu(2) site, when the Y Knight shift is assumed to be directly proportional to the Cu(2) Knight shift.

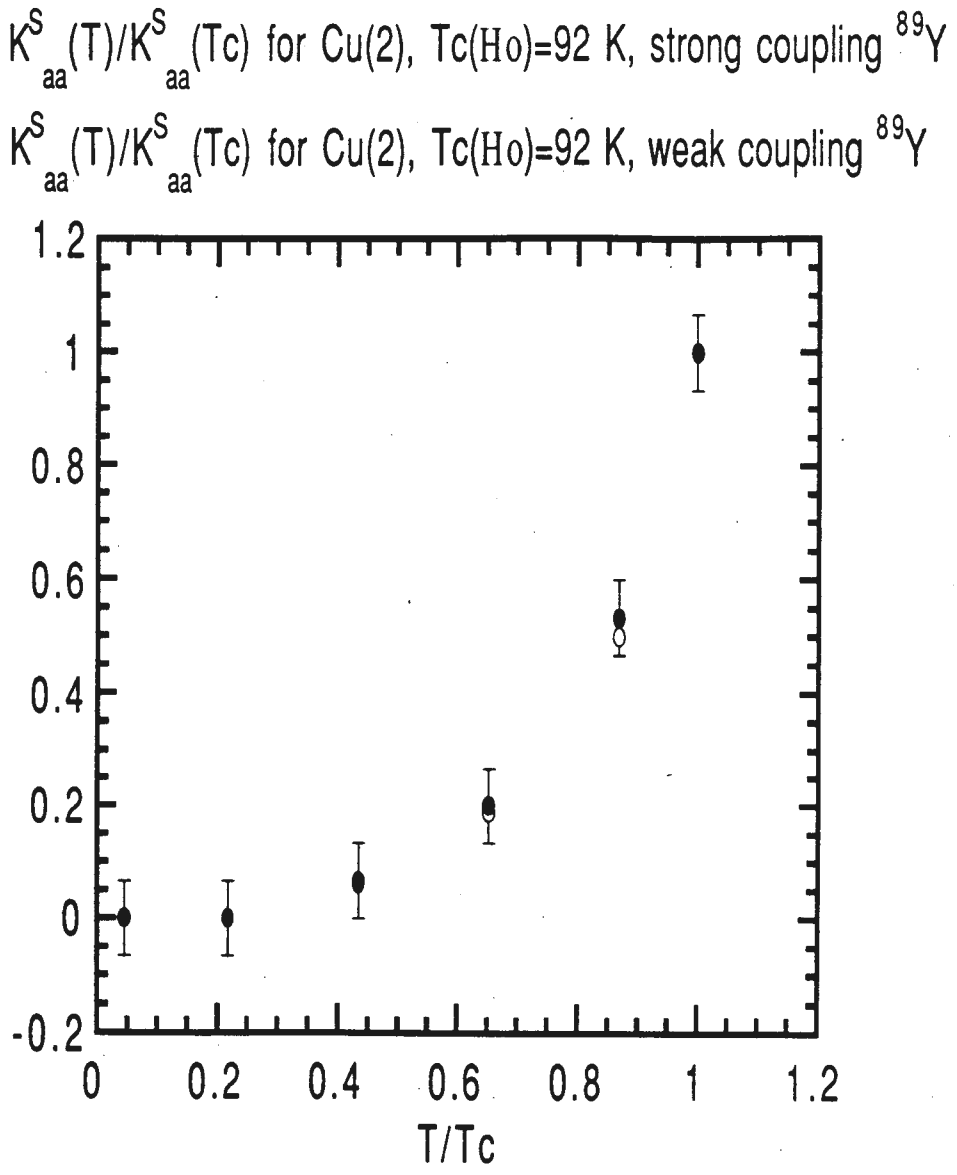

Figure 44. The dark circles are the normalized Knight shift data for the copper site in the planes, with $\vec{Ho} \perp \hat{c}$, using Tc(Ho) = 92 K, as presented in Section 6g. To obtain these data, we assumed that the ^{89}Y Knight shift was -300 ppm at T=100 K and that it had the temperature dependence of the BCS weak-coupling s-wave Yosida function. If we instead assume that the ^{89}Y Knight shift is directly proportional to the Cu(2) Knight shift as described in this section, we obtain the empty circles.

Chapter 7. ^{63}Cu(2) W1 Anisotropy Measurement

Section 7a. Introduction

In this chapter we report the results of the Slichter group's measurements of the ^{63}Cu(2) nuclear spin-lattice relaxation rates in the normal and superconducting states. Sections 7b through 7f cover the data included in the Barrett, Martindale, et al. Anisotropy Paper.[14] In Section 7g we briefly present the most recent data included in the Martindale, Barrett et al. Anisotropy Paper,[15,16] and compare these results to our earlier results. In Section 7h we will discuss the various interpretations and implications of these data sets. As in all of our recent High-T_c measurements, these experiments are largely collaborative efforts, and we will try to give credit to the group members who were responsible for the measurements and calculations presented.

These experiments involved several samples, and we will use the sample names consistent with the master identification Table II in Section 4b.

The motivation for this experiment is straightforward. In Section 5c we were reminded that a single-component model with an antiferromagnetically enhanced spin susceptibility was sufficient to explain all of the normal state magnetic shift and spin-lattice relaxation rate data in this material. Within this model, the expressions for the relaxation rates of the copper, oxygen, and yttrium sites are (i=63,17,89):

$$(7\text{-}1) \qquad {}^{i}\left(\frac{1}{T1}\right)_{\alpha} = \left(\frac{{}^{i}\gamma_n^2 \, k_B T}{2\,\mu_\beta^2}\right) \mathrm{Lim}_{\omega\to 0} \sum_{\vec{q},\alpha'\neq\alpha} \left|{}^{i}A_{\alpha'\alpha'}(\vec{q})\right|^2 \frac{\left\{\chi''_{\alpha'\alpha'}(\vec{q},\omega)\right\}}{\omega}$$

As we discussed in Section 5c, the difference in the rates for the ^{63}Cu(2),

$^{17}O(2,3)$, and ^{89}Y is contained in the magnitude and $\vec{q}$-dependence of the hyperfine form factors, $|{}^{i}A_{\alpha'\alpha'}(\vec{q})|^2$, which are obtained from the real space hyperfine coupling constants. The model which fits the normal state data implies that the various rates emphasize different regions of the $\chi''_{\alpha\alpha}(\vec{q},\omega)$ tensor. We can list these rates in order of decreasing sensitivity to the antiferromagnetic enhancement region ($\vec{q} \approx \vec{Q} = (\pi/a,\pi/a)$) of $\chi''_{\alpha\alpha}(\vec{q},\omega)$: $^{63}W1a$, $^{63}W1c$, $^{17}W1c$, and $^{89}W1c$.

Within this model, our measurement of the ratio $^{63}W1a/^{63}W1c$ can provide information on the relative temperature dependence of the $\vec{q}\approx 0$ and $\vec{q}\approx\vec{Q}$ regions of $\chi''_{\alpha\alpha}(\vec{q},\omega)$. In Section 5e, we discussed the results of Hammel et al. for the ratio $^{63}W1c/^{17}W1c$ in the normal and superconducting state.[90,91] This ratio should also probe the relative temperature dependences of the $\vec{q}\approx 0$ and $\vec{q}\approx\vec{Q}$ regions of $\chi''_{\alpha\alpha}(\vec{q},\omega)$. Because this ratio, $^{63}W1c/^{17}W1c$, was reported to be independent of temperature from 110 K down to 20 K, one would naively expect that all the relaxation rate ratios (e.g. the Cu(2) anisotropy ratio $^{63}W1a/^{63}W1c$) should be independent of temperature as the temperature is lowered through the superconducting transition. Our data show that this last prediction is incorrect.

Section 7b. Single Crystal Measurements

In the Slichter group, Dr. C. H. Pennington first tried to make measurements below T_c using the single crystal he studied for his thesis. His sample was a large (~1mg) single crystal. Unfortunately, because of the superconducting screening currents, the signal from his sample decreased markedly upon entering the superconducting state, and he was unable to

make any measurements. Prof. Slichter suggested that we needed to maximize the surface area to volume ratio of our sample, which was the traditional solution used in the study of single crystals of normal metals by NMR.[45] Dr. Dale Durand acted upon this advice by making a sample which we will call the Durand sample. This sample was composed of ~50 small single crystals with a total sample mass of 2-3 milligrams. This sample was completely aligned as was discussed in Section 4b. This sample was first used by Dr. Durand in the Knight shift experiment, as we discussed in Section 6b.

After the Knight shift experiment, we decided to use the Durand sample to measure the Cu(2) relaxation rate anisotropy in the superconducting state. The first measurement was made at T~56 K, and we obtained the surprising result that $2< {}^{63}W1a/{}^{63}W1c <3$. The temperature control and $^{63}W1$ error bars for this measurement left something to be desired, but our answer was definitely different from Pennington et al.'s normal state result of $^{63}W1a/^{63}W1c\sim4$. This tantalizing result was not followed up on for several months, while other experiments were completed.

When we returned to the Cu(2) relaxation rate anisotropy measurements, our strategy was to measure $^{63}W1a(T)$ in both the normal and superconducting states, and then repeat these measurements for $^{63}W1c(T)$. Dr. Pennington was instrumental in beginning these measurements, and he took the first few $^{63}W1a(T)$ points.

These measurements were made on the central transition of the $^{63}Cu(2)$ resonance (see Appendix C), using an inversion recovery pulse sequence, so the magnetization recovery curve followed the form $(\vec{Ho} \| \vec{\alpha})$:

$$(7\text{-}2) \qquad M(t_{inv})-M(\infty)=Mo(0.9e^{-4W1\alpha tinv} + 0.1e^{-2W1\alpha tinv/3}).$$

A typical fit this equation is shown in Figure 45. The ratio $Mo/M(\infty)$ was

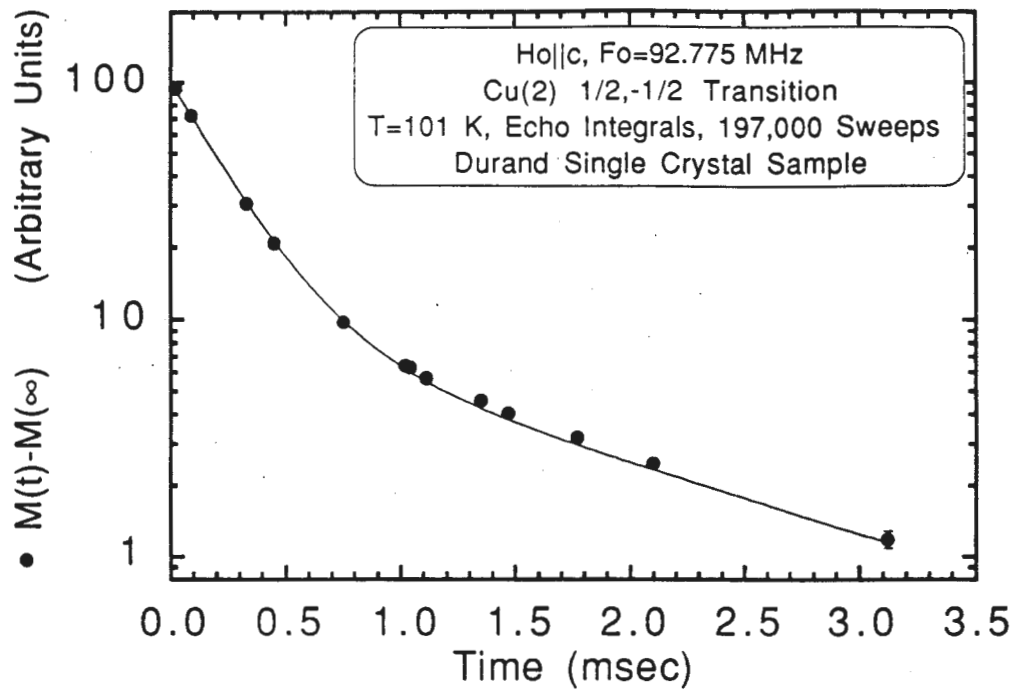

Figure 45. The filled circles are Cu(2), central transition, magnetization recovery data for the Durand aligned single crystal sample, obtained with an inversion recovery pulse sequence. The solid curve through the data is the expected recovery form given in Equation (7-2), where the inverted magnetization, M_o, and the spin-lattice relaxation rate, $W_{1\alpha}$, were adjusted to fit the data. For the fit shown, $M_o = 101.7$, and $W_{1c} = 1.05\ ms^{-1}$.

typically ~90% in the normal state, dropping to ~70% below T_c. This decrease was attributed to the H1 becoming increasingly inhomogeneous throughout the sample as the temperature was lowered below T_c.

The values of $^{63}W1\alpha(T)$ that were obtained from the above procedure are shown in Figure 46. Unfortunately, there aren't as many $^{63}W1c(T)$ points, because we accidentally liquified part of the plexiglass sample mount with a heat gun. The $^{63}W1c(T)$ points indicated by filled circles were taken before this accident, and the open circles were taken after with the surviving sample.

When plotting the ratio $^{63}W1a/^{63}W1c$ in the superconducting state, we need to take into account both the strong magnetic field applied and the superconducting state anisotropy of this material. The former fact will result in a depressed value of the T_c(Ho=81 kGauss), because the applied field (Ho) exceeds the upper critical field Hc_2 for a narrow temperature range just below the zero field $T_c(0)$. The latter fact results in a strong field T_c(81 kGauss) which depends on the orientation of the applied field, because $Hc_{2\alpha}(T)$ is strongly anisotropic. Based on the single crystal studies of Welp et al.,[126] and Hao et al.,[127] and our zero field $T_c(0)$=93 K, we find that $T_c(\vec{Ho} \parallel \hat{c}$=81 kGauss)=88 K and $T_c(\vec{Ho} \perp \hat{c}$=81 kGauss)=92 K. We use these values for our plots involving $T/T_c(\vec{Ho})$. The unfortunate implication of the above discussion is that a $^{63}W1a$ point and a $^{63}W1c$ point taken at the same temperature should not be directly compared in the superconducting state, since they are at different values of $T/T_c(\vec{Ho})$.

Although this experiment was prematurely ended, we can see in the data many interesting features. The ratio $^{63}W1a/^{63}W1c$ is only weakly temperature dependent in the normal state. Using an interpolation formula

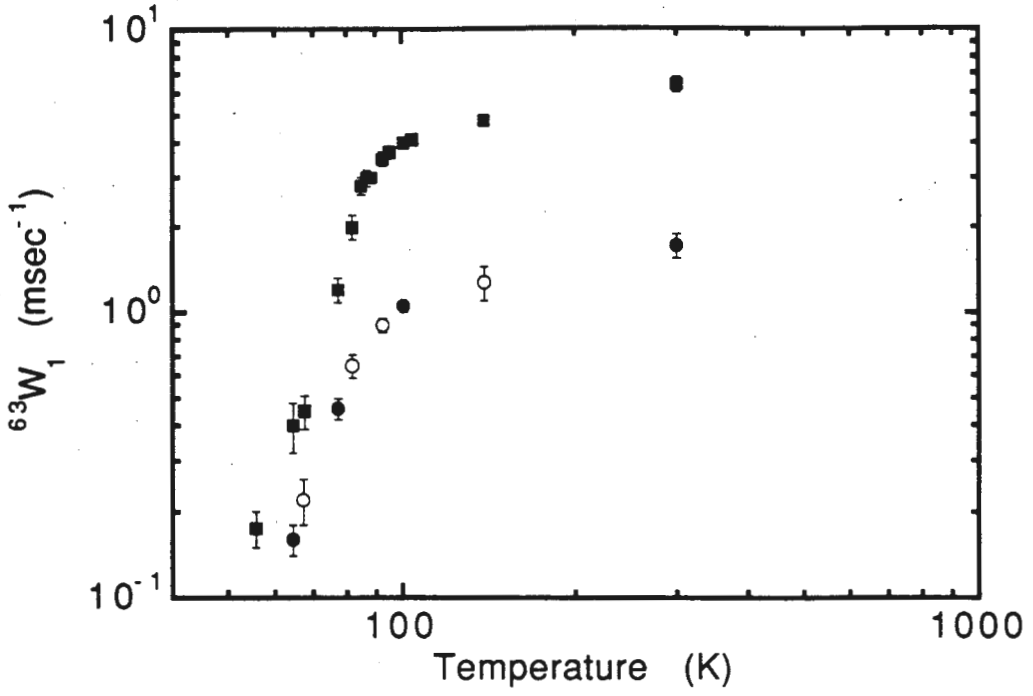

Figure 46. The ^{63}Cu(2) spin-lattice relaxation rate $^{63}W_{1\alpha}$ as a function of temperature in the Durand aligned single crystal sample. The filled squares were obtained with $\vec{Ho} \perp \hat{c}$ ($^{63}W_{1a}$). The circles were obtained with $\vec{Ho} \parallel \hat{c}$ ($^{63}W_{1c}$). The filled (empty) circles were obtained before (after) the sample holder was partially melted.

for $^{63}W1_\alpha(T/T_c)$ which we will describe in the next section, we can see that $^{63}W1a/^{63}W1c$ drops sharply just inside the superconducting state. This ratio continues to decrease slowly in this high field measurement as $T/T_c \rightarrow 0$, as we see in Figure 47.

These initial results were surprising, so we wanted to reduce the error bars on the data points in order to verify that this $^{63}W1a/^{63}W1c$ anisotropy drop was a real effect. To do this, larger samples were required. We set out to make these measurements in aligned powders.

Section 7c. Aligned Powder W1 Measurements (Ho=81 kGauss)

The goal of this experiment was to measure the $^{63}W1_\alpha$ tensor for the Cu(2) site. In an 81 kGauss field, as we discussed in Section 6c, the aligned powder sample spectra have intensity at places other than the distinct central transition resonance lines observed in a single crystal sample spectrum. Nevertheless, the features in the aligned powder sample spectra at these single crystal positions are prominent, and we attempted to measure the normal state relaxation rate at these positions. These initial attempts were all failures. We were measuring the relaxation rate at the central transition frequency by observing the magnetization recovery following an inversion pulse. The data should follow the form:

$$M(t_{inv})-M(\infty)=Mo(0.9e^{-4W1\alpha tinv} + 0.1e^{-2W1\alpha tinv/3}), \quad (7\text{-}3)$$

as the single crystal data do. We found that the the data for both $\vec{Ho} \,||\, \hat{c}$ and $\vec{Ho} \perp \hat{c}$ consistently deviated from this theoretical form. This behavior is consistent with the presence of a baseline in our powder pattern. In other words, at the frequency we are measuring the relaxation rate data, for

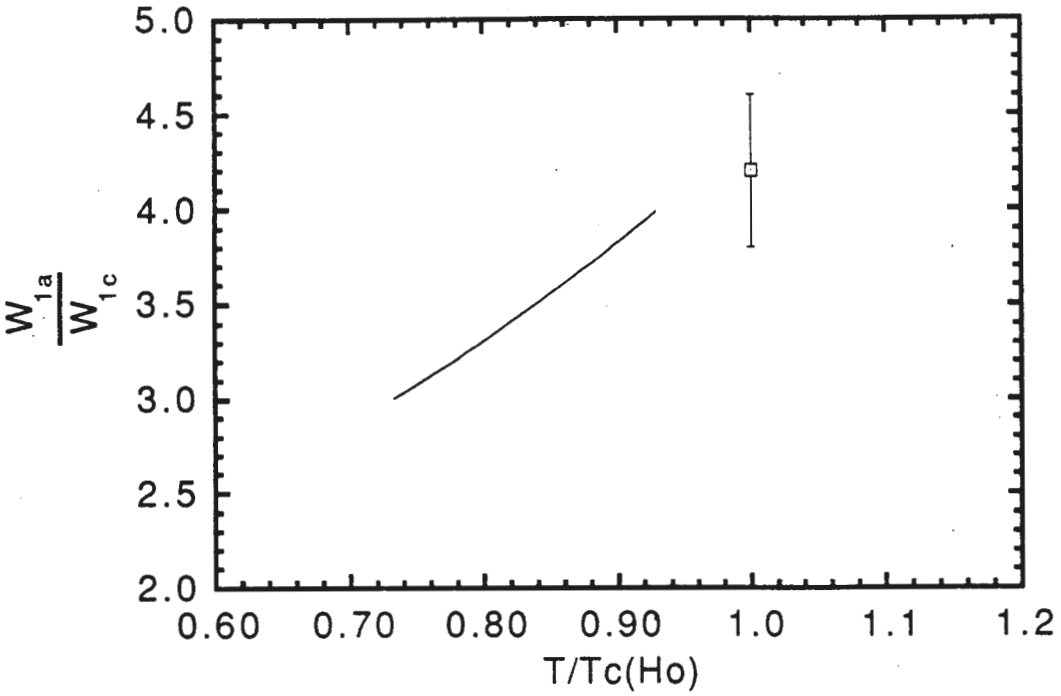

Figure 47. Plot of the ratio $W_{1a}(T/T_c)/W_{1c}(T/T_c)$ as a function of $T/Tc(\vec{Ho})$, for the Cu(2) nuclei in the Durand aligned single crystal sample. We have used an interpolation formula to be described in the next section to fit our $W_{1\alpha}(T/T_c(\vec{Ho}))$ data. The solid line shows the ratio we obtain over the range of our superconducting data points. The open square at T/Tc = 1 would be the ratio at this point if the $W_{1\alpha}$'s were continuous across the transition.

example the single crystal determined position of the $^{63}Cu(2)$ central transition for $\vec{Ho} \| \hat{c}$, there is at least one other contribution to the magnetization. A possible source of this extra signal is misaligned crystallites. This baseline contribution to the magnetization has a longer T2 and T1 than the magnetization which corresponds to the single crystal determined resonance line[43]. The T2 dependence is evident in the magnetization recovery data shown in Figure 48, which is taken in one sample, with the spacing between the $\pi/2$ and π pulses of the echo being the only parameter varied.

Clearly it would be advantageous to get rid of this baseline signal, so that aligned powder samples could be used for W1 measurements. To this end we worked to improve the alignment procedure, to try and reduce this background signal. Our attempts included smaller crystallite size (<18 μm), lower packing fraction, and a better sample making procedure, as we describe in Section 4b. In the end however, there was no way to completely remove this baseline background. We think this is because some of the larger crystallites have some smaller crystallites grown onto them at odd angles, as we discussed in Section 6c. When the large crystallites align in the field, the small crystallites are frozen into permanently misoriented directions, producing the baseline signal.

We have been able to make NMR measurements of W1 in these aligned powder samples using a baseline subtraction method. This method is possible because much of the poorly aligned signal intensity is spread over a wide range of frequencies. As a result the T1 and T2 of this poorly aligned signal is a slowly varying function of frequency. We see this by taking magnetization recovery data on the shelves on either side of the well aligned

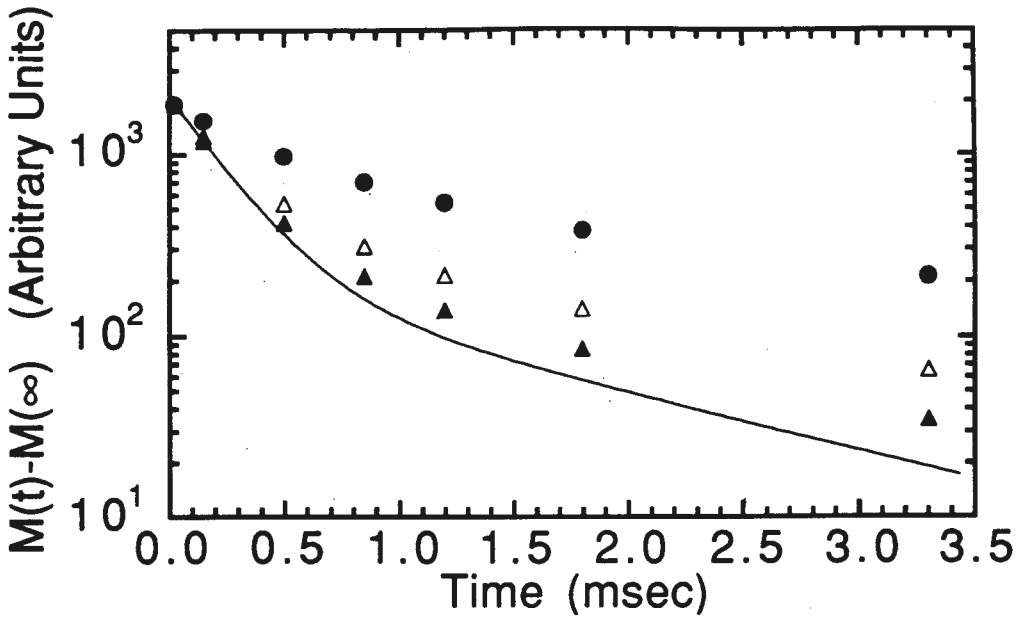

Figure 48. The effect of the spin echo pulse spacing on the NMR magnetization recovery data of the Cu(2), $\vec{Ho} \,||\, \hat{c}$, central transition in aligned powder Sample K. These data were obtained at T = 101 K using an inversion recovery pulse sequence (π - t_{inv} - $\pi/2$ - τ - π - τ - echo). The solid line is the fit that would be expected under these conditions since a previous NQR measurement in this sample yielded W_{1c} = 1.1 ms^{-1}. However, the NMR data deviates from this theoretical form as the delay time (τ) in the spin echo is varied, with everything else held constant. The solid triangles were obtained for τ = 50 μsec, the open triangles were obtained for τ = 100 μsec, and the solid circles were obtained for τ = 200 μsec. This delay time dependence of the data shows that there is a signal with a longer T1 and T2 at the same frequency as the Cu(2), $\vec{Ho} \,||\, \hat{c}$, central transition in aligned powder Sample K.

feature in the powder pattern. These shelves (shown in Figure 49) do not exist in an aligned single crystal spectrum.[43,74,75] The data from these shelf regions clearly do not follow the magnetization recovery curve obtained for a relaxation rate measurement at any peak in a single crystal sample, but they do track one another nicely, as is seen in Figure 50. The signal from the baseline underneath the peak should also track this shelf signal, because they are all presumably from the same poorly aligned source. To obtain the recovery of the signal at the peak frequency due to the well aligned signal alone, we can repeat a recovery experiment at the peak with the same parameters used at the shelf frequency, and subtract the two results. Since the baseline has both a longer T2 and T1, it contributes a larger fraction of the signal for larger pulse spacings in the echo, τ, and also for larger spacings between the inversion pulse and the echo, t_{inv}. We can improve the accuracy of the relaxation rates measured with this baseline subtraction technique by using only short times for both t_{inv} and τ in the inversion recovery pulse sequence:

(7-4) $\pi\text{-}t_{inv}\text{-}\pi/2\text{-}\tau\text{-}\pi\text{-}\tau\text{-echo}.$

For very short values of t_{inv} and τ the well aligned signal is quite large compared to the poorly aligned baseline signal, so the baseline subtracted data should fit the expected central transition recovery curve:

(7-5) $M(t_{inv})\text{-}M(\infty)=Mo(0.9e^{-4W1\alpha tinv} + 0.1e^{-2W1\alpha tinv/3}),$

as is shown in Figure 51. For these baseline subtracted data, the longest value of $t_{inv,max}$ was chosen so that $M(t_{inv,max})\text{-}M(\infty) \geq 0.3*Mo$. This is a much smaller time region than that used in the normal state single crystal measurements, where the longest value of $t_{inv,max}$ was chosen so that $M(t_{inv,max})\text{-}M(\infty) \geq 0.01*Mo$.

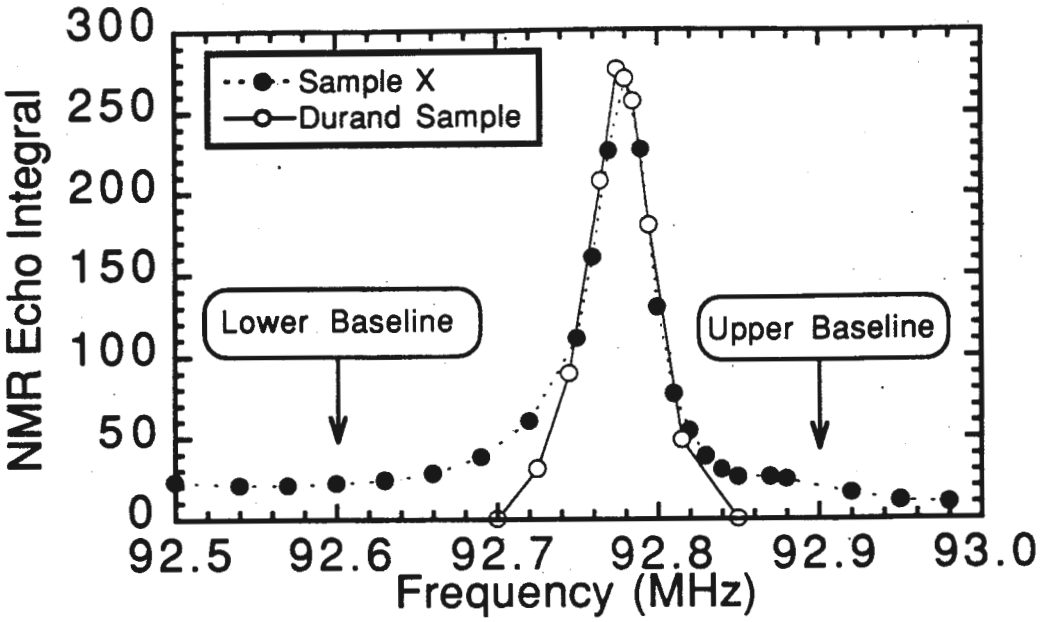

Figure 49. Comparison of the $^{63}Cu(2)$, $\vec{Ho} \| \hat{c}$, central transition obtained in the Durand aligned single crystal sample (open circles) and that obtained in the aligned powder Sample X (filled circles). The signal intensities have been scaled to agree at F = 92.78 MHz. The powder sample has rather significant "shelves" on either side of the main peak (e.g. at F=92.600 MHz and at F=92.900 MHz) which do not appear in the aligned single crystal spectra.

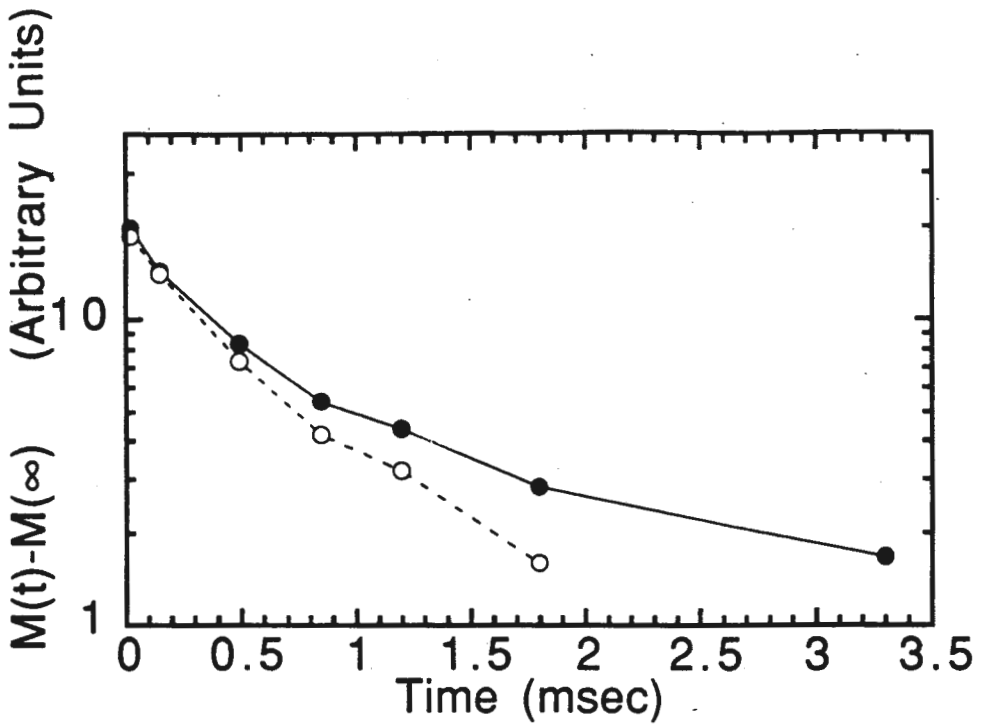

Figure 50. Magnetization recovery data for the $\vec{Ho} \mid \mid \hat{c}$, T= 101 K, baseline signal in aligned powder Sample X. The empty circles are for F_o=92.600 MHz, and the solid circles are for F_o=92.900 MHz, as pointed out in Figure 49. The solid and dotted line are to guide the eye. The two data sets overlap for the early time points (i.e. times ≤ 0.5 msec) used in the baseline subtraction procedure. These data were obtained using an inversion recovery sequence.

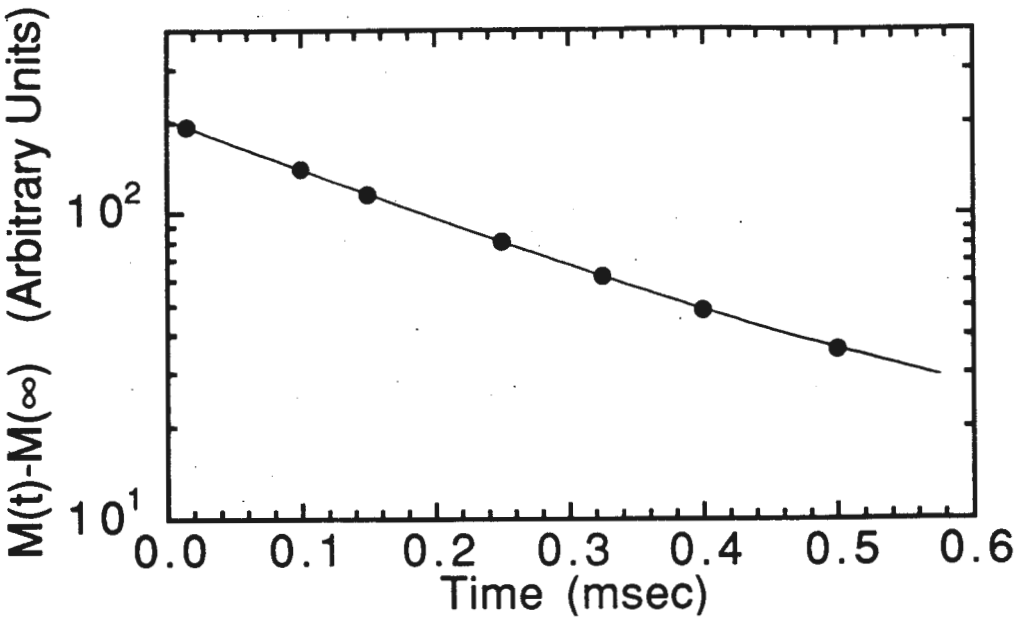

Figure 51. Magnetization recovery data at T = 101 K in aligned powder Sample X using the baseline subtraction technique. The solid points are the echo integrals measured at the $^{63}Cu(2)$ $\vec{Ho} \| \hat{c}$ peak signal (Fo=92.78 MHz), where we have subtracted the echo integrals measured (under the same conditions) at the upper baseline position (Fo=92.900 MHz). The solid line is the expected recovery curve given in Equation (7-5), adjusted by the method of least squares to fit the data. The relaxation rate which results (W_{1c} = 1.07 ms^{-1}) agrees (within experimental error) with both the NQR result of Sample X (W_{1c} = 1.10 ± 0.05 ms^{-1}) and the NMR result of the Durand aligned single crystal sample (W_{1c} = 1.05 ± 0.05 ms^{-1}).

Having determined that it would be possible to minimize the effect of baseline signal in our NMR measurements of $^{63}W1_{\alpha}$, we set out to measure the $^{63}W1a/^{63}W1c$ anisotropy ratio in the normal and superconducting states in an aligned powder sample. We used Sample X. This sample had only a 2% packing fraction and a total mass ≤ 75 mg. The $^{63}W1_{\alpha}$ data obtained in this sample in an applied field of Ho=81 kGauss as a function of temperature are shown together with our earlier single crystal results in Figure 52. The lowest temperature data for Sample X (40 K to 60 K) were obtained by J. A. Martindale and Dr. D. J. Durand.

There are several interesting features of these data. First, the normal state $^{63}W1a/^{63}W1c$ anisotropy ratio is essentially independent of temperature (inset of Figure 52). Second, we found that the relaxation rates in the superconducting state could be approximated by the interpolation formula:

$$^{63}W1_{\alpha} = A_{\alpha}\left(\frac{T}{T_c(Ho)}\right)\exp\left(B_{\alpha}\left(\frac{T}{T_c(Ho)}\right)\right) \qquad (7\text{-}6)$$

We will discuss this anomalous formula later; it may have no fundamental significance. This interpolation, shown in Figure 53, was used so that we could plot the $^{63}W1a/^{63}W1c$ anisotropy ratio as a function of $T/T_c(\vec{Ho})$, which is shown in Figure 54. This figure shows that $^{63}W1a/^{63}W1c$ has dropped sharply just inside the superconducting state ($1>T/T_c>0.8$), and then continues to decrease slowly with temperature. We recall that this result is completely consistent with our earlier single crystal results. As we discussed is Section 7a, our naive one-component model picture, incorporating the results of Hammel et al.,[90,91] would predict $^{63}W1a/^{63}W1c$ is a constant for $T<110$ K.

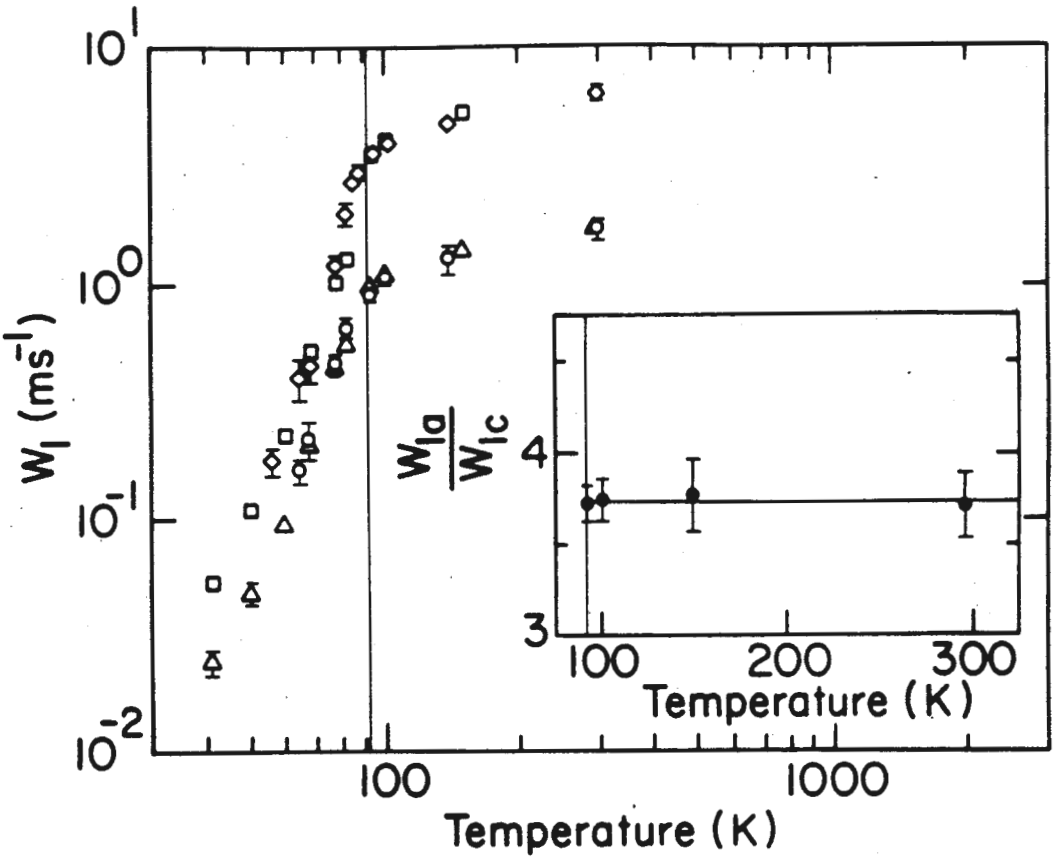

Figure 52. Main Figure: The $^{63}Cu(2)$ spin-lattice relaxation rate $^{63}W_{1\alpha}$ as a function of temperature. The open diamonds (open squares) are the data obtained in the Durand sample (Sample X) for $\vec{Ho} \perp \hat{c}$. The open circles (open triangles) are the data obtained in the Durand sample (Sample X) for $\vec{Ho} \parallel \hat{c}$. The vertical solid line is at 92 K. **Inset:** The normal state ratio W_{1a}/W_{1c} as a function of temperature for Sample X (solid circles). The horizontal line is at $W_{1a}/W_{1c} = 3.73$, and the vertical line is at 92 K.[14]

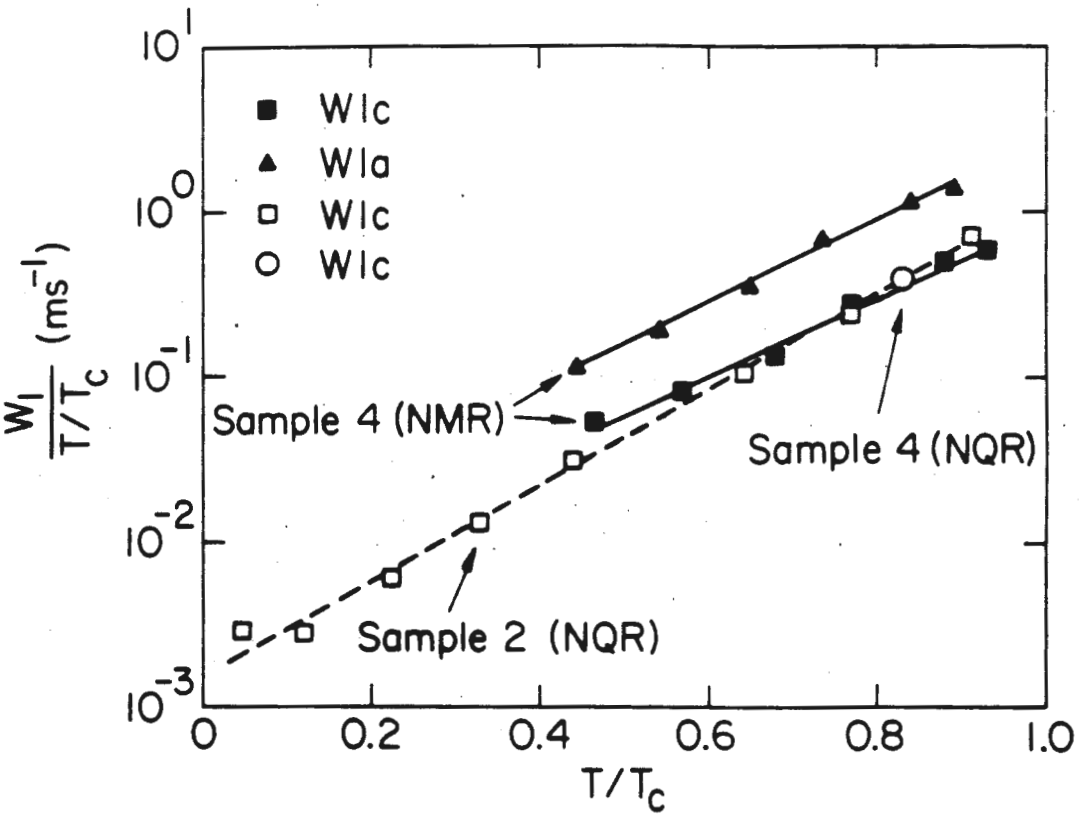

Figure 53. The $^{63}Cu(2)$ relaxation rate $^{63}W_{1\alpha}$ divided by $T/T_c(\vec{Ho})$ versus $T/T_c(\vec{Ho})$.[14] Sample 4 is Sample X, and Sample 2 is Sample Y41, as is listed in Table II. The lines through the data reveal the exponential dependence of this quantity.

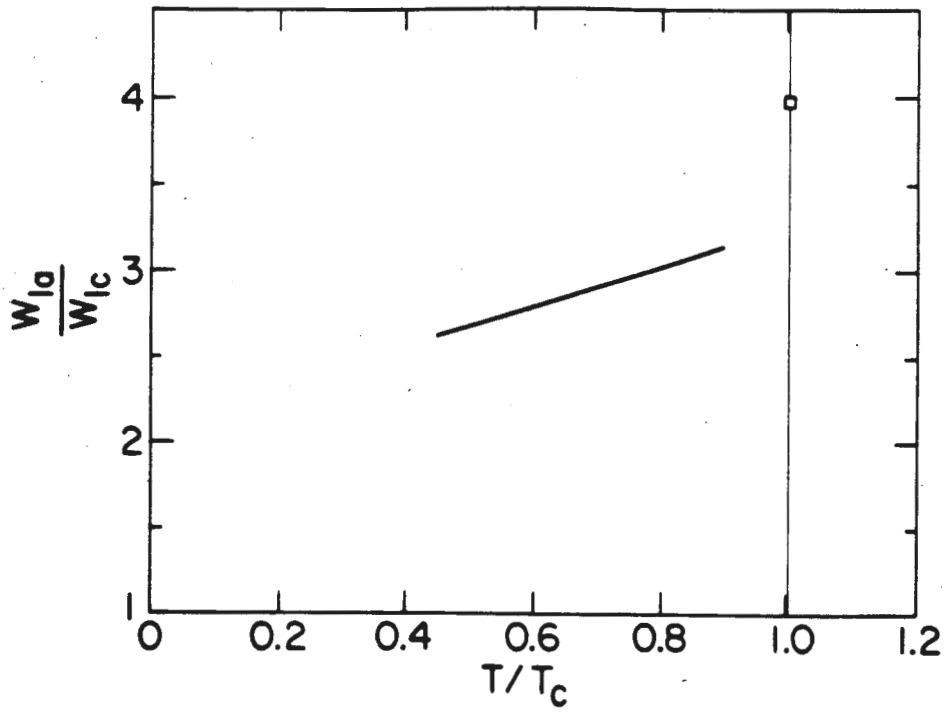

Figure 54. $^{63}W_{1a}/^{63}W_{1c}$ versus $T/T_c(\vec{H}o)$, where we have used the functional forms (Equation (7-6)) fitting the NMR data for Sample X in Figure 53. The solid curve is the ratio over the range of our superconducting state data. The square at T/Tc = 1 would be the ratio at this point (3.98) if the $^{63}W_{1\alpha}$'s were continuous across the transition.[14]

Section 7d. NQR Measurements of ^{63}W1c (Ho=0 kGauss)

As we discuss in Appendix C, the electric field gradient at the Cu(2) site is axially symmetric about the $\hat{c}$-axis.[76] As a result, the eigenstates of the Hamiltonian are the eigenstates of $\hat{I}_z$, the same eigenstates as one has with a strong field $\vec{Ho} \| \hat{c}$.[38] Transitions between these states are induced by the fluctuating fields H_x and H_y. One can then measure the same relaxation rate ^{63}W1c either with a strong field applied along the $\hat{c}$-axis (NMR) or with no static magnetic field along any axis (NQR). We have verified that the rates measured in either case are the same within experimental error in the normal state.

In the superconducting state, $^{63}W1c(T)_{NMR} \neq {}^{63}W1c(T)_{NQR}$. For example, we have measured these quantities in both Sample X and Sample OX at T=77 K. We find $^{63}W1c(T=77\ K)_{NQR} = 0.31\pm0.04\ ms^{-1}$, while $^{63}W1c(T=77\ K)_{NMR} = 0.44\pm0.02\ ms^{-1}$.

It is obviously important to take into account the depression of $T_c(\vec{Ho})$ by the magnetic field which we discussed in Section 6f. For these samples $T_c(Ho = 0\ kGauss) = 93$ K, while $T_c(\vec{Ho} \| \hat{c} = 81\ kGauss) = 88$ K.[126,127] Thus the NQR and NMR measurements at 77 K are at two different values of $T/T_c(\vec{Ho})$ (0.832 and 0.880, respectively). To correct for this difference in $Tc(\vec{Ho})$, we can use the interpolation formula for the strong field NMR data to calculate the value we would expect for $^{63}W1c(T^*)_{NMR}$ if it were measured at the same $T^*/T_c(\vec{Ho}) = 0.832$ which was used for the $^{63}W1c(T=77\ K)_{NQR}$ measurement. We find $^{63}W1c(T^*)_{NMR} = 0.29\pm0.01\ ms^{-1}$, which agrees well with $^{63}W1c(T=77\ K)_{NQR} = 0.31\pm0.04\ ms^{-1}$. The implication of this result is that the behavior of $^{63}W1c(T/T_c)$ is independent of magnetic field down to $T/T_c \sim 0.8$.

We have also made $^{63}W1c(T)_{NQR}$ measurements in a larger unaligned powder sample, Sample Y41. These data are shown along with $^{63}W1c(T)_{NMR}$ for Sample X in Figure 53, with the interpolation formula:

$$^{63}W1_{\alpha} = A_{\alpha}\left(\frac{T}{T_c(Ho)}\right)\exp\left(B_{\alpha}\left(\frac{T}{T_c(Ho)}\right)\right), \quad (7\text{-}7)$$

through each data set. Although the NMR and NQR data are very similar at large values of $T/T_c(\vec{Ho})$, there is a distinct deviation between the two data sets at low temperatures. As a result, the parameter B_{NMR} of the interpolation formula is smaller than the parameter B_{NQR}. This would result in a different temperature dependence for the ratio $^{63}W1a/^{63}W1c$ at low T/T_c if we were to plot $^{63}W1a(T/T_c)_{NMR}/^{63}W1c(T/T_c)_{NQR}$ rather than the original plot of $^{63}W1a(T/T_c)_{NMR}/^{63}W1c(T/T_c)_{NMR}$. We show in Figure 55 that the difference between these two quantities is primarily at low temperatures. The problem with using the ratio $^{63}W1a(T/T_c)_{NMR}/^{63}W1c(T/T_c)_{NQR}$ to describe the low temperature behavior of $^{63}W1a/^{63}W1c$ is that the NMR and NQR data were taken in two different samples. Thus there was some ambiguity as to whether the difference shown in the figure was a sample dependence or an additional field dependence. The recent work of Martindale et al. (Section 7g) answered this question.[15,16]

Section 7e. Weak Field Measurements of $^{63}W1a$ (Ho=4.5 kGauss)

The sharp change in the anisotropy ratio $^{63}W1a/^{63}W1c$ that we observed between $T/T_c=1$ and $T/T_c=0.8$ occurred in the presence of a strong field (81 kGauss). Our $^{63}Cu(2)$ NQR measurements showed that $^{63}W1c(T/T_c(\vec{Ho}))$ was independent of field in this region of T/T_c. There

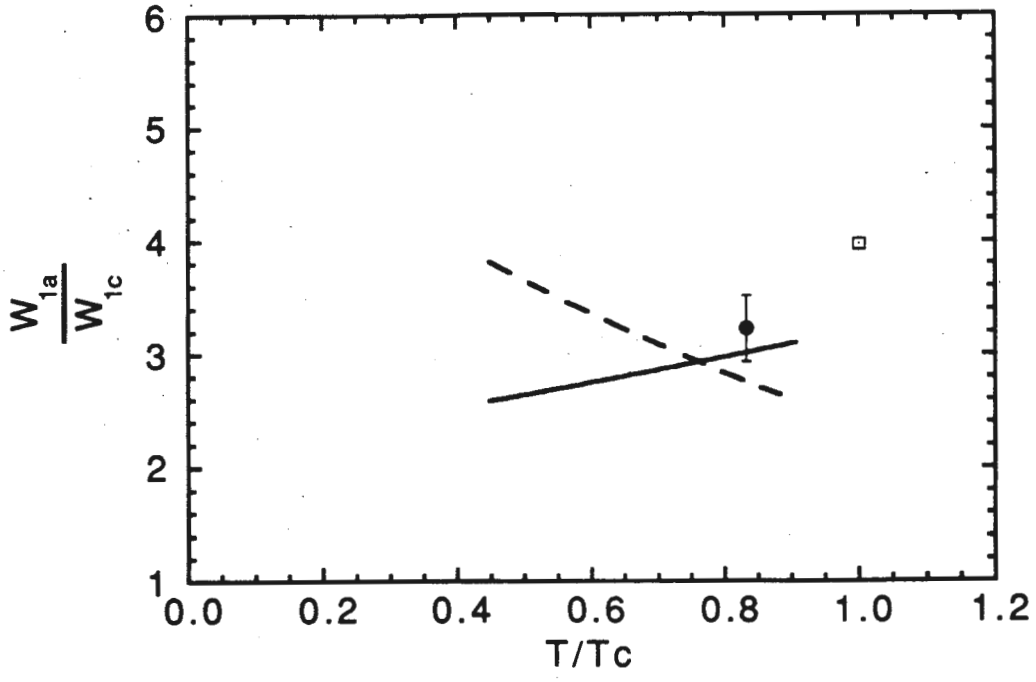

Figure 55. $^{63}W_{1a}/^{63}W_{1c}$ versus $T/T_c(\vec{Ho})$. The solid line is the curve shown in Figure 54, which is the ratio $^{63}W_{1a}$(Ho=81 kGauss, Sample X)/$^{63}W_{1c}$(Ho=81 kGauss, Sample X). The dashed curve is the ratio $^{63}W_{1a}$(Ho=81 kGauss, Sample X)/$^{63}W_{1c}$(Ho=0 kGauss, Sample Y41). The filled circle is the point $^{63}W_{1a}$(Ho=4.5 kGauss, Sample OX)/$^{63}W_{1c}$(Ho=0 kGauss, Sample OX), taken in liquid nitrogen. The empty square at T/Tc = 1 would be the ratio for Sample X at this point (3.98) if the $^{63}W_{1\alpha}$'s were continuous across the transition.

remained the possibility that the sharp drop in ^{63}W1a/^{63}W1c was caused by some field effect on ^{63}W1a. We wanted to check for this by measuring ^{63}W1a in the smallest possible applied field.

Prof. Slichter suggested that we could apply a weak field perpendicular to the $\hat{c}$-axis, perturbing the zero field NQR eigenstates. This is an unusual experimental situation, because the Zeeman term ($\propto \hat{I}_x$) is a perturbation to the Quadrupole Hamiltonian ($\propto \hat{I}_z^2$ for the Cu(2)). The transition probability between the new eigenstates would then involve both ^{63}W1c and ^{63}W1a. The perturbation theory result (calculated by Prof. Slichter, J. Martindale, K. O'Hara, and S. DeSoto) for this situation is shown in Figure 56.

We decided to measure this weak field ^{63}W1a in the above configuration with $\vec{Ho} \perp \hat{c}$ = 4.5 kGauss. We measured the relaxation recovery of the resonance that occurred at 10 MHz. For this field value, the perturbation theory result was not accurate enough to fit the data. The complete Hamiltonian was exactly diagonalized and the relaxation rate problem solved by two of us independently (K. O'Hara and S.E.B.). We used these exact forms for the magnetization recovery following an inversion pulse in a fitting program written by Dr. C. A. Klug to extract the weak field value of ^{63}W1a. The details of this calculation are given in Appendix D.

We performed this experiment on Sample OX. At 101 K we obtained the same answer for ^{63}W1a in both the strong field and weak field experiments. At 77 K, we found for Sample OX that (see Figure 55) $^{63}W1a(T/T_c=0.83)_{NMR,weakfield}/^{63}W1c(T/T_c=0.83)_{NQR} = 3.23 \pm 0.29\ ms^{-1}$. This weakfield ratio agrees well with the strong field NMR ratio in Sample X at $T/T_c=0.83$: $^{63}W1a(T/T_c=0.83)_{NMR,strongfield}/^{63}W1c(T/T_c=0.83)_{NMR,strongfield} = 3.06\ ms^{-1}$ (where we have used the interpolation formula).

NQR ($H_o = 0$)

$$\hat{H} = a\,(\hat{I}_z)^2$$

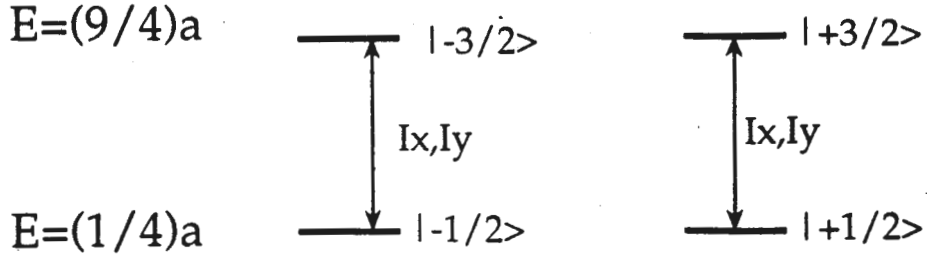

NMR (Small $\vec{H}_o \perp \vec{c}$)

$$\hat{H} = a\,(\hat{I}_z)^2 + b\,(\hat{I}_x)$$

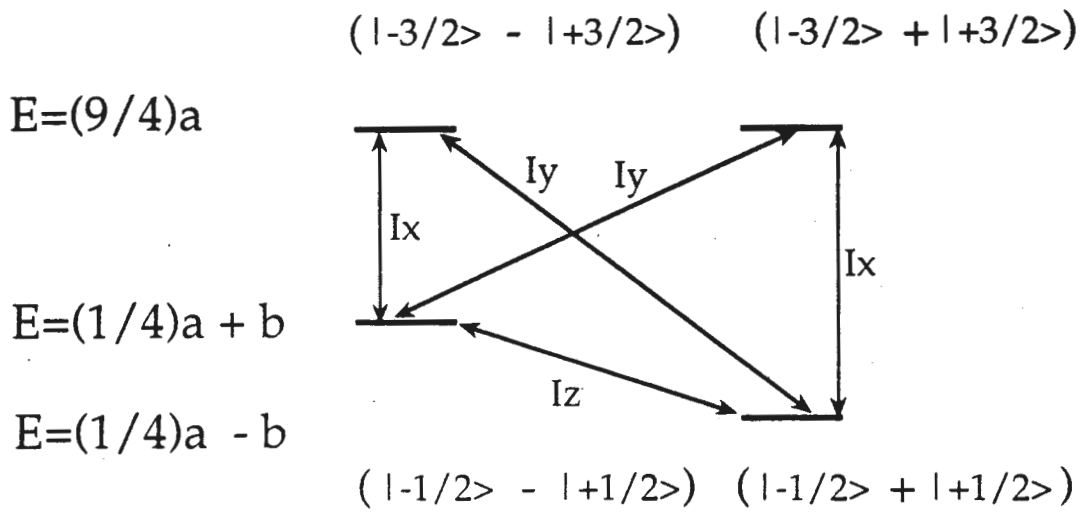

Figure 56. (**Top**): The NQR Hamiltonian for the case of an electric field gradient which is axially symmetric about the $\hat{z}$-axis has the simple form given above. The eigenstates, eigenvalues, and allowed magnetic transitions for a spin-3/2 nucleus are shown. Only the relaxation rate involving Ix and Iy may be measured (W1c). (**Bottom**): Turning on a small magnetic field along the $\hat{x}$-axis results in the new eigenstates, eigenvalues, and allowed magnetic transitions shown, correct to first order in perturbation theory. The relaxation rate involving Iz (W1a) may now be measured.

The most important conclusion of these experiments on the planar copper relaxation rate is that the anisotropy ratio $^{63}W1a(T/T_c)/^{63}W1c(T/T_c)$, undergoes a sharp drop between $T/T_c = 1$ and and $T/T_c = 0.8$, independent of the applied field. The implication of this result will be discussed in Section 7h.

Below $T/T_c = 0.8$ this $^{63}W1a(T/T_c)/^{63}W1c(T/T_c)$ ratio decreases (increases) when $^{63}W1c$ is measured in an 81 kGauss (0 kGauss) field. We were uncertain in our original paper whether this last effect was a true field dependence or just due to sample variation. The recent work of Martindale et al., discussed in Section 7g, indicates that this low temperature behavior reflects an extra field dependence.[15,16]

Section 7f. Strong Field O(2,3) and Y Relaxation Rates

As we discussed in Section 5c, the hyperfine form factors are different for the Cu(2), O(2,3), and Y sites. In a one component model of the CuO_2 planes, the relaxation rates of these sites weight the various regions of $\chi''_{\alpha\alpha}(\vec{q},\omega)$ differently. Given the surprising results we obtained in Section 7c for the Cu(2) $^{63}W1a/^{63}W1c$ ratio below T_c, we decided to measure the O(2,3) and Y nuclear relaxation rate anisotropies to place more constraints on possible explanations.

J. A. Martindale has made many measurements of the O(2,3) relaxation rate in both the normal and superconducting state, using Sample OX. We will present here only the values he obtained for T=101 K and T=77 K.[14] For the O(2,3) site, one can distinguish the ($\vec{Ho} \perp \hat{c}$ and $\vec{Ho} \parallel$ bond axis) resonance from the ($\vec{Ho} \perp \hat{c}$ and $\vec{Ho} \perp$ bond axis) resonance, where we are using the bond

axis assignment of Takigawa et al..[89] This is quite different from the case of the Cu(2) and Y, which have only a single resonance when $\vec{Ho} \perp \hat{c}$, so W1a≡W1b. For our purposes, we will define ^{17}W1a as the oxygen relaxation rate measured for the ($\vec{Ho} \perp \hat{c}$ and $\vec{Ho}$ | | bond axis) resonance. The measurements of ^{17}W1c and ^{17}W1a were made on satellite lines only, using the baseline subtraction method described in Section 7c. The baseline signal intensity was quite large compared to the peak intensity for the ^{17}W1a measurement, but this measurement was repeated on other satellites to check the consistency of these results. The measured values of ^{17}W1c are consistent with other published results.

We have also measured the relaxation rate anisotropy of the Y nucleus, using Sample K. These data were taken at 101 K and 77 K using an inversion recovery sequence and a modified inversion recovery sequence which included a Carr-Purcell-Meiboom-Gill echo train. No baseline subtraction was needed, presumably since this nucleus is spin 1/2, and therefore has no quadrupole broadened transitions.

The interesting feature of these data can be seen in Figure 57, where we plot ^{63}W1c/^{17}W1c, ^{63}W1c/^{89}W1c, ^{63}W1a/^{17}W1a, and ^{63}W1a/^{89}W1a at 101 K and 77 K. Since we are only comparing ratios of quantities taken with the same applied field orientation, there is no complication of $T/T_c(\vec{Ho})$. These ratios should change with temperature if the $\vec{q} \approx 0$ and $\vec{q} \approx \vec{Q}$ regions of $\chi''_{\alpha\alpha}(\vec{q},\omega)$ change relative to one another. We can see from the figure that only the first quantity, ^{63}W1c/^{17}W1c, is the same at both 101 K and 77 K. Every other ratio changes. The experimental situation below T_c is much more complicated than Hammel et al.'s original result would seem to imply.[90,91]

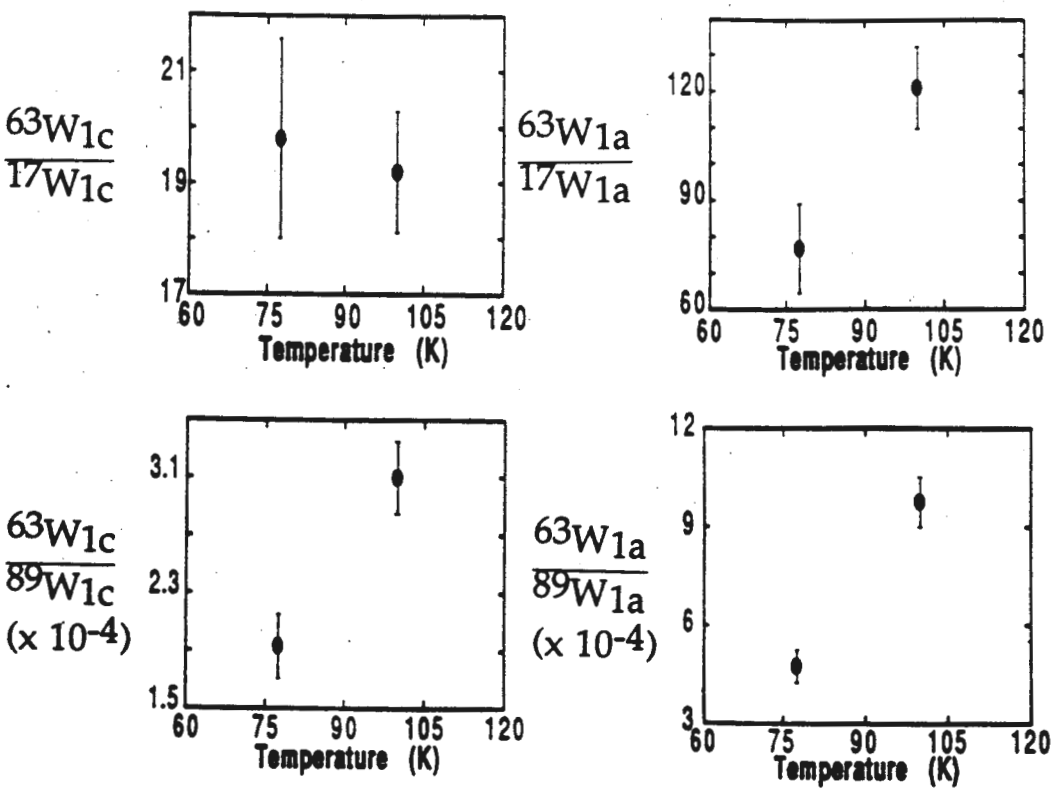

Figure 57. A comparison of the relaxation rates of the Cu(2), the O(2,3), and the Y ($^{63}W_{1\alpha}$, $^{17}W_{1\alpha}$, and $^{89}W_{1\alpha}$, respectively, when $\vec{Ho} \mid\mid \hat{\alpha}$) at T = 101 K and T = 77 K. We define $^{17}W_{1a}$ to be the relaxation rate of the O(2,3) $\vec{Ho}$ $\mid\mid$ bond axis resonance as described in the text. Only the ratio $^{63}W_{1c}/^{17}W_{1c}$ is the same on either side of the superconducting transition temperature.

There are several important caveats about the above results. First, the ratios we have taken involve three different samples: ^{63}W1 in Sample X, ^{17}W1 in Sample OX, and ^{89}W1 in Sample K. We have also measured ^{63}W1 in both Sample OX and Sample K, and then used these results in the four ratios. This changes the absolute values of these ratios slightly, but ^{63}W1c/^{17}W1c is still the only ratio which is the same at 101 K and 77 K.

The second caveat is that these results are all for the strong field case (Ho=81 kGauss). We have shown in the earlier part of this chapter that there is no appreciable field effect on ^{63}W1 at 77 K (other than $T_c(\vec{Ho})$), but it is possible that ^{17}W1 or ^{89}W1 could exhibit such an effect.

The third caveat is that we have measured the Y relaxation rate and lineshape in another sample (Sample Z, which is the aligned version of the Y41 powder). The Y lineshape is more asymmetric and the relaxation time is about 25% longer at 77 K for Sample Z than for Sample K, even though their copper spectra and relaxation rates are quite similar. The Y data may be much more sensitive to small variations in oxygen content or homogeneity, perhaps reflecting a large contribution to the relaxation rate which is not intrinsic to the best samples.

Section 7g. Single Sample Study of Cu(2) Anisotropy

As is shown in Figure 55 at the end of Section 7d, we obtained a different low T/T_c behavior of the ratio ^{63}W1a/^{63}W1c depending on whether we used $^{63}W1c_{NMR}$ or $^{63}W1c_{NQR}$. This unusual behavior could not be clearly identified as an extra field dependence (in addition to $T_c(\vec{Ho})$) of ^{63}W1c because we had used two different samples for the NMR and NQR

experiments.

To clear up this uncertainty, it was necessary to measure the NMR and NQR data in a single sample. J. A. Martindale led an experiment which measured the field dependence of ^{63}W1a and ^{63}W1c in Sample K, below T~100 K.[15,16]

The first results obtained were taken in the lowest fields possible, since these data should come closest to the behavior of the superconducting state in the absence of an applied field. This is important because many theoretical calculations of superconducting state properties (e. g. the dynamic spin susceptibility $\chi(\vec{q},\omega)$) are made in the zero-field limit. Another argument for emphasizing the lowest field relaxation rate results is that an applied magnetic field could provide another relaxation mechanism below T_c, for example the normal cores of fluxoids could in principle affect the overall relaxation rate.[46]

After we had obtained $^{63}W1c_{NQR}$(Ho=0 kGauss) and $^{63}W1a_{NMR}$(Ho=4.5 kGauss) for Sample K following the procedures in Sections 7d-7e, J. A. Martindale measured $^{63}W1a_{NMR}$(Ho=83 kGauss), $^{63}W1c_{NMR}$(Ho=41 kGauss), and $^{63}W1c_{NMR}$(Ho=41 kGauss) in this same sample. We present all of the data in Figure 58.

When we plot the ratio $^{63}W1a_{NMR}$(T,Ho=4.5 kGauss)/$^{63}W1c_{NQR}$(T,Ho=0 kGauss) versus temperature in Figure 59, two features are striking. First, there is definitely a drop in this ^{63}W1a/^{63}W1c ratio just below T_c ($0.8<T/T_c<1$), which is consistent with our previous strong field results presented in Section 7c. Second, for low T/T_c, this anisotropy ratio increases, actually surpassing the normal state anisotropy value. This result is in contradiction with the ^{63}W1a(Ho=81 kGauss)/^{63}W1c(Ho=81

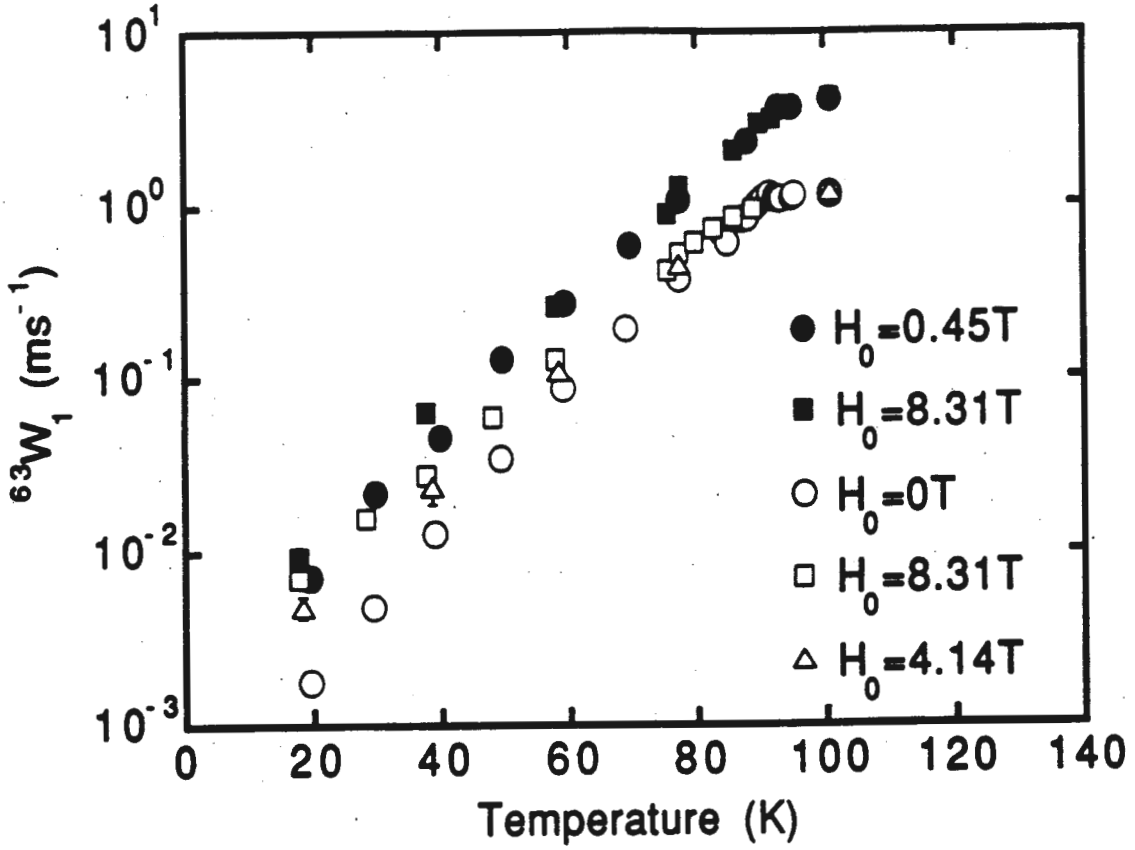

Figure 58. The $^{63}Cu(2)$ spin-lattice relaxation rate $^{63}W_{1\alpha}$ versus temperature for several applied fields in Sample K.[16] The filled circles are $^{63}W_{1a}$ data taken in a 4.5 kGauss magnetic field parallel to the $\hat{a}$-axis. The filled squares are $^{63}W_{1a}$ data taken in an 83.1 kGauss magnetic field parallel to the $\hat{a}$-axis. The open circles are $^{63}W_{1c}$ data taken in the absence of a magnetic field (NQR). The open squares are $^{63}W_{1c}$ data taken in a 83.1 kGauss magnetic field parallel to the $\hat{c}$-axis. The open triangles are $^{63}W_{1c}$ data taken in a 41.4 kGauss magnetic field parallel to the $\hat{c}$-axis. The zero-field transition temperature of this sample is $T_c(Ho=0)$ = 93 K.

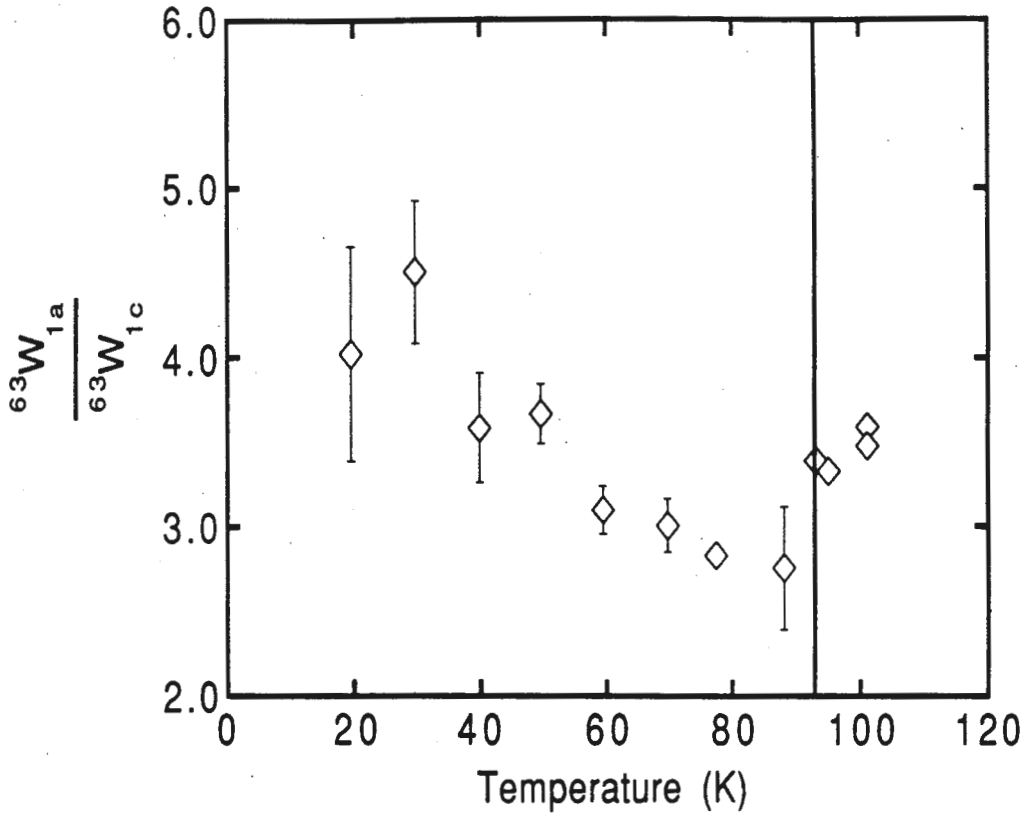

Figure 59. The open diamonds are the Sample K data for the ratio $^{63}W1a_{NMR}(T,Ho=4.5\ kGauss)/^{63}W1c_{NQR}(T,Ho=0\ kGauss)$ versus temperature. The vertical solid line is at Tc = 93 K (the small reduction of Tc for the $^{63}W1a_{NMR}$ measurement caused by the application of the 4.5 kGauss field along the CuO_2 planes is neglected).

kGauss) data in Section 7c, but it would be consistent with the ^{63}W1a(Ho=81 kGauss)/^{63}W1c(Ho=0 kGauss) ratio plotted in Figure 55 of Section 7d. Apparently ^{63}W1c has an additional field dependence (besides $T_c(\vec{Ho})$) below T/T_c~0.8.

This conclusion is convincingly demonstrated by J. A. Martindale's field dependence results shown in the Figures 60 and 61. ^{63}W1a may have some additional field dependence at low T/T_c, but the effect for ^{63}W1c is much larger. Some insight into the nature of this extra field dependence may be gained by plotting the relaxation rate at T/T_c~0.2 versus applied field. As we see in Figure 62, ^{63}W1c(Ho) is a linear function of the applied field.

Recently, M. Takigawa et al., intrigued by a preprint which contained the results described in Sections 7b-7f, have also performed low field measurements of ^{63}W1a/^{63}W1c, and have graciously shared their data with us prior to publication.[130] Their measurements agree with our results, as is seen in Figure 63. We now turn to an analysis of our nuclear spin-lattice relaxation rate measurements.

Section 7h. Analysis of W1(T,Ho) Data

The main result of the previous sections is the sudden drop in the ratio ^{63}W1a/^{63}W1c just below T_c ($0.8<T/T_c<1$), which we have found to be independent of field. As we discussed in Section 7a, within a one-component model, the planar nuclear relaxation rates W1 are given by:

$$(7\text{-}8) \qquad {}^{i}\left(\frac{1}{T1}\right)_{\alpha} = \left(\frac{{}^{i}\gamma_n^2 \, k_B T}{2\,\mu_\beta^2}\right) \mathrm{Lim}_{\omega\to 0} \sum_{\vec{q},\alpha'\neq\alpha} \left|{}^{i}A_{\alpha'\alpha'}(\vec{q})^2\right| \frac{\left\{\chi''_{\alpha'\alpha'}(\vec{q},\omega)\right\}}{\omega}$$

Hammel et al.'s ^{63}W1c/^{17}W1c measurement[90,91] was interpreted as evidence

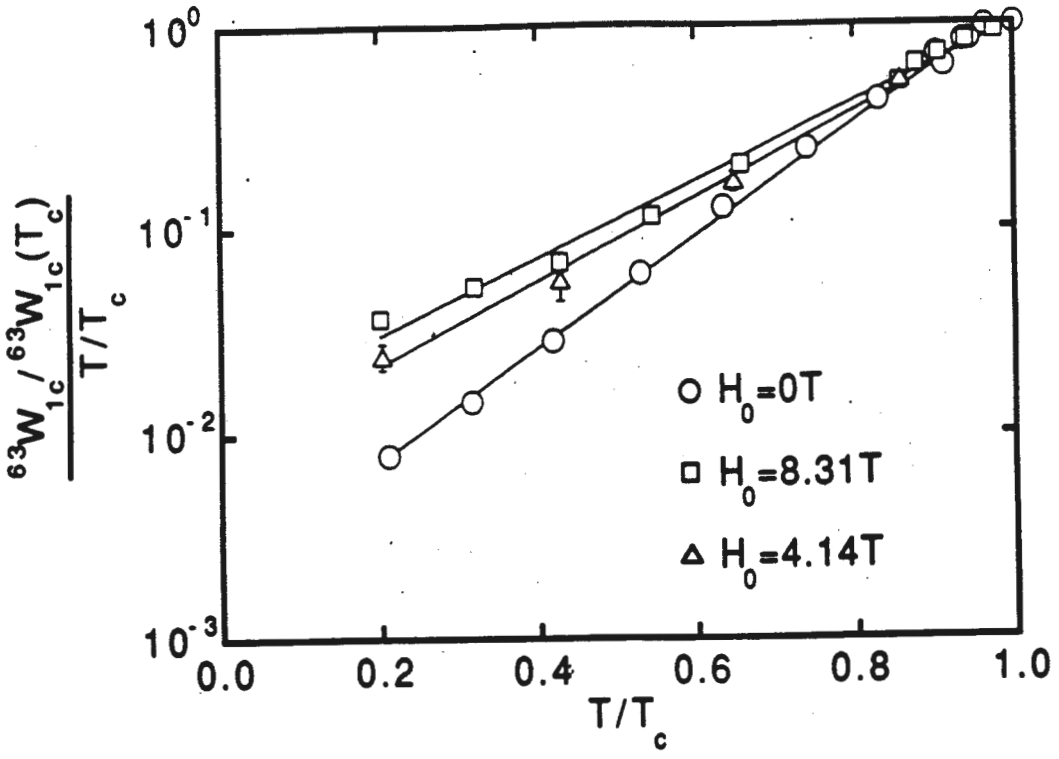

Figure 60. The normalized ^{63}Cu(2) spin-lattice relaxation rate $^{63}W_{1c}/^{63}W_{1c}(T_c(\vec{Ho}))$ divided by $T/T_c(\vec{Ho})$ versus $T/T_c(\vec{Ho})$ in Sample K.[16] The open circles are $^{63}W_{1c}$ data taken in the absence of a magnetic field (NQR). The open squares are $^{63}W_{1c}$ data taken in a 83.1 kGauss magnetic field parallel to the $\hat{c}$-axis. The open triangles are $^{63}W_{1c}$ data taken in a 41.4 kGauss magnetic field parallel to the $\hat{c}$-axis.

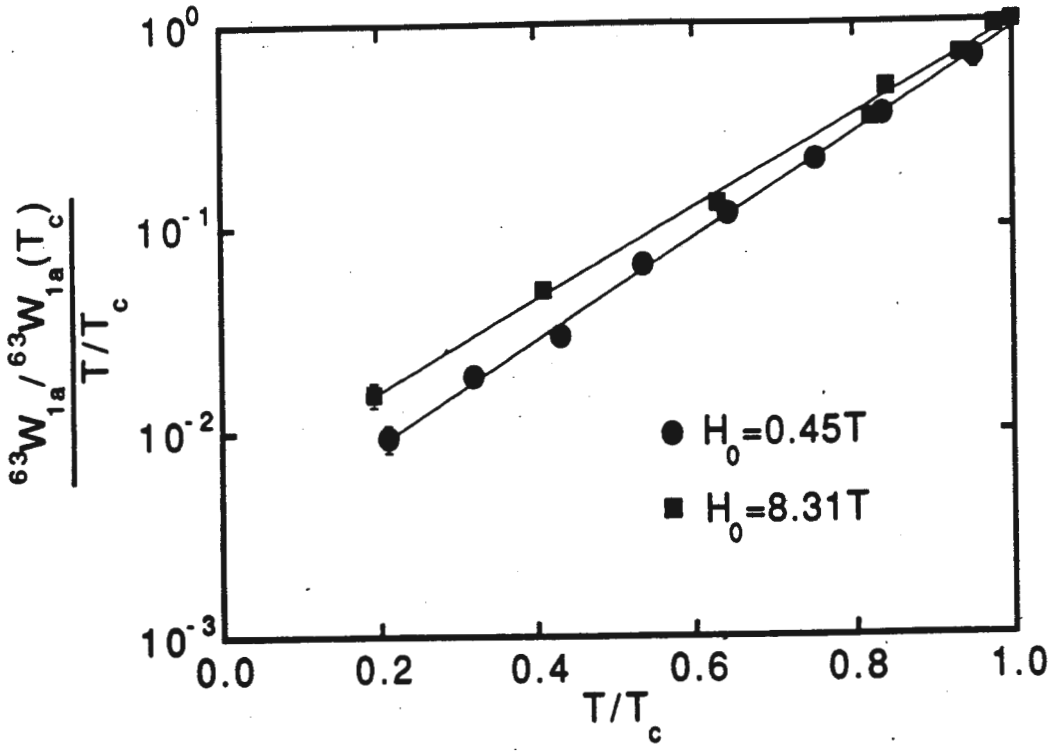

Figure 61. The normalized ^{63}Cu(2) spin-lattice relaxation rate $^{63}W_{1a}/^{63}W_{1a}(T_c(\vec{Ho}))$ divided by $T/T_c(\vec{Ho})$ versus $T/T_c(\vec{Ho})$ in Sample K.[16] The filled circles are $^{63}W_{1a}$ data taken in a 4.5 kGauss magnetic field parallel to the $\hat{a}$-axis. The filled squares are $^{63}W_{1a}$ data taken in an 83.1 kGauss magnetic field parallel to the $\hat{a}$-axis.

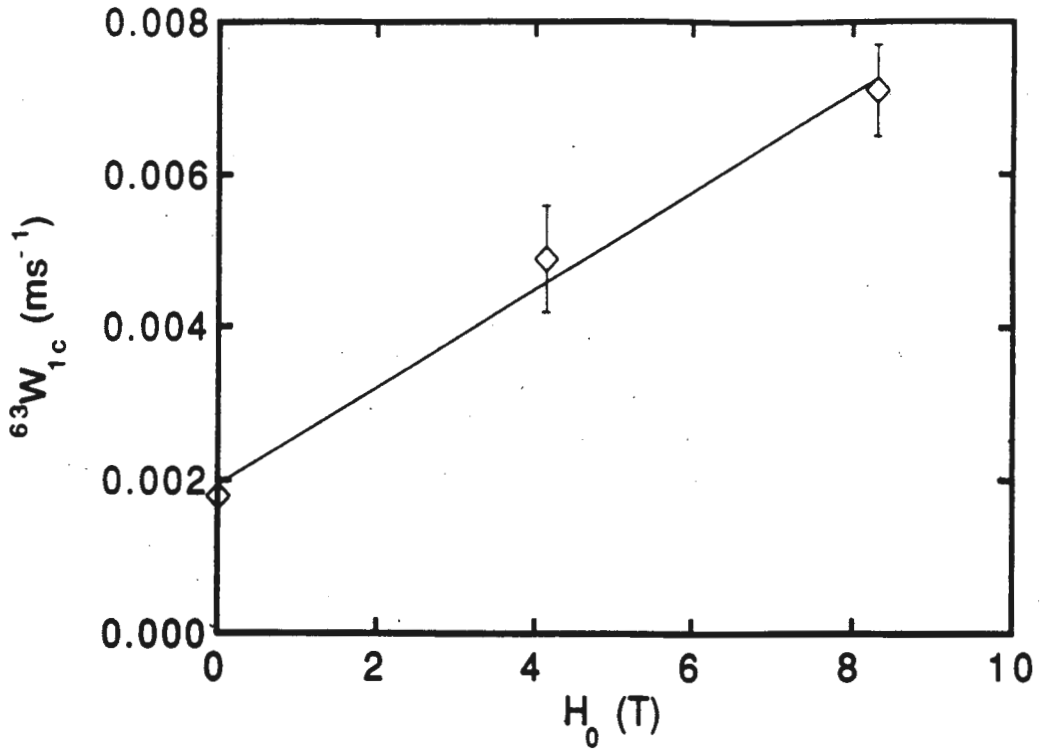

Figure 62. The spin-lattice relaxation rate $^{63}W_{1c}$ as a function of magnetic field (in Tesla) applied along the $\hat{c}$-axis at $T/T_c \approx 0.2$.[16]

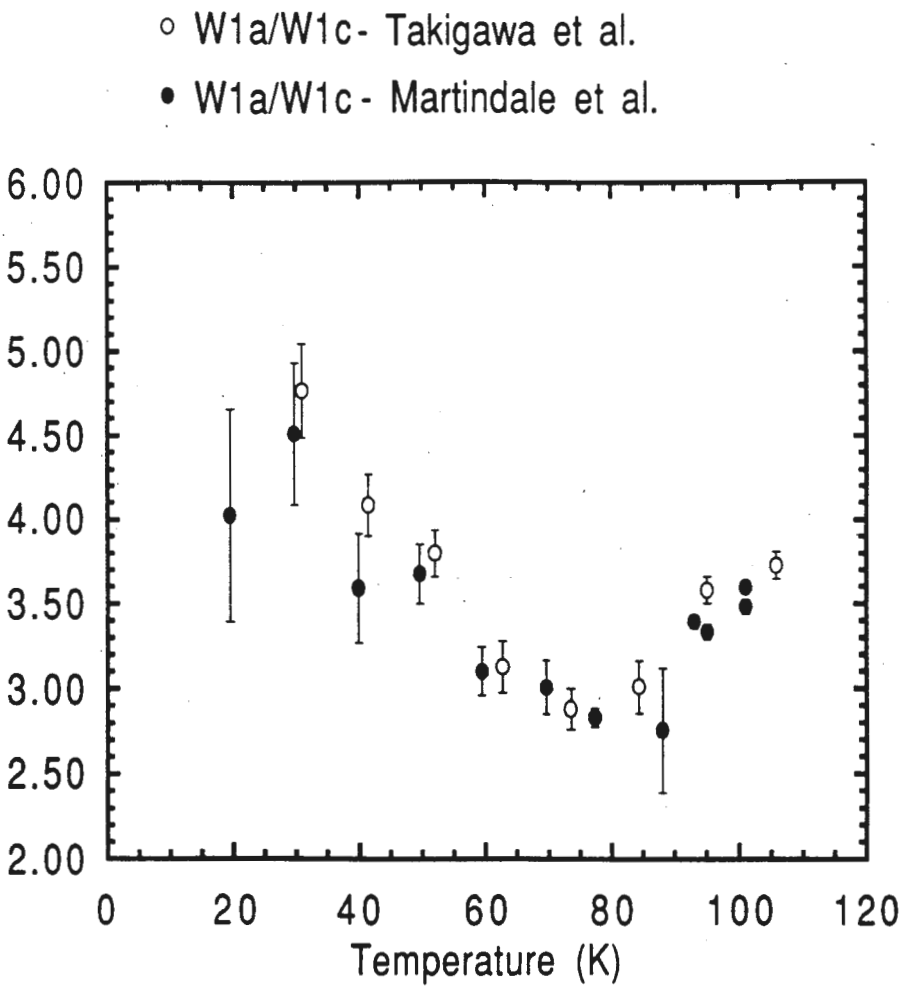

Figure 63. The filled circles are the weak field $^{63}W_{1a}/^{63}W_{1c}$ data described in the text.[16] The empty circles are the weak field $^{63}W_{1a}/^{63}W_{1c}$ data obtained by Takigawa et al..[130]

that below ~120 K (where $^{63}W1c \sim 19*(^{17}W1c)$), the $\vec{q}\approx 0$ and $\vec{q}\approx\vec{Q}$ regions of $\chi''_{\alpha\alpha}(\vec{q},\omega)$ shared the same temperature dependence, while above this crossover temperature they did not (where $^{63}W1c \approx A + BT$ while $^{17}W1c = CT$). In this simplest picture of the superconducting state spin susceptibility, we can write:

$$\chi''_{\alpha\alpha}(\vec{q},\omega,T<T_c) = F(T/T_c) * \chi''_{\alpha\alpha}(\vec{q},\omega,T=T_c), \tag{7-9}$$

where $F(T/T_c)$ contains all of the superconducting state temperature dependence. If we were to plug this expression into the above formula for W1, the $F(T/T_c)$ function would factor out to the front and would disappear in any ratio of two relaxation rates. Therefore all relaxation rate ratios should be independent of T/Tc, but our measurements have shown that this is not the case. This naive picture of the effect of superconductivity on $\chi''_{\alpha\alpha}(\vec{q},\omega,T=T_c)$ must be incorrect.

To explain our early results in Sections 7b-7f, we considered several generalizations of the simplest picture for $\chi''_{\alpha\alpha}(\vec{q},\omega,T<T_c)$. In order to do this quantitatively, we adopted the viewpoint of a particular one-component susceptibility model, that proposed by A. Millis, H. Monien, and D. Pines (MMP).[4,131] This phenomenological model proposed a form for the $\chi''_{\alpha\alpha}(\vec{q},\omega,T>T_c)$ which did an excellent quantitative job of fitting the normal state data. We discuss the parameters of their model in Appendix E.

The first phenomenological generalization of $\chi''_{\alpha\alpha}(\vec{q},\omega,T<T_c)$ which we attempted involved breaking spin-rotation invariance. In particular, we considered the case, $\chi''_{aa}(\vec{q},\omega,T<T_c) = \chi''_{bb}(\vec{q},\omega,T<T_c) \neq \chi''_{cc}(\vec{q},\omega,T<T_c)$. MMP have pointed out to us that this hypothesis would be consistent with a BCS spin-triplet pairing state,[118] while the Knight shift data (Section 6e) seem to require a spin-singlet pairing state. Nevertheless, they agree that an

anisotropy in $\chi''_{\alpha\alpha}(\vec{q},\omega,T<T_c)$ which is much larger near $\vec{q}\sim\vec{Q}$ then near $\vec{q}\sim(0,0)$ might be possible in principle. We explored this possibility in a calculation that invoked an anisotropic antiferromagnetic correlation length. We allowed $\xi_{||}/a$ to vary relative to $\xi_{\perp}/a$ below T_c. The details are in Appendix F. The relevant result for ^{63}W1a/^{63}W1c vs. $\xi_{||}/a$ is shown in Figure 64. By design, $\xi_{\perp}/a(T<T_c)= \xi_{\perp}/a(T=T_c)$, so ^{63}W1c/^{17}W1c remains a constant below T_c. In order to explain ^{63}W1c/^{89}W1c, we need to have interplane spin correlations developing, since the yttrium is relaxed by the CuO_2 planes above and below it. This toy calculation can explain the quantitative results we obtain, but it has the unsatisfactory feature that there is no obvious microscopic justification for breaking spin-rotation invariance in this way.

We next investigated an MMP-suggested generalization of $\chi''_{\alpha\alpha}(\vec{q},\omega,T<T_c)$ which retained spin-rotation invariance. [132] The idea was that the parameter β, which measures the contribution of the $\vec{q}\sim\vec{Q}$ region relative to the $\vec{q}\sim(0,0)$ part of $\chi''_{\alpha\alpha}(\vec{q},\omega,T<T_c)$, becomes temperature dependent. In order to explain the constant value of ^{63}W1c/^{17}W1c, the isotropic ξ/a must also depend on temperature. The motivation for this suggestion was that some sort of $\vec{q}$-dependent BCS energy gap (e.g. d-wave) would effectively change the shape of $\chi''_{\alpha\alpha}(\vec{q},\omega,T<T_c)$ in $\vec{q}$-space, and this toy calculation would simulate this effect. The detailed calculation was carried out with the assistance of Dr. C. A. Klug, and it is presented in Appendix G. The result for ^{63}W1a/^{63}W1c is shown in Figure 65. Our original calculation was unable to explain the temperature dependence of the strong field (Ho=81 kGauss) data. This generalization would also require the development of interplane spin correlations to explain the ^{63}W1c/^{89}W1c ratio.

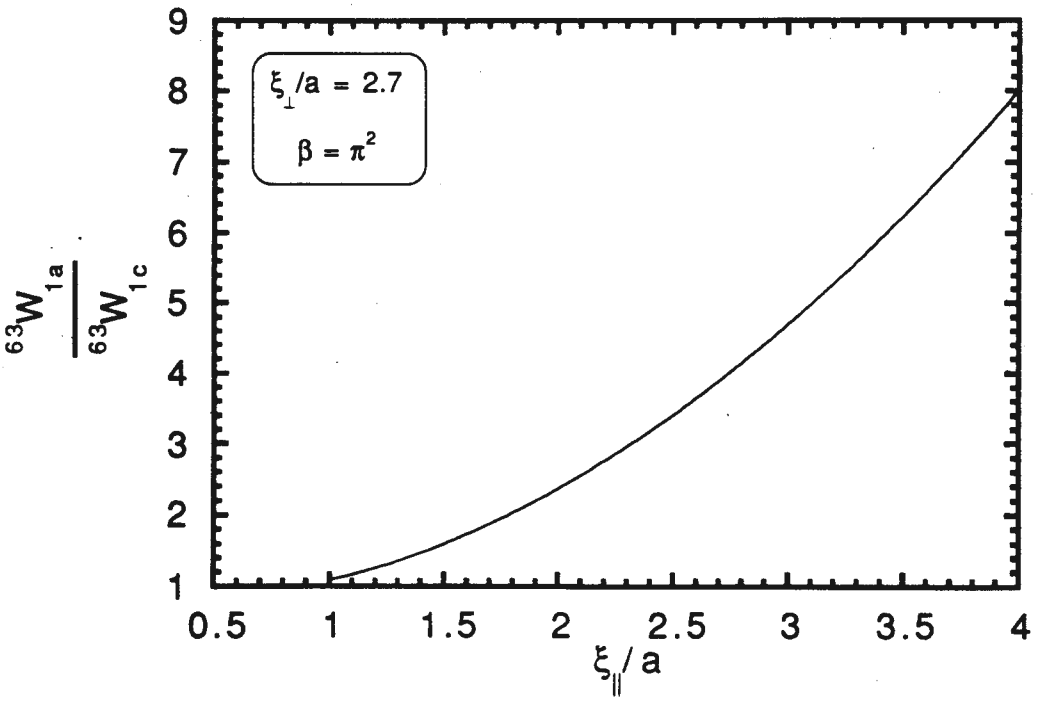

Figure 64. The solid curve is the dependence of $^{63}W_{1a}/^{63}W_{1c}$ on $\xi_{||}/a$, as is calculated in Appendix F.

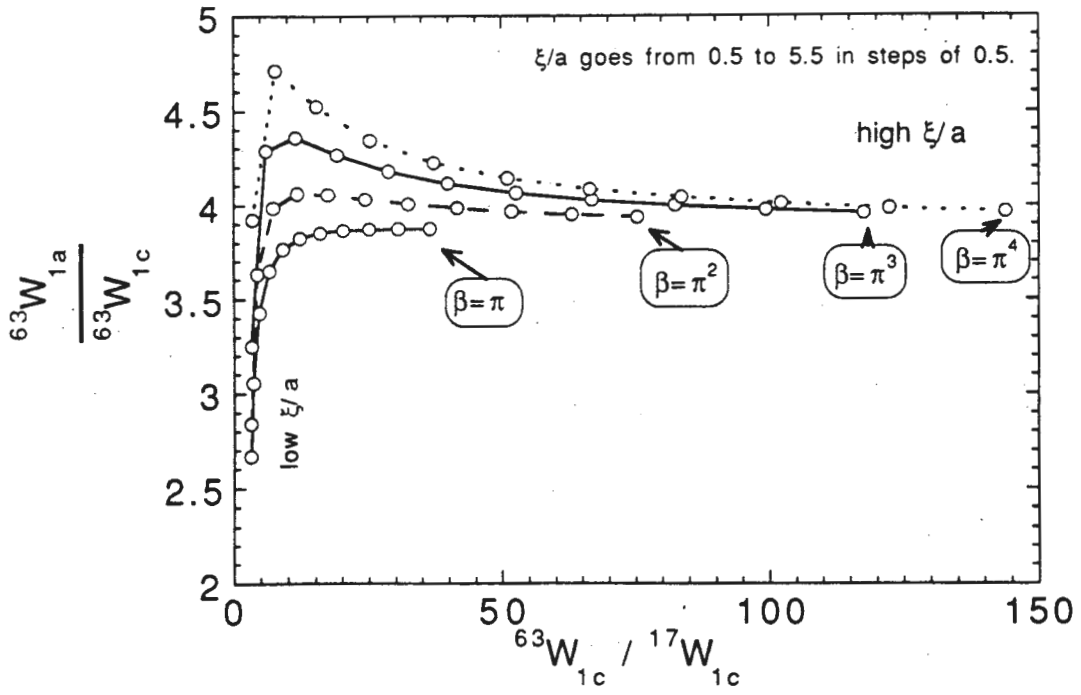

Figure 65. The $^{63}Cu(2)$ relaxation rate anisotropy ratio, $^{63}W_{1a}/^{63}W_{1c}$, versus the $^{63}Cu(2)$ to $^{17}O(2,3)$ relaxation rate ratio, $^{63}W_{1c}/^{17}W_{1c}$. This plot is the result of the calculation presented in Appendix G. There are four curves with different powers of π for β. The open circles along each curve occur every time the isotropic ξ/a increases by 0.5 as it varies from 0.5 to 5.5.

A third explanation we considered for the data of Sections 7b-7f was an orbital relaxation mechanism. This idea, proposed by Millis, Monien, and Pines, is that there is an additional magnetic mechanism for nuclear spin-lattice relaxation below T_c that is anisotropic and has a different temperature dependence from the electron spin induced relaxation rate.[132] Since the relaxation is so fast in the normal state, this orbital relaxation idea does not seem likely, but it cannot be ruled out.

The fourth explanation is that the application of the magnetic field affects the relaxation rate ratios, above and beyond the field dependent $Tc(\vec{Ho})$, which we are already taking into account. We have already shown that this is not the case in the region where $^{63}W1a/^{63}W1c$ drops sharply ($0.8<T/T_c<1$), but this does occur for low values of T/T_c.[15,16]

To summarize, we had tried several simple generalizations of $\chi''_{\alpha\alpha}(\vec{q},\omega,T<T_c)$, to explain our early data (Sections 7b-7f), but none of these potential explanations were completely satisfying.

The recent Martindale et al. data (Section 7g) have changed this situation.[15,16] J.P. Lu at Illinois[18] and N. Bulut and D. Scalapino at Santa Barbara[17] have independently proposed a novel explanation for the lowest field $^{63}W1a/^{63}W1c$ data. This explanation assumes that the one-component model for the normal state susceptibility is modified by a generalized BCS pairing theory below T_c. The complete BCS susceptibility expression is used in their calculations, which includes the pair creation and annihilation terms. They restrict their consideration to spin-singlet states, to be consistent with the Knight shift results. Both s-wave and d-wave orbital pairing states are considered, and they attempt to fit both $^{63}W1\alpha$ and $^{63}W1a/^{63}W1c$. In order to get the temperature dependence of $^{63}W1\alpha(T/T_c)$ right, temperature

dependent energy level broadening is assumed. A unique feature of this system is that the ^{63}Cu(2) nuclei couple to the Cu(2) electron spins with both an anisotropic on-site and an isotropic nearest neighbor transferred hyperfine coupling.[97] As both groups show, this last point makes the ratio ^{63}W1a/^{63}W1c a very sensitive probe of the $\vec{q}$-dependence of the energy gap. They conclude that the sharp drop in ^{63}W1a/^{63}W1c we observed just below T_c reveals the importance of the BCS coherence factors and requires nodes in the gap (as in d-wave pairing).

In Figure 66, we plot our low field ^{63}W1a/^{63}W1c data along with the theoretical calculations. Lu's d-wave calculation for $\Delta(\vec{q},T)=\Delta(T)(\cos q_x-\cos q_y)$, which assumed a Fermi liquid form for $\chi''_{\alpha\alpha}(\vec{q},\omega)$, clearly explains the drop below T_c, but fails to fit the low temperature increase.[18] Both groups find that in order to fit the whole data set ($0<T/T_c<1$), they need to include an antiferromagnetic enhancement of $\chi''_{\alpha\alpha}(\vec{q},\omega)$, as is required by the normal state data. The d-wave fits of Bulut and Scalapino[17] as well as Lu and Pines[19] which include this enhancement are shown in the figure. These calculations strongly imply that $YBa_2Cu_3O_7$ is a superconductor with a BCS spin-singlet pairing state and with nodes in the energy gap (e.g. orbital d-wave).

The interesting feature of the above calculations is that this anisotropy ratio ^{63}W1a/^{63}W1c could reveal nodes in the gap at temperatures very close to T_c. Typically, only the extremely low temperature data from such measurements as the Knight shift $K^S(T)$, the penetration depth $\lambda(T)$, and the lower critical field $H_{c1}(T)$ are considered probes of the presence of nodes in the gap. As we discuss in Martindale et al., the low temperature data from these experiments are often cited as evidence for s-wave pairing in $YBa_2Cu_3O_7$.[24] However, we have already seen (Section 6f) that the Knight shift data favor s-

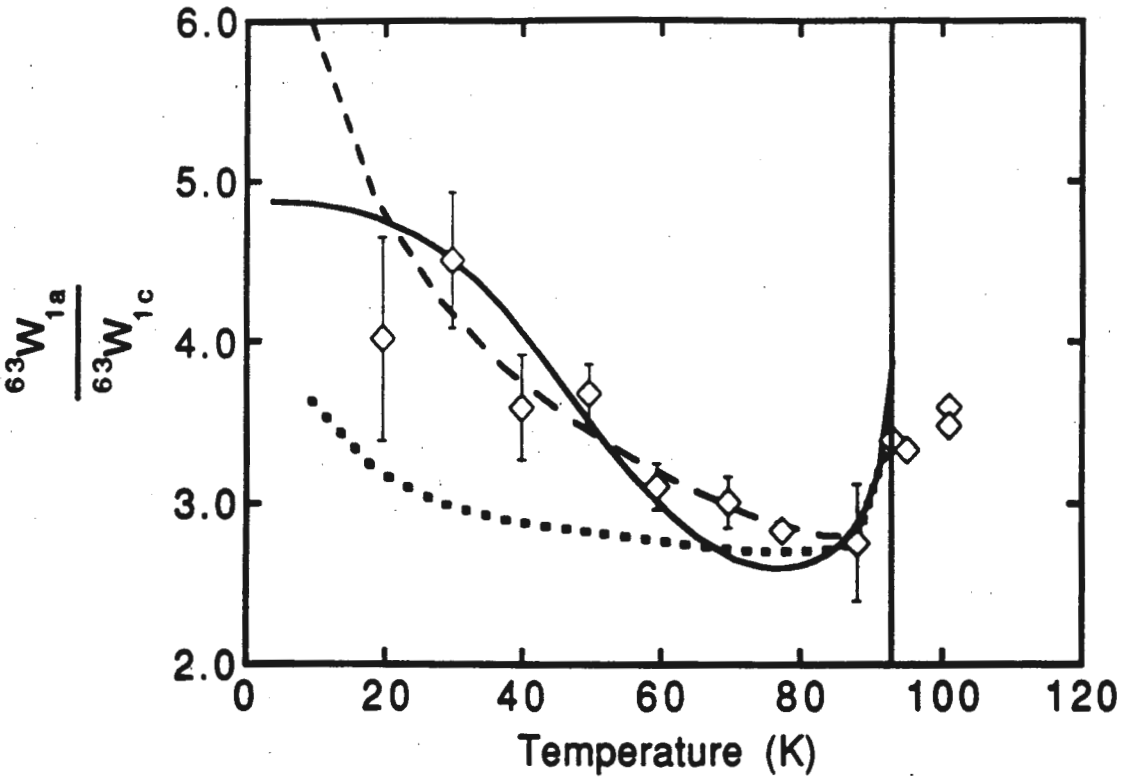

Figure 66. The open diamonds are the weak field $^{63}Cu(2)$ $^{63}W_{1a}/^{63}W_{1c}$ data versus temperature shown in Figure 59. The dotted line is Lu's d-wave fit to the data assuming a Fermi liquid form for the normal state spin susceptibility.[18] The dashed line is the d-wave fit of Lu and Pines[19] and the solid line is the d-wave fit of Bulut and Scalapino[17]. These last two fits include an antiferromagnetic enhancement of the normal state $\chi''_{\alpha\alpha}(\vec{q},\omega)$, as is required by the normal state data.[16]

wave pairing, but these data do not exclude from consideration higher even-l pairing states. In addition, analysis of the penetration depth measurements show that $\Delta\lambda_{ab}\sim T^2$ at low temperatures, a result which is difficult to interpret as favoring either s-wave or d-wave pairing.[133] Measurements of $H_{c1}(T)$ were fitted with an s-wave BCS calculation; however it is unclear whether a d-wave fit is ruled out by the data.[134] Thus the low temperature probes of nodes in the gap have not been able to answer clearly whether any nodes exist, so the orbital pairing state in $YBa_2Cu_3O_7$ seems to be an open question.[28] Perhaps our recent experiments will help to resolve this dilemma.

We now turn to a discussion of the low temperature field dependence of $^{63}W1c(T/T_c)$ observed by J. Martindale. The fact that $^{63}W1c(Ho)$ is a linear function of Ho suggests that there is some contribution to the relaxation rate due to the normal cores of fluxoids. Prof. Slichter has suggested a mechanism for this effect which can explain the magnitude of this extra relaxation. For his explanation, the nuclei in a normal core would relax at the rate characteristic of the normal state at that temperature. The next step would be either a rapid spin-diffusion of magnetization towards the cores to establish a common spin temperature, or the vortices move rapidly over all of nuclei establishing a common spin temperature. After this initial adjustment of the spin system, the magnetization relaxes with a common relaxation rate. We have indeed observed at low temperatures in a magnetic field a very fast relaxation recovery right after the spin system is prepared, followed by a much slower apparently single W1 relaxation recovery. It is not obvious that this behavior is consistent with either a spin-diffusion or a vortex motion model.

There have been other observations of field dependent relaxation rates

in the superconducting state of Type II BCS superconductors.[46] The explanations for these experiments invoked thermally activated vortex fluctuations or spin-diffusion. The former explanation is expected to be a very small effect compared to what we observe in this system. The latter explanation was refuted by an experiment of Genack and Redfield, which demonstrated that spin-diffusion in the presence of a field gradient due to a fluxoid lattice was unlikely to continue for very long.[135] There is no adequate explanation for field-dependent relaxation rates in the mixed state at the present time.

There is an important implication of a field dependent $^{63}W1_{\alpha}$(Ho). Unless we understand the mechanism for this field dependence, it is probably safe to assume that there is also a field dependence of $^{17}W1$ and $^{89}W1$, which may be quite different from $^{63}W1$(Ho). Thus any conclusions about the intrinsic behavior of $\chi''_{\alpha\alpha}(\vec{q},\omega)$ below T_c which are based on the the ratio of strong field W1 measurements (e.g. $^{63}W1c/^{17}W1c$)[90,91] may need to be re-examined.

Chapter 8. Conclusions

Our measurements of the ^{63}Cu Knight shift and $^{63}Cu(2)$ relaxation rate below T_c place important constraints on theoretical descriptions of the electronic spin system of $YBa_2Cu_3O_7$.

We have analyzed our data within the framework of a generalized BCS pairing theory. Unfortunately, at the present time there are no detailed predictions of NMR results for the more exotic theories of superconductivity (e.g. anyons).

Starting with the one-component model for the normal state electronic spin susceptibility in the CuO_2 planes, we find that our Knight shift data are consistent with a spin-singlet pairing state. The temperature dependence for the Cu(1) and Cu(2) site Knight shift is slightly different. The energy gap for the Cu(2) site seems to have a temperature dependence consistent with strong coupling. The size of the energy gap depends sensitively on which orbital-pairing state is assumed, but it is always larger than the weak coupling BCS gap.

The sharp drop in the planar copper spin-lattice relaxation rate anisotropy just below T_c has been interpreted as evidence for nodes in the spin-singlet pairing gap (e.g. orbital d-wave pairing). The absence of the Hebel-Slichter coherence peak is then explained by strong pair-breaking, but the presence of the coherence factors is revealed in the behavior of $^{63}W1a/^{63}W1c$ just below T_c. The low temperature behavior of $^{63}W1a/^{63}W1c$ has been interpreted as evidence for the persistence of antiferromagnetic correlations into the superconducting state. We have also observed a field dependence in $^{63}W1c$ at low temperatures which implies that the relaxation

rates at these temperatures should be measured in the smallest fields possible.

It is interesting to note that calculations by Monthoux et al.[136] and Moriya et al.[137] have shown that a generalized BCS pairing which is mediated by antiferromagnetic spin fluctuations would require spin-singlet, orbital d-wave (or higher L) pairing states.

The actual mechanism of High-T_c superconductivity in $YBa_2Cu_3O_7$ is not yet known, but any potential explanation must be reconciled with the strong constraints our experiments place on the behavior of the electronic spin system below T_c.

Appendix A. ^{17}O Enrichment

As we saw in Figure 1, there are four different oxygen sites in $YBa_2Cu_3O_7$, both in the planes (O(2,3)) and outside of them (O(1) and O(4)). This fact makes the investigation of the NMR properties of the oxygen nuclei an appealing prospect. Unfortunately, there is only a single oxygen isotope with a nuclear magnetic moment (^{17}O), and its natural abundance is quite small (0.037 %). In order to study the oxygen sites in this material with NMR, it is necessary to isotopically enrich a sample with ^{17}O.

We have successfully enriched a sample (Sample OX) with ^{17}O using a homemade exchange apparatus and enrichment procedure.

There were several constraints on our exchange apparatus design. The steep price and limited availability of ^{17}O gas restricted our gas supply to a few 0.1 liter vials of 40% enriched oxygen. A successful exchange is believed to require taking the sample to elevated temperatures (~900 Celsius) for extended periods of time.[87,88,89] The surface of $YBa_2Cu_3O_7$ is known to react with many materials in these conditions.[138]

After several preliminary attempts, we arrived at the final exchange apparatus design shown in Figure 67. Only a single 0.1 liter container of isotopically enriched gas is used in each exchange. This quantity of gas yields approximately one atmosphere of pressure in the exchange apparatus at 900 Celsius. The gas circulator and the cold trap were included to reduce moisture and impurities in the gas near the sample. The platinum foil boat which supported the $YBa_2Cu_3O_7$ powder pellet was the least reactive surface we could find. In operation, only the quartz tubing was inserted in a furnace, while the remainder of the apparatus stayed at room temperature. This

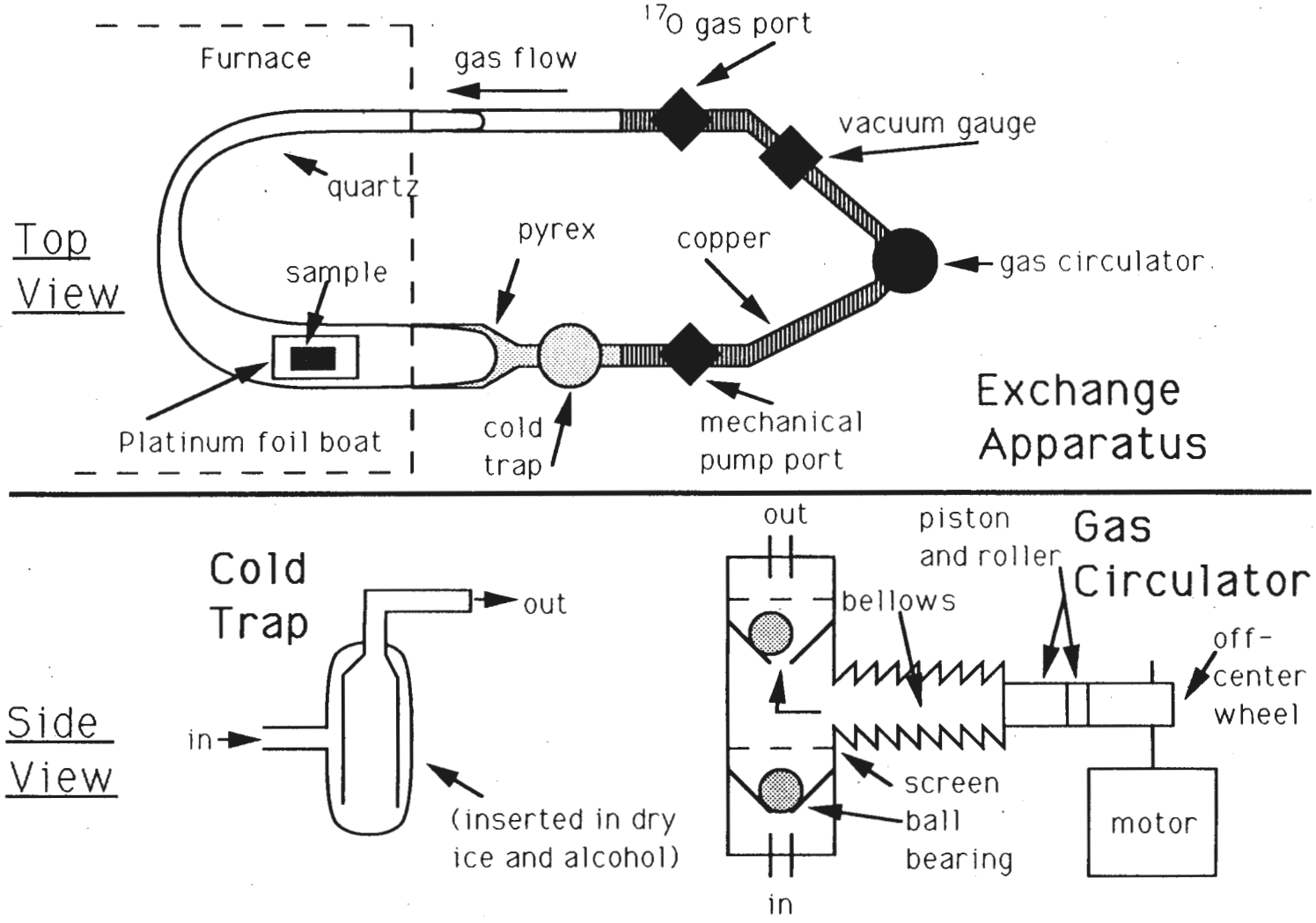

Figure 67. (Top): Schematic top view of the homemade ^{17}O enrichment apparatus. **(Bottom)**: Side view of the pyrex cold trap and the Durand gas circulation pump. The sealed pump was constructed using copper metal.

apparatus could be disassembled at the quartz/pyrex, the pyrex/copper, and the copper/quartz joints.

The temperature profile that Sample OX was subjected to during its enrichment is shown in Figure 68. The procedure started by placing 600 mg of loose $YBa_2Cu_3O_7$ powder on the platinum boat. The apparatus was sealed, and placed in the furnace. During the first part of the procedure, denoted by T1 in the figure, the mechanical pump kept the apparatus evacuated. At the beginning of time period T2, the pumping was stopped and the ^{17}O-enriched gas was drawn into the apparatus by collecting it in the cold trap using liquid nitrogen. The liquid nitrogen was then removed and the gas was free to circulate in the chamber. At the beginning of time period T3, the ^{17}O-enriched gas was drawn back into its container using liquid nitrogen. Then, the apparatus was disassembled and the sample was removed.

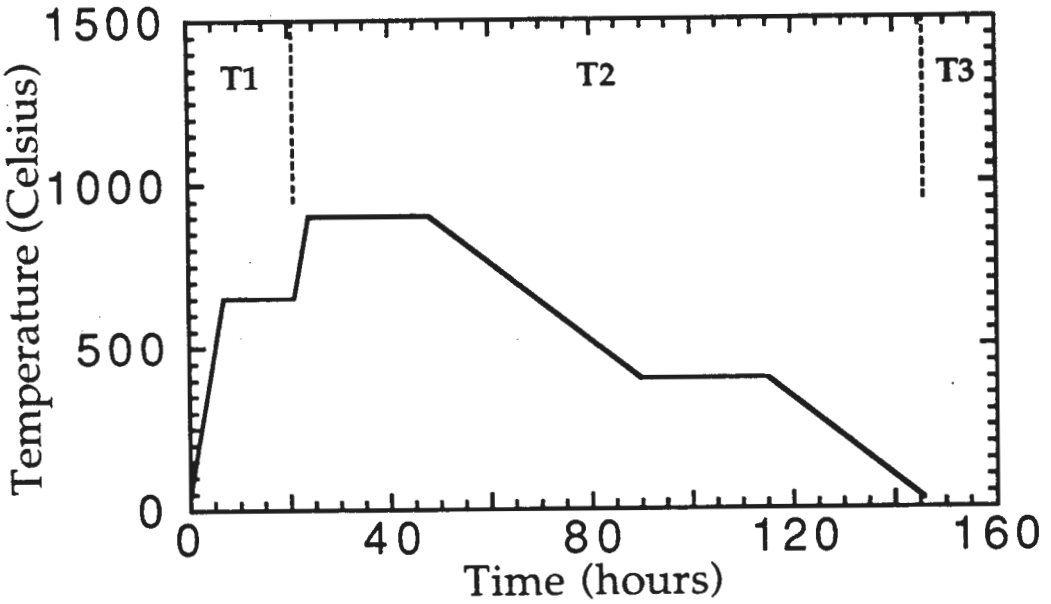

Figure 68. The temperature profile versus time of some $YBa_2Cu_3O_7$ powder during our ^{17}O enrichment procedure. This particular powder was used in Sample OX. During the time period T1, the sample apparatus was evacuated by a mechanical pump. During the time period T2, the sample apparatus contained approximately one atmosphere of 40% ^{17}O enriched oxygen gas. During the time period T3, the apparatus was opened and the sample was recovered.

Appendix B. Diagonalizing the Static Nuclear Spin Hamiltonian

In Chapter 3 the relevant nuclear spin Hamiltonian for the nuclei we have studied in this material was introduced in Equation (3-1). The energy levels of a given nucleus are determined by a magnetic dipolar (Zeeman) term and an electric quadrupolar term (where we define the coordinate axes (x,y,z) to be the principal axes of the electric field gradient tensor):

$$\hat{\mathbf{H}} = -\frac{\gamma_n}{2\pi} h\hat{I}_\alpha (1 + K_{\alpha\alpha}) Ho_\alpha + \frac{h}{2I(2I-1)}\left[\nu_{zz}\left(3\hat{I}_z^2 - \hat{I}^2\right) + \left(\nu_{xx} - \nu_{yy}\right)\left(\hat{I}_x^2 - \hat{I}_y^2\right)\right] \quad \text{(B-1)}$$

The second term in this total Hamiltonian is only included for nuclei with spins I>1/2 (e.g. ^{63}Cu, ^{65}Cu, and ^{17}O, but not ^{89}Y). We consider in detail now the case of ^{63}Cu to understand how the NMR or NQR transitions may be calculated.

The ^{63}Cu nucleus has I=3/2. For the case of a strong magnetic field applied along the z-axis ($\vec{Ho} \,||\, \hat{z}$), the appropriate nuclear spin Hamiltonian is:

$$\hat{\mathbf{H}} = -h\frac{^{63}\gamma_n}{2\pi} Ho(1+{}^{63}K_{zz})\hat{I}_z + \frac{h}{6}\left[{}^{63}\nu_{zz}\left(\hat{I}_z^2 - \hat{I}^2\right) + \left({}^{63}\nu_{xx} - {}^{63}\nu_{yy}\right)\left(\hat{I}_x^2 - \hat{I}_y^2\right)\right]. \quad \text{(B-2)}$$

In this expression, $^{63}\gamma_n$ is the gyromagnetic ratio for the copper 63 isotope and h is Planck's constant. The z-component of the total magnetic shift tensor is $^{63}K_{zz}$. The electric field gradient tensor $^{63}\nu_{\alpha\alpha}$ (measured in MHz) is defined in terms of the electric potential at the nucleus, V, as:

(B-3) $$^{63}\nu_{\alpha\alpha} \equiv \left(\frac{e\,^{63}Q}{2h}\right)\left(\frac{\partial^2 V}{\partial_\alpha \partial_\alpha}\right), \qquad \text{(where } \alpha=x,y,z\text{)}.$$

In this expression, e is the charge of an electron and ^{63}Q is the electric quadrupole moment of the copper 63 isotope. Since we have chosen the axes (x,y,z) to coincide with the principal axes of the electric field gradient tensor, $^{63}\nu_{\alpha\beta} \equiv 0$ for $\alpha \neq \beta$. Now we have defined all of the terms in our Hamiltonian, and we can proceed with our analysis.

Our goal is straightforward. We wish to solve for the eigenvalues of Equation (B-2), since the magnetic transitions between the corresponding eigenstates give rise to our observed NMR (and NQR) signals. We can proceed with a perturbation theory approach or an analytic approach. We will consider the former first.

When the applied magnetic field is large (e.g. Ho=81 kGauss), the Zeeman term dominates our Hamiltonian. In this case, the electric quadrupole term may be treated as a perturbation. If we ignore the perturbation, the eigenstates of the Hamiltonian are the eigenstates of the operator $\hat{I}_z$, and they may be labeled by the eigenvalue of this operator: m_z (m_z = -3/2, -1/2, +1/2, +3/2). We define the frequency ν_o to be:

(B-4) $$\nu_o \equiv \frac{^{63}\gamma_n}{2\pi}(1 + {}^{63}K_{zz})\,Ho.$$

We can see in Figure 69 that the Zeeman Hamiltonian alone yields three magnetic transitions all occurring at frequency ν_o. The inclusion of the quadrupole term as a perturbation modifies this result. The first and second order corrections to the transition frequencies are shown in Figure 69. There

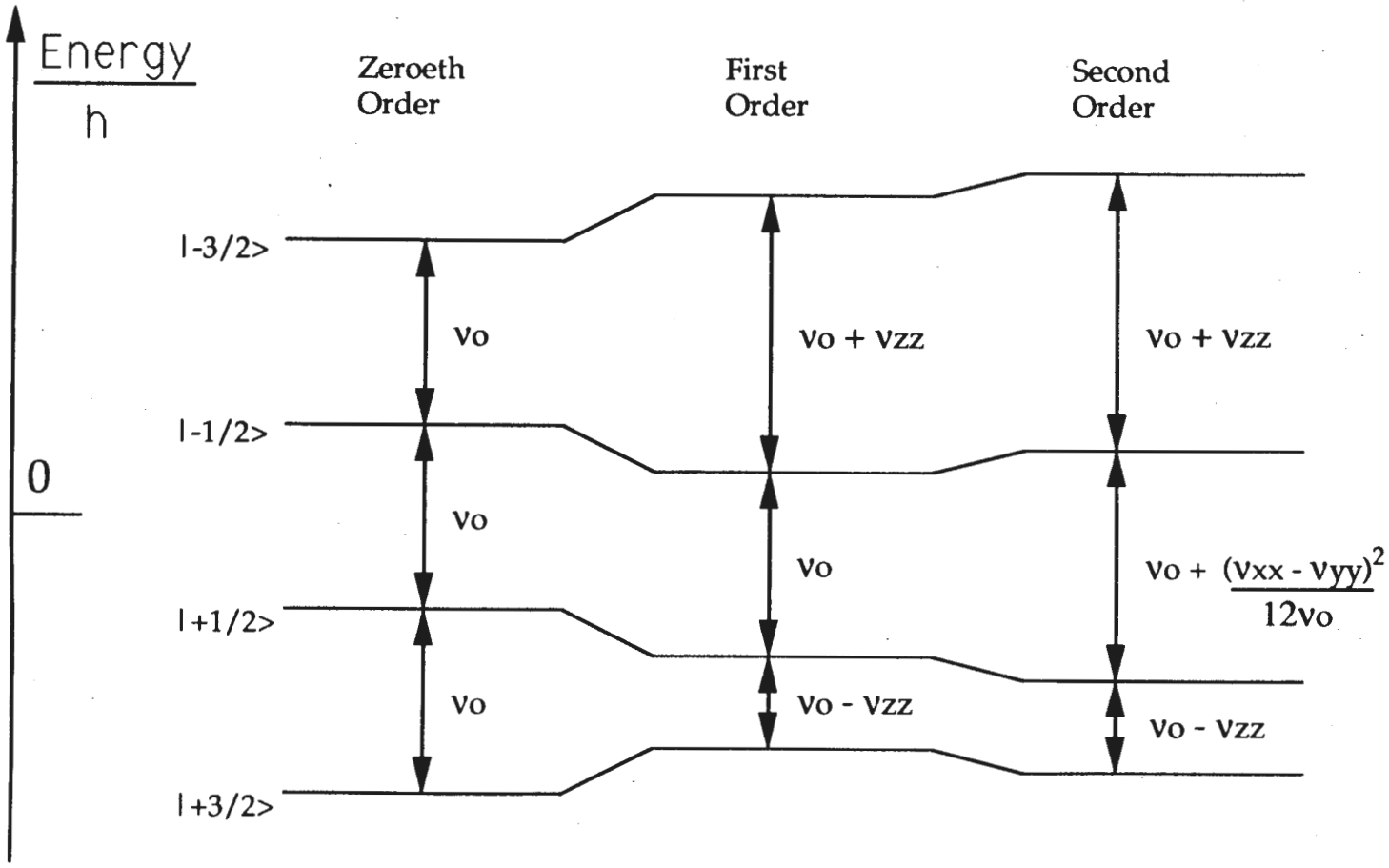

Figure 69. The allowed NMR transitions for the case of a spin-3/2 nucleus in a strong magnetic field applied along the z-axis. By treating the quadrupolar interaction as a perturbation to the dominant Zeeman interaction, we see the effect on the transitions to second order.

are now three distinct resonance frequencies, which are conventionally referred to as the lower satellite transition ($\nu_{lower} = \nu_o - \nu_{zz}$), the central transition ($\nu_{central} = \nu_o + \frac{(\nu_{xx} - \nu_{yy})^2}{12\nu_o}$), and the upper satellite transition ($\nu_{upper} = \nu_o + \nu_{zz}$). We have dropped the superscript referring to the isotope for brevity. This result gives the flavor of the result for the ^{17}O nucleus, although since the oxygen is spin-5/2, there is one central transition and four satellites. The result for the ^{89}Y nucleus (spin-1/2, so no quadrupole term) is much simpler, since there is only a single transition.

We have also diagonalized Equation (B-2) analytically, solving for the exact values of the allowed transition frequencies. We used matrix notation assuming the basis set of the operator $\hat{I}_z$. For this assumption, an arbitrary state Ψ ($\Psi = a|-3/2\rangle + b|-1/2\rangle + c|+1/2\rangle + d|+3/2\rangle$) may be written in the matrix notation as:

(B-5) $$\Psi = \begin{pmatrix} a \\ b \\ c \\ d \end{pmatrix}$$

This choice of a basis set makes the Hamiltonian matrix fairly easy to diagonalize. Our eigenvalue problem:

(B-6) $$\hat{H}_{mn} \Psi = E \Psi,$$

may be written in the matrix notation as:

$$(B\text{-}7)\quad \begin{pmatrix} \frac{3}{2}h\nu_o + \frac{1}{2}h\nu_{zz} & 0 & \frac{h}{2\sqrt{3}}(\nu_{xx} - \nu_{yy}) & 0 \\ 0 & \frac{1}{2}h\nu_o - \frac{1}{2}h\nu_{zz} & 0 & \frac{h}{2\sqrt{3}}(\nu_{xx} - \nu_{yy}) \\ \frac{h}{2\sqrt{3}}(\nu_{xx} - \nu_{yy}) & 0 & -\frac{1}{2}h\nu_o - \frac{1}{2}h\nu_{zz} & 0 \\ 0 & \frac{h}{2\sqrt{3}}(\nu_{xx} - \nu_{yy}) & 0 & -\frac{3}{2}h\nu_o + \frac{1}{2}h\nu_{zz} \end{pmatrix} \begin{pmatrix} a \\ b \\ c \\ d \end{pmatrix} = E \begin{pmatrix} a \\ b \\ c \\ d \end{pmatrix}.$$

When this eigenvalue problem is solved, it is convenient to define the quantity $\underline{\nu}\{\pm\}$:

$$(B\text{-}8)\qquad \underline{\nu}\{\pm\} \equiv \sqrt{\nu_o^2 + \left(\frac{\nu_{zz}}{2}\right)^2 \pm \nu_{zz}\nu_o + \left(\frac{\nu_{xx} - \nu_{yy}}{2\sqrt{3}}\right)^2}.$$

We can then write the exact expressions for the copper NMR transition frequencies as:

$$(B\text{-}9a)\qquad \nu_{lower} = \nu_o - \underline{\nu}\{+\} + \underline{\nu}\{-\};$$

$$(B\text{-}9b)\qquad \nu_{central} = -\nu_o + \underline{\nu}\{+\} + \underline{\nu}\{-\};$$

$$(B\text{-}9c)\qquad \nu_{upper} = \nu_o + \underline{\nu}\{+\} - \underline{\nu}\{-\}.$$

Equation (B-9b) was used in our Knight shift experiment to determine the value of the Knight shift at each temperature.

Finally, we consider the interesting case of a Nuclear Quadrupole

Resonance (NQR) experiment. In the absence of an applied field Ho, the total nuclear spin Hamiltonian for the copper (spin-3/2) is just:

$$\hat{H} = \frac{h}{6}\left[{}^{63}\nu_{zz}\left(\hat{I}_z^2 - \hat{I}^2\right) + \left({}^{63}\nu_{xx} - {}^{63}\nu_{yy}\right)\left(\hat{I}_x^2 - \hat{I}_y^2\right)\right]. \tag{B-10}$$

This Hamiltonian has two doubly degenerate eigenstates (which in general are quite different from the strong field eigenstates), and the frequency separation between these eigenstates gives the NQR absorption frequency, ν_Q:

$$\nu_Q \equiv \sqrt{(\nu_{zz})^2 + \left(\frac{\nu_{xx} - \nu_{yy}}{\sqrt{3}}\right)^2}\,. \tag{B-11}$$

For the planar copper atom (Cu(2)), the electric field gradient tensor is axially symmetric about the $\hat{z}$-($\hat{c}$-) axis. This statement means that $\nu_{xx} = \nu_{yy}$. In this simple case, the Hamiltonian is directly proportional to $\hat{I}_z^2$. Thus, written in the basis set of $\hat{I}_z$, $|-3/2\rangle$ and $|+3/2\rangle$ are the first pair of degenerate eigenstates, and $|-1/2\rangle$ and $|+1/2\rangle$ are the second pair of degenerate eigenstates. The splitting between these two levels is given by the NQR resonance frequency. We see from Equation (B-10) that this frequency is just $\nu_Q = \nu_{zz}$ (i.e. 31.5 MHz).

Appendix C. Solving the Normal Modes Problem for the Relaxation Rates

We consider the following problem. The static nuclear spin Hamiltonian has been solved, giving rise to several eigenstates and eigenvalues. The equilibrium population of each eigenstate is given by the Boltzmann factor. At time t=0, we perturb the populations of some of the levels. We wish to solve for the time-dependent recovery to equilibrium of the nuclear spin system. For the case of I=1/2, this recovery is exponential, but for spins greater than 1/2, the time-dependent recovery is often multi-exponential.

In order to see how this general problem may be solved, we consider a specific example. The eigenvalues of a spin-3/2 nucleus (e.g. ^{63}Cu or ^{65}Cu) in the presence strong magnetic field applied along the $\hat{z}$-axis are essentially the eigenvalues of the $\hat{I}_z$ operator, provided the quadrupole perturbation is small. We treat the case of magnetic relaxation, which has been shown to be the mechanism for relaxation in $YBa_2Cu_3O_7$. This means that transitions between the various eigenstates are induced by the fluctuating magnetic fields present at the nucleus. For $YBa_2Cu_3O_7$, the Cu^{++} electronic spins are believed to be the source of these fluctuating magnetic fields. We further assume that the correlation time for these fluctuating magnetic fields (τ_o) is very short compared to the time scale of the NMR resonance frequency (ν_o), so that $\nu_o\tau_o \ll 1$. This condition has been shown to be satisfied in $YBa_2Cu_3O_7$.[43]

The assumptions listed above yield the situation depicted in Figure 70. The eigenstates are the basis set of $\hat{I}_z$, so magnetic transitions (induced by $h_x\hat{I}_x$ and $h_y\hat{I}_y$) are only allowed between neighboring states. For example, the time dependence of the population of the $|-1/2\rangle$ state ($N_{-1/2}$) is given by:

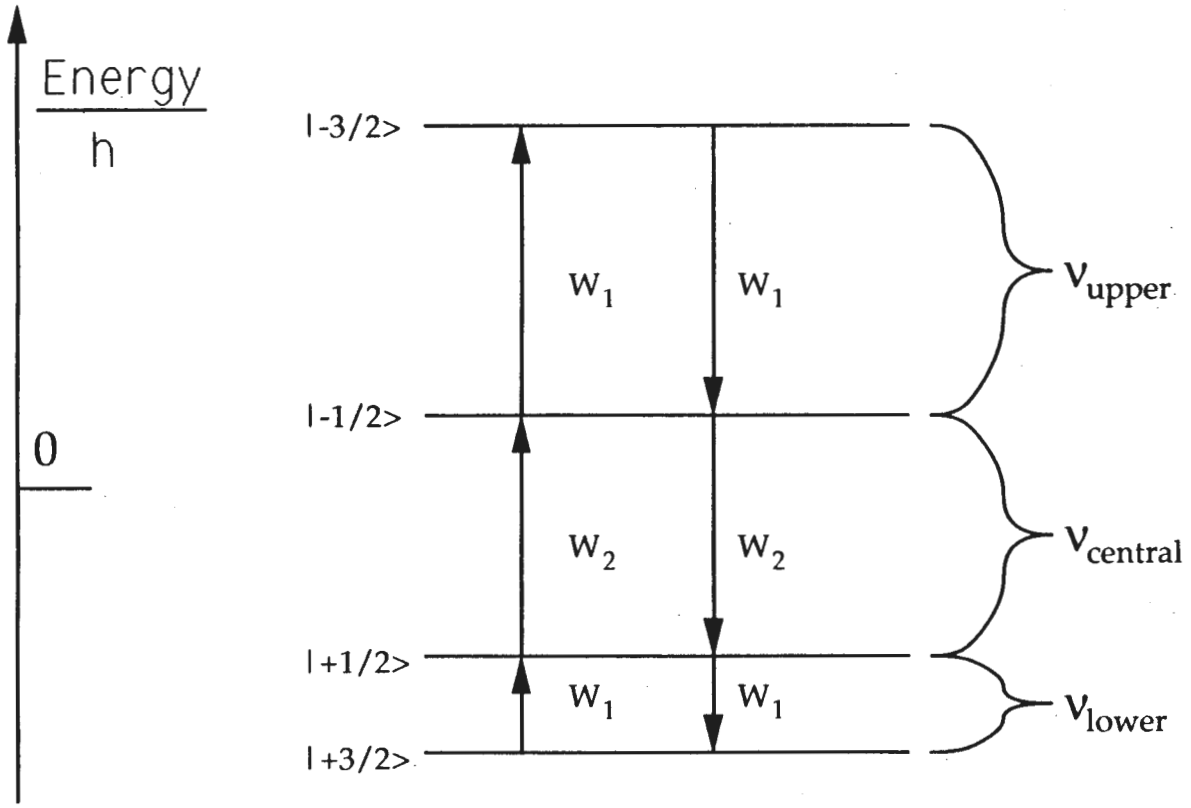

Figure 70. The allowed transitions induced by fluctuating magnetic fields in the short correlation time limit for the case of a spin-3/2 nucleus in a strong magnetic field applied along the z-axis. The primary effect of including a small quadrupole perturbation is that $\nu_{lower} \neq \nu_{central} \neq \nu_{upper}$. The fundamental rate is the same (W_1) for the upper and lower satellite transitions because $|\langle -3/2|\hat{I}^-|-1/2\rangle|^2 = |\langle +1/2|\hat{I}^-|+3/2\rangle|^2 \propto W_1$.

$$\text{(C-1)}\quad \frac{dN_{-1/2}}{dt} = +(W_{1\downarrow})\,N_{-3/2} - (W_{1\uparrow} + W_{2\downarrow})\,N_{-1/2} + (W_{2\uparrow})\,N_{+1/2}.$$

We can cast the problem in a useful way by writing Equation (C-1) at thermal equilibrium:

$$\text{(C-2)}\quad \frac{dN_{-1/2eq}}{dt} \equiv 0 = +(W_{1\downarrow})\,N_{-3/2eq} - (W_{1\uparrow} + W_{2\downarrow})\,N_{-1/2eq} + (W_{2\uparrow})\,N_{+1/2eq}.$$

We define the deviation from thermal equilibrium population of level α to be $n_\alpha \equiv N_\alpha - N_{\alpha,eq}$. Subtracting Equation (C-2) from Equation (C-1), we obtain the expression for the time dependence of the deviations from thermal equilibrium:

$$\text{(C-3)}\quad \frac{dn_{-1/2}}{dt} = +(W_{1\downarrow})\,n_{-3/2} - (W_{1\uparrow} + W_{2\downarrow})\,n_{-1/2} + (W_{2\uparrow})\,n_{+1/2}.$$

We can follow the same procedure for the populations of the other eigenstates, and we end up with four coupled linear equations.

These equations can be expressed concisely using matrix notation, where we define:

$$\text{(C-4)}\qquad \Psi = \begin{pmatrix} n_{-3/2} \\ n_{-1/2} \\ n_{+1/2} \\ n_{+3/2} \end{pmatrix}$$

In this notation, the four coupled linear equations giving the time dependence of the deviations from thermal equilibrium for each energy level may be written as:

$$\text{(C-5)}\quad \frac{d\Psi}{dt} = \begin{pmatrix} -W_1 & W_1 & 0 & 0 \\ W_1 & -(W_1 + W_2) & W_2 & 0 \\ 0 & W_2 & -(W_1 + W_2) & W_1 \\ 0 & 0 & W_1 & -W_1 \end{pmatrix} \Psi = \mathbf{M}\Psi.$$

For the temperatures of interest ($T \gg 10$ mK), we can set $W_\downarrow = W_\uparrow$. This

leading order approximation is justified since our assumption that the equilibrium population of each level is given by the Boltzmann factor implicitly includes the small difference between these rates ($W\downarrow, W\uparrow$).

We solve this problem by finding the normal modes of relaxation. In other words, we find the eigenvectors and eigenvalues of our matrix $\mathbf{M}$. These eigenvectors (ϕ_α) and eigenvalues (λ_α) are defined by the equations:

(C-6) $$\mathbf{M}\,\phi_\alpha = \lambda_\alpha \phi_\alpha, \qquad (\text{where } \alpha = 1 \ldots 4).$$

The benefit of this approach is that the state Ψ may be expressed at any arbitrary time in terms of these eigenvectors as:

(C-7) $$\Psi(t) = \sum_\alpha c_\alpha(t)\,\phi_\alpha.$$

Before solving for the eigenvectors (ϕ_α) of $\mathbf{M}$, we make use of the fact that our relaxation is magnetic and we are in the short correlation time limit. In this case, we know that:

(C-8) $$\frac{W_1}{W_2} = \frac{|\langle -3/2|\,\hat{I}^-\,|-1/2\rangle|^2}{|\langle -1/2|\,\hat{I}^-\,|+1/2\rangle|^2} = \frac{3}{4}.$$

We can now solve for the eigenvalues of matrix $\mathbf{M}$ in terms of a single parameter, W_1. When we do this, we obtain the following eigenvalues and eigenvectors:

(C-9) $\lambda_1 = 0$ $\lambda_2 = -2W_1$ $\lambda_3 = -2W_1/3$ $\lambda_4 = -4W_1$

(C-10)
$$\phi_1 = \begin{pmatrix} \frac{1}{2} \\ \frac{1}{2} \\ \frac{1}{2} \\ \frac{1}{2} \end{pmatrix} \quad \phi_2 = \begin{pmatrix} \frac{1}{2} \\ -\frac{1}{2} \\ -\frac{1}{2} \\ \frac{1}{2} \end{pmatrix} \quad \phi_3 = \begin{pmatrix} \frac{3}{2\sqrt{5}} \\ \frac{1}{2\sqrt{5}} \\ -\frac{1}{2\sqrt{5}} \\ -\frac{3}{2\sqrt{5}} \end{pmatrix} \quad \phi_4 = \begin{pmatrix} \frac{1}{2\sqrt{5}} \\ -\frac{3}{2\sqrt{5}} \\ \frac{3}{2\sqrt{5}} \\ -\frac{1}{2\sqrt{5}} \end{pmatrix}$$

We are now ready to solve for the time dependence of the deviation

from the thermal equilibrium population of each level. Substituting Equations (C-6) and (C-7) into Equation (C-5), we find that:

$$\text{(C-11)} \qquad \frac{d\Psi(t)}{dt} = \sum_{\alpha} \left(\frac{dc_\alpha(t)}{dt}\right)\phi_\alpha = \sum_{\alpha} c_\alpha(t)\ \mathbf{M}\ \phi_\alpha = \sum_{\alpha} \left(\lambda_\alpha\, c_\alpha(t)\right)\phi_\alpha .$$

This equation yields the time evolution of the various coefficients:

$$\text{(C-12)} \qquad c_\alpha(t) = c_\alpha(0)\, e^{\lambda_\alpha t} .$$

Now our problem is completely determined once we have the initial condition of the system.

We are now ready to look at some specific examples. We perturb the equilibrium populations at t=0, and let the system evolve back to its equilibrium configuration. In our notation,

$$\text{(C-13)} \qquad \Psi_{eq} = \Psi(t = \infty) = \begin{pmatrix} 0 \\ 0 \\ 0 \\ 0 \end{pmatrix}.$$

If we apply a 180° (or π) pulse to the central transition, we invert the populations of the $|-1/2\rangle$ and $|+1/2\rangle$ levels. This situation is experimentally attainable when the quadrupole interaction makes the upper and lower satellite frequencies sufficiently different. For example, the ^{63}Cu(2), $\vec{Ho} \,||\, \hat{z}$(or $\hat{c}$) central transition occurs at ~90 MHz for an 80 kGauss field, while the upper and lower satellite frequencies are ~120 MHz and ~60 MHz, respectively. Thus, when we invert the central transition's magnetization with a π pulse, the initial condition of the system is then:

$$\text{(C-14)} \qquad \Psi_{\pi,central}(t = 0) = \begin{pmatrix} 0 \\ +1 \\ -1 \\ 0 \end{pmatrix}.$$

The coefficients which describe this initial condition may be found by projecting (C-14) onto our eigenvector basis:

(C-15) $$c_\alpha(0) = (\phi_\alpha(0))^* \Psi_\pi(t = 0).$$

For instance,

(C-16) $$c_3(0) = \left(\frac{3}{2\sqrt{5}} \quad \frac{1}{2\sqrt{5}} \quad -\frac{1}{2\sqrt{5}} \quad -\frac{3}{2\sqrt{5}} \right) \begin{pmatrix} 0 \\ +1 \\ -1 \\ 0 \end{pmatrix} = \frac{1}{\sqrt{5}}.$$

In this way we find that the initial values of our coefficients are:

(C-17) $$c_1(0) = 0, \qquad c_2(0) = 0, \qquad c_3(0) = \frac{1}{\sqrt{5}}, \qquad c_4(0) = \frac{-3}{\sqrt{5}}.$$

The state of the system at all times after the initial π pulse has been applied to the central transition may now be obtained using Equations (C-7), (C-10), and (C-12):

(C-18) $$\Psi_\pi(t) = \frac{1}{\sqrt{5}} \begin{pmatrix} \frac{3}{2\sqrt{5}} \\ \frac{1}{2\sqrt{5}} \\ -\frac{1}{2\sqrt{5}} \\ -\frac{3}{2\sqrt{5}} \end{pmatrix} e^{-2W_1 t/3} + \left(\frac{-3}{\sqrt{5}} \right) \begin{pmatrix} \frac{1}{2\sqrt{5}} \\ -\frac{3}{2\sqrt{5}} \\ \frac{3}{2\sqrt{5}} \\ -\frac{1}{2\sqrt{5}} \end{pmatrix} e^{-4W_1 t}.$$

Experimentally, we sample the size of central transition's magnetization along the $\hat{z}$-axis (M(t)) at several different times following the application of the inversion pulse. One of those times is very long compared to the equilibration time of the system, and we take this magnetization to be the equilibrium magnetization (M(∞)). The quantity we typically plot is:

(C-19) $$M(t) - M(\infty) \propto n_{-1/2}(t) - n_{+1/2}(t).$$

Using Equation (C-18), we see that the time dependence of this quantity is given by:

$$M(t) - M(\infty) \propto (0.1)\, e^{-2W_1 t/3} + (0.9)\, e^{-4W_1 t}. \tag{C-20}$$

This equation shows that the relaxation recovery of the central transition's magnetization is multi-exponential following the application of an inversion pulse to only this transition. This form has been confirmed experimentally to describe the magnetization recovery of the copper nuclei in $YBa_2Cu_3O_7$.[43]

Another interesting experiment is the application of a π pulse to a satellite line (e.g. the upper satellite). In this case, the initial condition of the system is given by:

$$\Psi_{\pi,\text{upper}}(t = 0) = \begin{pmatrix} +1 \\ -1 \\ 0 \\ 0 \end{pmatrix}. \tag{C-21}$$

We can proceed with the same analysis outlined above, and we determine that the recovery of the upper satellite transition's magnetization is given by:

$$M(t) - M(\infty) \propto (0.5)\, e^{-2W_1 t} + (0.1)\, e^{-2W_1 t/3} + (0.4)\, e^{-4W_1 t}. \tag{C-22}$$

For the Cu(2) site in $YBa_2Cu_3O_7$, the electric field gradient tensor is axially symmetric about the $\hat{z}$-axis, so the eigenstates of the nuclear spin Hamiltonian in the absence of a magnetic field are just the same as the eigenstates in the presence of a strong magnetic field along the $\hat{z}$-axis. This situation (relevant for a nuclear quadrupole resonance experiment) was discussed at the end of Appendix B. We can therefore apply the above formalism to the problem of determining the NQR relaxation recovery behavior of the Cu(2) site. The application of a π pulse to the NQR absorption line inverts the populations of the $|-3/2\rangle$ and $|-1/2\rangle$ levels, while simultaneously inverting the populations of the $|+3/2\rangle$ and $|+1/2\rangle$ levels.

The initial condition of the system is then given by:

$$\Psi_{\pi,Cu(2),NQR}(t = 0) = \begin{pmatrix} +1 \\ -1 \\ -1 \\ +1 \end{pmatrix}. \qquad \text{(C-23)}$$

This is directly proportional to eigenvector ϕ_2, so we know immediately that the Cu(2) NQR spin-lattice relaxation recovery is given by the single exponential:

$$M(t) - M(\infty) \propto e^{-2W_1 t} . \qquad \text{(C-24)}$$

So, for the Cu(2) in a single sample of $YBa_2Cu_3O_7$, we may measure at one temperature in the normal state the relaxation recovery curve of several different transitions using an inversion recovery sequence. The time dependence of the data will be drastically different depending on whether we are measuring the NMR central transition, the NMR upper satellite transition, or the NQR transition (where the data $M(t) - M(\infty)$ will be fit by Equation (C-20), (C-22), or (C-24), respectively). Nevertheless, the values of the spin-lattice relaxation rate W1 obtained by fitting each data set with its appropriate theoretical curve are all the same within experimental error for T>Tc. This result has been confirmed by several groups.[43,82] The effect of strong magnetic fields on the superconducting state introduces complications, as we discuss in Chapter 7, and the NMR and NQR relaxation rates measured at the same temperature are no longer identical for T<Tc.

In this appendix, we have assumed that the strong field was along the $\hat{z}$-axis, so that transitions are induced by the fluctuating magnetic fields h_x and h_y. In general, these fluctuating magnetic fields may be anisotropic, so we need to keep track of the direction of the applied field relative to the crystalline axes. Therefore the spin-lattice relaxation rate measured with a

strong magnetic field applied along the $\hat{c}$-axis ($\hat{a}$-axis) will be referred to as W1c (W1a).

A general formula for the nuclear spin-lattice relaxation rate is given in Equations (3-10) and (7-1). For the copper nuclei, this general formula is related to the W_1 (e.g. W1c) discussed above by the relationship:

(C-25) $$^{63}\left(\frac{1}{T1}\right)_c \equiv \frac{2}{3} W1c.$$

Appendix D. Numerical Diagonalization and Relaxation Rates

We have seen in Appendix B and C that there are both perturbation theory and exact analytic approaches available to solve for the allowed NMR transition frequencies and for the time dependence of the corresponding relaxation recovery curves. However, we have only treated the case of a magnetic field applied along a principal axis of the electric field gradient tensor, in the limit that either the Zeeman term or the electric quadrupolar term, but not both, dominates the nuclear spin Hamiltonian. Experimentally, it is not always possible (or desirable) to work in the above limit. As a result, the actual eigenstates of the complete nuclear spin Hamiltonian can be quite different from the strong field eigenstates, and the previous approaches used to determine the allowed NMR transition frequencies and the time dependence of the corresponding relaxation recovery curves fail to be useful.

We can solve the most general problem numerically using a computer. Consider once again the specific case of the total nuclear spin Hamiltonian for the copper nucleus (spin-3/2):

$$\text{(D-1)} \quad \hat{H} = -h\frac{\gamma_n}{2\pi}\sum_{\alpha=x,y,z} Ho_\alpha(1+K_{\alpha\alpha})\hat{I}_\alpha + \frac{h}{6}\left[\nu_{zz}\left(\hat{I}_z^2-\hat{I}^2\right)+\left(\nu_{xx}-\nu_{yy}\right)\left(\hat{I}_x^2-\hat{I}_y^2\right)\right].$$

It is convenient to rewrite this expression using the conventional definition of the spherical coordinate angles θ,ϕ relative to the x,y,z ($\equiv$ a,b,c) axes. The components of the magnetic field Ho along the principal axes are:

$$\text{(D-2)} \quad Ho_x = Ho\cos(\phi)\sin(\theta),\ Ho_y = Ho\sin(\phi)\sin(\theta),\ Ho_z = Ho\cos(\theta).$$

We will again employ matrix notation to find the eigenstates and eigenvalues of this Hamiltonian, choosing as our basis set the eigenstates of the $\hat{I}_z$ operator. For this assumption, an arbitrary state Ψ ($\Psi = a|-3/2\rangle + b|-1/2\rangle +$

$c|+1/2> + d|+3/2>$) may be written in the matrix notation as:

$$\text{(D-3)} \qquad \Psi = \begin{pmatrix} a \\ b \\ c \\ d \end{pmatrix}$$

We define the frequency $\nu_o \equiv \frac{\gamma_n}{2\pi} Ho$ (note that this definition is different from the definition used in Equation (A-4) of Appendix B, since we are not including the magnetic shift yet). Our eigenvalue problem may now be written as:

$$\text{(D-4)} \qquad \hat{\mathbf{H}}_{mn} \Psi = E \Psi,$$

where $\hat{\mathbf{H}}_{mn}$ is the Hamiltonian matrix in our chosen basis. The matrix elements of $\hat{\mathbf{H}}_{mn}$ are straightforward to compute. The four (4 X 1) columns which make up $\hat{\mathbf{H}}_{mn}$ (from left to right) are listed below:

(D-5a) First column of $\hat{\mathbf{H}}_{mn}$ =

$$\begin{pmatrix} \frac{3}{2}h\nu_o\,(1 + K_{zz})\cos(\theta) + \frac{1}{2}h\nu_{zz} \\ \frac{-\sqrt{3}}{2}h\nu_o\{(1 + K_{xx})\cos(\phi)\sin(\theta) - i\,(1 + K_{yy})\sin(\phi)\sin(\theta)\} \\ \frac{h}{2\sqrt{3}}(\nu_{xx} - \nu_{yy}) \\ 0 \end{pmatrix}$$

(D-5b) Second column of $\hat{\mathbf{H}}_{mn}$ =

$$\begin{pmatrix} \frac{-\sqrt{3}}{2}h\nu_o\{(1 + K_{xx})\cos(\phi)\sin(\theta) + i\,(1 + K_{yy})\sin(\phi)\sin(\theta)\} \\ \frac{1}{2}h\nu_o\,(1 + K_{zz})\cos(\theta) - \frac{1}{2}h\nu_{zz} \\ -h\nu_o\{(1 + K_{xx})\cos(\phi)\sin(\theta) - i\,(1 + K_{yy})\sin(\phi)\sin(\theta)\} \\ \frac{h}{2\sqrt{3}}(\nu_{xx} - \nu_{yy}) \end{pmatrix}$$

(D-5c) Third column of $\hat{\mathbf{H}}_{mn}$ =

$$\begin{pmatrix} \frac{h}{2\sqrt{3}}(\nu_{xx} - \nu_{yy}) \\ -h\nu_o\{(1 + K_{xx})\cos(\phi)\sin(\theta) + i\,(1 + K_{yy})\sin(\phi)\sin(\theta)\} \\ -\frac{1}{2}h\nu_o\,(1 + K_{zz})\cos(\theta) - \frac{1}{2}h\nu_{zz} \\ \frac{-\sqrt{3}}{2}h\nu_o\{(1 + K_{xx})\cos(\phi)\sin(\theta) - i\,(1 + K_{yy})\sin(\phi)\sin(\theta)\} \end{pmatrix}$$

(D-5d) Fourth column of $\hat{\mathbf{H}}_{mn}$ =

$$\begin{pmatrix} 0 \\ \frac{h}{2\sqrt{3}}(\nu_{xx} - \nu_{yy}) \\ \frac{-\sqrt{3}}{2}h\nu_o\{(1 + K_{xx})\cos(\phi)\sin(\theta) + i\,(1 + K_{yy})\sin(\phi)\sin(\theta)\} \\ -\frac{3}{2}h\nu_o\,(1 + K_{zz})\cos(\theta) + \frac{1}{2}h\nu_{zz} \end{pmatrix}$$

We have used the conventional notation, $i=\sqrt{-1}$.

In order to determine the eigenstates of the nuclear spin Hamiltonian, we need to solve the eigenvalue problem given in Equation (D-4). We see from equation (D-5) that an analytic solution is quite daunting for the general case. However, for a specific case, we know the values of θ, ϕ, ν_o, $K_{\alpha\alpha}$, and $\nu_{\alpha\alpha}$, and we can evaluate all of the matrix elements of $\hat{H}_{mn}$ numerically. We now have a (4 X 4) Hermetian matrix with complex numbers for elements. The eigenvalue equation may now be solved using standard numerical techniques. We used the method of Jacobi transformations described in Chapter 11 of Numerical Recipes in Pascal.[139] We dealt with the problem of complex numbers by the method given in Section 11.4 of the same book.[139] The (4 X 4) complex eigenvalue problem (Equation (D-4)), written so that we emphasize the real and imaginary parts:

$$(D\text{-}6)\quad (\hat{H}_{mn,real} + i\,\hat{H}_{mn,imag.})\,(\Psi_{real} + i\,\Psi_{imag.}) = E\,(\Psi_{real} + i\,\Psi_{imag.}),$$

is the same as the (8 X 8) problem involving just real numbers:

$$(D\text{-}7)\quad \begin{pmatrix} \hat{H}_{mn,real} & -\hat{H}_{mn,imag.} \\ \hat{H}_{mn,imag.} & \hat{H}_{mn,real} \end{pmatrix} \begin{pmatrix} \Psi_{real} \\ \Psi_{imag.} \end{pmatrix} = E \begin{pmatrix} \Psi_{real} \\ \Psi_{imag.} \end{pmatrix}.$$

The one irritating side effect of doubling each dimension of the matrix (in order for the computer to handle the complex numbers) is that each eigenvalue of (D-7) is at least two-fold degenerate. If eigenvector $\begin{pmatrix} \Psi_{real} \\ \Psi_{imag.} \end{pmatrix}$ has eigenvalue E, then so does eigenvector $\begin{pmatrix} -\Psi_{imag.} \\ \Psi_{real} \end{pmatrix}$. These two eigenvectors are just Ψ and $i(\Psi)$. We only need to keep one eigenvector out of each of these pairs (i.e. 4 out of 8) to describe the four eigenstates of the total nuclear spin Hamiltonian.

Once we have the four eigenstates (Ψ_1 ... Ψ_4) and the associated

eigenvalues (E_1 ... E_4), we can find all of the possible NMR (or NQR) transitions induced by an applied alternating field ($\vec{H1}$). This involves evaluating matrix elements such as $|\langle\Psi_1|\vec{H1}\bullet\hat{I}|\Psi_2\rangle|^2$. If this matrix element is non-zero, then there is an observable transition at frequency $|E_1 - E_2|/h$, which has an intensity proportional to the size of the matrix element. The remaining allowed transitions may be found in the same way, by systematically stepping through all of the pairs of eigenstates.

At this point, our computer program is specialized to accomplish a specific task. When we are studying a uniaxially aligned powder sample, the observed lineshapes are restricted powder patterns (the c-axis of each crystallite is parallel to the c-axis of every other crystallite, but the a-axis of each crystallite is randomly oriented with respect to the a-axis of every other crystallite). We can calculate all of the allowed transitions that occur in such a sample by iterating through the above procedure, stepping systematically through all of the values of θ and ϕ that describe the experimental situation, and summing up all of the matrix elements at each frequency.

The total lineshape due to both copper isotopes and both copper sites may also be calculated. This is done by iterating through the above procedure, stepping systematically through the values of ν_o, $K_{\alpha\alpha}$, and $\nu_{\alpha\alpha}$, appropriate for each site and isotope, and summing up all of the matrix elements at each frequency. The Pascal program which accomplishes this for the copper sites in $YBa_2Cu_3O_7$ is called KaleidaPowderPattern.main.

We can also extend the above results to calculate the relaxation recovery behavior of any given transition. These numerical techniques were required for our weak field (4.5 kGauss) measurement of ^{63}W1a. For this application, we solve for the eigenstates (Ψ_1 ... Ψ_4) and the associated

eigenvalues (E_1 ... E_4) for a particular set of the parameters θ, ϕ, ν_o, $K_{\alpha\alpha}$, and $\nu_{\alpha\alpha}$. Then we calculate the intensity and frequency of the observable transitions as we described above.

The next step is to solve the normal modes problem, following the procedure given in Appendix C. Even though the relaxation mechanism is magnetic, the general normal modes problem can be quite complicated. This is because the exact eigenstates of the total nuclear spin Hamiltonian are linear combinations of the strong field ($\hat{I}_z$) eigenstates, and so transitions (in general) are possible between each pair of these eigenstates. Thus to find the normal modes of the system, we need to solve another complicated eigenvalue problem:

$$\begin{pmatrix} W_{11} & W_{12} & W_{13} & W_{14} \\ W_{21} & W_{22} & W_{23} & W_{24} \\ W_{31} & W_{32} & W_{33} & W_{34} \\ W_{41} & W_{42} & W_{43} & W_{44} \end{pmatrix} \Phi_\upsilon = \lambda_\upsilon \Phi_\upsilon, \quad \text{(where } \upsilon=1...4\text{)} \tag{D-8}$$

where we have used the exact eigenstates of the total nuclear spin Hamiltonian (Ψ_1 ... Ψ_4) as our basis set for the matrix. This problem looks much more difficult than the strong field case shown in Equation (C-5), but the computer can handle it. We now need to evaluate each of the above matrix elements, such as:

$$W_{12} \propto |\langle\Psi_1| h_x\hat{I}_x + h_y\hat{I}_y + h_z\hat{I}_z |\Psi_2\rangle|^2. \tag{D-9}$$

The fluctuating magnetic field components (h_α) are in general anisotropic. We can determine the ratios h_y^2/h_x^2 and h_z^2/h_x^2 using our knowledge of the strong magnetic field relaxation rate tensor, since each element of that tensor is given by:

(D-10) $$W_{1i} \propto (h_j^2 + h_k^2),$$

where i,j,k = x,y,z (=a,b,c) and cyclic permutations.

Thus, given the strong field relaxation rate tensor, we can evaluate matrix elements like Equation (D-9), plug them into the eigenvalue problem (D-8), and solve for the normal modes of relaxation (Φ_υ) and the associated fundamental rates (λ_υ). To determine the time dependence of the relaxation recovery of any given transition, we proceed as we did in Appendix C, by determining the initial condition of the system, and solving for the time dependent coefficients, $c_\upsilon(0)$. The time-dependent deviation from the thermal equilibrium population of any given eigenstate of the total nuclear spin Hamiltonian is obtained by looking at the appropriate row in the equation:

(D-11) $$\Psi(t) = \sum_{\upsilon} c_\upsilon(0)\, \phi_\upsilon\, e^{\lambda_\upsilon t}.$$

We are thus able to fit our M(t) - M(∞) data taken on any given transition for an arbitrary experimental set-up using Equation (D-11). However, we recall that the $c_\upsilon(0)$, ϕ_υ, and λ_υ appearing in Equation (D-11) were obtained using the strong field relaxation rate tensor in Equation (D-10). Each of these parameters could in general change if a different strong field relaxation rate tensor was inserted into Equation (D-10).

We will illustrate this dependence of the relaxation recovery expression on the strong field rates with a specific example. In a strong field $\vec{Ho} \perp \hat{c}$, there is only one observable resonance for the Cu(2) site, so W1a ≡ W1b. For the case of the Cu(2), $\vec{Ho} \perp \hat{c}$, weak field (4.5 kGauss) relaxation rate measurement described in Chapter 7, the conditions are such that the normal modes of relaxation are functions of the strong field relaxation rate anisotropy

ratio ($\phi_\upsilon = F_\upsilon(W1a/W1c)$). The associated fundamental relaxation rates are functions of both W1a and W1c ($\lambda_\upsilon = L_\upsilon(W1a/W1c, W1c)$). We used these facts to determine the strong field anisotropy ratio (W1a/W1c) in the weakest magnetic fields possible. We were able to do this by iterating through the above determination of ϕ_υ and λ_υ using a wide range of strong field ratios (W1a/W1c). The Pascal computer program which carried out this task is called PowderPattern.main.

The dependence of these quantities on W1a/W1c was then approximated by fitting the resulting functions with a polynomial (fourth order for ϕ_υ, second order for λ_υ). These interpolation formulas ($F_\upsilon(W1a/W1c)$ and $L_\upsilon(W1a/W1c, W1c)$) were then plugged into Equation (D-11). The value of W1c was taken from the NQR experiment at the same temperature, and the remaining free parameters (W1a/W1c and the magnitude of the inverted magnetiztion) were adjusted by the method of least squares to fit the magnetization recovery data. Dr. C. A. Klug's Pascal computer program which fit the low field data is called T1 Least Squares.Pas.

Appendix E. The Form of $\chi''_{\alpha\alpha}(\vec{q},\omega)$ Proposed by Millis, Monien, and Pines

The antiferromagnetic-Fermi-liquid theory of Millis, Monien, and Pines (MMP) is an attempt to reconcile all of the anomalous normal state NMR results using a one-component model for the spin-susceptibility of the CuO_2 planes. This phenomenological theory has been quite successful in quantitatively fitting the data for $YBa_2Cu_3O_7$.[4] With some modifications, their model has been used to fit the data for $YBa_2Cu_3O_{6.63}$ and $La_{1.85}Sr_{0.15}CuO_4$ as well.[131,140] We have attempted to extend their model to fit our superconducting state ^{63}W1a/^{63}W1c data quantitatively, inspired by the success of their model in describing the normal state data. The MMP description is not the only description of the normal state NMR data, but it was the model which was easiest for us to modify in an attempt to fit our superconducting state data quantitatively.

The MMP theory starts by assuming that there is one spin (S=1/2) per CuO_2 unit in the two-dimensional planes, which primarily resides on the Cu(2) site. The Mila-Rice hyperfine Hamiltonian:

$$\text{(E-1)}\ \sum_{i,\alpha} {}^{63}I_{i,\alpha}\, A_{\alpha\alpha}\, S_{i,\alpha} + \sum_{i,j,\alpha} {}^{63}I_{i,\alpha}\, B\, S_{j,\alpha} + \sum_{i,m,\alpha} {}^{17}I_{i,\alpha}\, C\, S_{m,\alpha} + \sum_{i,n,\alpha} {}^{89}I_{i,\alpha}\, D\, S_{n,\alpha},$$

(where $\alpha = (\hat{a},\hat{b},\hat{c}) = (\hat{x},\hat{y},\hat{z})$) is taken to be the correct expression for the coupling of each planar nucleus to the electronic spin degree of freedom. The on-site hyperfine coupling tensor for the Cu(2) is anisotropic, with $A_{cc} = A_{||}$ and $A_{aa}=A_{bb}=A_{\perp}$. The other three hyperfine couplings (B, C, and D) are assumed to be isotropic. The transferred hyperfine coupling term for the Cu(2) involves the sum over the four nearest neighbor Cu(2) sites (j) in the same CuO_2 plane. The transferred hyperfine coupling term for the O(2,3)

involves the sum over the two nearest neighbor Cu(2) sites (m) in the same CuO_2 plane. The transferred hyperfine coupling term for the Y involves the sum over the four nearest neighbor Cu(2) sites in the CuO_2 plane below and the four nearest neighbor Cu(2) sites in the CuO_2 plane above (n).

The nuclear spin-lattice relaxation rates of the planar nuclei arising from rapid fluctuations of the electronic spin-degree of freedom may now be calculated using Equation (7-1). The $\vec{q}$-dependent hyperfine form factors required in this expression follow from the assumed real-space hyperfine Hamiltonian (Equation (E-1)). Therefore the spin-lattice relaxation rates of the various nuclei are:

$$(E\text{-}2a)\quad {}^{63}W1c = \frac{6\pi}{8\mu_\beta^2 h}\lim_{\omega\to 0}\sum_{\vec{q}}\Big(\Big[A_\perp - 2B\{\cos(q_x a)+\cos(q_y a)\}\Big]^2 \mathcal{S}_\perp(\vec{q},\omega) + \Big[A_\perp - 2B\{\cos(q_x a)+\cos(q_y a)\}\Big]^2 \mathcal{S}_\perp(\vec{q},\omega)\Big),$$

$$(E\text{-}2b)\quad {}^{63}W1a = \frac{6\pi}{8\mu_\beta^2 h}\lim_{\omega\to 0}\sum_{\vec{q}}\Big(\Big[A_\parallel - 2B\{\cos(q_x a)+\cos(q_y a)\}\Big]^2 \mathcal{S}_\parallel(\vec{q},\omega) + \Big[A_\perp - 2B\{\cos(q_x a)+\cos(q_y a)\}\Big]^2 \mathcal{S}_\perp(\vec{q},\omega)\Big),$$

$$(E\text{-}2c)\quad {}^{17}W1c = \frac{6\pi}{8\mu_\beta^2 h}\lim_{\omega\to 0}\sum_{\vec{q}}\Big(\Big[2C_\perp^2\{1-\cos(q_x a)\}\Big]\mathcal{S}_\perp(\vec{q},\omega) + \Big[2C_\perp^2\{1-\cos(q_x a)\}\Big]\mathcal{S}_\perp(\vec{q},\omega)\Big),$$

$$(E\text{-}2d)\quad {}^{89}W1c = \frac{6\pi}{8\mu_\beta^2 h}\lim_{\omega\to 0}\sum_{\vec{q}}\Big(\Big[16D_\perp^2\{(1-\cos(q_x a))(1-\cos(q_y a))\}\Big] \times\Big(\cos^2\Big(\frac{q_z a}{2}\Big)\Big)\mathcal{S}_\perp(\vec{q},\omega) + \Big[16D_\perp^2\{(1-\cos(q_x a))(1-\cos(q_y a))\}\Big] \times\Big(\cos^2\Big(\frac{q_z a}{2}\Big)\Big)\mathcal{S}_\perp(\vec{q},\omega)\Big).$$

In the above expressions, a is the lattice spacing between nearest neighbor copper sites in the same plane, as well as in adjacent planes. $\mathcal{S}_\alpha(\vec{q},\omega)$ is the electronic dynamical structure factor, which in the limit of low frequency is related to the imaginary part of the electronic spin susceptibility by:

$$\text{(E-3)} \qquad \mathcal{S}_\alpha(\vec{q},\omega) \equiv \left(\frac{2\pi\, k_B T}{h\omega}\right) \chi''_{\alpha\alpha}(\vec{q},\omega)\,.$$

The discussion to this point is not unique to the MMP theory. The distinguishing feature of the MMP model is the proposed form for the electronic spin susceptibility:[4]

$$\text{(E-4)} \qquad \chi''_{\alpha\alpha}(\vec{q},\omega\rightarrow 0) \equiv \frac{\pi\chi_{o\alpha}\omega}{\Gamma}\left(1 + \beta_\alpha \frac{(\xi_\alpha/a)^4}{(1+\xi_\alpha^2 q^2)^2}\right).$$

The first term inside the large brackets represents a quasiparticle-like contribution, and the second term is due to the short wavelength antiferromagnetic correlations. The second term is arrived at using a mean-field approach, and the first term is included to compensate for the shortcomings of this approach. $\chi''_{\alpha\alpha}(\vec{q},\omega\rightarrow 0)$ is taken to be independent of q_z. $\chi_{o\alpha}$ is the uniform static susceptibility, and $\vec{q}$ is measured from the zone boundary: $\vec{Q} = (\pi/a,\pi/a)$. Γ is the characteristic spin fluctuation energy for the quasiparticle part, and β_α measures the relative strength of the antiferromagnetic paramagnon contribution to the static spin susceptibility. ξ_α is the antiferromagnetic correlation length, which is assumed to contain all of the normal state temperature dependence of $\chi''_{\alpha\alpha}(\vec{q},\omega\rightarrow 0)$ for the $YBa_2Cu_3O_7$ material. The temperature dependence which MMP proposed for this quantity is:

$$\text{(E-5)} \qquad \left(\frac{\xi_\alpha(T)}{a}\right)^2 = \left(\frac{\xi_\alpha(T=0)}{a}\right)^2 \frac{|Tx|}{Tx + T}\,,$$

with Tx ~ 120 K.

We can calculate the numerical values of the spin-lattice relaxation rates by substituting equations (E-3) through (E-5) into (E-2) and evaluating the integrals. In the original MMP papers, the method of moments was used to evaluate the integrals in order to determine which terms were dominating the relaxation rates. MMP define the following four moments of $\mathcal{S}_\alpha(\vec{q},\omega)$:

$$\text{(E-6a)} \qquad \mathcal{S}_{\alpha 0} = \left(\frac{a}{2\pi}\right)^2 \int d^2q \, \mathcal{S}_\alpha(\vec{q},\omega) \,,$$

$$\text{(E-6b)} \qquad \mathcal{S}_{\alpha 1} = \left(\frac{a}{2\pi}\right)^2 \int d^2q \left[1 - \frac{1}{2}\left\{\cos(q_x a) + \cos(q_y a)\right\}\right] \mathcal{S}_\alpha(\vec{q},\omega) \,,$$

$$\text{(E-6c)} \qquad \mathcal{S}_{\alpha 2} = \left(\frac{a}{2\pi}\right)^2 \frac{4}{5} \int d^2q \left[1 - \frac{1}{2}\left\{\cos(q_x a) + \cos(q_y a)\right\}\right]^2 \mathcal{S}_\alpha(\vec{q},\omega) \,,$$

$$\text{(E-6d)} \qquad \mathcal{S}_{\alpha 3} = \left(\frac{a}{2\pi}\right)^2 \int d^2q \left\{1 - \cos(q_x a)\right\}\left\{1 - \cos(q_y a)\right\} \mathcal{S}_\alpha(\vec{q},\omega) \,.$$

Substituting in the proposed form for $\mathcal{S}_\alpha(\vec{q},\omega)$, they evaluate the integrals and drop terms of order (a/ξ) and higher, obtaining:

$$\text{(E-7a)} \qquad \mathcal{S}_{\alpha 0} = \frac{2\pi^2 \chi_{o\alpha} k_B T}{h\Gamma}\left[1 + \frac{\beta_\alpha}{\pi^2}\left(\frac{\pi}{4}\left(\frac{\xi_\alpha}{a}\right)^2 - \left(\frac{1}{8\pi} + \frac{1}{4\pi^2}\right)\right)\right],$$

$$\text{(E-7b)} \qquad \mathcal{S}_{\alpha 1} = \frac{2\pi^2 \chi_{o\alpha} k_B T}{h\Gamma}\left[1 + \frac{\beta_\alpha}{\pi^2}\left(\frac{\pi}{8}\ln\left(\frac{\xi_\alpha}{a}\right) + 0.1703\right)\right],$$

$$\text{(E-7c)} \qquad \mathcal{S}_{\alpha 2} = \frac{2\pi^2 \chi_{o\alpha} k_B T}{h\Gamma}\left[1 + \frac{\beta_\alpha}{\pi^2}\left(0.2522\right)\right],$$

$$\text{(E-7d)} \qquad \mathcal{S}_{\alpha 3} = \frac{2\pi^2 \chi_{o\alpha} k_B T}{h\Gamma}\left[1 + \frac{\beta_\alpha}{\pi^2}\left(0.1986\right)\right].$$

Equations (E-2) can be rewritten using the moments defined in Equations (E-6), for example:

$$\text{(E-8)} \qquad {}^{63}W1c = \frac{6\pi}{4\mu_\beta^2 h}\left(\mathcal{S}_{\perp 0}\left(A_\perp - 4B\right)^2 + \mathcal{S}_{\perp 1}\left(A_\perp - 4B\right)8B + \mathcal{S}_{\perp 2}\left(20B^2\right)\right).$$

We can now rewrite the relaxation rate formulas such as Equation (E-8), using the approximate values for the moments given in Equations (E-7). MMP,

guided by their analysis of the NMR data, use for their hyperfine coupling constants $A_{\|} = -4B$ and $A_{\perp}/4B = 0.21$. MMP successfully fit the normal state data assuming that $\chi''_{\alpha\alpha}(\vec{q},\omega\rightarrow 0)$ is an isotropic tensor, so that $\chi''_{aa} = \chi''_{bb} = \chi''_{cc} = \chi''$. Thus they drop all of the α subscripts in Equation (E-3) and all subsequent formulas. We will keep the subscripts on $\frac{\xi_\alpha(T)}{a}$ in the formulas below since the purpose of Appendix F is to calculate the effect of an anisotropic $\frac{\xi_\alpha(T)}{a}$ on the Cu(2) relaxation rate anisotropy ratio. The phenomenological forms which MMP propose for the various relaxation rates are:

$$\text{(E-9a)}\quad {}^{63}W1c = \frac{48\pi^3}{8\mu_\beta^2 h^2} B^2 k_B T \left(\frac{\chi_o}{\Gamma}\right)\left(0.294 + \frac{\beta}{\pi^2}\left(0.49\left(\frac{\xi_\perp}{a}\right)^2 - 0.62\ln\left(\frac{\xi_\perp}{a}\right) + 0.0125\right)\right),$$

$$\text{(E-9b)}\quad {}^{63}W1a = \frac{48\pi^3}{8\mu_\beta^2 h^2} B^2 k_B T \left(\frac{\chi_o}{\Gamma}\right) \times \left(0.772 + \frac{\beta}{\pi^2}\left(0.25\left(\frac{\xi_\perp}{a}\right)^2 + 1.58\left(\frac{\xi_{\|}}{a}\right)^2 - 0.31\ln\left(\frac{\xi_\perp}{a}\right) - 0.79\ln\left(\frac{\xi_{\|}}{a}\right) + 0.307\right)\right),$$

$$\text{(E-9c)}\quad {}^{17}W1c = \frac{6\pi^3}{8\mu_\beta^2 h^2} C^2 k_B T \left(\frac{\chi_o}{\Gamma}\right)\left(1 + \frac{\beta}{\pi^2}\left(0.39\ln\left(\frac{\xi_\perp}{a}\right) + 0.17\right)\right),$$

$$\text{(E-9d)}\quad {}^{89}W1c = \frac{24\pi^3}{8\mu_\beta^2 h^2} D^2 k_B T \left(\frac{\chi_o}{\Gamma}\right)\left(1 + \frac{\beta}{\pi^2}(0.2)\right).$$

The remaining free parameters may be adjusted to fit the normal state data quantitatively. The optimal fit to the normal state data in $YBa_2Cu_3O_7$ was obtained when Tx~120 K, $\beta = \pi^2$, and $\frac{\xi_\alpha(T=100\text{ K})}{a} = 2.7$.

These formulas contain all of the characteristics necessary to explain the normal state data in $YBa_2Cu_3O_7$. The Cu(2) rates are dominated by the

term proportional to $\left(\frac{\xi_\alpha(T)}{a}\right)^2$, so recalling the temperature dependence of this quantity (Equation (E-5)), we expect that the $^{63}W1_\alpha$ are almost independent of temperature for T»Tx. On the other hand, the O(2,3) and Y relaxation rates are only weakly dependent on $\left(\frac{\xi_\alpha(T)}{a}\right)$, so they should be Korringa-like, that is W1 $\propto$ T, but with some enhancement over the Korringa slope.

Appendix F. Calculation of $^{63}W1a/^{63}W1c$ Assuming an Anisotropic ξ_α/a

The MMP theory as we have described it in the last appendix was designed to fit the normal state data in $YBa_2Cu_3O_7$ quantitatively.[4] This model was not intended to explain the superconducting state data. Nevertheless, Hammel et al.'s report[90,91] that the relaxation rate ratio $^{63}W1c/^{17}W1c$ was constant below T~120 K strongly suggested that the MMP picture could be simply extended below T_c.[4] To see why, we write down the MMP expression for this ratio, using Equations (E-9) from the last appendix:

$$(F\text{-}1)\quad \frac{^{63}W1c}{^{17}W1c} = \left\{\frac{8\,B^2}{C^2}\right\} \frac{\left(0.294+\frac{\beta}{\pi^2}\left(0.49\left(\frac{\xi_\perp}{a}\right)^2 - 0.62\ln\left(\frac{\xi_\perp}{a}\right)+0.0125\right)\right)}{\left(1+\frac{\beta}{\pi^2}\left(0.39\ln\left(\frac{\xi_\perp}{a}\right)+0.17\right)\right)}.$$

We have assumed that β and $[\chi_o/\Gamma]$ are isotropic. In the normal state, this ratio has a temperature dependence, because:

$$(F\text{-}2)\qquad \left(\frac{\xi_\alpha(T)}{a}\right)^2 = \left(\frac{\xi_\alpha(T=0)}{a}\right)^2 \frac{|Tx|}{Tx+T},$$

with Tx ~ 120 K. Hammel et al.'s result[90,91] implies that this temperature dependence must cease below T~120 K, i.e. $\left(\frac{\xi_\perp}{a}\right)$ is independent of temperature for T < 120 K. The implication of this statement is that the short-range antiferromagnetic correlations persist into the superconducting state.

We can also write down the MMP expression for the ratio $^{63}W1a/^{63}W1c$, using Equations (E-9) from the last appendix:

$$(F\text{-}3)\quad \frac{^{63}W1a}{^{63}W1c} = \frac{\left(0.772+\frac{\beta}{\pi^2}\left(0.25\left(\frac{\xi_\perp}{a}\right)^2+1.58\left(\frac{\xi_\parallel}{a}\right)^2-0.31\ln\left(\frac{\xi_\perp}{a}\right)-0.79\ln\left(\frac{\xi_\parallel}{a}\right)-0.307\right)\right)}{\left(0.294+\frac{\beta}{\pi^2}\left(0.49\left(\frac{\xi_\perp}{a}\right)^2-0.62\ln\left(\frac{\xi_\perp}{a}\right)+0.0125\right)\right)}.$$

We have observed that the ratio $\frac{^{63}W1a}{^{63}W1c}$ drops just inside the superconducting state (T<93 K). Starting with the assumption that $\left(\frac{\xi_{\perp}}{a}\right)$ is independent of temperature for T < 120 K, the only free parameter left in Equation (F-3) to explain the superconducting $\frac{^{63}W1a}{^{63}W1c}$ data is the temperature variation of $\left(\frac{\xi_{\parallel}}{a}\right)$ below T~120 K. We calculated $\frac{^{63}W1a}{^{63}W1c}$ as a function of $\left(\frac{\xi_{\parallel}}{a}\right)$, and the results are displayed in Figure 64.

Our results imply that it would be possible to simultaneously explain the temperature independence[90,91] of $^{63}W1c/^{17}W1c$ below T~120 K and our observation of the temperature dependence of the ratio $^{63}W1a/^{63}W1c$ below T_c. The values of $\left(\frac{\xi_{\alpha}(T)}{a}\right)$ which we obtain may then be substituted into the equations for the other Y and O(2,3) relaxation rates, which may then be checked against the data, placing additional constraints on this explanation. We found that the strong magnetic field (80 kGauss) O(2,3) relaxation rate data are consistent with this explanation, but to explain the Y relaxation rate data below Tc, we need to assume that $\chi''_{\alpha\alpha}(\vec{q},\omega\rightarrow 0)$ becomes dependent on q_z. This would be the case if some sort of interplanar correlations developed between the electronic spins.

The difficulty with these results is that we have broken spin-rotation invariance below T_c. In other words $\chi''_{\parallel}(T/T_c) \neq \chi''_{\perp}(T/T_c)$. MMP have pointed out to us that this would be consistent with a BCS, spin-triplet pairing state.[118,132] However, the Knight shift data are consistent with a BCS, spin-singlet pairing state, as we have discussed in Chapter 6. MMP do agree that an anisotropy in $\chi''_{\alpha\alpha}(\vec{q},\omega\rightarrow 0)$ which is much larger near $\vec{q} \sim \vec{Q}$ than near $\vec{q} \sim 0$ might be possible in principle, but we have no microscopic picture for why

this unusual anisotropy might develop below T_c.

The utility of this calculation is that we now have a qualitative feeling for the effect of anisotropy in the spin-susceptibility tensor.

Appendix G. Calculation of ^{63}W1a/^{63}W1c Assuming $\beta(T)$ and $\xi(T)/a$

MMP suggested an alternative extension of their normal state model to explain our superconducting state data.[132] This explanation retained spin-rotation invariance in the superconducting state, so that $\chi''_{\parallel}(T/T_c) = \chi''_{\perp}(T/T_c) = \chi''(T/T_c)$. They postulated that one could simultaneously explain both the temperature independence of ^{63}W1c/^{17}W1c and the temperature dependence of 63W1a/63W1c for T<Tc, provided that both $\beta(T)$ and $\xi(T)/a$ are temperature dependent in the superconducting state. The motivation for this proposal was that some sort of $\vec{q}$-dependent energy gap (e.g. d-wave) would effectively modify the shape in $\vec{q}$-space of the $\chi''_{\alpha\alpha}(\vec{q},\omega\rightarrow 0)$ which comes into the expressions for the relaxation rates. The temperature dependent $\beta(T)$ and $\xi(T)/a$ may simulate this effect.

Acting upon their suggestion, we have independently calculated the quantity $\frac{^{63}W1a}{^{63}W1c}$ as a function of $\frac{^{63}W1c}{^{17}W1c}$, for a range of values of β and ξ/a. Our results are shown in Figure 65, where we have assumed that $A_{\parallel} = 4B$ and $A_{\perp}/B = 0.225$, and we have used the MMP-proposed form of the imaginary part of the electronic spin susceptibility (Equation (E-4)). This form of the susceptibility has a large peak at the antiferromagnetic wavevector: $\vec{q}=\vec{Q} = (\pi/a,\pi/a)$.

In order to obtain these results, we calculated the spin-lattice relaxation rates using the exact MMP expressions given in Equations (E-2). This was necessary because we wished to consider small values of ξ/a, and our approximate expressions for the various moments of the structure factor, Equations (E-7), break down in this limit. To calculate the relaxation rates

using Equations (E-2), we evaluated the $\vec{q}$-space integrals numerically using a two-dimensional Simpson's rule procedure.[139]

We have also investigated the effect on these curves of making the peak in $\chi''_{\alpha\alpha}(\vec{q},\omega\rightarrow 0)$ be incommensurate (peaking at $\vec{q}=\vec{Q}+\vec{\delta}$). In Figure 71, we show the curves calculated assuming that $\vec{\delta} = (\pm 0.3/a, \pm 0.3/a)$, which is approximately one tenth of the distance from the zone corner to the zone center. The hyperfine coupling constants and the range of ξ/a is the same as in Figure 65. For a given value of β and ξ/a, the calculated point in Figure 71 lies at a lower value of the ratio ^{63}W1c/^{17}W1c than the analogous point in Figure 65. We can understand this by noting that the peak in $\chi''_{\alpha\alpha}(\vec{q},\omega\rightarrow 0)$ is quite large compared to the $\vec{q}= 0$ contribution. When the peak is commensurate, ^{17}W1c is dominated by the $\vec{q}= 0$ contribution, while ^{63}W1c has a large contribution from the peak region, because the hyperfine form factors for the two rates are different. As the peak is moved away from the $\vec{q}=\vec{Q}$ region (which ^{17}W1c is insensitive to), both ^{63}W1c and ^{17}W1c become dominated by this part of $\chi''_{\alpha\alpha}(\vec{q},\omega\rightarrow 0)$, so the ratio ^{63}W1c/^{17}W1c decreases.

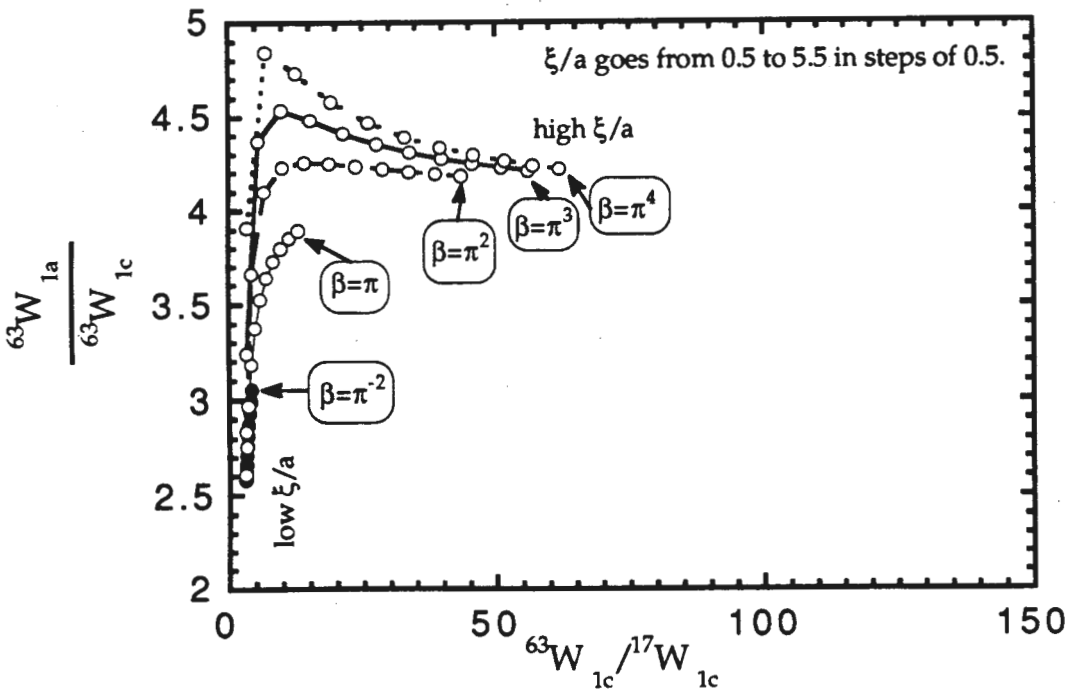

Figure 71. The $^{63}Cu(2)$ relaxation rate anisotropy ratio, $^{63}W_{1a}/^{63}W_{1c}$, versus the $^{63}Cu(2)$ to $^{17}O(2,3)$ relaxation rate ratio, $^{63}W_{1c}/^{17}W_{1c}$. This plot assumes that the large peak in $\chi''_{\alpha\alpha}(\vec{q},\omega\rightarrow 0)$ is incommensurate (peaking at $\vec{q}=\vec{Q}+\vec{\delta}$, where $\vec{Q} = (\pi/a,\pi/a)$ and $\vec{\delta} = (\pm 0.3/a,\pm 0.3/a)$). There are five curves each with different powers of π for β. The circles along each curve occur every time the isotropic ξ/a increases by 0.5 as it varies from 0.5 to 5.5. The results for the commensurate case ($\vec{\delta} = (0,0)$) are shown in Figure 65.

References

1 J. G. Bednorz and K. A. Müller, Z. Phys. B **64**, 189 (1986).

2 K. Levin, J. H. Kim, J. P. Lu, and Q. Si, Physica C **175**, 449 (1991).

3 C. M. Varma, P. B. Littlewood, S. Schmitt-Rink, E. Abrahams, and A. E. Ruckenstein, Phys. Rev. Lett. **63**, 1996 (1989).

4 A. J. Millis, H. Monien, and D. Pines, Phys. Rev. B **42**, 167 (1990).

5 P. W. Anderson, Science **235**, 1196 (1987).

6 R. B. Laughlin, Science **242**, 525 (1988).

7 L. C. Hebel and C. P. Slichter, Phys. Rev. **107**, 901 (1957).

8 L. C. Hebel and C. P. Slichter, Phys. Rev. **113**, 1504 (1959).

9 H. E. Bommel, Phys. Rev. **96**, 220 (1954).

10 R. W. Morse, and H. V. Bohm, Phys. Rev. **108**, 1094 (1957).

11 J. Bardeen, L. N. Cooper, and J. R. Schrieffer, Phys. Rev. **108**, 1175 (1957).

12 BCS Nobel Prize Lectures, reprinted in Physics Today **26**, 23 (1973).

13 S. E. Barrett, D. J. Durand, C. H. Pennington, C. P. Slichter, T. A. Friedmann, J. P. Rice, and D. M. Ginsberg, Phys. Rev. B **41**, 6283 (1990).

14 S. E. Barrett, J. A. Martindale, D. J. Durand, C. H. Pennington, C. P. Slichter, T. A. Friedmann, J. P. Rice, and D. M. Ginsberg, Phys. Rev. Lett. **66**, 108 (1991).

15 J. A. Martindale, S. E. Barrett, C. A. Klug, K. E. O'Hara, S. M. DeSoto, C. P. Slichter, T. A. Friedmann, and D. M. Ginsberg, to be published in the Proceedings of the M^2S-HTSC III Conference, 7/22/91-7/26/91, Kanazawa, Japan.

16 J. A. Martindale, S. E. Barrett, C. A. Klug, K. E. O'Hara, S. M. DeSoto, C. P. Slichter, T. A. Friedmann, and D. M. Ginsberg, submitted to Phys. Rev. Lett.

17 N. Bulut and D. Scalapino, preprint.

18 J. P. Lu, preprint.

19 J. P. Lu and D. Pines, Private Communication.

20 M. K. Wu, J. R. Ashburn, C. J. Torng, P. H. Hor, R. L. Meng, L. Gao, Z. J. Huang, Y. Q. Wang, and C. W. Chu, Phys. Rev. Lett. **58**, 908 (1982).

21 J. B. Boyce, F. Bridges, T. Claeson, and M. Nygren, Phys. Rev. B **39**, 6555 (1989).

22 M. A. Beno, L. Soderholm, D. W. Capone, II, D. G. Hinks, J. D. Jorgensen,

J. D. Grace, I. K. Schuller, C. U. Segre and K. Zhang, App. Phys. Lett. **51**, 57, (1987).

23 J. M. Tranquada, A. H. Moudden, A. I. Goldman, P. Zolliker, D. E. Cox, G. Shirane, S. K. Sinha, D. Vaknin, D. C. Johnston, M. S. Alvarez, A. J. Jacobson, J. T. Lewandowski, and J. M. Newsam, Phys. Rev. B **38**. 2477 (1988).

24 B. Battlogg in High Temperature Superconductivity: Proc. Los Alamos Symp. 1989, K. S. Bedell, D. Coffey, D. E. Meltzer, D. Pines, and J. R. Schrieffer, eds., (Addison-Wesley, Redwood City, 1990).

25 S. L. Cooper and M. V. Klein, Comments on Condensed Matter Physics **XV**, 99 (1990).

26 compiled from Physical Properties of High Temperature Superconductors I, D. M. Ginsberg, ed., (World Scientific, Singapore, 1989).

27 D. M. Ginsberg, Chapter 1, Physical Properties of High Temperature Superconductors I, D. M. Ginsberg, ed., (World Scientific, Singapore, 1989).

28 J. F. Annett, N. Goldenfeld, and S. R. Renn, Chapter 9, Physical Properties of High Temperature Superconductors II, D. M. Ginsberg, ed., (World Scientific, Singapore, 1990).

29 R. M. Hazen, Chapter 3, Physical Properties of High Temperature Superconductors II, D. M. Ginsberg, ed., (World Scientific, Singapore, 1990).

30 R. J. Birgeneau and G. Shirane, Chapter 4, Physical Properties of High Temperature Superconductors I, D. M. Ginsberg, ed., (World Scientific, Singapore, 1989).

31 Z. Schlesinger, R. T. Collins, F. Holtzberg, C. Feild, S. H. Blanton, U. Welp, G. W. Crabtree, Y. Fang, and J. Z. Liu, Phys. Rev. Lett. **65**, 801 (1990).

32 T. A. Friedmann, M. W. Rabin, J. Giapintzakis, J. P. Rice, and D. M. Ginsberg, Phys. Rev. B **42**, 6217 (1990).

33 J. C. Campuzano, G. Jennings, M. Faiz, L. Beaulaigue, B. W. Veal, J. Z. Liu, A. P. Paulikas, K. Vandervoort, H. Claus, R. S. List, A. J. Arko, and R. J. Bartlett, Phys. Rev. Lett. **64**, 2308 (1990).

34 Handbook of Thermophysical Properties of Solid Materials, Volume I:

Elements, Revised Edition, A. Goldsmith, T. Waterman, and H. Hirschhorn, eds., (Macmillan, New York, 1961).

35 J. P. Rice, J. Giapintzakis, D. M. Ginsberg, and J. M. Mochel, to appear in Phys. Rev. B.

36 S. L. Cooper, A. L. Kotz, M. A. Karlow, M. V. Klein, W. C. Lee, J. Giapintzakis, and D. M. Ginsberg, preprint.

37 J. Rossat-Mignod, L. P. Regnault, C. Vettier, P. Bourges, P. Burlet, J. Bossy, J. Y. Henry, and G. Lapertot, preprint.

38 C. P. Slichter, Principles of Magnetic Resonance, 3rd Edition, (Springer, New York, 1989).

39 V. Jaccarino in Theory of Magnetism in Transition Metals, International School of Physics, "Enrico Fermi", Course XXXVII, (Academic, New York, 1967).

40 C. P. Slichter, S. E. Barrett, L. Becerra, D. J. Durand, C. A. Klug, J. A. Martindale, C. H. Pennington, J. H. Ross, S. Shore, Z. Wang, and D. Zax, Chapter III, Pulse Techniques in Magnetic Resonance, A Recognition of E. L. Hahn, to be published by Oxford University Press.

41 E. L. Hahn, Phys. Rev. **80**, 580 (1950).

42 V. H. Schmidt in Pulsed Magnetic and Optical Resonance, Proceedings of the Ampère International Summer School III, Basko polje, 2-13 September, 1971, R. Blinc, ed., (University of Ljubljana, Ljubljana, Yugoslavia, 1972), pp. 75-83.

43 C. H. Pennington, Ph. D. thesis, University of Illinois at Urbana-Champaign, 1989.

44 T. Moriya, J. Phys. Soc. Jpn. **18**, 516 (1963).

45 J. Winter, Magnetic Resonance in Metals, (Clarendon, Oxford, 1971).

46 D. E. MacLaughlin in Solid State Physics, **31**, H. Ehrenreich, F. Seitz, and D. Turnbull, eds., (Academic, New York, 1976).

47 see, for example, M. Tinkham, Introduction to Superconductivity, (McGraw-Hill, New York, 1975).

48 F. Reif, Phys. Rev. **102**, 1417 (1956).

49 W. D. Knight, G. M. Androes, and R. H. Hammond, Phys. Rev. **104**, 852 (1956).

50 H. L. Fine, M. Lipsicas, M. Strongin, Phys. Lett. **29A**, 366 (1969).

51 J. J. Spokas and C. P. Slichter, Phys. Rev. **113**, 1462, (1959).

52 J. J. Spokas, Ph. D. thesis, University of Illinois at Urbana-Champaign, 1958.
53 A. G. Redfield and A. G. Anderson, Phys. Rev. **116**, 583 (1959).
54 K. Yosida, Phys. Rev., **110**, 769 (1958).
55 Y. Masuda and A. G. Redfield, Phys. Rev. **125**, 159 (1962).
56 P. Pincus, A. C. Gossard, V. Jaccarino, and J. H. Wernick, Phys. Lett. **13**, 21 (1964).
57 J. -M. Delrieu and J. -M. Winter, Solid State Commun. **4**, 545 (1966).
58 Y. Masuda and N. Okubo, J. Phys. Soc. Jpn. **26**, 309 (1969).
59 B. G. Silbernagel, M. Weger, and J. H. Wernick, Phys. Rev. Lett. **17**, 384 (1966).
60 J. P. Rice, E. D. Bukowski, and D. M. Ginsberg, J. Low Temp. Phys. **77**, 119 (1989).
61 D. E. Farrell, B. S. Chandrasekhar, M. R. DeGuire, M. M. Fang, V. G. Kogan, J. R. Clem, and D. K. Finnemore, Phys. Rev. B **36**, 4025 (1987).
62 D. J. Durand, Ph. D. thesis, University of Illinois at Urbana-Champaign, 1989.
63 H. Y. Carr and E. M. Purcell, Phys. Rev. **94**, 630 (1954).
64 S. Meiboom and D. Gill, Rev. Sci. Instrum. **29**, 688 (1958).
65 J. H. Ross, Jr., Ph. D. thesis, University of Illinois at Urbana-Champaign, 1986.
66 see, for example, E. Fukushima and S. B. W. Roeder, Experimental Pulse NMR, A Nuts and Bolts Approach, (Addison-Wesley, Reading, MA, 1981).
67 for a recent review, C. H. Pennington and C. P. Slichter, Chapter 5, Physical Properties of High Temperature Superconductors II, D. M. Ginsberg, ed., (World Scientific, Singapore, 1990).
68 for a recent review, R. E. Walstedt and W. W. Warren, Jr., Science **248**, 1082 (1990).
69 for a recent review, A. J. Millis in High Temperature Superconductivity: Proc. Los Alamos Symp. 1989, K. S. Bedell, D. Coffey, D. E. Meltzer, D. Pines, and J. R. Schrieffer, eds., (Addison-Wesley, Redwood City, 1990).
70 H. Lütgemeier and M. W. Pieper, Solid State Commun. **64**, 267 (1987).
71 M. Mali, D. Brinkmann, L. Pauli, J. Roos, H. Zimmermann, and J. Hullinger, Phys. Lett. A **124**, 112 (1987).

72 {when reading this early paper, Cu(2) should replace the authors' Cu(1), and Cu(1) should replace the authors' Cu(2)} R. E. Walstedt, W. W. Warren, Jr., R. F. Bell, G. F. Brennert, G. P. Espinosa, J. P. Remeika, R. J. Cava, and E. A. Reitman, Phys. Rev. B **36**, 5727 (1987).

73 {when reading this early paper, Cu(2) should replace the authors' Cu(1), and Cu(1) should replace the authors' Cu(2)} W. W. Warren, Jr., R. E. Walstedt, G. F. Brennert, G. P. Espinosa, J. P. Remeika, Phys. Rev. Lett. **59**, 1860 (1987).

74 C. H. Pennington, D. J. Durand, D. B. Zax, C. P. Slichter, J. P. Rice, and D. M. Ginsberg, Phys. Rev. B **37**, 7944 (1988).

75 C. H. Pennington, D. J. Durand, C. P. Slichter, J. P. Rice, E. D. Bukowski, and D. M. Ginsberg, Phys. Rev. B, **39**, 274, (1989).

76 C. H. Pennington, D. J. Durand, C. P. Slichter, J. P. Rice, E. D. Bukowski, and D. M. Ginsberg, Phys. Rev. B, **39**, 2902, (1989).

77 R. E. Walstedt, W. W. Warren, Jr., R. F. Bell, G. F. Brennert, G. P. Espinosa, R. J. Cava, L. F. Schneemeyer, and J. V. Waszczak, Phys. Rev. B **38**, 9299 (1988).

78 R. E. Walstedt, W. W. Warren, Jr., R. F. Bell, G. P. Espinosa, Phys. Rev. B **40**, 2572 (1989).

79 T. Imai, T. Shimizu, T. Tsuda, H. Yasuoka, T. Takabatake, Y. Nakazawa, and M. Ishikawa, J. Phys. Soc. Jpn. **57**, 1771 (1988).

80 T. Imai, T. Shimizu, H. Yasuoka, Y. Ueda,and K. Kosuge, J. Phys. Soc. Jpn. **57**, 2280 (1988).

81 T. Imai, H. Yasuoka, T. Shimizu, Y. Ueda, K. Yoshimura, and K. Kosuge, Physica C, **162-164**, 169, (1989).

82 T. Imai, Ph. D. thesis, Institute for Solid State Physics, The University of Tokyo, 1991.

83 J. T. Markert, T. W. Noh, S. E. Russek, and R. M. Cotts, Solid State Commun. **63**, 847 (1987).

84 H. Alloul, P. Mendels, G. Collin, and P. Monod, Phys. Rev. Lett. **61**, 746 (1988).

85 G. Balakrishnan, R. Dupree, I. Farnan, D. McK Paul, and M. E. Smith, J. Phys. C **21**, L847 (1988).

86 H. Alloul, T. Ohno, and P. Mondels, Phys. Rev. Lett. **63**, 1700 (1989).

87 H. Bleier, P. Bernier, D. Jerome, J. M. Bassat, J. P. Coutres, B. DuBois, and

Ph. Odier, J. Phys. (Paris) **49**, 1825, (1988).

88 C. Coretsopoulos, H. C. Lee, E. Ramli, L. Reven, T. Rauchfuss, and E. Oldfield, Phys. Rev. B **39**, 781 (1989).

89 M. Takigawa, P. C. Hammel, R. H. Heffner, Z. Fisk, K. C. Ott, and J. D. Thompson, Phys. Rev. Lett. **63**, 1865 (1989).

90 P. C. Hammel, M. Takigawa, R. H. Heffner, Z. Fisk, K. C. Ott, Phys. Rev. Lett. **63**, 1992 (1989).

91 P. C. Hammel, M. Takigawa, R. H. Heffner, Z. Fisk, K. C. Ott, Physica C **162-164**, 177 (1989).

92 D. L. Cox and B. R. Trees, Phys. Rev. B **41**, 11260 (1990).

93 F. C. Zhang and T. M. Rice, Phys. Rev. B **37**, 3759 (1988).

94 M. Takigawa, A. P. Reyes, P. C. Hammel, J. D. Thompson, R. H. Heffner, Z. Fisk, K. C. Ott, Phys. Rev. B **43**, 247 (1991).

95 W. W. Warren, Jr., R. E. Walstedt, G. F. Brennert, R. J. Cava, R. Tycko, R. F. Bell, and G. Dabbagh, Phys. Rev. Lett. **62**, 1193 (1989).

96 R. E. Walstedt in High Temperature Superconductivity: Proc. Los Alamos Symp. 1989, K. S. Bedell, D. Coffey, D. E. Meltzer, D. Pines, and J. R. Schrieffer, eds., (Addison-Wesley, Redwood City, 1990).

97 F. Mila and T. M. Rice, Physica C **157**, 561 (1989).

98 M. Takigawa, P. C. Hammel, R. H. Heffner, and Z. Fisk, Phys. Rev. B **39**, 7371 (1989).

99 E. Oldfield, C. Coretsopoulos, S. Yang, L. Reven, H. C. Lee, J. Shore, O. H. Han, E. Ramli, and D. S. Hinks, Phys. Rev. B **40**, 6832 (1989).

100 B. S. Shastry, Phys. Rev. Lett. **63**, 1288 (1989).

101 F. Mila and T. M. Rice, Phys. Rev. B **40**, 11382 (1989).

102 this figure was inspired by: T. Imai, Figs. 5-1, 5-2 and 5-3, Ph. D. thesis, Institute for Solid State Physics, University of Tokyo, 1991.

103 J. Rossat-Mignod, L. P. Regnault, C. Vettier, P. Burlet, J. Y. Henry, and G. Lapertot, Physica B **169**, 58 (1991).

104 T. Machi, I. Tomeno, T. Miyatake, N. Koshizuka, and S. Tanaka, T. Imai, and H. Yasuoka, Physica C **173**, 32 (1991).

105 H. Zimmerman, M. Mali, D. Brinkmann, J. Karpinski, E. Kaldis, and S. Rusiecki, Physica C **159**, 681 (1989).

106 R. E. Walstedt, R. F. Bell, and D. B. Mitzi, to appear in Phys. Rev. B1, October 1991.

107 K. Fujiwara, Y. Kitaoka, K. Asyama, H. Sasakura, S. Minamigawa, K. Nakahigashi, S. Nakanishi, M. Kogachi, N. Fukuoka, and A. Yanase, J. Phys. Soc. Jpn. **58**, 380 (1989).

108 B. Battlogg, Physica B **169**, 7, (1991).

109 G. Shirane, R. J. Birgeneau, Y. Endoh, P. Gehring, M. A. Kastner, K. Kitazawa, H. Kojima, I. Tanaka, T. R. Thurston, and K. Yamada, Phys. Rev. Lett. **63**, 330 (1989).

110 R. E. Walstedt, R. F. Bell, L. F. Schneemeyer, J. V. Waszczak, and G. P. Espinosa, submitted to Phys. Rev. B.

111 T. Shimizu, H. Yasuoka, T. Tsuda, K. Koga, and Y. Ueda, Bull. Magn. Reson. **12**, 39 (1990).

112 Y. Yoshinari, H. Yasuoka, et al., poster at the M^2S-HTSC III Conference, 7/22/91-7/26/91, Kanazawa, Japan, and private communication.

113 J. Martindale, private communication.

114 N. L. Huang, R. Orbach, E. Šimánek, J. Owen, and D. R. Taylor, Phys. Rev. **156**, 383 (1967).

115 D. J. Durand, S. E. Barrett, C. H. Pennington, C. P. Slichter, T. A. Friedmann, J. P. Rice, and D. M. Ginsberg, in Strong Correlation and Superconductivity: Proceedings of the IBM Japan International Symposium, Mt. Fuji, Japan, 21-25 May, 1989, H. Fukuyama, S. Maekawa, and A. P. Malozemoff, eds., (Springer-Verlag, Berlin; New York, 1989).

116 S. E. Shore, J. -Ph. Ansermet, C. P. Slichter, and J. H. Sinfelt, Phys. Rev. Lett. **58**, 953 (1987).

117 M. Takigawa, P. C. Hammel, R. H. Heffner, Z. Fisk, J. D. Thompson, and M. Maley, Physica C **162-164**, 175 (1989).

118 A. J. Leggett, Rev. Mod. Phys. **47**, 331 (1975).

119 H. Monien and D. Pines, Phys. Rev. B **41**, 6297 (1990).

120 R. H. Hammond and G. M. Kelly, Phys. Rev. Lett. **18**, 156 (1967).

121 F. Reif, Phys. Rev. **106**, 208 (1957).

122 P. W. Anderson, Phys. Rev. **96**, 266 (1954).

123 M. Horvatíc, Y. Berthier, P. Butaud, Y. Kitaoka, P. Ségransan, C. Berthier, H. Katayama-Yoshida, Y. Okabe, and T. Takahashi, Physica C **159**, 689 (1989).

124 M. Takigawa, P. C. Hammel, R. H. Heffner, Z. Fisk, K. C. Ott, and J. D. Thompson, Physica C **162-164**, 853 (1989).

125 J. -M. Duan and A. J. Leggett, preprint.
126 U. Welp, W. K. Kwok, G. W. Crabtree, K. G. Vandervoort, and J. Z. Liu, Phys. Rev. Lett. **62**, 1908 (1989).
127 Z. Hao, J. R. Clem, M. W. McElfresh, L. Civale, A. P. Malozemoff, and F. Holtzberg, Phys. Rev. B, **43**, 2844 (1991).
128 H. Monien, private communication.
129 M. Tachiki and S. Takahashi, preprint.
130 M. Takigawa, J. L. Smith, and W. L. Hults, submitted to Phys. Rev. B.
131 H. Monien, D. Pines, and M. Takigawa, Phys. Rev. B **43**, 258 (1991).
132 A. J. Millis, H. Monien, and D. Pines, private communication.
133 J. Annett, N. Goldenfeld, and S. R. Renn, Phys. Rev. B **43**, 2778 (1991).
134 S. Sridhar, D. H. Wu, and W. Kennedy, Phys. Rev. Lett. **63**, 1873 (1989).
135 A. Z. Genack and A. G. Redfield, Phys. Rev. Lett. **31**, 1204 (1973).
136 P. Monthoux, A. V. Balatsky, and D. Pines, preprint.
137 T. Moriya, Y. Takahashi, and K. Ueda, J. Phys. Soc. Jpn. **59**, 2905 (1990).
138 T. A. Friedmann and J.P. Rice, private communication.
139 W.H. Press, B.P. Flannery, S. A. Teukolsky, W.T. Vetterling, Numerical Recipes in Pascal, (Cambridge University Press, Cambridge, 1989).
140 H. Monien, P. Monthoux, and D. Pines, Phys. Rev. B **43**, 275 (1991).
141 J.P. Lu, private communcation.

Vita

Sean Eric Barrett was born in Yonkers, New York on August 20, 1965. He graduated from The Albany Academy in Albany, New York in 1983. He then entered Princeton University in Princeton, New Jersey as a National Merit Scholar. From September, 1985 to June, 1986, he was a Laboratory Teaching Assistant for Professor Sigurd Wagner's course: EECS 286-"The Physical Foundations of Electrical Engineering". Sean's Senior Thesis resulted in one publication: Experimental Search for Dynamic Current Oscillations in the Quantum Hall Effect, V.J. Goldman, S.E. Barrett, D.C. Tsui, and K. Alavi, Phys. Lett. A **123**, 311, (1987). He graduated from Princeton in June, 1987 with an A. B. in Physics, Cum Laude. He also received a Certificate in Engineering Physics, with a Concentration in Electronic Materials and Devices.

Sean entered the Physics Department of the University of Illinois at Urbana-Champaign in August, 1987. He was a Teaching Assistant for Physics 101 and 102 from August, 1987 to June, 1988. He joined Professor C. P. Slichter's group as a Research Assistant in June, 1988. Sean received his M.S. in Physics in October, 1988. He was a University Fellow from September, 1989 to August, 1990. He was an IBM Predoctoral Fellow from September, 1990 to June, 1991.